Design and Modeling of Structural Joints in Precast Concrete Structures

Sørensen, Jesper Harrild

Publication date:
2018

Document Version
Publisher's PDF, also known as Version of record

Design and Modeling of Structural Joints in Precast Concrete Structures

Jesper Harrild Sørensen

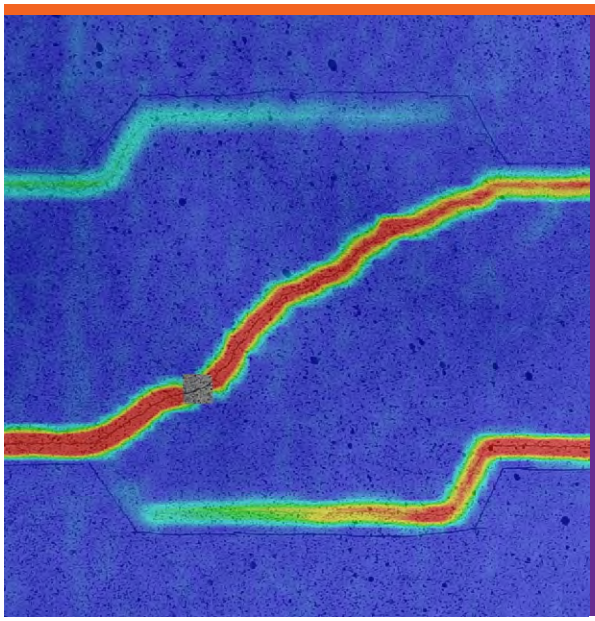

Jesper Harrild Sørensen

PhD Thesis

Department of Civil Engineering
2018

DTU Civil Engineering R-384

DTU Civil Engineering
Department of Civil Engineering

Design and Modeling of Structural Joints in Precast Concrete Structures

Jesper Harrild Sørensen

PhD Thesis

Department of Civil Engineering
Technical University of Denmark

July 2017

Supervisors:

Professor Linh Cao Hoang
Associate Professor John Forbes Olesen
Associate Professor Gregor Fischer

Assesment Committee:

Professor Rune Brincker, DTU Civil Engineering, Denmark
Professor Dr.-Ing, Josef Hegger, Institute of Structural Concrete, RWTH Aachen University, Germany
Senior Scientist, Miguel Fernandez Ruiz, École Polytechnique Fédérale de Lausanne, Switzerland

Design and Modeling of Structural Joints in Precast Concrete Structures

Printed by -
Department of Civil Engineering
Technical University of Denmark
ISBN: 9788778774798

Preface

This thesis is submitted as a partial fulfillment of the requirements for obtaining the Danish PhD degree. The study has been undertaken at the Department of Civil Engineering, Technical University of Denmark, under supervision of Professor, PhD Linh Cao Hoang and co-supervised by Associate Professor, PhD John Forbes Olesen and Associate Professor, PhD Gregor Fischer.

During the study, a new design of a structural connection for precast concrete shear walls has been investigated and the results are promising. The thesis gives an overview of the different load carrying mechanisms that have been studied during the period of the project. A collection of papers is appended.

Jesper Harrild Sørensen
Kgs. Lyngby
July 2017

Preface to Published Version

The thesis was defended at a public defense on Monday the 22nd of January 2018. Subsequently the PhD degree was awarded from the Technical University of Denmark.

Compared to the version submitted for assessment, a small number of minor changes have been implemented. The status of Paper I has changed from accepted to published and Paper III has changed from submitted to published.

Jesper Harrild Sørensen
Kgs. Lyngby
January 2018

Acknowledgments

First and foremost, I would like to express my sincere appreciation for the great support and the always enthusiastic and helpful guidance from my supervisors, Professor Linh Cao Hoang, Associate Professor John Forbes Olesen, and Associate Professor Gregor Fischer, all from the Department of Civil Engineering at the Technical University of Denmark (DTU). Furthermore, I wish to express my gratitude to Professor Aurelio Muttoni, École Polytechnique Fédérale de Lausanne, EPFL, for a very interesting research stay with his group in the structural concrete laboratory, IBETON, during the summer of 2016.

I also wish to acknowledge a number of people who supported the project. The experimental work has been supported by the Danish Precast Concrete Association, the COWI foundation, and CRH Concrete A/S. Furthermore participation in conferences and the realization of the external research stay have been financially supported by the Otto Mønsted Foundation, Professor H. I. Hannovers scholarship, and Erik Hegentofts scholarship. The contributions are much valued.

Furthermore, a number of students have assisted in the experimental campaigns performed within the scope of this thesis. M.Sc. Baldur Halldórsson is acknowledged for his contributions to the triaxial tests and for the support with the single shear key tests. B.Sc. Frederik Jensen and B.Sc. Frederik Vind are acknowledged for support with triaxial tests. For the tests on the tensile capacity of the loop connections, M.Sc. Jacob Svejgaard and Lasse Øvrelid are acknowledged. For tests on the shear capacity of the keyed shear connections, B.Eng. Rune Pedersen, B.Eng. Mads Herløv, M.Sc. Jacob Svejgaard, M.Sc. Lasse Øvrelid, M.Sc. Jakob Olsen and M.Sc. Rasmus Hou are acknowledged for their contributions. Finally, for support with the tests on double-sided dowel joints, M.Sc. Nikolai Bach and M.Sc. Martin Hansen are acknowledged. Furthermore, the technical staff of the structural laboratory at the Technical University of Denmark is greatly acknowledged. Without the support of the above mentioned persons, the planning and execution of the experimental investigations would not have been possible. I sincerely appreciate the contributions.

In addition, colleagues from the Department of Civil Engineering, DTU, and colleagues from IBETON, are thanked for many interesting conversations on various topics and for the always encouraging approach to the life as a PhD student.

Abstract

Precast reinforced concrete components are widely used for construction of buildings in many industrialized countries. The benefits of the precast method, as compared to the cast in-situ method, lie primarily in the easier quality and production control of the structural components and in the on-site construction speed. The challenges appear in the on-site assembly phase, where structural integrity has to be ensured by in-situ cast connections in narrow zones. These connections are essential for the overall structural behavior and for this reason, strong and ductile connections that at the same time comply with the construction sequences for the particular structure, are important for a well-performing solution.

Current best practice for design of shear connections has been developed over decades and has primarily been aimed at solutions that are easy to implement on the construction site. The related calculation methods are mostly based on experience and empirical formulas. The strength and ductility of the current connection design are not necessarily adequate for structures, where large loads have to be transferred. The potential for improvement of the structural connections is therefore significant, as better solutions may enhance the overall structural behavior and lead to more economic designs.

This study concerns an investigation of in-plane connections between precast shear walls. A new design with '2-on-2' loop connections is suggested. The significance of the new design is the orientation of the U-bar loops and the use of a double T-headed rebar in the overlapping area of the U-bars. The investigation covers several independent research topics, which in combination provides a broad knowledge of the behavior of keyed shear connections.

As the first topic, the structural behavior of mortar is investigated. This is relevant as mortar with small aggregates is typically used to grout the narrow connections between the precast components. The study comprises triaxial tests and push-off tests aiming to investigate the behavior of mortar during failure. Next, the tensile capacity of the new loop connection design is tested and analyzed by use of upper bound plasticity models. This study is relevant as the ability of the U-bar loops to transfer tension is a prerequisite for the shear connection to transfer shear loads. The established models, supported by tests, can be used to design the loop connection in such a way, that the tensile capacity is governed by yielding of the U-bars and not by a brittle failure of the grout. This is important in order to obtain a ductile

response when the connection is loaded in shear.

The main focus of the thesis is test and modeling of keyed shear connections. An extensive experimental program is presented. The particular layout of the test specimens allows for a direct comparison of the conventional shear connection design with the new design concept. The performance of the two designs is evaluated and it is found that the new design is superior in terms of strength and ductility. Upper and lower bound plasticity models are developed for strength prediction and satisfactory agreements are obtained when comparing the models with the test results. A theoretical exact solution is not possible to obtain, as the models are based on assumptions that are not fully identical. However, the establishment of both types of models provides a range of expected results and thus valuable information for practical applications.

Finally, second-order plastic modeling is used to establish the load-displacement relationship for a casting joint loaded in shear and transversely reinforced with rebars. Despite the simplicity of the model, rather satisfactory agreement with tests is found. The model may be used to predict the available plastic energy and has potential for practical assessment of structural robustness.

Resumé

Præfabrikerede betonelementer benyttes i stor udstrækning til nybyggeri i mange industrialiserede lande. Fordelene ved at bygge med præfabrikerede elementer, sammenlignet med traditionel pladsstøbt beton, findes primært i en lettere kvalitets- og produktionskontrol samt i opførelseshastigheden. Udfordringerne findes i udførselsfasen, hvor strukturel sammenhæng skal sikres gennem pladsstøbte samlinger i smalle åbninger. Disse samlinger er essentielle for den overordnede strukturelle opførsel og af samme årsag, er samlinger, der er stærke og duktile og som på samme tid passer ind i udførelsesprocesserne på pladsen, vigtige for velfungerende løsninger.

Den nuværende best practice for udførslen af forskydningssamlinger er blevet udviklet i løbet af årtier og løsningerne har primært været orienteret mod udførselsfasen på byggepladsen. De tilhørende beregningsmetoder er i de fleste tilfælde baseret på erfaring og empiri. Styrken og duktiliteten af de nuværende samlinger er ikke nødvendigvis tilstrækkelig i tilfælde af, at der skal overføres større laster. Potentialet for forbedringer er dermed betydeligt, eftersom bedre løsninger kan styrke den overordnede strukturelle opførsel og i sidste ende føre til mere økonomiske designs.

Dette studie omfatter en undersøgelse af plane samlinger mellem præfabrikerede forskydningsvægge. Et nyt design med '2-på-2' U-bøjle samlinger er foreslået. Kendetegnet for det nye design er, at U-bøjlerne er orienteret anderledes end i det konventionelle design og at der er brugt dobbelt T-hovedet armering i U-bøjlernes overlappende areal. Undersøgelsen dækker flere uafhængige forskningstemaer, som i kombination giver en bred viden om fortandede forskydningssamlingers opførsel.

Som det første undersøges mørtels strukturelle egenskaber. Det er relevant at undersøge, da mørtel med små tilslag typisk benyttes til at udstøbe de smalle samlinger mellem de præfabrikerede betonelementer. Studiet omfatter triaxiale tests og push-off tests, som har til formål at undersøge mørtel under brud. Som det næste, testes trækkapaciteten af den nye U-bøjle samling og bæreevnen analyseres ved brug af plastiske øvreværdi metoder. Undersøgelsen er relevant, idet det er en forudsætning for forskydningssamlingens evne til at overføre forskydning, at U-bøjlerne er i stand til at overføre træk. De udviklede modeller er understøttet af tests og kan bruges til at designe U-bøjle samlingerne således, at trækkapaciteten er bestemt af flydning i U-bøjlerne og ikke af et sprødt brud i udstøbningsmaterialet. At opnå flydning i U-bøjlerne er vigtigt for at opnå et duktilt respons, når samlingen

belastes i forskydning.

Afhandlingens hovedfokus er test og modellering af fortandede forskydningssamlinger. Et omfattende eksperimentelt program er præsenteret. Den pågældende udformning af forsøgselementerne tillader en direkte sammenligning mellem det konventionelle design og det nye design koncept. Testresponset for de to design sammenlignes, og det findes, at det nye design er bedre med hensyn til styrke og duktilitet. Plastiske øvre- og nedreværdi modeller udvikles for estimering af bæreevnen og tilfredsstillende overensstemmelse mellem model og testresultater findes. Det er ikke muligt at udvikle en teoretisk eksakt løsning, da modellerne er baseret på antagelser, der ikke er helt identiske. Ikke desto mindre fører etableringen af begge typer af modeller til en afgrænsning af forventede resultater, og dermed til værdifuld information for praktisk anvendelse.

Til slut er andenordens modellering benyttet til at etablere last-flytningsrelationen for en støbt samling armeret på tværs med armeringsstænger og belastet i forskydning. På trods af modellens simpelhed, findes overraskende tilfredsstillende overensstemmelse mellem tests og modelrespons. Modellen kan benyttes til at estimere den tilgængelige plastiske energi og den har potentiale for praktisk anvendelse i forhold til vurdering af strukturel robusthed.

Contents

Additional Work (not appended)

1. *Construction-friendly Ductile Shear Joints for Precast Concrete Panels*
   Jesper H. Sørensen, Linh C. Hoang, Gregor Fischer, John F. Olesen.
   Published in: Fernando, D., Teng, J. G., and Torero, J., editors, *Proceedings of the Second International Conference of Performance-based and Life-cycle in Structural Engineering*, pages 640-649, Queensland University, Brisbane, Australia, 2015

2. *Catenary Action in Rebars Crossing a Casting Joint Loaded in Shear*
   Jesper H. Sørensen, Linh C. Hoang, John F. Olesen, Gregor Fischer.
   Published in: Maekawa, K., Kasuga, A., and Yamazaki, J., editors, *Proceedings of the 11th fib International PhD Symposium in Civil Engineering*, pages 735-742, University of Tokyo, Tokyo, Japan, 2016

3. *Tensile Capacity of U-bar Loop Connections with Precast Fiber Reinforced Dowels*
   Jesper H. Sørensen, Linh C. Hoang, John F. Olesen, Gregor Fischer.
   Published in: Beuhausen, H., editor, *Proceedings of the fib Symposium 2016 - Performance-based approaches for concrete structures*, University of Cape Town, Cape Town, South Africa, 2016

Notation

Abbreviations

DIC	Digital Image Correlation
FELA	Finite Element Limit Analysis
LVDT	Linear Variable Displacement Transducer
w/c	Ratio between water and cement in a mixture

List of Symbols

a	Distance between innermost U-bars
a	Geometric length (Chapter 8)
A_c	Circular area of U-bar overlap
A_d	Area of diagonal yield line (Chapter 7)
A_i	Area of inclined yield line in a shear key (Chapter 7)
A_k	Area of one shear key
A_l, A_t	Area of tensile failure plane (Chapter 5)
A_l, A_t	Stress resultants (Chapter 8)
A_s	Reinforcement area
A_{sL}	Reinforcement area of lacer bar (Chapter 5)
A_{sL}	Reinforcement area of locking bar (Chapters 6-9)
b	Width of connection
c	Cohesion
c	Strength enhancement factor for concrete (Chapters 8-10)
C_l, C_t	Stress resultants (Chapter 8)
d	Diameter of rebar
d_k	Depth of shear key
$d_{\max}$	Maximum grain size
D	Amount of energy dissipated (Chapter 2)
D	Internal bend diameter of U-bar (Chapters 5-9)
e	Optimization parameter (Chapter 8)
e_1, e_2	Geometric length (Chapter 8)
f	Yield condition
f_c	Compression strength of concrete
$f_{c,0}$	Reference strength of concrete
f_{cc}	Enhanced average strength of concrete

f_t	Tensile strength of concrete
f_u	Ultimate strength of reinforcement
f_y	Yield strength of reinforcement
f_{uL}	Ultimate strength of locking bar
f_{yL}	Yield strength of lacer bar (Chapter 5)
f_{yL}	Yield strength of locking bar (Chapters 6-9)
h_k	Height of shear key
H	Overlapping length of U-bars
k	Material parameter
K	Factor influencing ν
l	Longitudinal direction
l	Material parameter
l_1, l_2	Distances describing the position of plastic hinges
L	Total length of shear connection
L_k	Length of shear key
m	Material parameter
M	Moment in rebar
M_p	Plastic moment capacity
n	Number of shear keys
N	Tensile load on loop connection (Chapter 5)
N	Tension force in rebar (Chapter 10)
N_0	Cracking load of loop connection (Chapter 5)
N_0	Initial tension force in rebar (Chapter 10)
N_p	Plastic tension capacity
P	Shear load
P_{cal}	Calculated shear capacity (Chapters 7-9)
P_f	Shear resistance from friction (Chapter 10)
P_{FP}	Recorded first peak load
P_l, P_t	Stress resultants (Chapter 8)
P_s	Shear resistance of a smooth interface (Chapter 10)
P_{total}	Total shear resistance (Chapter 10)
P_{U}	Recorded ultimate load
q_i	Generalized strains
Q_i	Generalized stresses
s, s_1	Distance between outermost U-bars
t	Transverse direction
t	Thickness of precast concrete element
t	Time (Chapter 10)
u	Shear displacement parallel to interface (Chapter 10)
$u_{\max}$	Shear displacement capacity (Chapter 10)
$\mathbf{u}$	Vector containing the relative displacements in a yield line
$\lvert\mathbf{u}\rvert$	Length of displacement vector

u_a, u_b	Displacement vector of segment IIa and IIb (Chapter 5)
u_l	Displacement in the l-direction
u_t	Displacement in the t-direction
V	Volume of body (Chapter 2)
V	Shear force (Chapters 4+5)
V	Shear force in rebar (Chapter 10)
V_{peak}	Maximum recorded shear force
W	Plastic work
W_E	External work
W_I	Internal work

Greek letters

α	Angle of displacement vector
β	Inclination of yield line to the l-direction
δ	Increment of displacement or strain
Δ	Increment of plastic deformation (Chapter 2)
Δ	Elongation in plastic hinge (Chapter 10)
$\dot{\Delta}$	Rate of elongation in plastic hinge (Chapter 10)
$\Delta_{\max}$	Maximum elongation in plastic hinge (Chapter 10)
$\bar{\varepsilon}$	Strain vector
γ	Slope of inclined yield line in a shear key
λ	Indeterminate positive factor
μ	Coefficient of friction
ν	Effectiveness factor, concrete in compression
ν_t	Effectiveness factor, concrete in tension
ϕ	Diameter
ϕ_L	Diameter of lacer bar (Chapter 5)
ϕ_L	Diameter of locking bar (Chapters 6-9)
Φ	Degree of transverse reinforcement
Φ_L	Reinforcement degree, lacer bar (Chapter 5)
Φ_L	Reinforcement degree, locking bar (Chapters 6-9)
φ	Internal angle of friction
σ	Normal stress
σ_1, σ_2, σ_3	Principal stresses
σ_A, σ_B	Compressive stress in Struts A and B
σ_c	Concrete stress
σ_s	Reinforcement stress
τ	Shear stress
θ	Rotation in plastic hinge (Chapter 10)
$\dot{\theta}$	Rate of rotation in plastic hinge (Chapter 10)
θ_A, θ_B	Inclination of Struts A and B (Chapter 8)
θ_k	Inclination of key corner (Chapter 8)

1 Introduction

1.1 Precast Concrete Structures

Precast concrete structures represent a branch of structural concrete, where the structural components are cast at controlled conditions in a factory and later assembled on-site. The precast method is often used for buildings or bridges, however, the method is applicable for any kind of structure and possibly in combination with traditional in-situ cast solutions. The approach is considered as an economic, environmental friendly, durable, and well-performing method with a vast potential.

A precast solution is, however, not to be considered as an attempt to replace an in-situ cast structural design with precast components assembled on-site to achieve an overall similar structural behavior as the corresponding in-situ cast solution. Constructing with precast concrete elements is to be considered as the employment of a system, where the individual elements and solutions influence the structural performance and hence the overall design. Elaborated descriptions for precast solutions can be found in various design guidelines, see e.g. *fib* Bulletin 74 (fib, 2014).

After the Second World War, the precast construction method gained popularity as the demand for fast completion of economical buildings increased. Many industrialized countries adopted this construction method and completed a large number of buildings. Today construction with precast concrete is (when applicable) the preferred method in Denmark. One of the reasons is related to a change in the Danish Building Regulation in 1958, requiring residential dwellings to be designed according to a modular concept. The choice of construction method was voluntary, however, a market for precast components fulfilling these modular requirements was created (Kjærbye and Mork, 1998). Investments in the industry combined with the apparent benefits of the precast technology eventually dominated the building industry and the tradition of constructing with precast elements is continued today.

Another reason for the implementation and retention of the precast method in Denmark is believed to be found in the preferred design methods used for concrete structures. The Danish school of concrete plasticity counts a number of excellent engineers contributing to the development of design methods for concrete structures. The most prominent contributions to be mentioned count Ingerslev (1921, 1923), Johansen (1931, 1943), and M. P.

Nielsen (summarized in (Nielsen and Hoang, 2011)). Continuous development in this field enables the Danish engineers to explore and challenge the traditional designs of precast concrete structures. A brilliant example of such an achievement is the design and construction of the Bella Sky Hotel in Copenhagen, Denmark, where precast technology was used in combination with in-situ cast solutions to construct a leaning landmark building (Dahl, 2014; Jørgensen, 2015). Another example is the Tietgen Dormitory, a residence hall in Copenhagen, Denmark. Both buildings can be seen in Figure 1.1.

(a) Bella Sky Hotel, photo: Dahl (2014) (b) Tietgen Dormitory

Figure 1.1: *Examples of landmark buildings in Denmark, built using precast concrete technology*

The prefabrication process promotes quality control, precision, and production speed as key features. Nevertheless, the overall performance of precast structures is highly influenced by the performance of the joints between the precast elements. The capacity of the precast components are easily assessed by e.g. the theory of plasticity, however, the major challenge for the overall performance is the capacity of the structural joints. Clearly, construction-friendly and ductile connections are essential for well performing and economical structures. An overview of the current best practice, including design guidelines, for structural connections in precast concrete buildings is given in the *fib* Bulletin 43 (fib, 2008). These solutions are based on decades of construction with precast components, however, the research and development of sound structural solutions lag behind the development in e.g. numerical tools and general improvements in the building industry. This is exemplified in the code provisions (including the European Norm for

concrete structures (CEN, 2004)), where empirical relations dominate the design of connections.

1.2 Motivation of Study

For low rise buildings, the strength requirements for the structural connections are often met with the available design solutions. However, for heavier loaded elements, such as in high rises or other non-ordinary structures, there is a potential for development of connections with a higher capacity, which at the same time are very ductile. This study is motivated by the need from the industry to have solutions that ease the processes on the construction site and meanwhile improve the structural performance of the connections. The improved performance must be reflected in the design methods. In this relation, it should be noted that changes in design and calculation methods do not alone improve the structural solutions. On-site inspections often reveal examples of insufficient execution of the on-site grouting. This compromises the structural performance and hence underlines that the need for construction-friendly designs is accompanied by requirements to the workmanship on the construction site.

This study is focused on in-plane connections between shear wall panels and limited to the case of indented (keyed) shear connections. These connections are important, as they provide overall resistance against horizontal loads to shear walls consisting of precast panels. A sound design of these connections may provide a strength which is similar to the shear wall panel itself, however, the connections may preferably be designed with a lower strength to ensure a well-defined failure mode of the structure. In this case, a ductile connection is essential for the overall structural safety.

1.2.1 Development of Design

The conventional design of keyed shear connections between precast elements is constituted by U-bar loops protruding from adjacent elements and overlapping in a horizontal plane, see Figure 1.2(a). A challenge for this design arises in case a shear panel has to be lowered immediately next to another as the U-bars are overlapping in the horizontal plane. This problem appears e.g. when continuous vertical reinforcement (post-tensioning) in corrugated tubes are needed to resist overturning moments. A common way to overcome this challenge is to pre-bend the U-bars and place them hidden in the shear keys, when the panels are fabricated. This procedure also protects the reinforcement loops during transportation. On the construction side the U-bars are subsequently straightened to form the overlap, and a vertical locking bar is installed in the full length of the connection, see

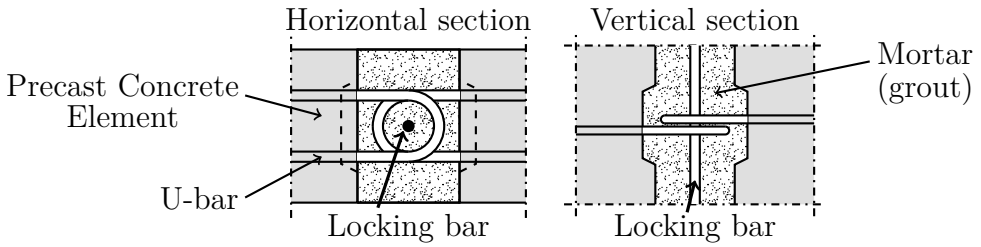

(a) Conventional design

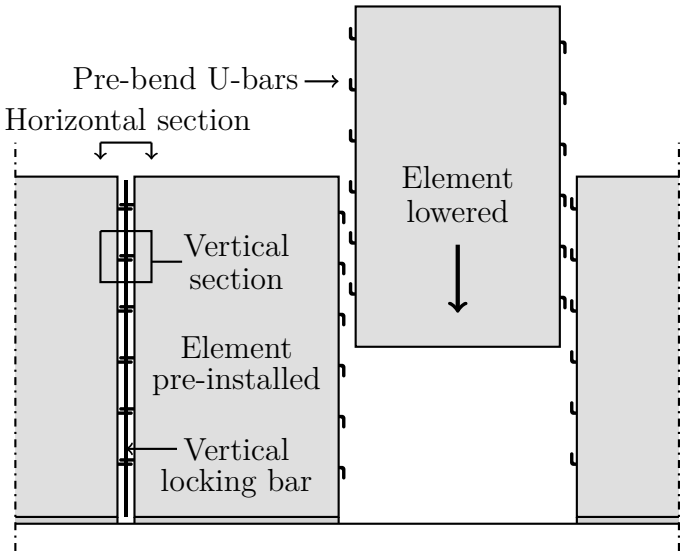

(b) Assembly phase of conventional design

Figure 1.2: *Conventional design of shear wall connection, illustrations from Sørensen et al. (2017b)*

Figure 1.2(b) for procedure during lowering and appearance before grouting. This procedure imposes a manual workload, which sometimes has to be performed within a very narrow opening, as the appearance of the connection on the surface of the panel wall is preferably minimized. Often, the assembly phase is performed inadequately. Poor quality of the grouting process may lead to a lack of the required structural continuity or to a limited ductility. The overall performance of the connection is hence not as assumed in the design.

Another challenge for the designer is the requirement to the reinforcement used as U-bars. It has to be strong enough to provide the required strength, on the other hand, the strength cannot exceed the ability of the worker to straighten the U-bars and the reinforcement has to possess a ductility that allows for bending and straightening without breaking.

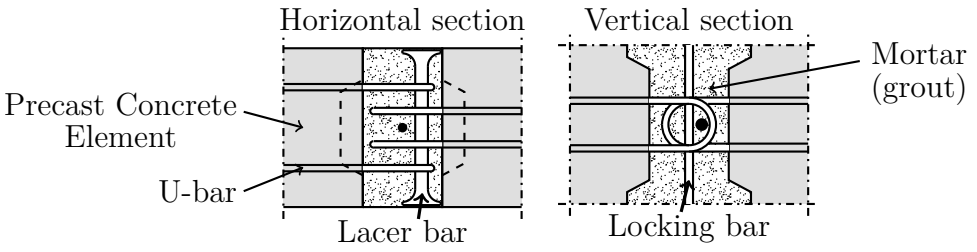

(a) New design

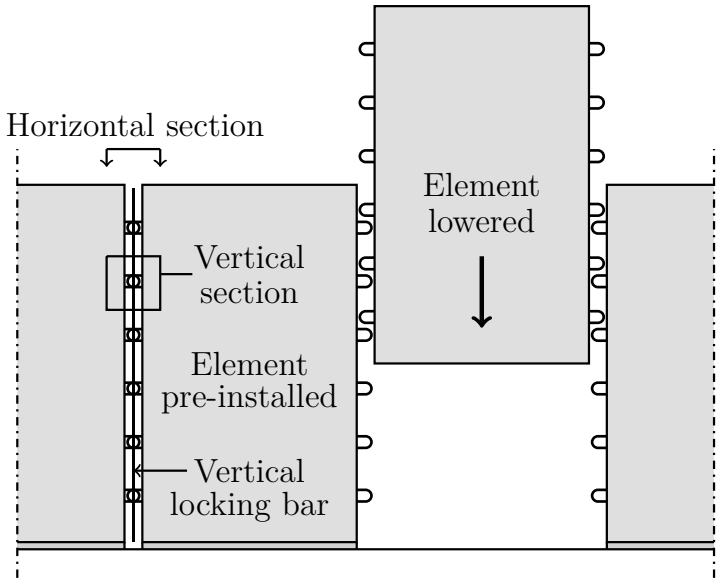

(b) Assembly phase of new design

Figure 1.3: *New design of shear wall connection, illustrations from Sørensen et al. (2017b)*

These challenges can be overcome by a change of design. Figure 1.3(a) shows a new design for U-bar loop connections between precast shear wall panels. The significance of the new design is the orientation of the U-bar loops. Contrary to the conventional design, the U-bars are placed in the same plane as the panel, with a mutual spacing. The spacing enables vertical lowering of the panels without problems of rebar clashing or the need for post-processing of bend U-bars, see Figure 1.3(b). To ensure the required structural continuity, the U-bar loop connections are reinforced transversely with double T-headed bars (lacer bars). In addition to the lacer reinforcement, the design allows for installation of a vertical locking bar similar to the conventional solution. Throughout the thesis the short double T-headed rebar placed in the overlapping U-bar area will consistently be denoted lacer reinforcement. The lacer reinforcement can be considered as transverse re-

inforcement or a type of locking bar, however, to distinguish between the transverse reinforcement of the shear connection in shape of U-bars, the short T-headed lacer reinforcement placed in the overlapping area of the U-bars, and the vertical locking bar placed along the entire joint, the notation (as introduced in Figure 1.3(a)) is consistently adopted. The design concept can be expanded to include other types of connections, e.g. corner joints or T-joints, where the loading may consist of a combination of actions. Such an investigation is beyond the scope of this thesis.

1.3 Objectives of Thesis

The overall objectives of this thesis are to develop a new design for structural joints in precast concrete, perform experiments to validate the design, and develop suitable design models for strength prediction. The goal is to obtain connection solutions that:

- are easy to complete on the construction site
- provide the necessary structural continuity
- ensure a ductile behavior in the ultimate limit state

The objectives are all improvements of current best practice, as the risk of errors while handling the important structural connections is reduced and at the same time, an overall more robust structure is obtained.

1.4 Organization of the Thesis

The thesis has been organized to give a thorough description of the structural performance of the proposed loop connection design for keyed shear wall connections. The content of the thesis can be seen in Table 1.1. Some of the main findings have been published in journals, these are appended and denoted as described in Table 1.1. All details of the development of the models included in the papers will not be repeated, but a general overview of the models and the obtained results will be given. Where additional information is required the reader will be referred to the relevant paper. Instead, the models will be subjected to a parametric study or compared to additional test results generated within the study but not yet published. Section 1.4.2 contains an overview of the conducted experimental programs and their appearance in relevant papers.

Chapter 2 contains an introduction to the theory of plasticity, including the application of the theory to reinforced concrete. This chapter serves as a general basis for the theoretical interpretation adopted in the thesis.

Table 1.1: *Content of the thesis divided by chapter*

No.	Content	Contained in
2	Theory of Plasticity	
3	Test of Mortar in Triaxial Compression	-
4	Failure of a Mortar Shear Key	-
5	Tensile Capacity of Loop Connections	Paper I
6	Tests of Shear Connections	Paper II+III
7	Upper Bound Solutions for Shear Connections	Paper II
8	Lower Bound Solutions for Shear Connections	Paper III
9	Comparison of Upper and Lower Bound Models	-
10	Dowel and Catenary Action in Rebars	Paper IV

Chapter 3 presents experimental results of triaxial tests on mortar and concrete. The tests establish estimates of the failure envelopes for the materials, which provide information on the internal angle of friction, φ, for the materials.

Chapter 4 contains a study of the failure process of a mortar shear key. The chapter presents experimental results and observations from push-off tests on specimens with a single shear key. The failure process of the key is studied by use of digital image correlation (DIC).

Chapter 5 deals with the tensile capacity of the new loop connection design. The study focuses on establishing the amount of lacer reinforcement required to ensure tensile yielding of the U-bars. Once yielding of the U-bars is ensured, the optimal shear capacity can be utilized. The theoretical solutions related to the tensile capacity of the loop connection can be found in the appended Paper I (Sørensen et al., 2017a).

Chapter 6 presents experimental tests on shear connections and shows representative results in terms of load-displacement relationships and general observations. The tests comprise both the conventional design and the new design. The results form the basis for a comparison between test results and the theoretical models developed in Chapters 7 and 8.

Chapter 7 introduces upper bound solutions for keyed shear wall connections. The solutions have been developed and presented in the appended Paper II (Sørensen et al., 2017b). In the chapter, a comparison to the test results presented in Chapter 6 is performed.

Chapter 8 contains lower bound solutions for the shear capacity of the keyed connections. The solutions have been developed in the appended

Paper III (Sørensen et al., 2018) and the theoretical results are compared with the experimental results presented in Chapter 6.

Chapter 9 evaluates the developed upper and lower bound models. The solutions supplement each other, and together they can be used to bound the theoretical exact solution from below and above. The comparisons provide information for practical application and inputs to the calibration of model parameters.

Chapter 10 introduces second-order plastic modeling for the assessment of available plastic energy in a shear joint. A model is presented that considers the combination of dowel and catenary action in rebars crossing a casting joint loaded in shear. Paper IV (Sørensen et al., 2017c) contains the development of the model, and in the chapter it is compared to test results of a shear connection without shear keys. In addition, a discussion on possible model extensions is given.

Chapter 11 summarizes the major findings of the experimental results and draws conclusions on the theoretical models.

As the overall objective of the thesis is focused on the shear connection design, the chapters are organized towards the assessment of the shear connections. Table 1.2 shows the main bodies of the content as they appear in the thesis, guiding the reader from the basic mechanisms over test results to the modeling aspects.

Table 1.2: *Main bodies of content*

Chapter 1			Introduction
Chapter 2			Theoretical basis
Chapter 3 Triax	Chapter 4 Key shearing	Chapter 5 Tension	Material properties + basic mechanisms
Chapter 6			Shear connection tests
Chapter 7 Upper bound	Chapter 8 Lower bound	Chapter 9 Comparison	1st order modeling
Chapter 10			2nd order modeling
Chapter 11			Conclusions

1.4.1 Reading Guide

In this section a guide is given to the reader on how the information contained in the appended papers should be related to the chapters of the thesis.

Chapter 1 and *2* serve introductory purposes. Additional information cannot be found in the papers. The results presented in *Chapter 3* and *4* have not been published yet and additional information cannot be found in the appended papers.

Chapter 5 gives a brief introduction to the results of Paper I. Details on the experimental program and the development of the models can be found in Paper I. The chapter contains an additional parametric study on some of the essential parameters included in the models. The reader may benefit from reading Paper I before the chapter.

Chapter 6 presents an overview of the experimental work conducted on shear connections. For specific information on the test procedure the reader is referred to the experimental sections of Paper II and Paper III. The aim of the chapter is, besides a presentation of the experimental program, to distinguish between tests already published and tests not yet published. Details on the specimens are contained in Appendix B.

Chapter 7 briefly summarizes the findings of Paper II. The reader may benefit from reading the part of Paper II that describes the model development before reading the chapter. In the chapter the solutions are briefly introduced and thereafter compared to the results of all the tests presented in Chapter 6.

Chapter 8 has the same structure as Chapter 7. Paper III is summarized and compared to the available test results. The reader may benefit from reading the theoretical part of Paper III before the chapter. *Chapter 9* elaborates some of the discussions given in Paper III.

Chapter 10 repeats the theoretical derivation given in Paper IV. For details on the experimental tests and for additional comparisons of the model with test results the reader is referred to Paper IV. The reader may read the paper before the chapter. In the chapter, the model is linked to the shear connections and a discussion is given on possible model extensions that can be considered in future works.

1.4.2 Overview of Experimental Work

The theoretical investigation of the new design for loop connections has been supported by extensive experimental programs. The programs have been realized with financial support from the collaborators mentioned in the acknowledgement and with support from a number of student projects designed and supervised by the author and the supervisors. The involvement of students in the experimental work made it possible to perform numerous tests and it also allowed the author to focus on the design of the experimental programs and interpretation of the obtained results along with the execution. Table 1.3 contains an overview of the tests included in the thesis, the relation to the student projects, and, if published, the appearance in the appended papers. All tests were performed at the Department of Civil Engineering at the Technical University of Denmark.

Table 1.3: *Experiments performed in relation to the PhD study*

Type of tests	**Method**	**No. of tests**	**Project**	**Status**
Triaxial tests	Oil chamber	40	*a*	Unpublished
	Oil chamber	43	*b*	Unpublished
Tension tests	Tension	9	*c, d*	Paper I
	Tension	23	-	Paper I
Key shearing	Push-off	20	*a*	Unpublished
Shear connections	Push-off	22	*e*	Paper II
	Push-off	8	*c*	Paper II
	Push-off	10	*d*	Paper II
	Push-off	12	*f*	Paper III
	Push-off	12	*g*	Unpublished
Dowel action	Push-off	42	*h*	Paper IV

The test results of the following student projects have been included in the thesis (remaining tests were performed by the author):

Master theses:

- *a* *Experimental Study of Strength and Fracture of Mortar under Complex Stress States*, Baldur Pór Halldórsson, DTU Department of Civil Engineering, July 2016.
- *c* *Test and Analysis of Keyed Shear Joints between Precast Concrete Walls - Influence of Indent Area on the Load Bearing Capacity*, Jacob Svejgaard, DTU Department of Civil Engineering, July 2015
- *d* *Test and Analysis of Keyed Shear Joints between Precast Concrete Walls - Influence of Key Depth on Failure Mode*, Lasse Herstad Øvrelid, DTU Department of Civil Engineering, July 2015.
- *f* *Test and Analysis of Keyed Joints Reinforced with Vertical U-bar Loops - Influence of Key Depth on the Shear Behavior*, Rasmus Malte Hou, DTU Department of Civil Engineering, July 2016.
- *g* *Test and Analysis of Keyed Joints Reinforced with Vertical U-bar Loops - Influence of Key Length and Grouting Material on the Shear Behavior*, Jakob Schmidt Olsen, DTU Department of Civil Engineering, July 2016.
- *h* *Dowel- and Catenary Action in Rebars Embedded in Concrete and Crossing an Interface Loaded in Shear*, Nikolai Schjøtt Bach and Martin Hansen, DTU Department of Civil Engineering, February 2016.

Bachelor theses:

- *b* *Failure Criteria for Concrete and Mortar Subjected to Triaxial Stress States*, Frederik Jensen and Frederik Vind, DTU Department of Civil Engineering, June 2017.
- *e* *Forskydningsbæreevnen af montagevenlige elementsamlinger (English: Shear Capacity of Construction-friendly Joints for Precast Concrete Structures)*, Rune Pedersen and Mads Herløv, DTU Department of Civil Engineering, January 2015.

1.5 Contributions to the Field of Research

The theoretical models developed in this study apply to structural connections for precast concrete shear walls. However, the theoretical framework is applicable for a number of other structural solutions, if modified accordingly. The novel contributions to the field of research can be summarized as:

- ⋆ Experimental verification of the internal angle of friction for mortar ($\varphi = 30°$).
- ⋆ Development and experimental verification of upper bound plasticity models for the tensile capacity of loop connections (based on a '2-on-2' loop configuration).
- ⋆ Experimental demonstration of ductile test responses for a new keyed shear connection design. The significance of the new design is that the U-bar loops are placed in the same plane as the shear panel and that a double T-headed rebar is used as lacer reinforcement in the overlapping U-bar loop area.
- ⋆ Development of upper bound solutions for keyed shear connections, accounting for a failure of the shear key by local key corner crushing or complete key cut off.
- ⋆ Development of analytical lower bound solutions considering struts with different inclinations and stress transfer by friction in the indented interfaces.
- ⋆ Development of a second-order plasticity model for estimation of the in-elastic load-displacement relationship for a casting joint crossed by a rebar and loaded in shear. The model establishes a unique link between the imposed shear displacements and the sectional forces in the rebar by use of the kinematical conditions for the mechanism and the normality condition of plastic theory.

2 Theory of Plasticity

A material experiencing zero strains at stresses below the yield limit and arbitrary large plastic strains for stresses at the yield limit is defined as a *perfectly rigid-plastic material*. Such a material does not exist in reality, however, it is a convenient assumption for material behavior, when dealing with determination of the load carrying capacity of structures. The theory related to such an idealized material behavior is applicable, when the plastic strain capacity of the material is much larger than the elastic strain domain. The assessment of structural capacity based on this theory is called *limit analysis* and it is adopted in the modeling throughout the thesis. In the following a brief description of the theory will be given as a theoretical basis for the work presented in the remaining chapters. For further description, see e.g. Nielsen and Hoang (2011).

The general theory of plasticity was first developed by Gvozdev in Russia and before it was known to the western world in the late 1950s (Gvozdev, 1960), a similar theory was developed by the Prager school at Brown University, see i.a. Drucker et al. (1952). Important aspects of the theory include the concepts of *yield condition*, *normality condition*, and *extremum principles*. These matters define the theory of plasticity and despite the rough assumptions for the material behavior, the theory is elegant and its simplicity provides a powerful tool for structural analysis.

2.1 Yield Condition

The yield condition describes the combinations of generalized stresses, Q_i, which cause yielding. The yield condition is assumed to be convex and enclosing the point of no stresses, i.e. $Q_i = 0$. Following the notation of Nielsen and Hoang (2011), the yield condition can be defined as:

$$f\left(Q_1, Q_2, \ldots, Q_n\right) = 0 \tag{2.1}$$

According to the perfectly plastic material behavior, combinations of stresses fulfilling $f < 0$ will cause no strain in the material (and thereby no failure) and combinations fulfilling $f = 0$ may cause arbitrary large strains. Combinations of stresses resulting in $f > 0$ are not possible. The corresponding generalized strain to a generalized stress, Q_i, is denoted q_i. In a three dimensional continuum, the generalized stresses consist of the nine

stress components and the generalized strains are the corresponding nine strain components. The generalized stresses and strains can also be chosen as sectional forces and corresponding sectional deformation quantities. An example of the latter is given in Paper IV, also treated in Chapter 10.

2.2 Normality Condition

The product of the generalized stresses and the corresponding generalized strains defines the work per characteristic dimension. For an increment in the plastic deformation, Δq_i, the amount of energy dissipated over a certain volume, D, then becomes:

$$D = \int_V (Q_1 \Delta q_1 + ...)\, dV = \int_V W dV \tag{2.2}$$

where W denotes the plastic work per unit volume.

At yield, von Mises hypothesis of maximum work (Mises, 1928) states that the stresses corresponding to a given strain field attain such values that the plastic work, W, becomes as large as possible. When the yield condition is convex and differentiable (without plane surfaces or apexes), the condition is fulfilled when the strain vector satisfies the following:

$$q_i = \lambda \frac{\partial f}{\partial Q_i}, \qquad i = 1, 2, ..., n \tag{2.3}$$

where λ is an indeterminate positive factor. Hence, the magnitude of the strains is unknown, only the strain rate (and thereby the direction) is known. Fulfilling the condition, the strain vector becomes an outward directed normal to the yield surface. Equation (2.3) is usually referred to as the *normality condition* of plastic theory, however, it is also named 'the associated flow rule' or 'von Mises flow rule'.

In case the yield condition contains a straight part, the strain vector will be normal to this line/plane all along the straight parts and hence no unique relation between the stresses and the strains can be determined. However, W is uniquely determined from $\bar{q} = (q_1, q_2, ..., q_n)$. If the yield condition contains an apex, the strain vector, $\bar{q}$, may attain any angle between the normals to the two adjoining parts of the yield condition, see Figure 2.1 for a graphical representation of a two dimensional yield condition that contains both a plane part, apexes, and smooth differentiable parts.

2.3 Extremum Principles

The capacity of a structure (or the *limit load*, where unlimited deformations are possible), can be determined by use of some very useful theorems of

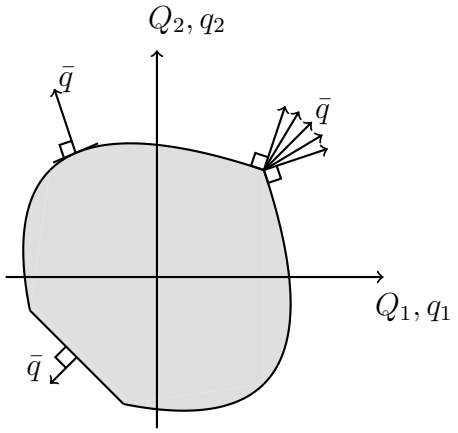

Figure 2.1: *Normality condition for a two dimensional yield condition*

the theory of plasticity. The theorems were formulated independently by Gvozdev (1960) and Drucker et al. (1952). Assuming that the yield condition is convex and that the normality condition is fulfilled, some useful concepts are introduced (quoted from Nielsen et al. (1978)):

1. A *statically admissible stress distribution* is a distribution of stresses which satisfies the equilibrium equations and the statical boundary conditions.
2. A *safe stress distribution* is a distribution of stresses corresponding to a point within or at the yield surface, $f \leq 0$.
3. A *failure mechanism* is a displacement field, compatible with the geometrical boundary conditions.
4. The *load-carrying capacity* or *yield load* of a structure of rigid-plastic materials is the lowest load by which deformations are possible.

Based on the first two concepts, the *lower bound theorem* can be established:

> *When a safe and statically admissible stress distribution can be found for a given load, the load is less than or equal to the yield load of the structure.*

From the two remaining concepts, the *upper bound theorem* can be established:

> *The load required to form a postulated failure mechanism will be larger than or equal to the yield load of the structure.*

From the extremum principles the capacity of a structure can be assessed either by lower bound solutions, e.g. analysis of stress fields, or by upper bound solutions, e.g. established by use of the work equation, where the rate of work performed by the external loads equals the rate of internal dissipation. If the loads found from the two theorems are equal, the exact yield load of the structure is found. This is called the *uniqueness theorem*. It was noted by Jensen (1976) that the work equation is not identical to the principle of virtual work, as the stresses belonging to a chosen deformation are not required to fulfill the equilibrium equations. However, in order to fulfill the uniqueness theorem, the equilibrium conditions must be fulfilled.

2.3.1 Capacity beyond Yield Load

Despite the fact that the yield load is defined as the load where deformation occurs, corresponding to a stress state on the yield surface and thereby failure of the structure, a material or a structure may possess capacity beyond the yield load. This applies to e.g. work hardening materials where additional capacity can be obtained with deformations beyond yield (see e.g. Drucker (1950) for stress-strain relationships for work hardening materials) or structures with boundary conditions that activate constrains as deformation occurs. Membrane action in slabs is an example of the latter phenomenon. Analysis of problems where change of structural geometry is important requires second-order modeling and is not covered by the simple first-order theory. Paper IV contains an example of such a second-order analysis where the change of structural geometry is taken into account in the modeling of a load-displacement relationship for a rebar crossing a casting joint exposed to shear displacements.

2.4 Failure Criterion for Cementitious Materials

Structural steel is an example of a material that is close to fulfill the assumption of perfectly plastic behavior whereas structural concrete is a quasi-brittle material more than a plastic material (Karihaloo, 1995). However, when adopting appropriate reduction factors (see Section 2.4.1), structural concrete can be treated by the theory of plasticity. A precise and complete yield criterion for concrete and similar cementitious materials has not yet been formulated. Instead, Coulombs frictional hypothesis (Coulomb, 1776) has generally been considered as an acceptable failure criterion for concrete. The hypothesis assumes a sliding failure in the material along a failure surface. The condition is described in terms of shear stress, τ, and normal

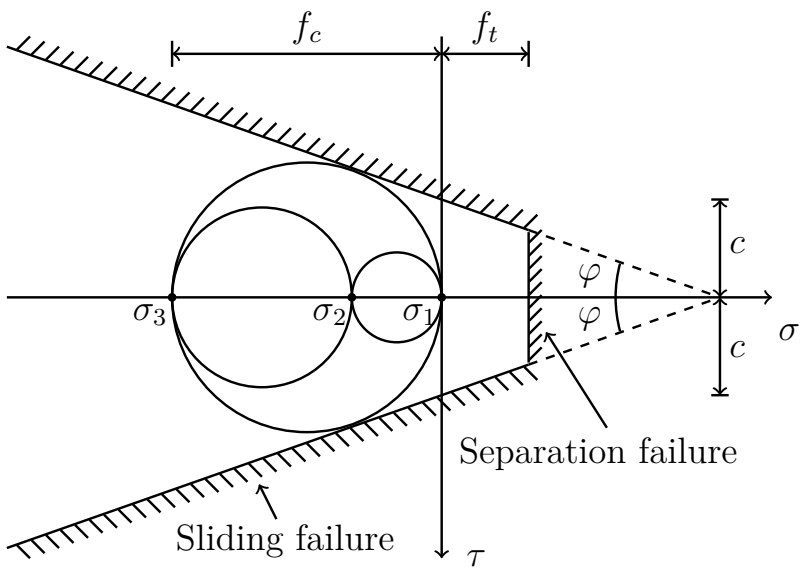

Figure 2.2: *Modified Coulomb frictional failure criterion*

stress, σ:

$$|\tau| = c - \mu\sigma \tag{2.4}$$

where c is the cohesion and μ is the coefficient of friction. The internal angle of friction, φ, relates to the coefficient of friction by: $\tan\varphi = \mu$. Introduction of a limitation on the tensile stress leads to the definition of a modified Coulomb material. The related failure mode is a separation failure, described by the tensile strength of the concrete:

$$\sigma = f_t \tag{2.5}$$

The modified failure criterion can be seen in Figure 2.2, where Mohr's circle is illustrated as well. The failure of a modified Coulomb material can hence be assessed by the principal stresses, $\sigma_3 \leq \sigma_2 \leq \sigma_1$, tension taken as positive. It should be noted that the magnitude of the intermediate principal stress does not influence the failure of the material.

In terms of principal stresses, the failure criterion for a modified Coulomb material can be formulated in the following way:

$$\frac{\sigma_1 - \sigma_3}{2} = c\cos\varphi - \frac{\sigma_1 + \sigma_3}{2}\sin\varphi \tag{2.6}$$

$$\sigma_1 = f_t \tag{2.7}$$

Introducing the parameter k defined as:

$$k = \frac{1 + \sin\varphi}{1 - \sin\varphi} \tag{2.8}$$

the criterion for sliding failure can then be reduced to:

$$k\sigma_1 - \sigma_3 = 2c\sqrt{k} \tag{2.9}$$

As both c and φ are regarded as material constants, it is seen from Equation (2.9) that the smallest principal stress can be decreased when the largest principal stress is decreased as well. Such a situation is achieved when a material is subjected to e.g. triaxial compression (this will be discussed in Chapter 3). When considering a uniaxial stress state, i.e. $\sigma_1 = \sigma_2 = 0$ and $\sigma_3 = -f_c$, the following relation is found:

$$f_c = 2c\sqrt{k} \tag{2.10}$$

2.4.1 Structural Concrete

Unlike reinforcement steel, where the material behavior with good accuracy can be simplified as rigid-plastic, concrete experiences softening after reaching the uniaxial strength. Due to this behavior, an appropriate reduced strength has to be introduced in order to apply plastic theory to structural concrete (and other cementitious materials). Furthermore, structural concrete as it appears in structures is rarely loaded in a similar way as standard tests used for determination of the uniaxial strength. An effective plastic strength of concrete in compression for plastic analysis can be defined by introduction of an *effectiveness factor*, ν:

$$f_{c,\text{ef}} = \nu f_c \tag{2.11}$$

In this context it is important to note that the effectiveness factor is introduced to account for softening effects, size effects, and loading conditions. Different values of the factor may therefore apply for different problems. Regarding the tensile strength of concrete, a similar reduction factor has to be introduced:

$$f_{t,\text{ef}} = \nu_t f_t \tag{2.12}$$

where f_t is the uniaxial tensile strength of concrete. The concept of effective strengths can be illustrated as shown in Figure 2.3. Throughout the thesis, the compressive strength of the cementitious materials considered has been estimated from uniaxial test on ϕ100x200 mm cylinders, when these have been available, and the tensile strength, when needed, has been calculated by the following relation:

$$f_t = 0.26 f_c^{2/3} \tag{2.13}$$

In this context is it relevant to note, that the tensile strength of concrete normally is neglected in plastic analysis of reinforced concrete structures.

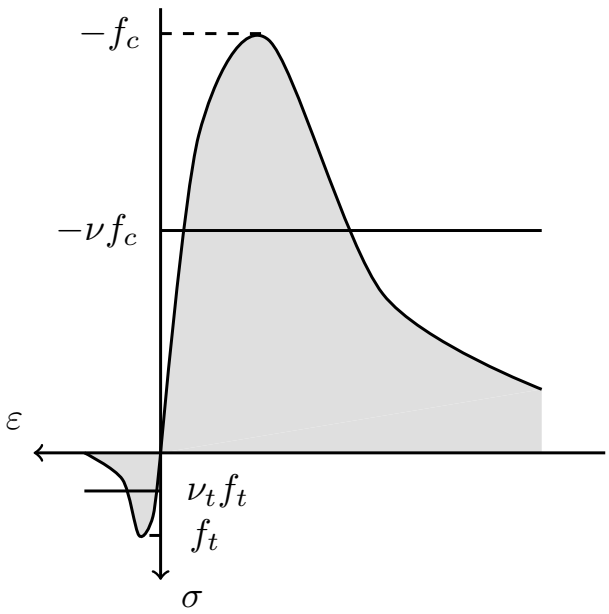

Figure 2.3: *Real and idealized stress-strain relationship for structural concrete, including indication of effective strengths for plastic analysis*

This is primarily due to the fact, that concrete loaded in tension usually cracks before the reinforcement is activated and when the reinforcement is yielding the tensile strength of the concrete has vanished.

2.4.2 Dissipation Formulas for Concrete

In upper bound analysis, the capacity is assessed by use of the work equation for a given failure mechanism. This requires calculation of the internal dissipation along yield lines or yield planes. Expressions for the dissipation along lines of discontinuity in concrete were developed by Jensen (1976) and can generally be expressed as:

$$W_A = \frac{1}{2}\nu f_c\,(1-\sin\alpha)\,|\mathbf{u}| + f_t\frac{\sin\alpha-\sin\varphi}{1-\sin\varphi}|\mathbf{u}|, \qquad \varphi \le \alpha \le \pi-\varphi \quad (2.14)$$

where W_A denotes the dissipation per unit area of a failure plane, $|\mathbf{u}|$ expresses the relative displacement between the two parts separated by the yield line, and α describes the angle between the displacement vector, $\mathbf{u}$, and the yield line. Introducing the following parameters:

$$l = 1 - 2\frac{\nu_t f_t}{\nu f_c}\frac{\sin\varphi}{1-\sin\varphi} \quad (2.15)$$

$$m = 1 - 2\frac{\nu_t f_t}{\nu f_c}\frac{1}{1-\sin\varphi} \quad (2.16)$$

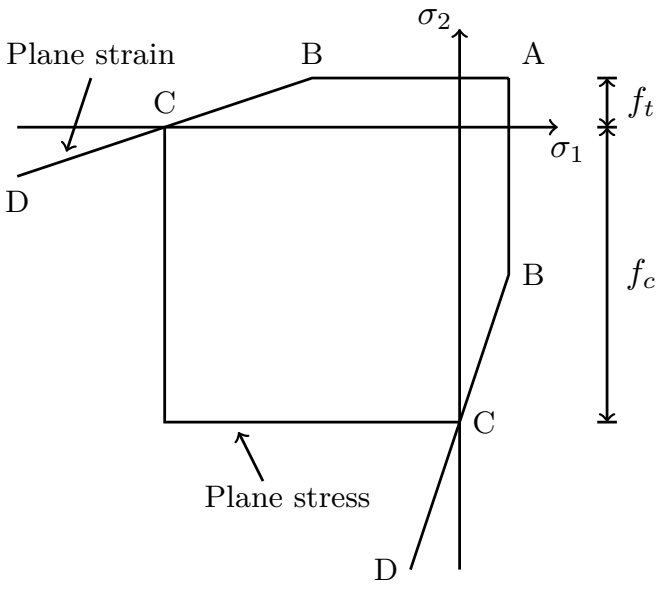

Figure 2.4: *Failure criteria for plane strain and plane stress conditions*

the dissipation can be expressed by the more simple expression:

$$W_A = \frac{1}{2}\nu f_c \left(l - m\sin\alpha\right)|\mathbf{u}|, \qquad \varphi \leq \alpha \leq \pi - \varphi \tag{2.17}$$

It should be noted that when the tensile strength of concrete is disregarded, the parameters l and m reduce to unity and Equation (2.17) simplifies slightly. The restriction on the angle of displacement relates to the normality condition (Equation (2.3)). The restriction is thereby dictated by the yield condition adopted. Figure 2.4 shows the failure criteria for a modified Coulomb material in plane strain and plane stress conditions, expressed in principal stresses. A sliding failure corresponds to the regime between B and D.

For plain strain conditions, the normality condition dictates that the angle of displacement for all stress states has to be larger than or equal to φ. In the apexes, i.e. $\sigma_i = f_c - kf_t$, $i = 1, 2$ (Point B), the angle may attain values between φ and $\pi/2$, and for smaller principal stresses the direction of the strain vector has to be normal to the yield condition. The only exception is the stress state $\sigma_1 = \sigma_2 = f_t$ (Point A). For plane stress conditions, the same restriction does not apply as α may attain other values in the apexes of $\sigma_i = f_c$, $i = 1, 2$ (Point C). See Nielsen and Hoang (2011) for an in-depth description. The dissipation formulas are summarized in Table 2.1 for plane strain and plane stress, respectively. These will be used in the following chapters, when upper bound models are developed.

Table 2.1: *Dissipation formulas for plane strain and plane stress conditions for a modified Coulomb material*

	Plane strain	**Plane stress**
$\underline{f_t \neq 0}$		
$0 \leq \alpha < \varphi$	Not possible	$W_A = \frac{1}{2}\nu f_c (1 - \sin\alpha) \lvert\mathbf{u}\rvert$
$\varphi \leq \alpha \leq \pi - \varphi$	$W_A = \frac{1}{2}\nu f_c (l - m\sin\alpha) \lvert\mathbf{u}\rvert$	$W_A = \frac{1}{2}\nu f_c (l - m\sin\alpha) \lvert\mathbf{u}\rvert$
$\pi - \varphi < \alpha \leq \pi$	Not possible	$W_A = \frac{1}{2}\nu f_c (1 - \sin\alpha) \lvert\mathbf{u}\rvert$
$\underline{f_t = 0}$		
$0 \leq \alpha < \varphi$	Not possible	$W_A = \frac{1}{2}\nu f_c (1 - \sin\alpha) \lvert\mathbf{u}\rvert$
$\varphi \leq \alpha \leq \pi - \varphi$	$W_A = \frac{1}{2}\nu f_c (1 - \sin\alpha) \lvert\mathbf{u}\rvert$	$W_A = \frac{1}{2}\nu f_c (1 - \sin\alpha) \lvert\mathbf{u}\rvert$
$\pi - \varphi < \alpha \leq \pi$	Not possible	$W_A = \frac{1}{2}\nu f_c (1 - \sin\alpha) \lvert\mathbf{u}\rvert$

3 Tests of Mortar in Triaxial Compression

This chapter presents experimental results of triaxial tests on mortar and concrete with the aim of establishing the failure envelopes for the materials. Connections in buildings made of precast concrete elements are often grouted with mortar (opposed to e.g. bridge structures where concrete grout is typically used). This is because mortar contains smaller aggregates, which makes it easier to fill the narrow construction zone. The main motivation for performing the tests was to obtain an estimate of the material parameters of normal strength mortar to be applied in plastic modeling. Low strength and high strength mortars are not considered.

3.1 Mortar versus Concrete

Mortar and Concrete are both cementitious materials that consist of the same ingredients, namely cement, water, and aggregates. However, the properties of the mixtures may deviate despite similarities in e.g. compressive strengths. Figure 3.1 shows the constituents of a concrete mixture. It can

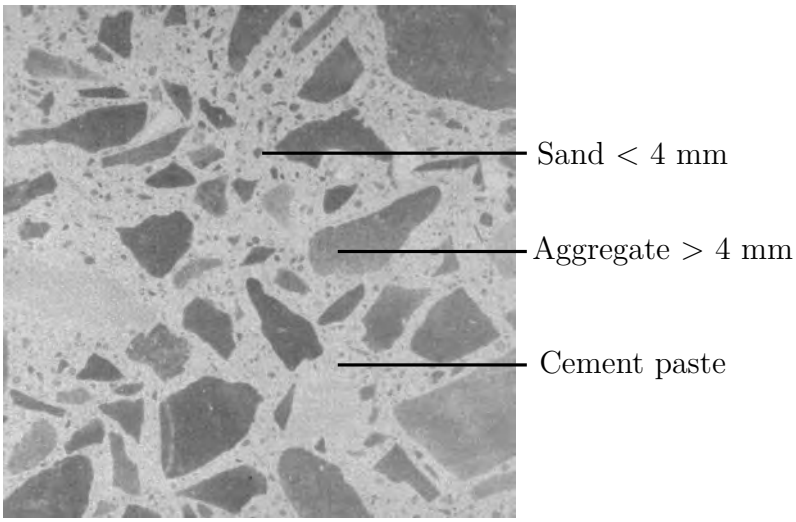

Figure 3.1: *Constituents of a concrete, picture from St John et al. (1998)*

be seen that the concrete consists of a combination of smaller aggregates (smaller than 4 mm, denoted sand), larger aggregates, and a cement paste that glues the constituents together. The composition of the aggregates may vary depending on application. In this study, the distinction between mortar and concrete is defined by the maximum grain size of the mixture. Mixtures with a maximum grain size of 4 mm or lower are considered as mortars whereas mixtures with larger maximum grain sizes are considered as concretes, see Table 3.1. Inclusion of admixtures may change the properties of the mixtures, however, the categories remain based on the same definition. Mixtures of pure cement paste are not considered in this study.

Table 3.1: *Ingredients in cement paste, mortar, and concrete mixtures*

Ingredient	Mixture
Cement	Paste
Water	Mortar
Sand 0-4 mm	Concrete
Aggregates > 4 mm	

3.1.1 Influence of Maximum Grain Size

The most important factor influencing the compressive strength of a concrete mixture is the water to cement ratio (normally measured by weight). A decrease in ratio increases the strength. This relation was described early in the 20th century e.g. by Abrams (1919) as a 'water-cement ratio law'. For a given cement content, the grain size distribution affects the amount of water required to obtain a workable mixture. Smaller aggregates require more water to make the mixture workable and hence, a strength increase is obtained by the use of larger aggregates.

The change in water consumption may be significant when adding larger aggregates to the mixture, thus design of strong and workable concrete by use of the water-cement ratio law includes the use of larger aggregates. However, the increase is not infinite. Walker and Bloem (1960) showed that the use of aggregates with a maximum size larger than 3/4 inches (19 mm) does not lead to an increased compression strength. Nevertheless, when comparing mortar to concrete, the larger maximum grain size of the concrete is expected to lead to a larger strength of the hardened mixture (assuming a proper proportioning of the aggregates).

3.1.2 Influence of Aggregate Content

As shown in Table 3.1, a concrete consists of two main constituents, aggregates and cement paste. For normal strength concretes, the aggregates are considered to be stronger than the cement paste. After initial failure of the cement paste, the aggregates will remain intact and possess the ability to transfer shear stresses by aggregate interlocking. If the grains are small the ability to transfer stresses will be reduced compared to a mixture with larger aggregates. However, it is not only the maximum grain size that influences this ability. The aggregate content of the mixture (often measured as a volume percentage) also has an influence. Tests reported in the literature show that a lower aggregate content leads to a lower strength increase, when tested in triaxial compression.

Zhang (1997b) developed a micromechanical model that takes the composition of the concrete mixture into account. The model assumes that the aggregates displace the path of the failure through the paste, and hence addition of aggregates displaces the path further, resulting in a higher strength of the confined concrete. Fewer aggregates (that are considered strong enough to resist sliding failure) may result in a decreased strength, as failure occurs in the cement paste. The model also considers a ratio of effective aggregates in order to take into account the number of aggregates that are weaker than the cement paste. Naturally, the effective aggregate ratio is decreased as the strength of the cement paste is increased. Examples of cracked aggregates are given in Section 3.5.

3.2 Triaxial Strength of Concrete

The strength of concrete in triaxial compression is higher than the uniaxial strength. Throughout the last century several researchers have performed tests confirming this relation. Among many experimental investigations, the tests of Richart et al. (1928), Balmer (1952), Hobbs (1971), Dahl (1992b), Imran and Pantazopoulou (1996), and Malecot et al. (2010) can be mentioned. From the experimental results, the combination of principal stresses that lead to failure can be used to establish the failure envelope of the material tested. Figure 3.2 shows e.g. how Mohr's circle for three sets of principal stresses (a, b, c) relate to the modified Coulomb failure criterion in a $\tau - \sigma$ coordinate system.

The Coulomb criterion is characterized by a linear relation for increasing confining pressures. However, the actual failure envelope of a concrete is non-linear and the shape depends on a number of factors. The shape can be approximated by a modification to the Coulomb criterion. Dahl (1992b) suggested the following two-stage failure criterion (only compressive stresses

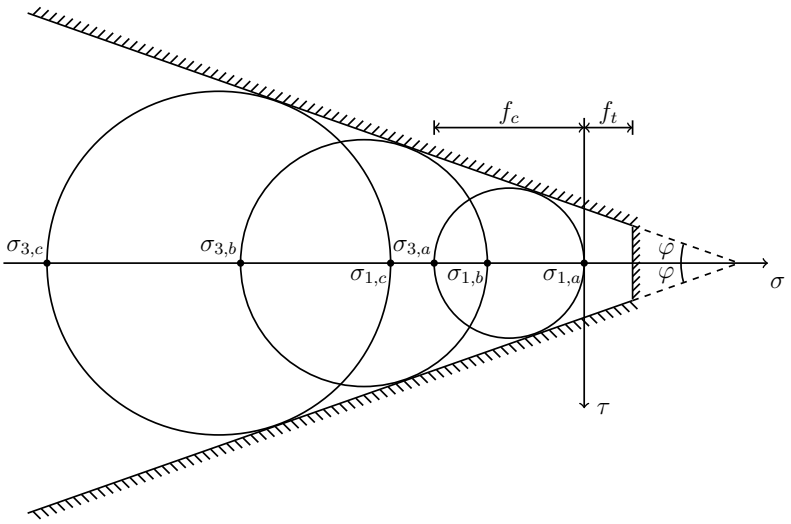

Figure 3.2: *Combinations of principal stresses fulfilling the Coulomb failure criterion*

considered):

$$\sigma_3 = \max \begin{cases} 4\sigma_1 - f_c \\ 3\sigma_1 - 1.5 f_c \end{cases} \tag{3.1}$$

The criterion can be seen in Figure 3.3. This relation captures the test results of normal and high strength concrete better, however, it still consti-

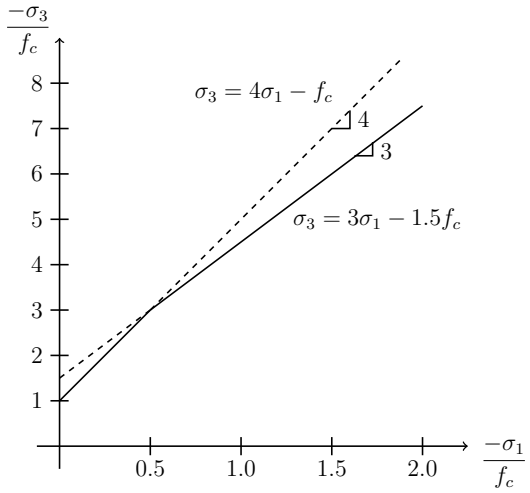

Figure 3.3: *Modified two-stage failure criterion, in terms of principal stresses, suggested by Dahl (1992b)*

tutes a simple approximation as the actual failure envelope is smooth. The simple appearance makes it a suitable choice compared to more complex models, see Section 3.2.1. Similar bilinear suggestions were made by Nielsen (1998) for high strength concrete. The criteria are expressed in principal stresses, which is preferred compared to a criterion expressed in terms of stress invariants or octahedral stresses (Smee, 1967). Smee describes that the stress invariants are insensitive to changes in the major principal stress and hence, the criteria may not distinguish adequately between safe and unsafe domains.

For mortar, the failure envelope contains the same characteristics as the failure envelope of a concrete. However, the difference in maximum grain size and aggregate content of the mixture influence the shape. Smee (1967) established that an increase in maximum grain size increases the strength of the mixture, when loaded in triaxial compression. Figure 3.4 shows failure envelopes as a function of both maximum grain size and the uniaxial compression strength of the mixture. The investigation included a mixture with sand as the only aggregates. In the study, sand was classified as passing No. 4 sieve, corresponding to a maximum grain size of 4.75 mm. For a comparison to the current study, the mixture qualifies as a mortar. When comparing the estimated failure envelopes of concrete and mortar it is seen that the strength increase is less for a mortar and that the difference magnifies with increasing normal stress (σ). Besides an influence of the maximum grain size, Smee also found that the uniaxial compression strength of

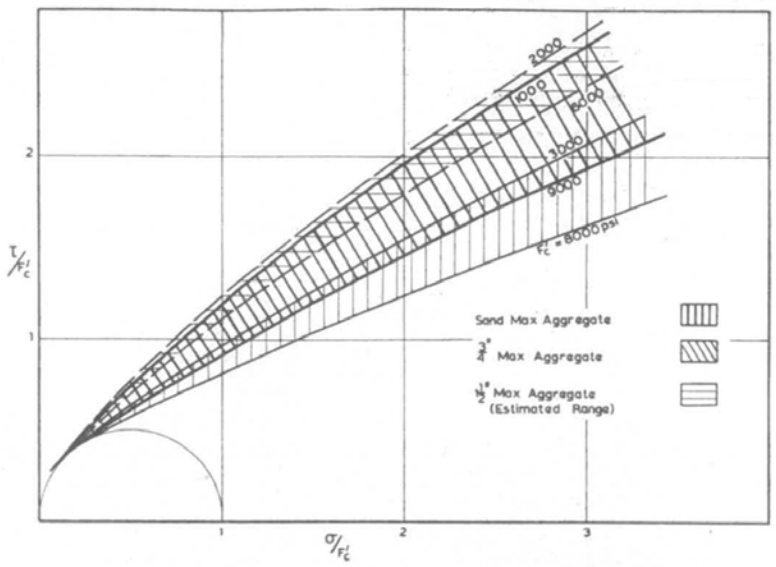

Figure 3.4: *Failure envelopes established by Smee (1967)*

the mixture influences the triaxial strength, where an increase in uniaxial strength leads to a decrease in confined strength.

Despite the general knowledge of the failure envelope of mortar, studies of the value of the internal angle of friction for mortar seem scarce in the literature. For normal strength concrete, a value of $k = 4$, corresponding to $\varphi = 37°$, is commonly adopted, see e.g. Richart et al. (1928), Johansen (1958), Chen (2007), and Nielsen and Hoang (2011). However, a similar commonly acknowledged value for mortar has to the best knowledge of the author not been established. Nielsen (1998) indicated that a value of $\varphi = 30°$ can be adopted for high strength paste and mortar. Naturally, the value depends on a number of factors, some of them are addressed in the above. In order to establish the shape of the failure envelope for well-defined mortar mixtures, a number of triaxial tests were performed.

3.2.1 Alternative Failure Criteria

A number of attempts have been made to describe the non-linear failure envelope of concrete subjected to triaxial compression. Chen (2007) gave an overview of the most common failure criteria proposed, classified by the number of parameters included in the models. Examples of one-parameter models are the Rankine maximum tensile stress criterion or the Tresca maximum shear stress criterion. The Coulomb criterion is an example of a two-parameter model. Drucker and Prager (1952) introduced a smooth approximation to the modified Coulomb failure surface as another example of a two-parameter model. This modification is useful e.g. for numerical applications.

Examples of three-parameter models are the Bresler-Pisner criterion and the Willam-Warnke criterion (Willam and Warnke, 1975). The Willam-Warnke criterion can be extended to a five parameter model. A more interesting and generally acknowledged failure criterion is the four-parameter model developed by Ottosen (1977). This model has been adopted in the *fib* Model Code (fib, 2013) for assessment of concrete subjected to multiaxially stress states. In addition to the mentioned models a number of empirical relations have been established based on curve fitting with experimental results.

3.3 Experimental Investigation

The experimental program was conducted in two parts, *a* and *b*. The primary aim of the tests was to investigate the influence of the maximum grain size on the internal angle of friction. As a consequence, the volume content of aggregates in the mixtures was also varied.

The tests were performed on ϕ100x200 mm cylinders in a triaxial cell, where oil pressure was applied as confining pressure. This entails that two of the principal stresses were equal during the test, i.e. $\sigma_1 = \sigma_2$. Hilsdorf et al. (1973) made a review of experimental procedures for multiaxial testing of concrete and concluded that this method is sufficient to obtain reliable results.

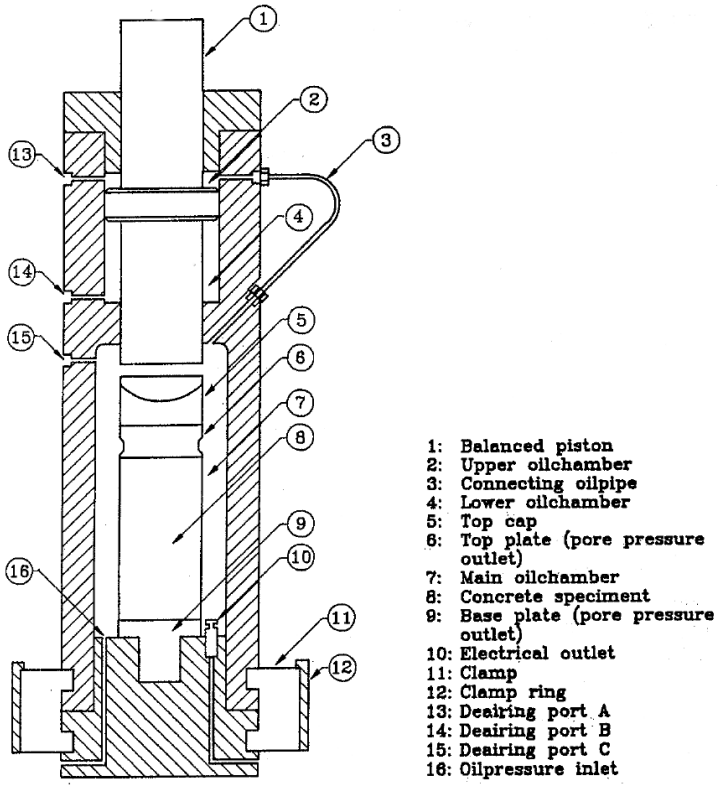

Figure 3.5: *Test setup used by Dahl, illustration from (Dahl, 1992c)*

The testing equipment used in the campaign was identical to the equipment used by Dahl (1992b), Hansen (1995), and Nielsen (1998). The cross section of the triaxial cell is depicted in Figure 3.5 and the reader is referred to Dahl (1992c) for a detailed description of the test setup and the test procedure. It is emphasized that the load applied was first a hydrostatic pressure until a predefined confinement level (the design of the cell ensured

a hydrostatic stress state when applying oil pressure in the chamber) before imposing additional axial compressive load until failure of the specimen. Failure was defined as the point where axial deformation continued without a further increase of the load. For each mixture, only one test was performed at the same confinement pressure. Nevertheless, the expected smooth failure envelope was captured well, which is explained by the controlled testing conditions, where failure was observed gradually and not instantly.

3.3.1 Mixture Proportions

The experimental program included seven mixtures with varying maximum grain sizes and volume percentages of aggregates. The mixture proportions can be seen in Table 3.2, where the mixtures are identified by a C denoting a cementitious material, a number referring to the maximum grain size, $d_{\max}$, of the mixture, and an adjoining letter referring to the two parts of the campaign. Ordinary Portland cement was used in all mixtures. The densities used when calculating the volume percentages (vol%) were 3100 kg/m^3 for the cement, 2610 kg/m^3 for the aggregates, and 1000 kg/m^3 for the water. All specimens within a mixture were cast from the same batch.

Table 3.2: *Mixtures used in the triaxial test program, values given in kg/m^3*

	Project *a*				Project *b*		
Mixture	C2a	C4a	C8a	C16a	C4b	C8b	C16b
Cement	451.9	470.6	404.5	283.1	313.6	317.5	243.2
Water	317.1	289.0	255.5	198.6	220.0	222.8	170.7
Aggr. 0-2	1401.8	0	0	0	0	0	0
Aggr. 0-4	0	1459.6	1256.1	878.0	1765.2	1378.6	927.5
Aggr. 4-8	0	0	346.4	242.3	0	380.6	256.0
Aggr. 8-16	0	0	0	733.0	0	0	774.7
Plasticizer	0	0	0	0	2.50	0.60	0.60
Unit weight	2170.8	2219.1	2262.5	2334.9	2301.3	2300.2	2372.7
w/c ratio	0.70	0.61	0.63	0.70	0.70	0.70	0.70
vol% aggr.	0.55	0.56	0.61	0.71	0.68	0.67	0.75

For a mortar, a smaller volume percentage of aggregates is normally required to obtain a workable mixture because the smaller aggregates require more water. A method to obtain workable mixtures with a large volume

content of aggregates is addition of plasticizers. This has been adopted in the *b* mixtures to obtain mortar mixtures with a volume content of aggregates that are comparable to the concrete mixtures.

3.3.2 Specimen Behavior During Test

The compression failure of a concrete is associated with volume expansion. In the case of triaxially compressed cylinders, the extent of volume expansion at failure depends on the confining pressure applied. For increasing confinement pressures, the deformation capacity of the material is increased. For a triaxial test performed in a triaxial cell, the cylinder is naturally compressed in the axial direction with corresponding expansion in the lateral direction. The resulting shape of the specimen is a barrel shape, see Figure 3.6, which shows the specimens of Mixtures C4a and C8a after removal from the triaxial cell. The specimens are ordered from left to right by increasing confining pressure applied during the triaxial test.

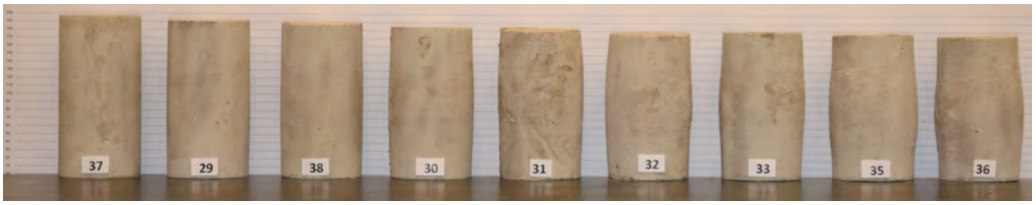

(a) Mixture C4a

(b) Mixture C8a

Figure 3.6: *Appearance of specimens after triaxial testing*

The tendency of increased deformation capacity with increased confining pressure is clearly observed. In the high confinement region, a test can be continued after reaching the peak strength of the cylinder until the deformation capacity of the testing apparatus is reached. Figure 3.7 shows an example of such a specimen that was tested with a confinement pressure of $2.15 f_c$. The initial height of 200 mm was reduced to around 137 mm after testing. It is interesting to note that the cylinder was not broken into pieces despite the extensive damage of the matrix, visible on the surface. It is also observed, that the permanent deformations on the surface seem to originate from an hour-glass shaped failure pattern.

Figure 3.7: *Example of highly deformed specimen from Mixture C2a*

3.4 Interpretation of Test Results

The results of the triaxial tests can be compared in a normalized $\sigma_1 - \sigma_3$ principal stress coordinate system. The primary aim is to estimate the internal angle of friction for the tested materials in the low confinement region and secondly, to assess the strength in the high confinement region.

Figure 3.8 contains the results from all the conducted tests (the test results are also reported in Appendix A). The overall tendency observed is that for small confinement pressures (below approximately $0.5 - 0.6\ f_c$) the failure envelopes can be described fairly well by a linear relation. However, for larger confinement stresses the rate of strength increase is declining. The overall shape of the failure envelope can be described as smooth and convex. In the figure, the Coulomb criterion with $k = 4$ is also indicated. The failure criterion seems to agree well with the tests of the concrete specimens of Mixture C16a, whereas a slight overestimation is seen for the remaining mixtures at low confinement pressures and a larger deviation is observed for higher confinement pressures. This corresponds well with tests from the literature, see e.g. Dahl (1992b).

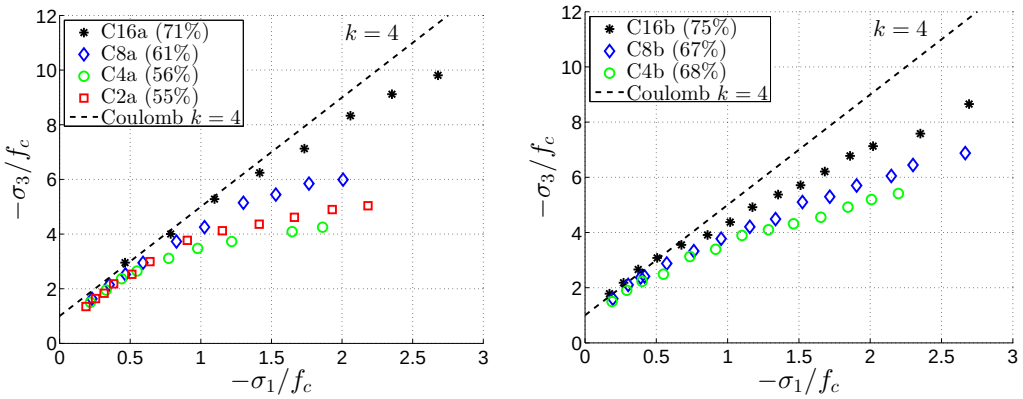

(a) Mixtures *a* (b) Mixtures *b*

Figure 3.8: *Test results compared to the Coulomb failure criterion with* $k = 4$ *(corresponding to* $\varphi = 37°$*)*

3.4.1 Low Confinement Pressures

Figure 3.9 contains the results for confinement pressures up to $\sigma_1 = \sigma_2 = -f_c$ with inclusion of the Coulomb failure criterion for $k = 4$ and $k = 3$. A value of $k = 3$ corresponds to $\varphi = 30°$. It can be seen that for low confinement pressures, the internal angle of friction for mortar should be approximated with a value closer to 30° rather than 37°. This corresponds well with the

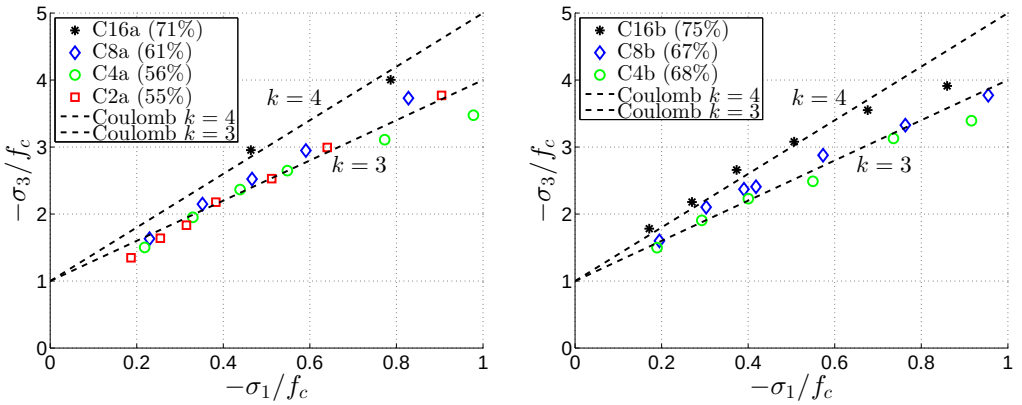

(a) Mixtures *a* (b) Mixtures *b*

Figure 3.9: *Test results from all mixtures in the low confinement region*

test results of Nielsen (1998), who suggested the same value for high strength mortar.

The results also show that the mixtures with a maximum grain size of $d_{\max} = 8$ mm have a smaller strength increase than the mixtures with 16 mm grains. However, a larger strength increase is observed for the mixtures with maximum 8 mm grains than for the mixtures with maximum 4 mm grains. This leads to the conclusion that an increase in maximum grain size positively influences the triaxial strength. Yet, the conclusion is partly based on a simultaneous increase in aggregate volume content, which also influences the properties.

3.4.2 High Confinement Pressures

Figure 3.10 contains the test results for confining pressures larger than 0.5 f_c. The Coulomb failure criteria with $k = 4$ and $k = 1$ are also included. A value of $k = 1$ corresponds to an internal angle of friction of 0°. It can be seen that the inclination of the failure envelopes for the mixtures with smaller $d_{\max}$ tend towards a linear relation described by $k = 1$. For larger $d_{\max}$, the transition between the initial inclination and the decreased inclination for increased confinement pressure appears at relatively higher confinement pressures and the decrease in inclination is smaller. In this relation, the actual expression for the estimated failure criterion (intersection with the ordinate) is less important. It is more relevant to note, that the failure criterion of all test series with reasonable accuracy can be describe by a bi-linear relation as suggested by Dahl (Equation (3.1)), adopting appropriate k values for the two regimes. For the mortars tested the relationship should

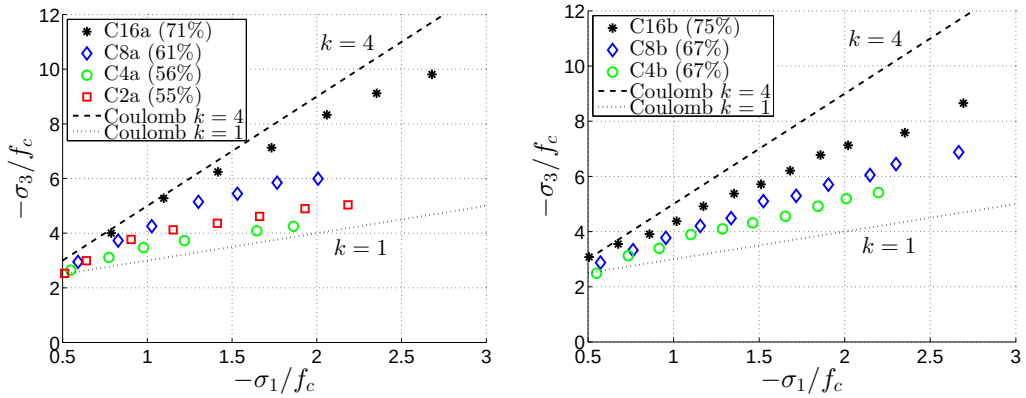

(a) Mixtures *a* (b) Mixtures *b*

Figure 3.10: *Test results from all mixtures in the higher confinement region*

describe an internal angle of friction of 30° for low confinement pressures and conservatively $\varphi = 0°$ can be suggested for the higher confinement region. The coefficients to adopt would then increase with increasing maximum grain size and aggregate content of the mixtures.

From a micromechanical point of view, the change in inclination of the failure envelope can be interpreted as a transition to failure only in the cement paste without any significant additional strength gained from the aggregates. This is in accordance with the findings of Palaniswamy and Shah (1974) who observed that the fracture of concrete at low confinement pressures was governed by bond failure (between aggregates and cement paste) whereas the failure at high confining pressures was governed by paste strength.

3.4.3 Evaluation of Aggregate Content

When comparing the results of C8b and C4b it can be concluded that an increase in maximum grain size has a positive influence on the triaxial strength. However, the difference is not great and when relating to the results of the *a* mixtures it seems that the aggregate content has a greater influence on the strength increase.

In this relation, it should be noted that the results of Mixture C2a lie above the results of C4a. This is believed to be due to the fact that the specific surface area of the aggregates were greater for the C2a mixture compared to C4a (smaller aggregates with similar volume percentage of aggregate content implies a larger total surface area). The larger surface area may have an impact similar to an increased volume content. It is also worth

mentioning that the C16b mixture deviates more from the Coulomb criterion with $k = 4$ at higher confining pressures than the C16a mixture. As the compressive strengths and maximum grain sizes were similar, the difference must be found in the aggregate content. It seems that an increase in volume percentage above a certain limit does not have a positive influence on the triaxial strength at high confining pressures. Alternatively, the difference can be explained by the quality of the aggregates used.

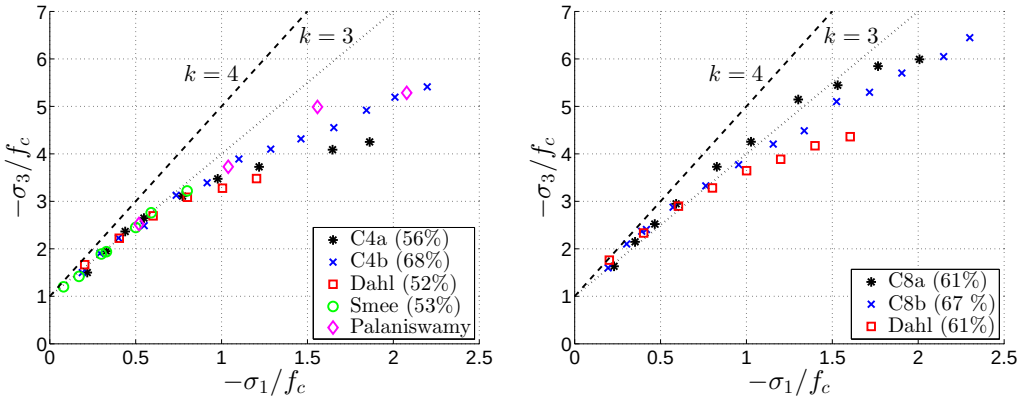

(a) $d_{\max} = 4$ mm (b) $d_{\max} = 8$ mm

Figure 3.11: *Comparison of test results with identical maximum grain sizes*

In Figure 3.11 comparisons of the mixtures with maximum 4 mm and 8 mm grains are shown. In the figure the results of Dahl (1992a), Smee (1967), and Palaniswamy and Shah (1974) are also included (with estimated volume percentages) in order to widen the basis for comparison. For the 4 mm mixtures, it is found that the behaviors at low confinement pressures are comparable (agreeing well with the Coulomb criterion using $k = 3$). At the higher confinement pressures (after the transition on the failure envelope), an increase in aggregate content typically affects the strength increase positively. For the 8 mm mixtures the same tendency is not unambiguously observed (comparing e.g. the results of Dahl (61 %) to C8a (61 %)). Some of the explanations may be found in the fact that the mixture tested by Dahl had a higher concrete strength ($f_c = 69.61$ MPa) than Mixture C8a ($f_c = 41.2$ MPa). For low confinement pressures, the test results are comparable and the inclination of the failure envelope is greater than for the mixtures with a maximum grain size of 4 mm.

In general, the observations emphasize that the proportions of the mixtures influence the test response more than the difference in the maximum aggregate size. Nevertheless, it has been shown, that increases in the aggre-

gate content and the maximum grain size generally have a positive influence on the triaxial strength.

3.5 Thin Section of Tested Specimen

To gain knowledge of the failure process of a cylinder tested in triaxial compression, a thin section analysis was conducted for some of the specimens of the C4a mixture. The analysis consisted of small 32x47 mm samples impregnated with epoxy. The impregnation reveals any cracking or failure of the matrix when inspected in a microscope.

Figure 3.12 shows an example from an untested specimen. It can be seen that the mixture appears homogeneous without lumped aggregates. The figure also shows that no significant cracking from creep or shrinkage had developed at the time of analysis. The age of the specimens was not less than the specimens tested in triaxial compression and hence it constitutes a sound basis for evaluation of load induced cracks in the matrix.

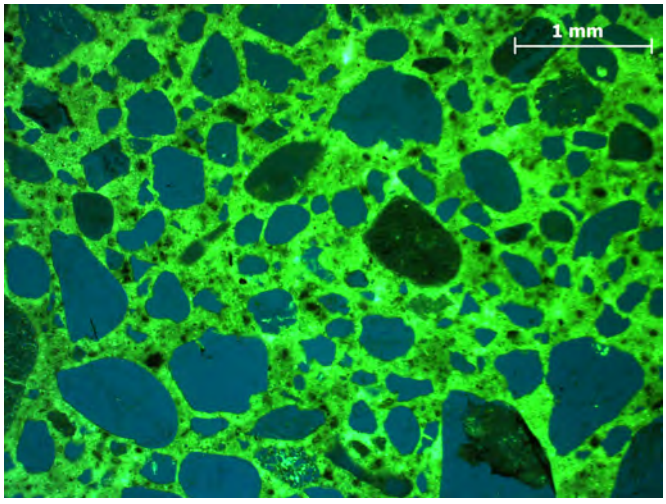

Figure 3.12: *Thin section of untested specimen with a maximum grain size of 4 mm*

According to Bongers and Rutten (1998), cracks in concrete subjected to multiaxial loading can be described by different phenomenon's, including:

1. crushing at the interface between aggregate and paste (bond failure)
2. cracking between and around the aggregates (in the cement paste)
3. failure through the aggregates

The first phenomenon initiates before reaching the peak strength as the interfacial zones between the aggregates are bond zones with a higher porosity than the cement paste and the aggregates. Failure of this zone (by crushing) explains the initial inelastic compaction of the cylinder. An increase of the load induces cracking either in the cement paste (phenomenon 2) or through the aggregates (phenomenon 3) depending on the local strengths of these. By a combination of the phenomenons, shear cracks form in and around the aggregates. The development of shear cracks changes the volumetric behavior from compaction to dilatation (volume expansion).

In the following, the main observations from thin section analysis of a specimen tested with a confinement pressure of $1.62 f_c$ will be presented. The confined strength of the concrete corresponded to 4.06 f_c. Figure 3.13 shows an example of the crack pattern at the midsection of the deformed cylinder. Figure 3.13(a) shows where the thin section analysis was performed on the longitudinal section of the cylinder (cylinder cut in half) and also the specific area where the crack pattern was observed. All three phenomenon's were present at the midsection, see Figure 3.13(b). Crushing of the interfacial zone was less pronounced compared to cracks through the cement paste and through the aggregates. A high number of failed aggregates was also observed at the midsection for specimens tested with smaller confinement pressures. However, tests conducted with a higher confinement pressure generally led to a larger extent of cracked aggregates.

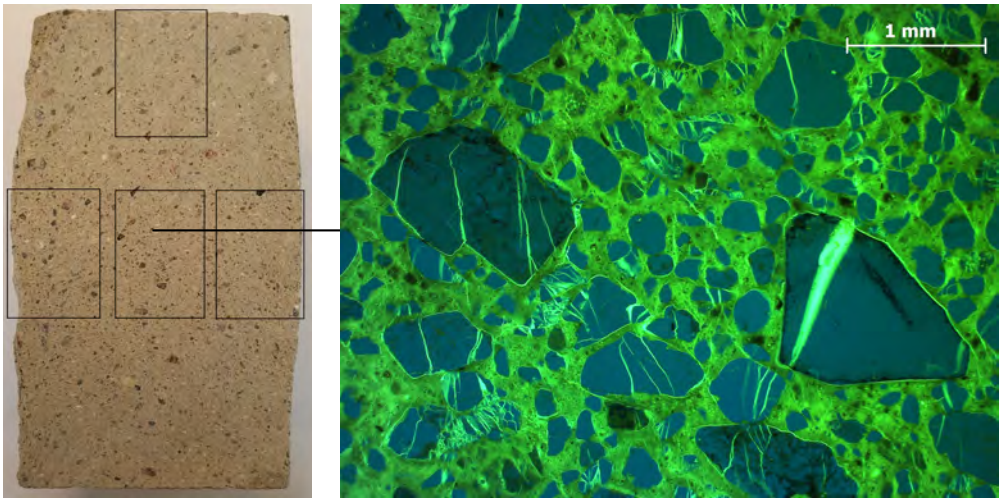

(a) (b)

Figure 3.13: *Crack pattern at the midsection of a cylinder tested to failure with a confinement pressure of* $1.62 f_c$

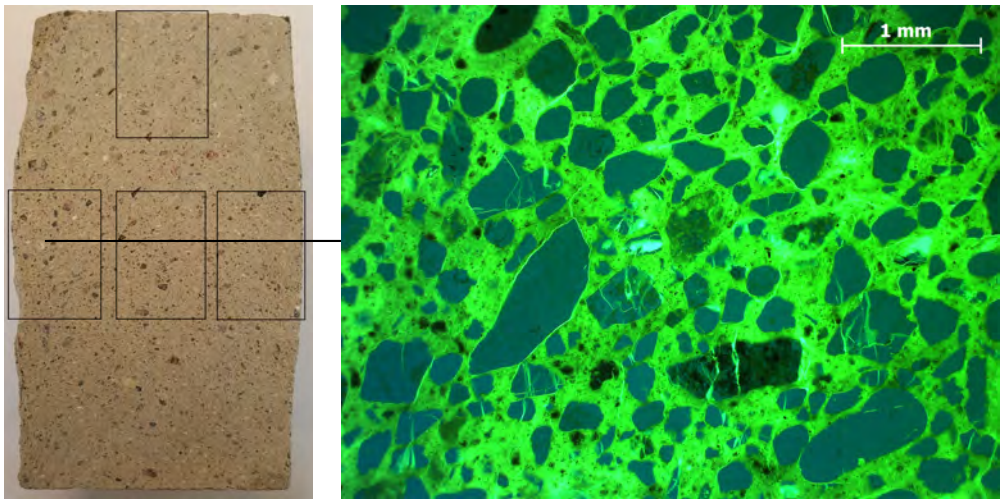

(a) (b) Cracks in the side section

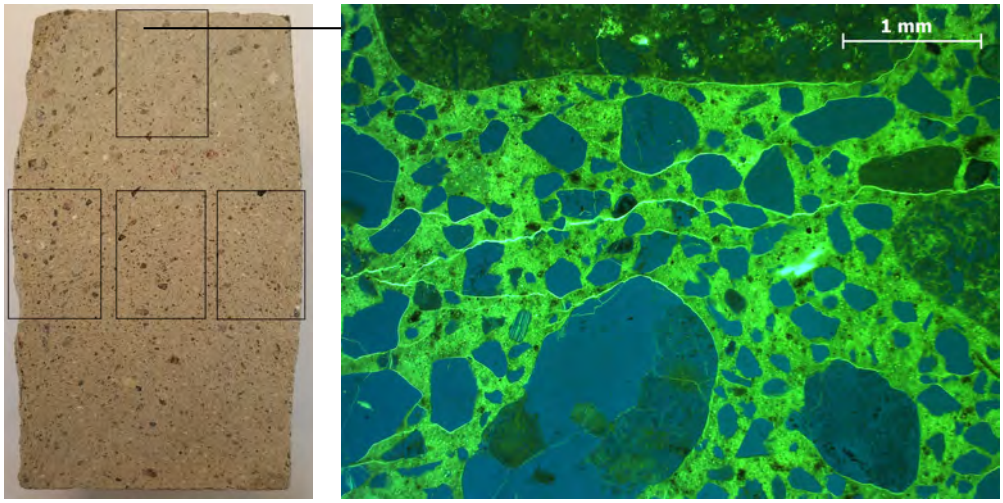

(c) (d) Cracks in the top section

Figure 3.14: *Apperance of cracks at (a)+(b) the side of the cylinder and (c)+(d) at the top section of the specimen*

At the sides of the cylinder, see Figure 3.14(b), fewer cracks through the aggregates were observed. The cracks in the cement paste had a vertical orientation or a slightly inclined orientation. The cracks appear primarily around the aggregates and cracks only developed through the weak grains. Generally, fewer cracks were observed near the side of the specimen compared to the midsection and they were more difficult to identify.

At the top section the cracks consisted primarily of horizontal cracks both in the interfacial bond zone but also in the paste, see Figure 3.14(d). Combining the observed crack patterns with the shape of a tested specimen (see e.g. Figure 3.7), the overall crack pattern in the cylinder can be established, see Figure 3.15. The shape can be described as an hour-glass shape, where the top and bottom parts of the cylinder may be considered as cones. Along the cones, cracks develop with an inclined orientation towards the midsection of the specimen. In the remaining part of the cross section, additional cracks develop to accommodate the overall volume expansion of the specimen. This includes horizontal cracking of the top and bottom part of the specimen.

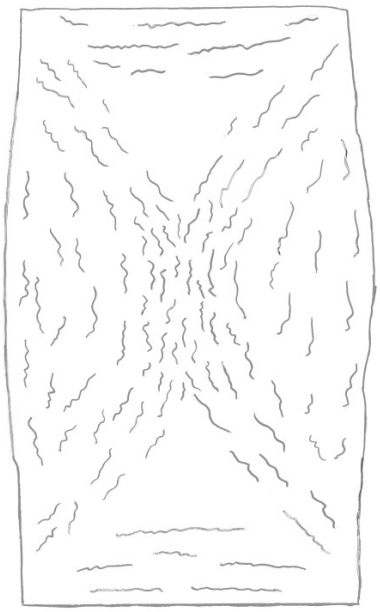

Figure 3.15: *Interpretation of crack pattern in a cross-section of the cylinder after triaxial testing*

3.6 Concluding Remarks

This chapter presented results of triaxial tests on mortar and concrete. The mixtures had maximum grain sizes of $d_{\max} = 2$, 4, 8, and 16 mm. When comparing the test results to the literature, it is evident that mortar possesses a smaller strength when confined, compared to concrete mixtures. The decrease in triaxial strength is a result of the smaller maximum grain size but also of the aggregate content of the mixture. The shape of the failure envelope is hence a result of the mixture proportions. The main findings of the experimental tests are summarized as follows:

- ⋆ For low confinement pressures (up to about $0.5 - 0.6\ f_c$) the shape of the failure envelope can be considered as linear.
  - ◇ For concrete mixtures, a value of $k = 4$ ($\varphi = 37°$) may with good accuracy be adopted to describe the failure envelope.
  - ◇ For mortar mixtures, the value of k to be adopted should be taken lower than $k = 4$. For assessment of the limit load a value of $k = 3$ ($\varphi = 30°$) can be used with reasonable accuracy.
- ⋆ For larger confinement pressures the shape of the failure envelope is dependent on the maximum grain size of the mixture as well as the volume percentage of aggregates.
  - ◇ For concrete mixtures, the slope of the failure envelope is less than $k = 4$ however greater than $k = 1$.
  - ◇ For mortar mixtures, the slope of the failure envelope can be estimated with an inclination of $k = 1$ (also for larger aggregate contents).
- ⋆ When combining the findings of the low and high confinement regimes, the convex failure envelope of both mortar and concrete, can with reasonable accuracy be described by a simple bi-linear extension of the Coulomb failure criterion (when reasonable k factors are adopted reflecting the proportions of the mixture).
- ⋆ The failure mode of the specimens tested in the high confinement regime can be characterized by an hour-glass shape.

4 Failure of a Mortar Shear Key

In this chapter, an experimental study of the failure of a mortar shear key will be presented. The investigation of the failure process was conducted on small specimens containing a single shear key loaded in pure shear in a push-off setup, see Figure 4.1. The main motivations for conducting the tests were to identify the failure of a mortar shear key and to gain knowledge of the test response before and after failure of the shear key. A non-contact measurement technique, in shape of digital image correlation (DIC), was used to analyze the relative displacements on the surface of the specimens.

Only a few investigations have been made on the behavior of indented interfaces containing a single shear key. The investigations have mainly been focused on applications for precast segmental bridges, which are typically cast with concrete. As examples, the work of Zhou et al. (2005) and Issa and Abdalla (2007) can be mentioned. These works include numerical modeling and comparisons to standards. Kaneko et al. (1993a,b) developed a mechanical model for the analysis of concrete shear key joints based on test results of Bakhoum (1991). Common for the investigations was the focus on

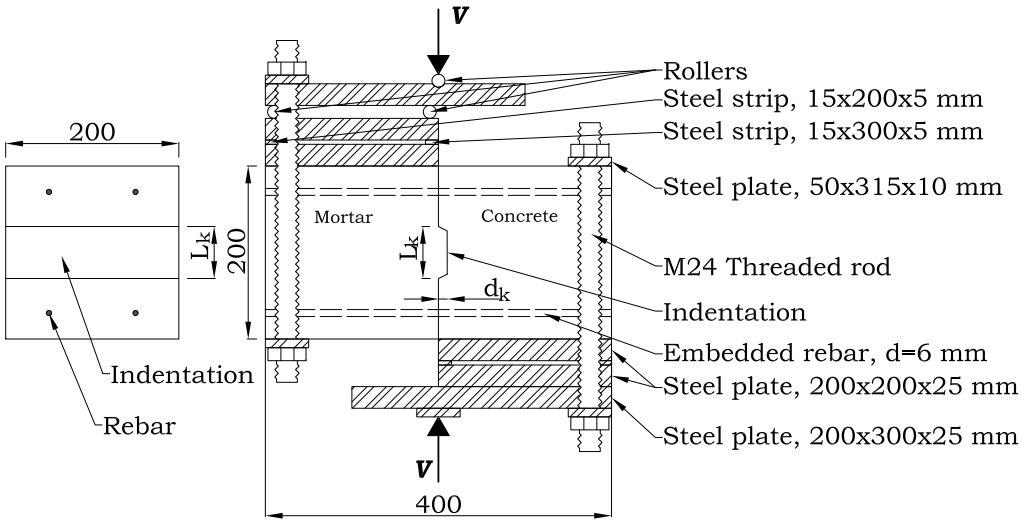

Figure 4.1: *Push-off test setup used for tests of an indented interface containing a single shear key*

Table 4.1: *Summary of specimen data and recorded peak loads*

Series	ID	Key length	$f_{c,C}$	$f_{c,M}$	V_{Peak}
T40	a	40 mm	42.1 MPa	35.3 MPa	72.78 kN
	b				75.12 kN
	c				75.68 kN
	d				80.11 kN
T50	a	50 mm	42.5 MPa	34.4 MPa	97.22 kN
	b				97.92 kN
	c				98.60 kN
T60	a	60 mm	39.9 MPa	36.3 MPa	109.80 kN
	b				112.03 kN
	c				122.46 kN
T70	a	70 mm	38.8 MPa	36.7 MPa	123.90 kN
	b				124.84 kN
	c				127.52 kN
	d				132.90 kN
T80	a	80 mm	35.4 MPa	33.8 MPa	136.54 kN
	b				138.71 kN
	c				138.99 kN

dry joints or joints with epoxy applied. None of these are traditionally used for joints in buildings. Connections cast in-place with mortar are usually used, and the current investigation provides experimental evidence of the failure of such a key, when the anchorage conditions for the reinforcement are sufficient to develop yielding.

4.1 Experimental Investigation

The experimental program consisted of 17 push-off tests on specimens with a 200x200 mm cross section. The specimens were made of two blocks each reinforced with stirrups. The blocks had a length of 200 mm resulting in an overall length of the specimen of 400 mm, see Figure 4.1. The concrete block was cast against smooth formwork and the indented interface was not

treated before casting the mortar against it. The concrete mixture had a maximum grain size of $d_{\max} = 16$ mm, whereas the mortar was a commercial mortar with $d_{\max} = 2$ mm. The depth of the key, d_k, was for all specimens equal to 10 mm. The only geometric parameter varied was the key length, L_k. The in-plane dimension of the key was equal to the specimen's width (200 mm) to allow for detection of key failure on the surface of the specimen. Five key lengths were tested, see Table 4.1 for details on geometry, material strengths ($f_{c,C}$ is the compression strength of the concrete and $f_{c,M}$ is the compression strength of the mortar), and the recorded peak loads, V_{Peak}. The interface was reinforced with four rebars with a diameter of $d = 6$ mm placed perpendicular to the interface. The reinforcement had a yield strength of $f_y = 607$ MPa and an ultimate strength of $f_u = 705$ MPa.

4.1.1 Test Setup

The test setup is illustrated in Figure 4.1. The setup is a modification of the widely used L-shaped elements, e.g. used by Mattock and Hawkins (1972) and Walraven and Reinhardt (1981) for monolithic joints (cracked and uncracked), by Zhou et al. (2005) and Issa and Abdalla (2007) for the single keyed joints, and e.g. by Cholewicki (1971) for joints with multiple keys. The arrangement of steel plates ensured that the thrust line of the load coincided with the plane of the interface. In addition, rollers were introduced to allow for unrestrained movement during failure of the shear key.

During the tests, the load was applied in deformation control with a constant rate of 1.00 mm/min piston movement. The relative shear displacements were measured with linear variable displacement transducers (LVDT's) between the two blocks. The relative displacements in the interface on one surface (where the key was visible) were in addition recorded with images for DIC analysis.

4.1.2 Test Results

Figure 4.2 contains examples of the tested load-displacement relationships, where the displacements are relative between the two blocks and measured with LVDT's in the load direction. The test results can be described by a linear phase until the peak load was reached. The peak load was followed by a drop in load and a subsequent stabilization and gradual increase of the load until rupture of the reinforcement took place at relatively large shear displacements.

The peak load was for all specimens related to a failure by complete key cut off, see Figure 4.3 for examples of failure planes observed after testing.

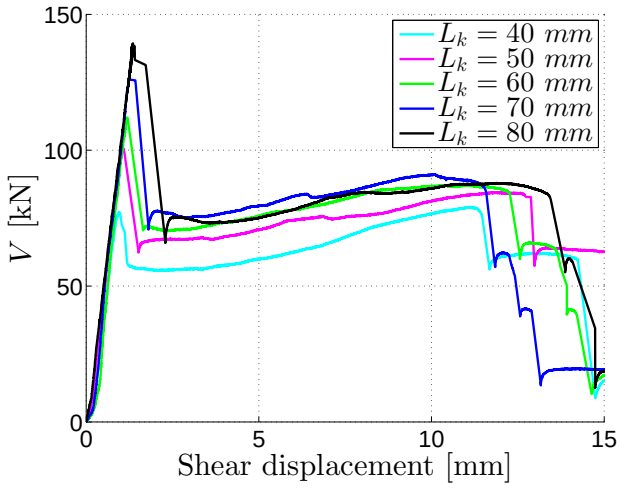

Figure 4.2: *Load-displacement relationships obtained from push-off tests on single key specimens*

It can be seen, both from Table 4.1 and Figure 4.2, that a larger key area increased the first peak load.

The complete key cut off means that the residual capacity after peak load was governed primarily by the capacity of the reinforcement. The test results in Figure 4.2 demonstrate that the residual load levels varied less than the peak loads, when the key length was varied.

4.2 Analysis by Digital Image Correlation

During the tests, pictures were taken manually with a digital camera (24.5 megapixel resolution) with a frequency of up to two pictures per second around the peak load. In the following, the results of the analysis will be used to show examples of how the failure by complete key cut off developed and furthermore give an example of the entire displacement field measured over the crack that governed the failure of the shear key.

4.2.1 Detection of Key Failure

Figures 4.4 and 4.5 contain examples of crack development observed in the shear key around the peak load for a key length of 40 mm and 70 mm, respectively. The results are presented in terms of major principal strain (superimposed on the original image to visualize the actual crack when visible to the unaided eye). The recordings reveal displacement primarily at the interface and cracking of the mortar at the position of the key. The pre-

(a) $L_k = 40$ mm

(b) $L_k = 70$ mm

Figure 4.3: *Observed failure planes after testing, representative for all specimens in the experimental campaign*

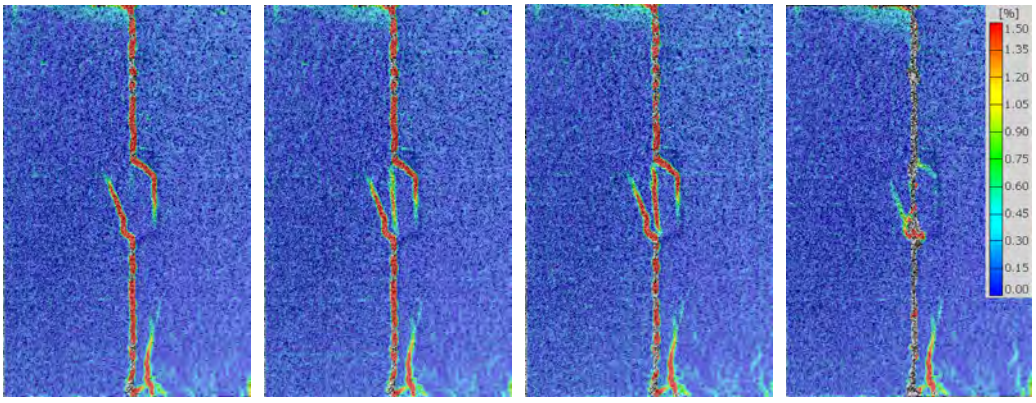

(a) $V = 78.48$ kN (b) $V = 79.15$ kN (c) $V = 81.17$ kN (d) $V = 62.93$ kN

Figure 4.4: *Development of key failure around peak load, Specimen T40d, detected by use of DIC (major principal strain displayed)*

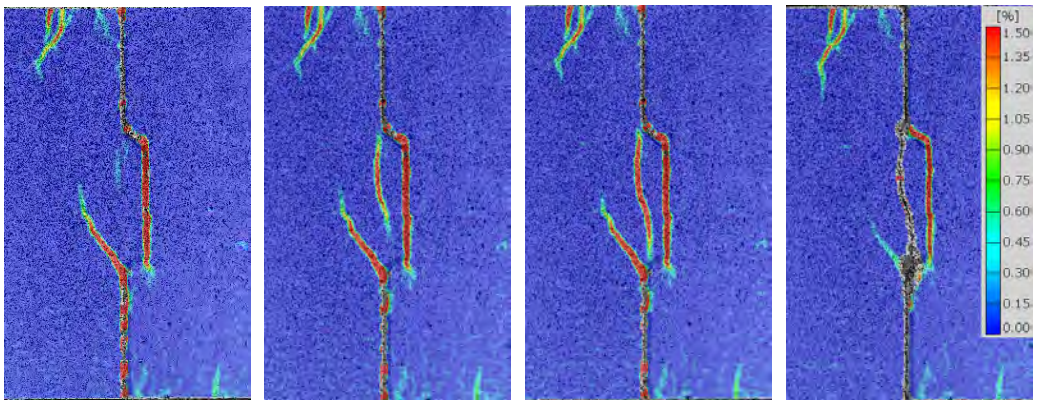

(a) $V = 124.53$ kN (b) $V = 126.01$ kN (c) $V = 127.00$ kN (d) $V = 51.84$ kN

Figure 4.5: *Detection of key failure around peak load, Specimen T70c, detected by DIC (major principal strain displayed)*

sented stages are carefully selected to show how the fracture developed in the mortar. Before reaching the peak load, some displacements were recorded in all parts of the interface except at the lower key corner, see Figures 4.4(a) and 4.5(a). This shows that the lower part of the keyed interface was in compression. The distributions of major principal strain show that before failure (by shearing) initiated, a small amount of displacement (including dilatation) had taken place in the interface and a diagonal crack had formed originating from the lower key corner. These observations are in accordance with the crack patterns observed by Zhou et al. (2005) and Bakhoum (1991) for dry single key joints.

From the detailed DIC analysis, it is also found that the failure by shearing of the key developed more or less instantly. It was generally observed, that the failure did not evolve from the key corner. The strain measurements indicate that the failure developed within the key and then progressed to the edges of the key, eventually resulting in complete shearing. In this relation it should be mentioned that the existing diagonal crack closed partly upon failure and for Specimen T40d, the strains in the indentation was reduced (compare part (d) to part (c) in Figure 4.4). For Specimen T70c the strains in the remaining key area were not relieved as much as in Specimen T40d, however, the diagonal crack closed. It is also observed that the failure plane for Specimen T70c was not completely straight. This means, that further shear displacement had to overcome the roughness of the failure plane. As will be shown in the next section, this entails transverse displacements.

4.2.2 Analysis of Displacement Field

In the following a detailed example of the displacements measured over the crack that led to complete key cut off will be given. The displacements can be divided into several characteristic phases, each described by a displacement vector and an angle of the displacement vector to vertical. In Figure 4.6 the failure of a shear key by complete key cut off is schematically illustrated. Here $\mathbf{u}_1$ describes the relative displacements over the crack in Phase 1 and α_1 is the direction of the displacement vector. In the succeeding phases similar parameters can be determined.

In the following, the relative displacements over the governing crack of specimen T40d will be presented. Three measurements were performed over the length of the key, at the top, at the center, and at the bottom of the key, see Figure 4.7. As indicated by the measurement lengths, the results are solely related to displacements in the crack, i.e. not influenced by any slip in the interface or diagonal cracking developed in the specimen.

In Figure 4.8 the shear displacement, measured parallel to the interface at the center line, versus the shear load, can be seen. Referring to Figure 4.4, where no strains were detected at a load close to the peak load, no significant displacements can be measured before failure of the shear key

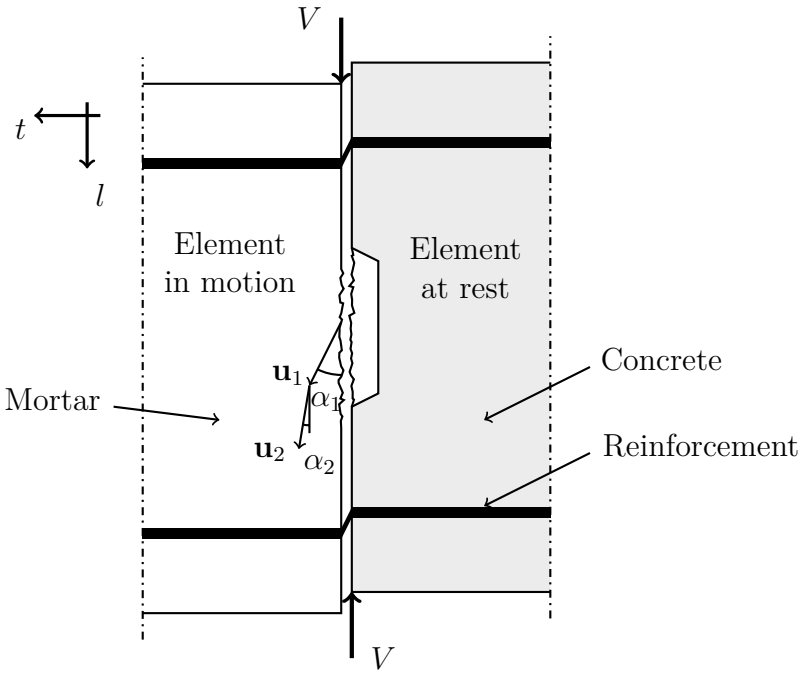

Figure 4.6: *Idealized relative displacements measured over the governing crack in a shear key*

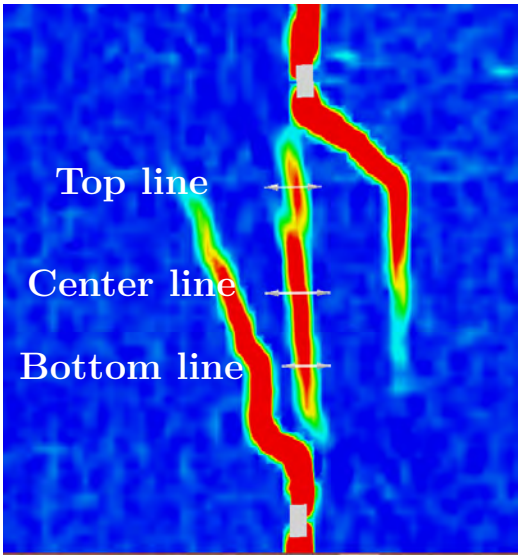

Figure 4.7: *Position of measurement points for DIC analysis of relative displacements at key failure, Specimen T40d*

(the peak load is marked with a green circle). After failure of the shear key the shear displacements over the crack increases until termination of the measurements.

In Figure 4.9 the transverse displacements measured at the center line is shown. Here, it can be seen, that some transverse displacement can be measured before reaching the peak load. This corresponds to the crack initiation shown in Figure 4.4. After the peak load, a drop in load is seen, and from this point the load and the transverse displacements increase until the end of the test. In the figure, some displacement regimes (from A to H) are indicated. These are carefully chosen as characteristic points in the displacement field. Regime A contains the displacement regime before reaching the peak load, whereas Regime B contains the drop. In these regimes, the relative shear displacements are small compared to the total shear displacements and therefore they are difficult to identify in Figure 4.8.

In Figure 4.10 the relationships between the shear displacements and the transverse displacements for the three lines in the different regimes are shown (note the differences in units on the axes). For illustrative purposes, a shear key with a crack corresponding to complete key cut off is also shown. It should be mentioned that the displacements are relative (the shear displacements on the ordinate only apply to the top line). In general it can be seen, that the direction of the displacements changes from an initial relative large inclination to a smaller inclination and in the end of Regime H, the displacements are almost parallel to the interface.

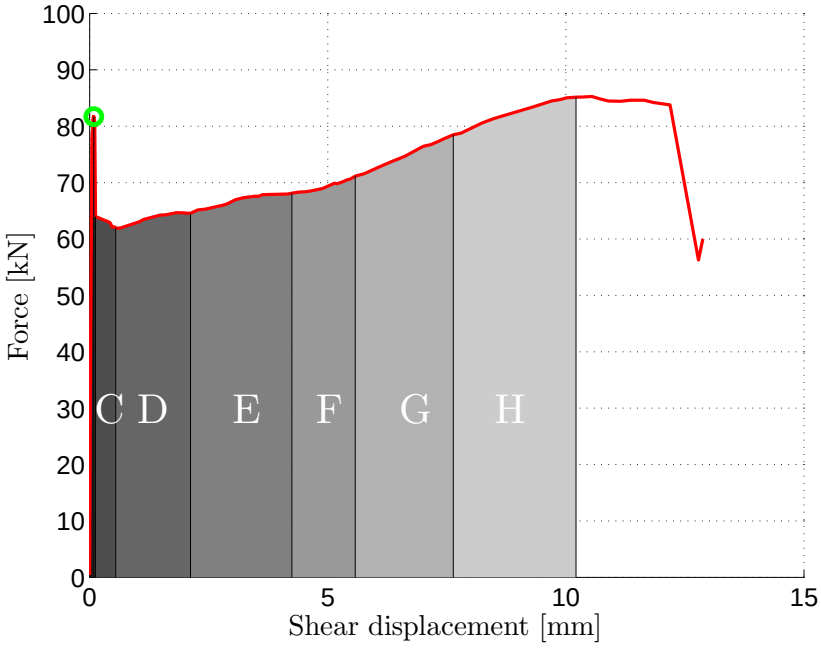

Figure 4.8: *Relationship between the recorded load and shear displacements measured by DIC over the crack in the mortar key, Specimen T40d*

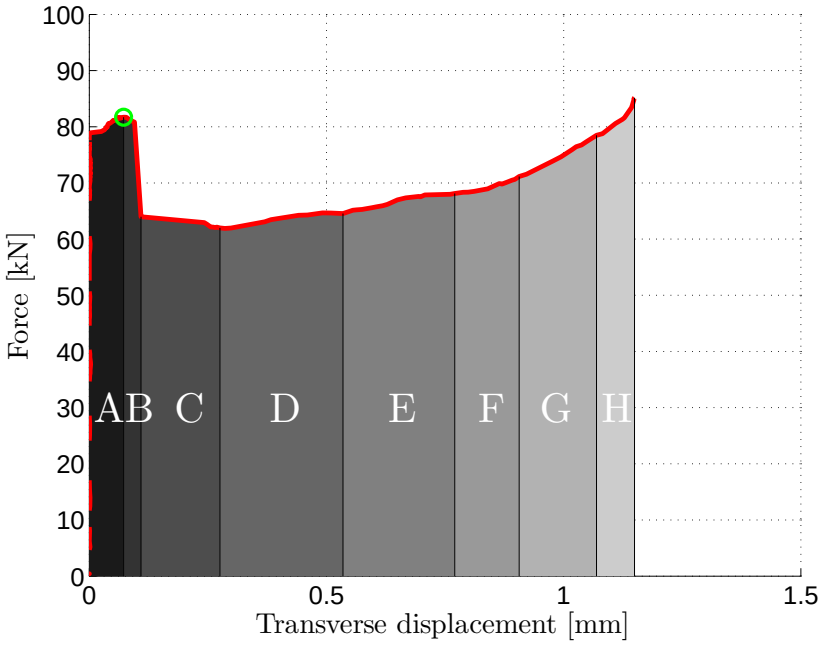

Figure 4.9: *Relationship between the recorded load and transverse displacements measured by DIC over the crack in the mortar key, Specimen T40d*

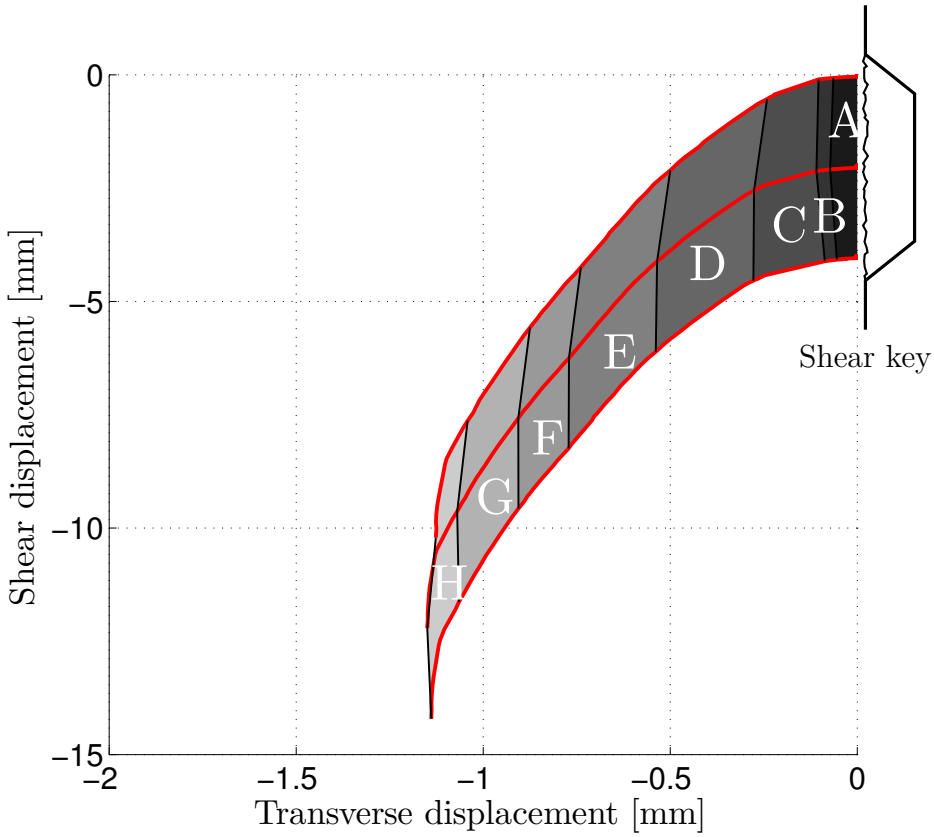

Figure 4.10: *Relative displacements recorded by DIC over the crack in the mortar key, Specimen T40d*

Table 4.2 contains the calculated inclinations (to vertical) of the relative displacements in the shear key. It is interesting to note that the angles in the pre-peak regime, Regime A, are in a order of magnitude close to φ (which with reasonable accuracy can be expected to be within $30 - 37°$). The drop in load occurs when the failure of the shear key develops fully (Regime B). In this regime the angles of the displacements are slightly increased. For further shear displacements beyond Regime B, the angles decreases and approaches displacements parallel to the interface.

The general crack pattern and the displacement field observed in a shear key before and after failure are representative for what can be anticipated for the behavior of a larger connection with multiple keys. The behavior can be expected, when tensile yielding of the transverse reinforcement takes place.

Table 4.2: *Average angles of displacement over a crack in a mortar shear key, measured in the different displacement regimes (measured by DIC)*

Regime	Bottom line	Middle line	Top line
α_A	42.3°	39.4°	34.2°
α_B	50.9°	45.0°	41.7°
α_C	17.6°	21.5°	24.0°
α_D	9.3°	9.4°	9.4°
α_E	6.4°	6.3°	6.2°
α_F	5.8°	5.8°	5.8°
α_G	4.6°	4.5°	4.4°
α_H	1.9°	1.8°	1.6°

4.3 Concluding Remarks

In this chapter, the failure of a mortar shear key was investigated. Experimental results of push-off tests were presented and analyzed by use of digital image correlation. Examples of the development of failure in the shear key around the peak load were presented. In addition, the displacement field for one specimen was presented and the directions of the relative displacements were estimated in the entire load-displacement regime. The results established the general behavior of a keyed joint loaded in shear and indicated the behavior that can be anticipated in a keyed shear connection with multiple keys. The findings of the chapter are summarized as follows:

- ⋆ The peak load of the single key interface was associated with failure of the shear key and a larger key area led to a larger peak load.
- ⋆ The residual load carrying capacity after failure of the shear key was governed primarily by the capacity of the reinforcement.
- ⋆ The failure of the shear key was detected by use of digital image correlation. The failure by complete shearing of the key developed quickly, without a significant increase of load, once the crack initiated.
- ⋆ The failure of a mortar key loaded in shear was associated with transverse displacements.

5 Tensile Capacity of Loop Connections

This chapter contains an evaluation of the tensile capacity of the new loop connection design. The chapter is based on Paper I where upper bound plastic models for the tensile capacity of '2-on-2' loop connections were developed. The models give information on the amount of lacer reinforcement that should be provided in a loop connection in order to obtain yielding in the U-bars and thereby avoid a brittle premature failure of the grout. Through a parametric study, the influence of some parameters on the capacity of the connection will be highlighted.

When considering a keyed shear connection between precast elements, the ability of the loop connections to transfer tension is a prerequisite for it to be able to transfer shear forces. Figure 5.1 shows how a shear load, V, can be transferred by uniaxial strut action (compression) between the indentations. The strut action may consist of single struts over one or more shear keys or a combination of struts with different inclinations, see e.g. Chapter 8. The diagonal compression struts must be accompanied by tension in the transverse reinforcement (U-bar loops) in order to maintain equilibrium. This can be seen in Figure 5.1(b) where the vertical force resultant of the uniaxial stress field between a pair of keys is balanced by the applied shear load (red arrows), while the horizontal force component must be balanced by tension in the reinforcement (blue arrows). The largest capacity is obtained when the reinforcement is stressed to yielding, however, this requires a sufficient strength of the uniaxial compression strut to avoid failure of the grout. When the reinforcement is stress to yielding, it is possible to obtain ductile test responses, see e.g. Figure 4.2, where an increase in load was seen after failure of the shear key.

In the conventional design of shear connections, see Figure 1.2, the longitudinal locking bar provides a passive confining effect on the mortar placed within the overlapping area of the U-bar loops. Therefore, when the overlapping U-bars are placed closely together (i.e. with contact), the strength of the confined mortar is sufficient to develop yielding in the U-bar loops. If the overlapping loops are placed with a mutual distance, the capacity of the compressed mortar might be less than the yield capacity of the U-bars. This is not considered in design recommendations for shear joints, see e.g. (CEN, 2004; fib, 2008). Recently Herfelt et al. (2016) developed a numerical

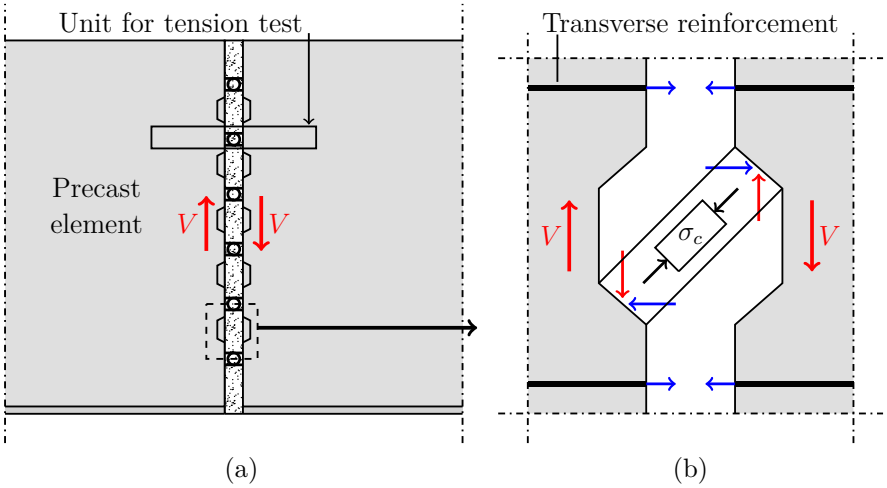

Figure 5.1: *(a) Loading of shear wall connection and (b) activation of reinforcement, when strut action is developed between the shear keys*

method based on finite element limit analysis which accounts for a spacing between the U-bars, however, in practice such tools are rarely available. For the new shear connection design, an essential feature is that the U-bars are placed with a mutual distance. This has to be considered when assessing the capacity. In this relation, it should be noted that contrary to the conventional design, the inclusion of a vertical locking bar in the new design does not improve the ability of the loop connections to transfer tension.

5.1 Prediction of Capacity

In order to assess the tensile capacity related to grout failure in the new loop connection design, tensile tests were performed on specimens representing one unit of a U-bar loop connection, see Figure 5.1(a). The tested connection is classified as a symmetric '2-on-2' connection. Besides a variation of transverse reinforcement (amount of lacer reinforcement), two different grouting materials were tested - a concrete with maximum aggregate size of $d_{\max} = 16$ mm and a mortar with $d_{\max} = 2$ mm. Details on the experimental program can be found in Paper I.

In addition to experimental tests, Paper I also contains upper bound models for assessment of the ultimate capacity of the connection related to grout failure. The theoretical calculations are based on two models - one where the tensile strength of the grout is disregarded (to be used when lacer reinforcement is provided) and one where the tensile strength is included (to be used when no lacer reinforcement is provided). The model disregarding

the tensile strength of the grout is inspired by the work of Jørgensen and Hoang (2013) who tested symmetric '3-on-2' connections. The geometry is adjusted to the proposed '2-on-2' connection design. The model including the tensile strength of the grout is inspired by the work of Jørgensen and Hoang (2015a). A main difference in the development of the models (besides the change from '3-on-2' connections to '2-on-2' connections) is that the works of Jørgensen and Hoang only considered a concrete grout, whereas this study also considers the use of mortar as grouting material. As shown in Chapter 3 the material properties of concrete and mortar are different. The models have to account for this.

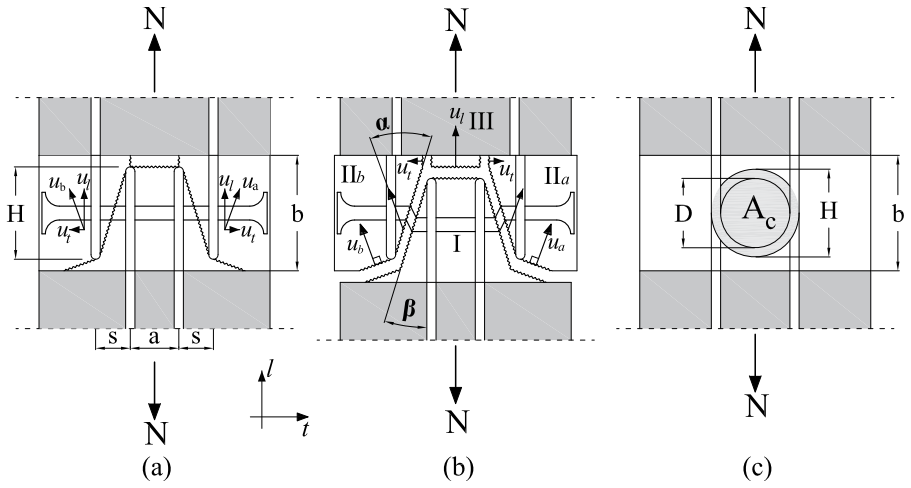

Figure 5.2: *Failure mechanism for '2-on-2' loop connection loaded in tension, illustrations from Paper I*

The assumed failure mechanism for a '2-on-2' connection including lacer reinforcement can be seen in Figure 5.2, where s is the spacing of the U-bars from each element, a is the distance between the innermost U-bars, H is the overlapping length of the U-bars, and b is the width of the connection. The inclination of the yield lines between the tips of the U-bars with vertical is described by β and α is the angle between the displacement vector and the yield line. The optimal value of α can be calculated by Equation (5.1), see Paper I for detailed derivation.

$$\alpha = \beta + \arcsin\left(\frac{1 - 2\dfrac{\Phi_L}{\nu}}{\sqrt{1 + \left(\dfrac{s}{H}\right)^2}}\right), \qquad \alpha \geq \varphi \tag{5.1}$$

where φ is the internal angle of friction. The criterion of $\alpha \geq \varphi$ ensures that the normality condition is fulfilled. The capacity related to grout failure

(including lacer reinforcement) can be assessed by Equation (5.2), where the optimal value of α according to Equation (5.1) has been inserted:

$$\frac{N}{\nu A_c f_c} = \begin{cases} \sqrt{\left(\frac{s}{H}\right)^2 + \frac{4\Phi_L}{\nu}\left(1 - \frac{\Phi_L}{\nu}\right)} - \frac{s}{H} & \text{for } \alpha \geq \varphi \text{ and } \varphi \geq \beta \quad (5.2a) \\ \dfrac{\left(1 + \left(\frac{s}{H}\right)^2\right)\left(\frac{1}{\cos\varphi} - \tan\varphi\right) + \frac{2\Phi_L}{\nu}\left(\tan\varphi - \frac{s}{H}\right)}{1 + \frac{s}{H}\tan\varphi} & \text{for } \alpha < \varphi \text{ and } \varphi > \beta \quad (5.2b) \\ \sqrt{1 + \left(\frac{s}{H}\right)^2} - \frac{s}{H} & \text{for } \alpha < \beta \text{ and } \varphi \leq \beta \quad (5.2c) \end{cases}$$

In Equation 5.2, A_c is the circular overlapping area of the U-bars, f_c is the compressive strength of the grout, ν is the effectiveness factor for concrete in compression, and Φ_L is the reinforcement degree of lacer reinforcement.

Comparison of test results with the theoretical models can be seen in Figure 5.3. The test results are captured well by the models when the proportions of the grout mixtures are accounted for in the choice of internal angle of friction and effectiveness factor. Detailed discussion of φ and ν are given below. The capacity related to yielding of the U-bars is included as an upper limit for the tensile capacity of the loop connection (to explain the test results above the yield capacity of the U-bars in Figure 5.3(a), the ultimate strength limit, f_u, related to hardening of the reinforcement is included with a dashed line). It should be noted that Figure 10(a) in Paper I contrary to Figure 5.3(a) is plotted with a minor mistake. The plateau for small degrees of Φ_L is plotted with a slightly smaller value of $N/(\nu A_c f_c)$ than calculated by the model. The theoretical representations and equations are correct.

5.2 Parametric Study

From Equation (5.2) it can be seen that besides the amount of transverse reinforcement (i.e. the double T-headed lacer bar), a number of factors influence the capacity related to failure of the grout. The following parameters will be varied in order to highlight and assess their influence:

- Spacing between the U-bars (s)
- Internal angle of fiction (φ)
- Effectiveness factor (ν)

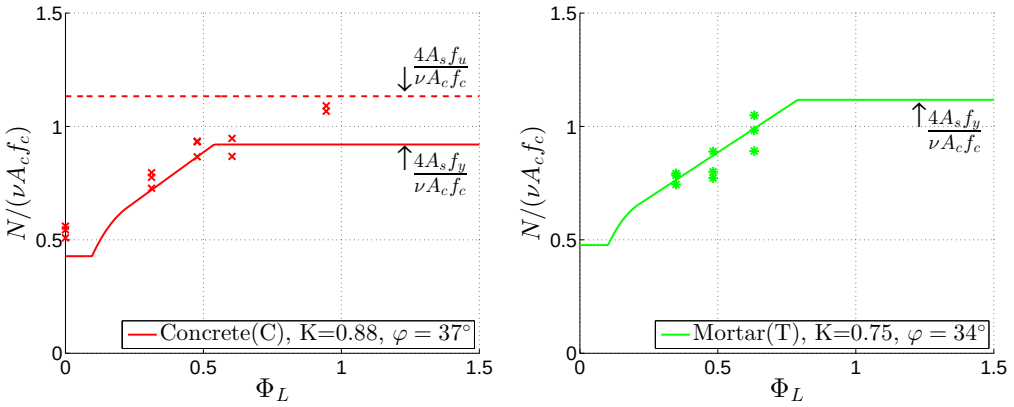

(a) Concrete, $d_{max} = 16\ mm$ (b) Mortar, $d_{max} = 4\ mm$

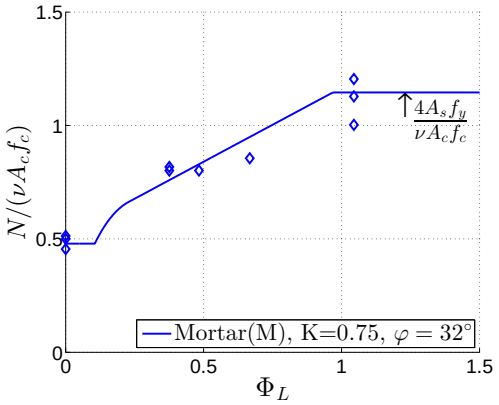

(c) Mortar, $d_{max} = 2\ mm$

Figure 5.3: *Comparison between test results and models, reproduced from Paper I*

Another parameter which also influences the capacity to a great extent is the overlapping length of the U-bars, H. In the model, H is taken as the outer mandrel diameter, which results in a circular overlapping area. If the overlapping area is to be increased, the width of the connection (i.e. b in Figure 5.2) will also increase, which is not always a desirable change of design. Nevertheless, it is obvious that an increase in overlapping area also increases the capacity related to grout failure. This was e.g. shown by Leonhardt et al. (1973). From a practical point of view, a more interesting parameter to adjust is the spacing between the U-bars, s, as this indicates the tolerances for vertical lowering of a shear panel (confer Section 1.2.1). In this relation, it should be noted that the spacing s refers to the spacing of the outermost placed U-bars. The spacing between the innermost U-bars (denoted a in Figure 5.2(a)) can be varied as well. The values given in Table

Table 5.1: *Basic values of parameters adopted in the parametric study of the tensile capacity related to grout failure*

Geometry		**Grout**		**U-bars**		**Lacer Bar**	
s	30 mm	f_c	30 MPa	ϕ	8 mm	ϕ_L	12 mm
D	60 mm	φ	37°	f_y	550 MPa	f_{yL}	560 MPa
a	42 mm	ν	0.6				
b	100 mm						

5.1 will be used as basic parameters when performing the parametric study.

5.2.1 Spacing between the U-bars

The ratio between the spacing of the outermost U-bars and the overlapping length of the U-bars, s/H, (see Figure 5.2(a)) is influencing the capacity of the connection to a high extent. The ratio influences both the calculation of α, Equation (5.1), and the capacity determined by Equation (5.2). For the practical operations on the construction site, the tolerances for vertical lowering can be expressed in terms of s (refer to Figure 1.3). The greatest capacity is achieved when the U-bars are placed closely together (i.e. $s \approx 0$). However, this is practically impossible to achieve with the new design (no post-processing of the U-bars on the construction site is intended). Hence, some spacing has to be provided while the connection still has to be designed to develop yielding of the U-bars.

Figure 5.4 contains calculations, where the spacing of the U-bars is varied. The capacities calculated by Equations (5.2a)-(5.2c) are included to illustrate which solution that is governing for the design parameters used, see Table 5.1. It can be seen that for a small spacing, the tensile capacity of the loop connection is governed by yielding of the U-bars. However, for a spacing larger than approximately $s = 10$ mm, the capacity is governed by failure of the grout. The capacity corresponds to a situation where the angle α is restricted by the normality condition (i.e. α as calculated by Equation (5.1) is smaller than φ and hence $\alpha = \varphi$ is adopted in the calculation). For increased spacing (i.e. increased inclination, β, of the yield lines) the capacity of the connection decreases. For a spacing larger than approximate 60 mm, the inclination of the yield line, β, becomes larger than φ and as an inwards relative displacement is not possible, α must be restricted by $\alpha = \beta \geq \varphi$ in this regime (Equation (5.2c)), see Paper I for details.

The calculated values of α and β for increasing s can be seen in Figure 5.4(b), where also the value of φ is included. From the calculated values, it

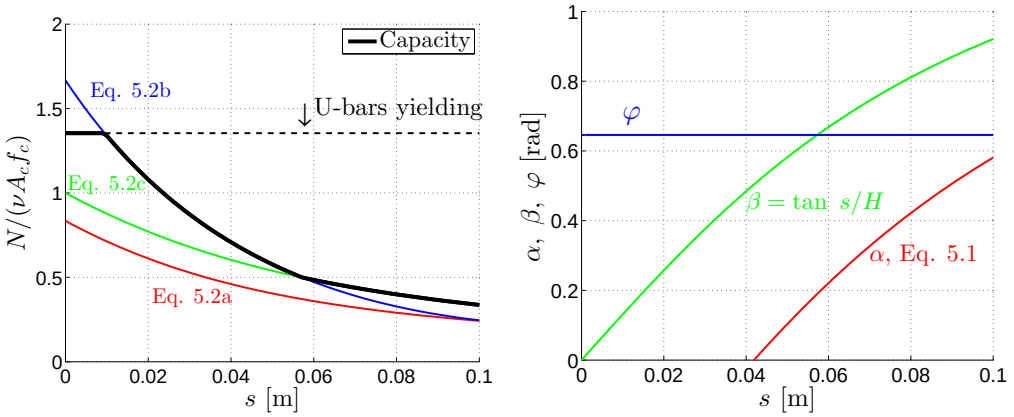

Figure 5.4: *Tensile capacity calculated with a variation of the spacing, s, between the outermost U-bars*

should be noted that for the internal bend diameter of the U-bar loop and the degree of lacer reinforcement considered, the value of α as calculated by Equation (5.1) is not applicable for any spacing of the U-bars. Hence, the capacity is governed by the restriction of the normality condition. In this relation, it should be mentioned that for the situation where $\alpha > \beta > \varphi$ (which is not explicitly covered by Equation (5.2)), the capacity can be calculated by Equation (5.2a) as well.

For practical applications, a larger amount of lacer reinforcement, i.e. larger lacer bar diameter, is recommended in order to allow for a larger spacing between the U-bars. A decrease in the yield capacity of the U-bars would also allow for a larger spacing.

5.2.2 Internal Angle of Friction

In Paper I different values of the internal angle of friction, φ, were adopted for the grout materials used in the experimental program. Furthermore, different values for the effectiveness factor, ν, were also adopted, depending on the grout material. Hence, the direct influence of a change in φ was not clearly illustrated. In the following, the value of the internal angle of friction will be varied. The results are shown in Figure 5.5.

It can be seen, that for smaller values of φ, a larger amount of lacer reinforcement is required to obtain yielding of the U-bars. This is highly relevant when using a mortar as grouting material. Referring to the findings of Chapter 3, the proportion of the mixtures must be considered because factors like the maximum grain size and volume content of aggregates influence

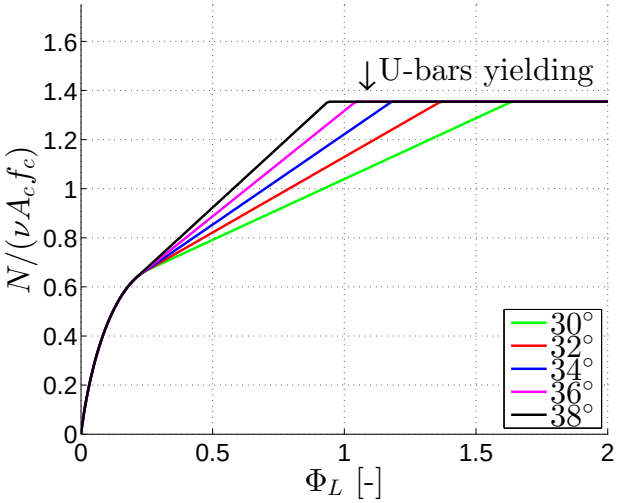

Figure 5.5: *Influence of φ on the tensile capacity of loop connections according to the upper bound model*

the properties of the mixtures. Therefore, in order to design a connection layout that is not governed by failure of the grout, an accurate estimate of φ must be adopted in the modeling. Referring to Chapter 3, a choice of $\varphi = 30°$ is a reasonable estimate, when detailed information of the mortar is not available. Comparing to the experimental results, the choices of $\varphi = 34°$ for the mixture with $d_{max} = 4$ mm and $\varphi = 32°$ for the mixture with $d_{max} = 2$ mm provided good agreement, see Figure 5.3. A choice of $\varphi = 30°$ would be slightly conservative for the considered mixtures. The results of the tensile tests confirm the findings of the triaxial tests, as a value of $\varphi = 30°$ is to be considered as a lower limit. If detailed knowledge of the triaxial behavior of the mixture is available, the choice of φ can be adjusted accordingly.

5.2.3 Effectiveness Factor

When using rigid-plastic theory to structural concrete, a proper choice of effectiveness factor, ν, must be adopted to account for the quasi-brittle behavior of concrete. The influence of the choice of effectiveness factor is shown in Figure 5.6. As expected, it is found that a decrease in effectiveness factor increases the amount of lacer reinforcement required to obtain yielding of the U-bars.

The failure of a mortar material is more brittle compared to failure in concrete. This effect was seen in the tests reported in Paper I and originates partly from the ability of cracks/yield lines to transfer shear via aggregate

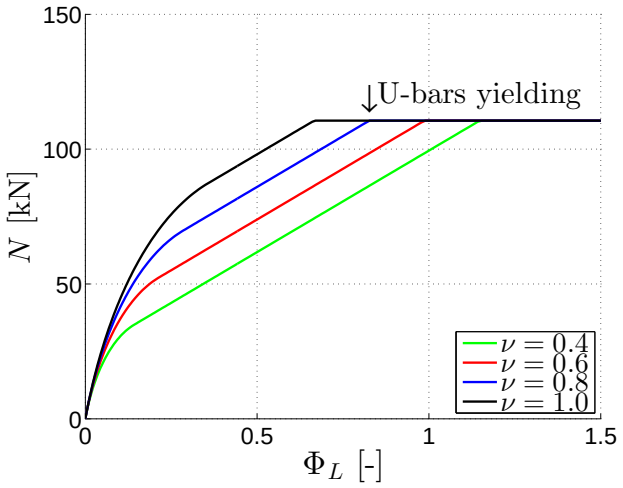

Figure 5.6: *Influence of the effectiveness factor for the grout in compression, ν, on the tensile strength on the loop connection*

interlocking. The effect is reflected in the choice of effectiveness factor, where a smaller value of ν accounts for a more brittle failure.

In Paper I, the effectiveness factor was estimated based on a formula originating from beam shear tests (Zhang, 1997a). Jørgensen and Hoang (2013) adopted the formula for the tensile capacity of loop connections. By introduction of the factor K to account for differences in brittleness between concrete and mortar, the effectiveness factor was calculated by Equation (5.3):

$$\nu = \frac{K}{\sqrt{f_c}} \left(1 + \frac{1}{\sqrt{H}}\right), \qquad (f_c \text{ in MPa and } H \text{ in m}) \qquad (5.3)$$

In Paper I, K was taken as 0.88 for concrete and 0.75 for mortar (based on the suggestion of Jørgensen and Hoang (2015b)), which corresponded to an effectiveness factor of $\nu = 0.63$ for concrete and $\nu = 0.55 - 0.57$ for the mortar materials. Despite the fact, that the basic formula was developed for beams in shear, the formula seems to apply well for the tension tests as well. The effectiveness factor accounts for brittleness effects and size effects. The brittleness effects are accounted for by the term involving f_c, which entails that higher values of f_c decreases ν. This relation is well known. By decreasing the factor K, the higher brittleness of e.g. a mixture with fewer and smaller aggregates is accounted for.

The size effect is also related to softening/brittleness effects. This has to be accounted for when using a plasticity approach as the average strength over the length of the yield line decreases with increasing length. Since the overlapping area was kept constant, the size effect (expressed in terms of the

characteristic length H) cannot be evaluated in the current test program. However, it can be mentioned that the adopted size effect factor $\left(1+\frac{1}{\sqrt{H}}\right)$ makes the theoretical model fit the test results well and that the results of similar tension tests on symmetric loop connections performed by Jørgensen and Hoang (2013) showed reasonable correlation with calculations, when the characteristic length was varied.

5.2.4 Connections without Lacer Reinforcement

For the connections without lacer reinforcement, the tensile capacity assessed by an upper bound solution depends entirely on the tensile strength of the grout. This constitutes a challenge for practical applications, simply because the tensile strength of grouts is relatively low and the tensile behavior is extremely brittle. When using a mortar as grout material all these effects become more pronounced compared to a concrete grout, due to the smaller grain sizes. Nevertheless, the capacity does not vanish entirely if lacer reinforcement is omitted.

The capacity of a connection without lacer reinforcement was in Paper I estimated by Equation (5.4), assuming a slightly simplified failure mechanism.

$$\frac{N_0}{\nu A_c f_c} = \frac{l - m\sin\alpha}{\cos\beta\cos(\alpha-\beta)} + 4\frac{A_t\nu_t f_t}{\nu A_c f_c}\tan(\alpha-\beta) + \frac{A_l\nu_t f_t}{\nu A_c f_c}, \qquad \alpha \geq \varphi \tag{5.4}$$

The parameters l and m are given in Equations (2.15) and (2.16) and are related to the tensile strength of the grout. The optimal angle of displacement is given by Equation (5.5).

$$\alpha = \beta + \arcsin\left(\left(\frac{m}{l} - \frac{4A_t}{lA_c}\frac{\nu_t f_t}{\nu f_c}\right)\frac{1}{\sqrt{\left(\frac{s}{H}\right)^2+1}}\right), \qquad \alpha \geq \varphi \tag{5.5}$$

From the equations it is observed that the effective tensile strength, $\nu_t f_t$, influences the capacity to a high extent. In Paper I, the effectiveness factor for concrete in tension, ν_t, was estimated by a formula adopted for concrete. This formula was not reduced when applied to mortar and a general value of $\nu_t = 0.65$ was calculated for the geometry tested. This ν_t-formula combined with the estimation of the tensile strength based on the compressive strength, Equation (2.13), might overestimate the effective strength of the mortar. On the other hand, the conservative determination of the areas included in the failure mechanism counteracts the possible overestimate of the strength and in summary, the capacity is estimated well, see Figure 5.3(c).

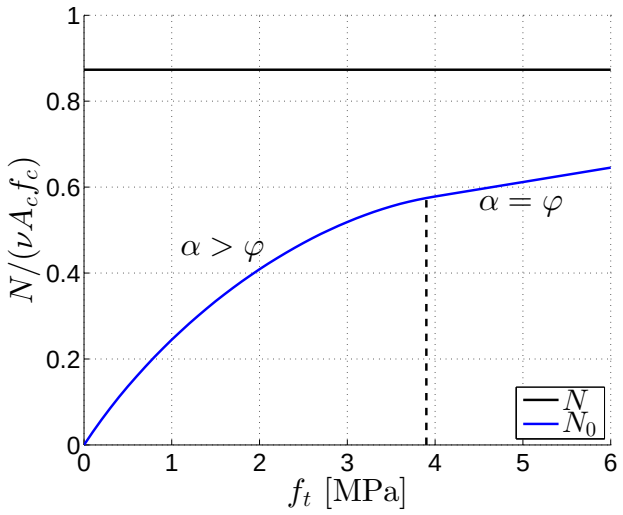

Figure 5.7: *Tensile capacity of loop connections versus the tensile strength, f_t, of the grout*

Figure 5.7 shows the influence of the tensile strength of the grout on the tensile capacity of the loop connections, using the basic parameters given in Table 5.1. For comparison, the strength estimated by Equation (5.2) is also included. As expected, an increase in tensile strength increases the tensile capacity assessed by the model without lacer reinforcement. It can be seen that the mechanism assuming yielding of the lacer reinforcement estimates a higher capacity. For small reinforcement degrees (under-reinforced with respect to lacer reinforcement) the actual capacity is governed by a combination of tensile yielding of the lacer bar and a contribution from the residual tensile strength, as the crack may not be complete stress free at the time of reinforcement yielding. This combination is, however, rather complex to model. Therefore, for simplicity, the tensile capacity of under-reinforced connections has to be estimated by ignoring the contribution from the lacer reinforcement and include the effective tensile strength of the grout. The purpose of such a solution is to avoid under-reinforced connections, where failure is brittle. In practice, however, the connection should always be designed for U-bar yielding, as the most ductile response is obtained by this and not by failure of the grout.

5.3 Concluding Remarks

The chapter discussed the tensile capacity of the proposed '2-on-2' loop connection design. The development of the models and presentation of test results are contained in Paper I. The models predict the tensile capacity related to grout failure, and based on this, the amount of lacer reinforcement that should be provided in order to achieve yielding of the U-bar loops, can be estimated. The chapter outlines the influence of some theoretical aspects when applying upper bound modeling. The discussion was presented as a parametric study and the following remarks should be considered when applying the design:

- ⋆ The shear capacity of a keyed shear joint is dependent on the tensile capacity of the transverse reinforcement (i.e. the U-bar loops).
- ⋆ The spacing of the outermost U-bars in the symmetric '2-on-2' connection influences the capacity to a high extent. A larger spacing can be obtained without a decrease in capacity, when the amount of lacer reinforcement is increased.
- ⋆ The capacity can be assessed by upper bound models with reasonable accuracy, when adopting appropriate material parameters and effectiveness factors for the grout material used in the connection.
    - ◇ The internal angle of friction influences the capacity significantly and a lower value should be adopted for a mortar grout compared to a concrete grout.
    - ◇ The effectiveness factor should account for the brittleness of the grout, i.e. a smaller value should be adopted for a mortar grout compared to a concrete grout.
- ⋆ For under-reinforced connections, the capacity can be assessed by inclusion of the tensile strength of the grout, however, for practical applications the connections should always be designed to obtain yielding of the U-bars (ductile response).

6 Tests of Shear Connections

In this chapter, experimental tests of shear connections will be presented. The purpose of this chapter is partly to describe details and results of the experimental campaign and partly to make it easier for the reader to navigate between test series already published (Paper II and III) and test series not yet published. The campaign provided a basis of experimental results that can be compared with the theoretical models described in the following chapters. The test series included specimens with the conventional shear connection design, but the experimental campaign primarily focused on the new design. Table 6.1 contains an overview of the test series included and the main parameters varied in the different series. The overall focus was on the geometry of the shear keys, with the aim of identifying the important factors for a strong and ductile connection. In this chapter, the shear load applied in the tests will be denoted P, following the notation adopted in Paper II.

6.1 Experimental Campaign

The test specimens were designed as two L-shaped reinforced concrete elements connected by grouted U-bar loop connections. The specimens contained three ($n = 3$) shear keys and four ($n + 1$) loop connections. Figure 6.1 illustrates the general layout of the test specimens, including definition

Table 6.1: *Overview of the experimental series*

Series	**Design**	**Layout**	**U-bars**	**Variation**	**Grout**
1	Conventional	'1-on-1'	8 mm	none	mortar
2	New design	'1-on-2'	8 mm	key depth	mortar
3	New design	'1-on-2'	10 mm	key depth	mortar
4	New design	'2-on-2'	6 mm	key depth	mortar
5	New design	'2-on-2'	8 mm	key length	mortar
6	New design	'2-on-2'	8 mm	key depth	mortar
7	New design	'2-on-2'	10 mm	key length	mortar/concrete

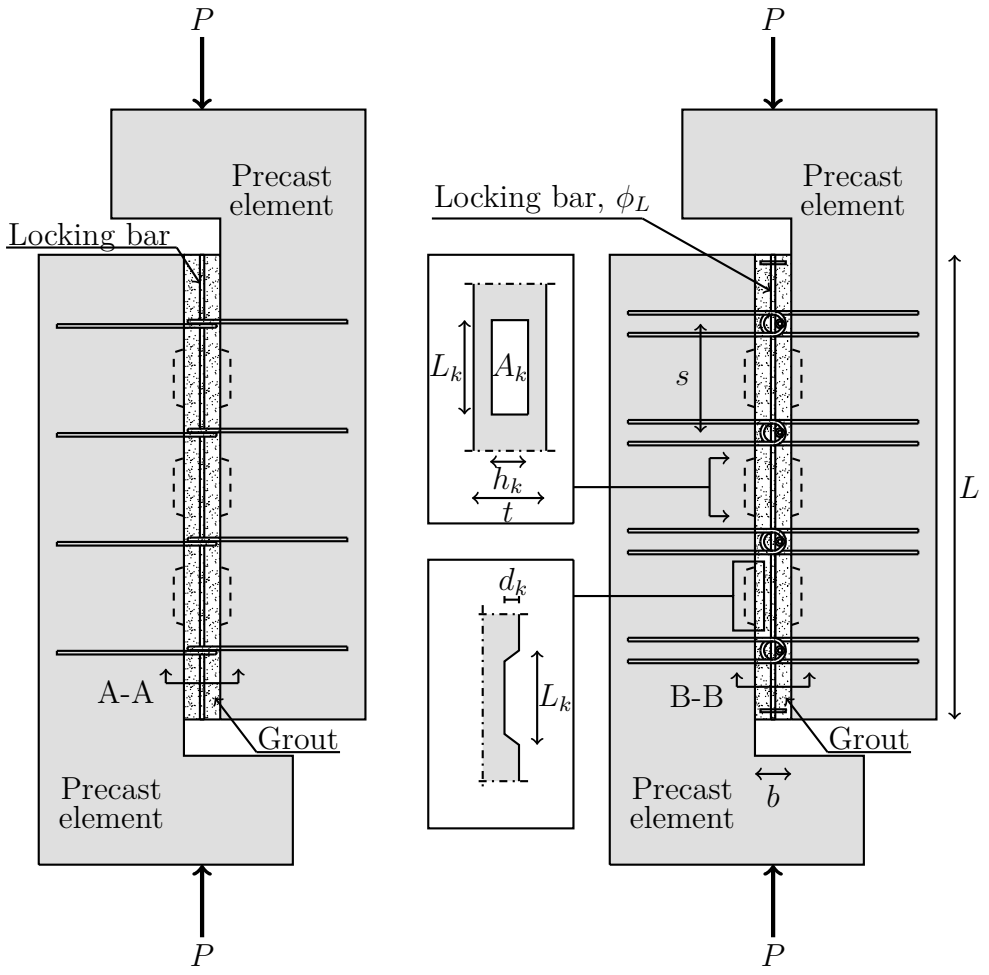

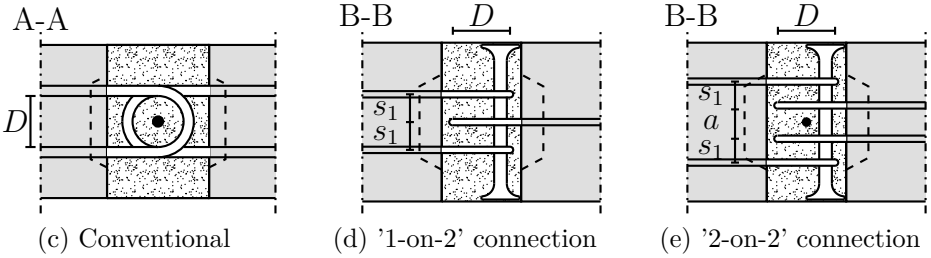

Figure 6.1: *Layout of test specimens used in the experimental campaign and indication of the load application points*

of geometrical parameters related to the shear keys and the loop connection design. A particular feature of the tested connections was that the U-bar loop connections, as seen in Figure 6.1, were placed outside the indented zones.

The test campaign comprised 64 specimens. In Table 6.1 the campaign is divided into 7 series, identifying the design and the three different layouts of loop connections that were tested. In Series 1, the conventional design, see Figures 6.1(a) and 6.1(c), was tested. The series included 6 identical specimens denoted R1-R6. In Series 2, the new design with a '1-on-2' loop configuration, see Figures 6.1(b) and 6.1(d), with 8 mm U-bars was tested. The series contained 4 specimens, S1-S4, with a smooth interface without shear keys and 8 specimens with shear keys, P1-P8. Tests on this configuration functioned as pilot tests that were used to benchmark the new design against the conventional design (Specimens P1-P4 had the same amount of reinforcement in the weakest side of the connection and an identical geometry of the shear keys as Specimens R1-R6). In Series 3, the '1-on-2' configuration was tested with 10 mm U-bars, P9-P12. In Series 4-7 tests were conducted for the new design with a '2-on-2' loop configuration, see Figure 6.1(e). Series 4 tested 6 mm U-bars and a varying key depth. The specimens are denoted D followed by a number indicating the key depth. The results have been presented in Paper III. In Series 5 and 6 specimens with 8 mm U-bars were tested. These specimens are denoted with roman numbers and contained in Paper II. Specimens R1-R3 and P1-P4 are also part of Paper II. Finally, in Series 7 specimens with 10 mm U-bars were tested. In this series the key length was varied and both mortar and concrete was used as grouts. For this reason the specimens are denoted with M and C followed by a number representing the key length.

Table 6.2: *Geometrical parameters used in the experimental campaign, all dimensions in [mm], including references to Appendix B*

	Layout	b	s	L	h_k	L_k	d_k	ϕ_L	Appendix
1	Reference	80	300	1280	85	160	16	12	B.1
2	'1-on-2'	80	300	1280	85	160	0-30	-	B.2
3	'1-on-2'	80	300	1280	85	160	16-30	-	B.2
4	'2-on-2'	80	300	1280	200	140	10-20	12	B.3
5	'2-on-2'	100	300	1280	100	120-180	28	12	B.4
6	'2-on-2'	100	300	1280	200	140	10-28	12	B.4
7	'2-on-2'	120	320	1340	200	120-180	10	12	B.5

In the new design, the diameter of the lacer bar was carefully designed (according to the model presented in Chapter 5) to ensure that the tensile capacity of the overlapping loops was governed by tensile yielding and not crushing of the mortar. In the '2-on-2' connections, anchorage plates were mounted in each end of the locking bar in order to eliminate any boundary effect regarding the anchorage conditions for the locking bar. Table 6.2 contains an overview of the geometrical parameters of the test series. Appendix B contains all details on the specimens including the recorded first peak load, P_{FP}, and the ultimate load, P_{U}, recorded at large shear displacements.

6.1.1 Test Arrangement

The tests were performed with the specimens placed horizontally in a steel frame build on a strong floor. In Appendix B a schematic overview and a brief description of the test arrangement can be found. The precast elements rested, on each side of the connection, on smooth plates in order to minimize friction and allow for unrestricted out of plane deformation of the joint grout. In Figure 6.1, the load application points are indicated. The thrust line ensured pure shear at the midsection of the connection. The precast L-shaped elements were designed with an overstrength to ensure failure in the connection. A similar test arrangement has been used by e.g. Halasz and Tantow (1966), Cholewicki (1971), Pommeret (1972), and Fauchart and Cortini (1972). In this relation, it should be noted that the loading conditions do not ensure pure shear at the position of the keyed interface. However, as the connection has a width, b, the condition of pure shear must refer to the midsection of the connection.

6.2 Test Results

A number of investigations have previously been conducted on the behavior of conventional keyed shear connections. The main findings in these investigations were summarized by Hansen et al. (1976). The results of the reference tests performed in relation to the current study, comply well with the descriptions by Hansen et al. (1976). Nevertheless, when comparing to tests from the literature, a difference in the capacity is observed. It appears that the reference specimens of the current study possessed a higher capacity compared to previous test specimens, where the loops were placed inside the indented areas. This can be explained by the fact that the grout in-between a pair of shear keys is utilized both to ensure the activation of the transverse reinforcement and to carry the diagonal strut, when the loops are placed within the keys (see also Figure 5.1 for illustration of strut action between the keys). This naturally decreases the capacity and emphasizes that

the position of the U-bar loops outside the indented zones ensures a better structural integrity, than when the loops are placed inside the indented areas.

For small shear displacements, the test results for the new design displayed great similarities to the results for the conventional design. For larger shear displacements, the test responses of the new design proved much more ductile than the responses of the reference specimens. In the following, examples of typical load-displacement relationships will be given. This includes a comparison of the conventional layout with the new layout, as well as a presentation of additional results, which has not been covered by Papers II and III.

(a) Complete key cut off, Specimen D20B

(b) Local key corner crushing, Specimen D12A

Figure 6.2: *Examples of the two experimentally observed failure modes of the shear keys*

The failure mode of the shear keys could be identified either from examinations of the specimens after testing or by use of DIC. Contrary to the results of the single key specimens, where only failure by complete key cut off was observed, two distinctive failure modes were observed for the shear connections, see Figure 6.2. For the larger key depths, a failure by complete key cut off was identified as the dominating failure mode, while the specimens with smaller key depths could suffer from local key corner

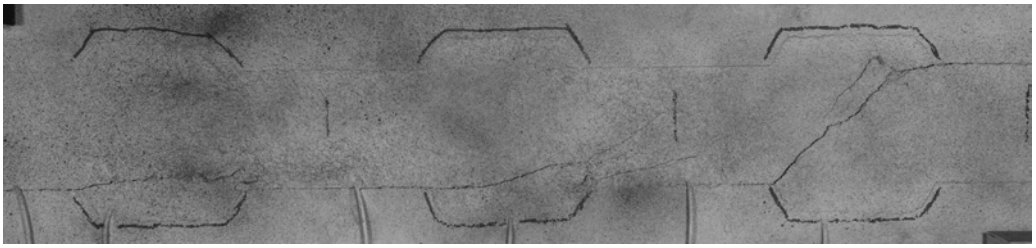

(a) Complete key cut off and diagonal cracking, Specimen I2

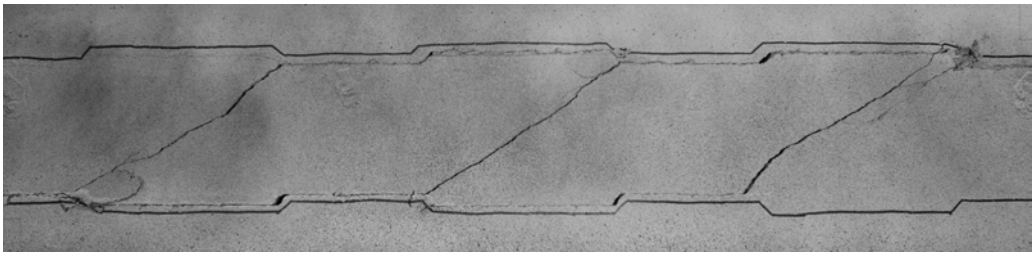

(b) Local key corner crushing and diagonal cracking, Specimen M180A

Figure 6.3: *Examples of diagonal cracking developed in combination with (a) complete key cut off and (b) local key corner crushing*

crushing. In Figure 6.2(a), the interface between the grout and the precast element has been indicated with a red line to visualize the geometry of the key. For the failure by local key corner crushing, the contour of the interface can easily be identified, see Figure 6.2(b). The two failure modes have been reported in the literature for the conventional loop connection layout, and as both failure modes were observed for the new design, the observation is not unique for any of the designs. As will be shown in the following, the failure mode in the shear keys influenced the load-displacement relationship of the connection after the failure of the keys had occurred.

The local failure in the shear keys was a part of the global failure mode of the shear connections. The global failure mode identified for many of the specimens included a diagonal crack on the surface. This was observed for a failure by complete key cut off as well as for the local key corner failure, see Figure 6.3. The extent of diagonal cracking varied for the specimens. Some experienced one diagonal crack while others experienced several diagonal cracks. The tests were continued until rupture of the transverse reinforcement and for this reason, the crack pattern that could be assessed after the test, was not necessarily representative for the global failure mode that initiated the failure of the shear keys. In Paper II, digital image correlation (DIC) was used to identify the global failure mechanisms at the instant of key failure (estimated based on the crack pattern on the surface). In this relation, it can be mentioned that a failure mode by sliding along the in-

clined interface of the shear key, as described e.g. by Eriksson (1978), was not observed in the tests.

6.2.1 New Design versus Conventional Design

In Paper II, a comparison between the conventional and the new design was given. Figure 6.4 repeats the comparison of the tested load-displacement relationships. It should be noted that all depicted response curves correspond to failure by local crushing of the key corners. The main differences between the load-displacement relationships of the two designs are:

- The new design displayed a stiffer behavior before reaching the first peak load.
- The first peak loads (corresponding to failure of the shear keys) were comparable for identical reinforcement degrees and key geometries.
- The responses after the first peak load were significantly different:
  - The new design displayed a ductile response and reached an ultimate capacity (corresponding to rupture of the reinforcement loops) at relatively large shear displacements.
  - The conventional design did not display a pronounced ductile behavior after the first peak load and the shape of the load-displacement curves seemed random.

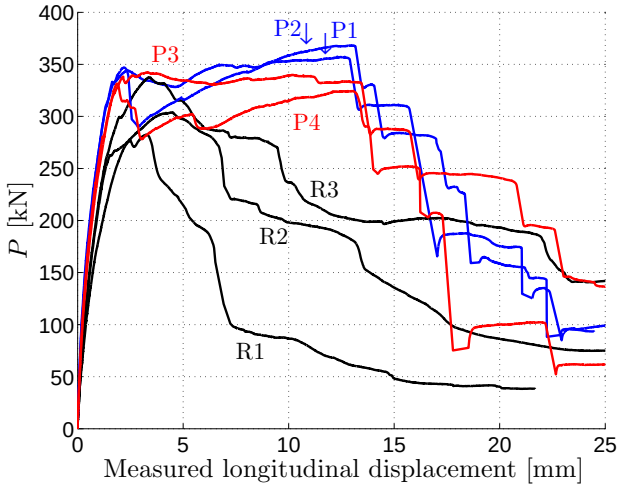

Figure 6.4: *Comparison of tested load-displacement relationships for the conventional design (Specimens R1-R3) and the new design ('1-on-2' design, P1-P4), graphs from Paper II*

(a) U-bars pushed away from each other (Specimen R1)

(b) U-bars pushed towards each other (Specimen R6)

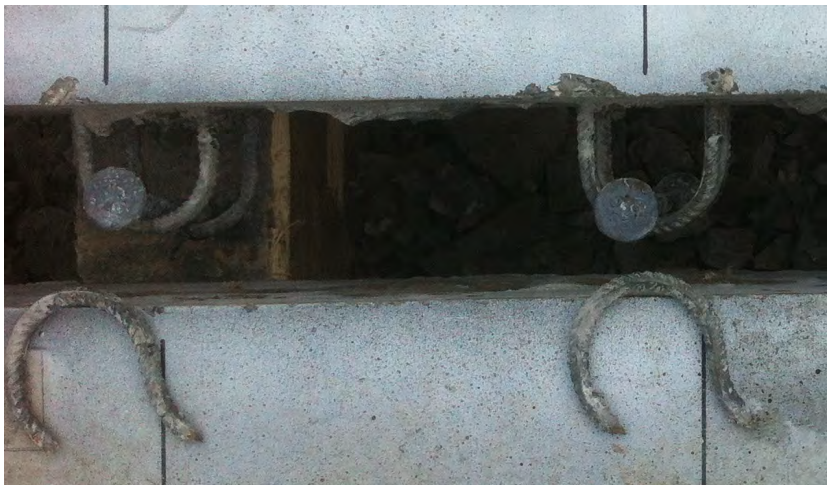

(c) New design '1-on-2' design (Specimen P12)

Figure 6.5: *Deformation of U-bar loops observed after testing*

The gain in ductility of the new design compared to the conventional design is ascribed to the difference in orientation of the transverse U-bar loops and the presence of the double T-headed lacer bar. The double T-headed lacer bar functions as passive confinement for the grout in the area, where the U-bars overlap. When comparing the deformations of the U-bars in the two designs after testing, different deformation patterns were observed. In addition, a dependency of the load direction on the U-bar deformation was observed for the conventional design. This was not the case for the new design as the orientation of the U-bars ensures that the response do not depend on the load direction.

Figure 6.5(a) shows an example of how the U-bars in the conventional design had deformed, when the U-bars were pushed away from each other, when exposed to shear displacement (the grout was removed after test). It was found that the extent of U-bar deformation was little despite of the large shear displacements imposed during the test. In return, the grout was extensively cracked at the end of the test.

In Figure 6.5(b), an example is given, where the U-bars of the conventional design were pushed towards each other during the test. It can be seen that the load direction ensured a self-locking effect between the U-bars, when the shear displacement was increased. For this reason, the extent of U-bar deformation was greater (U-bars clashing during shear displacement). It was also observed that the U-bars deformed out of the plane that they were placed in. In addition, extensive cracking was observed in the grout at the end of the test, including a diagonal crack running through the center of the area, where the U-bars overlapped. Loading in this direction provided a greater residual capacity after failure of the shear keys than if the U-bars were pushed away from each other. In the latter case, the softening response after the peak load was very pronounced. Figure 6.4 contains examples of both cases. The response curve of Specimen R1 represents a situation, where the U-bars were pushed away from each other, while Specimens R2 and R3 represent the opposite situation. The difference is clearly seen, both in terms of the recorded first peak loads and in the ability to carry load after the first peak capacity was reached. In a real structure, the direction of the shear load in a connection depends e.g. on the wind load direction. This makes it impossible to ensure that the better of the two types of response in the conventional design is always governing.

For the new design, the U-bars deformed differently, see Figure 6.5(c). The deformations in the U-bars were concentrated at the interface, and the remaining part of the rebars in overlap remained more or less intact. This was observed for all diameters of the U-bars tested, both for the '1-on-2' and the '2-on-2' configuration. In addition to the different U-bar deformations, it can also be mentioned that fewer cracks were observed on the surface

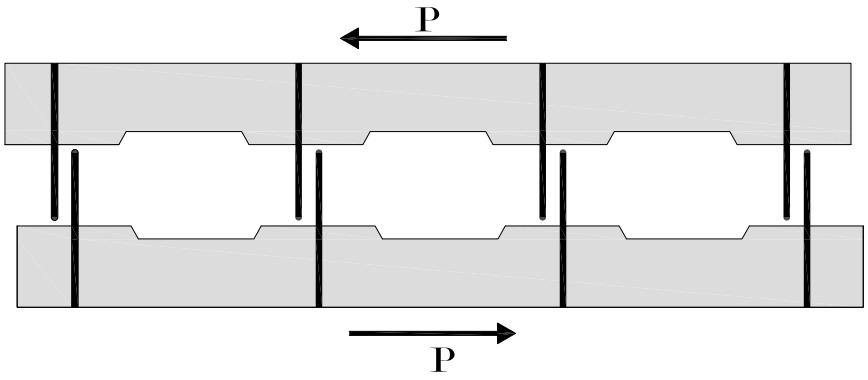

(a) Conventional layout, displacement away from the loops

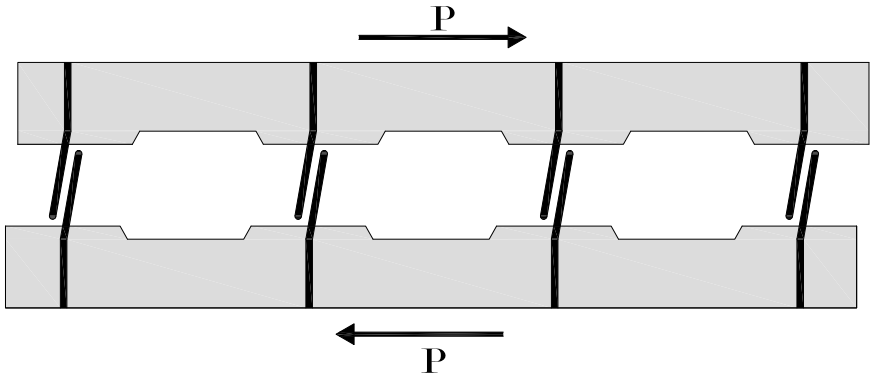

(b) Conventional layout, displacement towards the loops

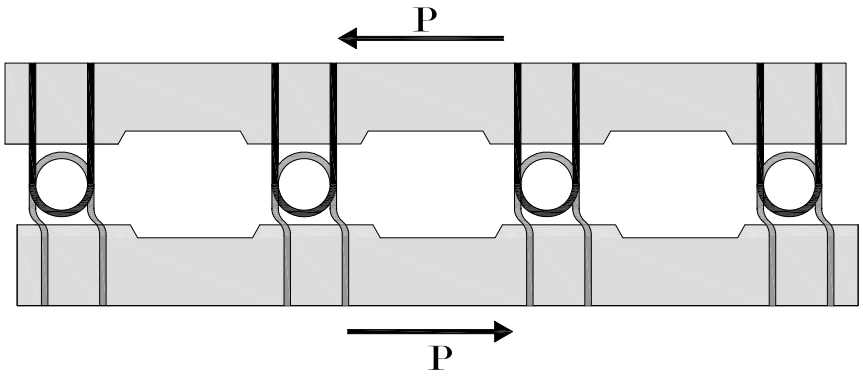

(c) New layout, independent on load direction

Figure 6.6: *Idealized deformations of U-bar loops observed after testing*

of the connection for the new design compared to the conventional design. The idealized deformation patterns of the U-bars in the two designs are summarized in Figure 6.6. It should also be mentioned that some U-bars of specimens with the new design had deformed as shown in Figure 6.7. It is not possible to distinguish whether the deformations appeared as a consequence of very large displacements or if the U-bars deformed as shown during the entire test (from when plastic deformations were initiated). Nevertheless, the response curves show that the new design, with an orientation of the U-bars in the same plane as the precast element and with the double T-headed lacer bar used as transverse reinforcement, displayed a significant ductility compared to the conventional design. In this relation, the ability of the confined concrete core in the U-bar overlaps to remain intact during displacement is a deciding factor for a ductile response. It was observed that the response curve of the new design had the ability to increase the load again after the first peak capacity, and eventually reach a load level similar to or higher than the first peak load, P_{FP}. The second local maximum was recorded as P_{U}, see Appendix B. In the ultimate state, the failure of the specimens with the new design was governed by rupture of the rebars, and not failure of the grout. This was not always possible to achieve with the conventional design.

Figure 6.7: *U-bar deformation observed with the new design, Specimen P2*

The positive influence on ductility, when changing the orientation of the U-bars, was most clearly observed in tests on the new '1-on-2' design, where shear keys were omitted, see Figure 6.8. The interfaces of these specimens were cast against smooth formwork and greased before casting the grout. The test response did not display a distinct first peak load due to the lack of shear keys. However, the response is still very ductile, displaying an increase in load until rupture of the U-bars. The transitions in the load-displacement relationships at small displacements (from an initially stiff response to an almost perfect plastic/hardening response) are consequences of the reinforce-

ment yielding. Examinations of the transverse reinforcement after testing showed plastic deformation of the U-bars similar to the example shown in Figure 6.5(c).

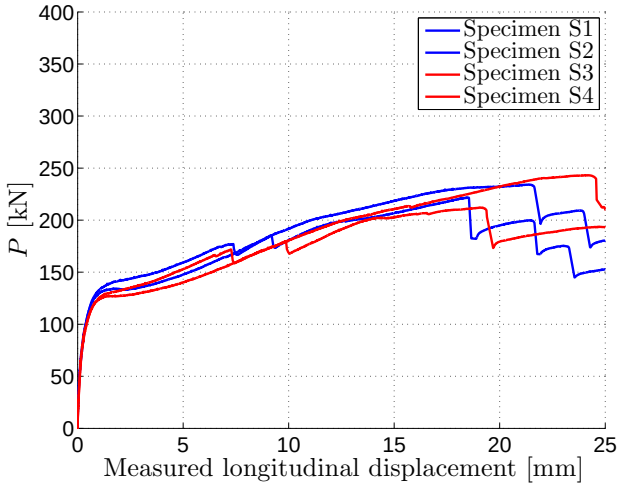

Figure 6.8: *Tested load-displacement relationships for shear connections with smooth and greased interfaces without shear keys (8 mm U-bars '1-on-2' configuration)*

6.2.2 New Design - '2-on-2' Connections

In the following, test results of the proposed '2-on-2' connection layout will be presented. Tests of the conventional design with comparable transverse reinforcement degrees have not been carried out. Figure 6.9 contains examples of response curves for specimens with 6 mm U-bars (also presented in Paper III). The test results in the figure are divided in two graphs, relating to the observed failure modes of the shear keys, confer Figure 6.2.

For the specimens suffering complete key cut off, a drop in load was observed after the peak load, P_{FP}. Subsequently, a stable residual load level was maintained until rupture of the U-bars at large shear displacements. For these specimens, the ultimate load, P_{U}, was smaller than P_{FP}, see Figure 6.9(a). For the specimens suffering local key corner crushing, the first peak capacity was clearly dependent on the depth of the shear keys. For increasing key depth, an increase in peak load was seen until a limiting depth, where the specimens (for the particular transverse reinforcement degree) suffered complete key cut off. The drop after the peak capacity was less pronounced compared to failure by complete key cut off and subsequently, the residual load stabilized at a higher level (larger values of P_{U}, see Appendix B.3) than seen for the specimens suffering complete key cut off.

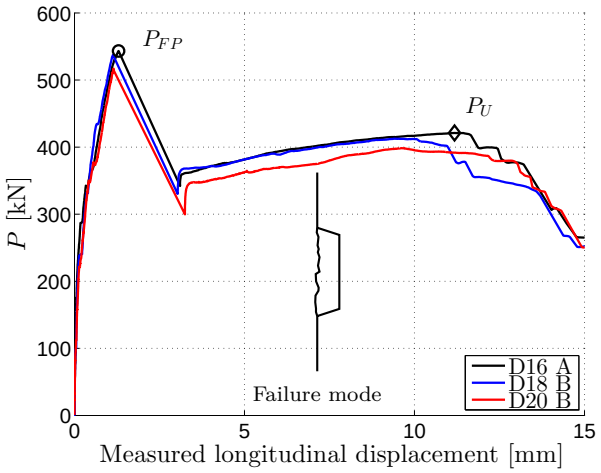

(a) Complete key cut off

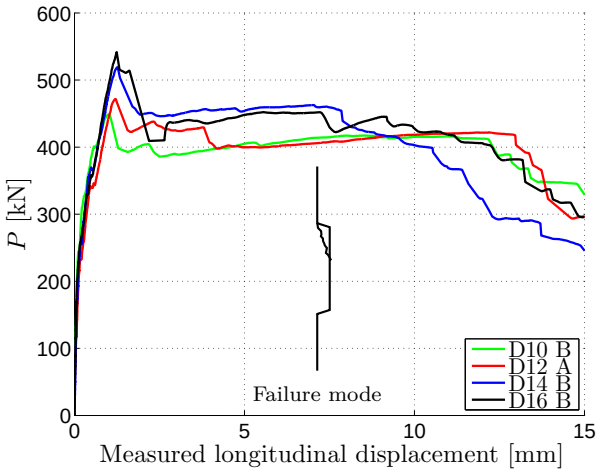

(b) Key corner crushing

Figure 6.9: *Tested load-displacement curves for new design with 6 mm U-bars ('2-on-2' configuration), graphs from Paper III*

In Chapter 4, the failure of the single shear key was associated with displacements in the transverse direction of the joint. This was also observed for both types of local key failure in the larger shear connections. In Figure 6.10, the relationships between the measured transverse and longitudinal displacements are shown for the same specimens as the ones referred to in Figure 6.9. In order to identify jumps in the displacements, the results are presented as points. For both failure modes, a jump in displacement was observed around a longitudinal displacement of 1.5 mm. This corresponded to failure of the shear keys and was also observed in the tests of single key specimens presented in Chapter 4. The results confirm that the failure by

complete key cut off was more brittle than the local key corner crushing. It was found that the amount of transverse displacements was small prior to the failure of the key, and for all specimens, the amount of transverse displacement increased with increasing shear displacement. The relationships for the complete key cut off appear somewhat linear, whereas the development for the failure by local key corner crushing appears slightly more random. Nevertheless, it can be concluded that the displacement fields for all specimens included transverse displacements, and that the displacement fields were influenced by the failure of the shear keys.

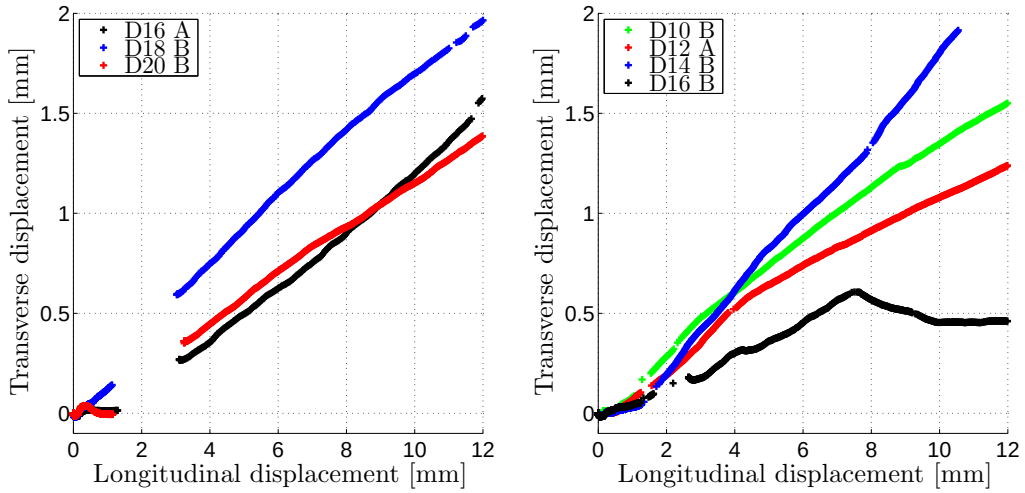

(a) Complete key cut off (b) Key corner crushing

Figure 6.10: *Relationships between longitudinal and transverse displacements, specimens with 6 mm U-bars ('2-on-2' configuration)*

In Figure 6.11, test results for specimens with 8 mm U-bars are presented (the results are also presented in Paper II). The test series with 8 mm U-bars had specimens suffering complete key cut off as well as specimens failing by local key corner crushing. In the figure, examples of response curves for specimens suffering complete key cut off can be seen (Specimens II2 and VIII2), where an initial peak load was observed followed by a drop and a subsequent increase in load until rupture of the reinforcement. Specimen V2 suffered from local key corner crushing. The load-displacement relationship of this specimen confirms that the development after initial peak is dependent on the failure mode of the shear key. Unlike the results shown in Figure 6.9, the tests with 8 mm U-bars constitute examples, where the residual capacity can be greater or similar to the load corresponding to failure of the shear keys. However, a drop in load after key failure was still observed and the

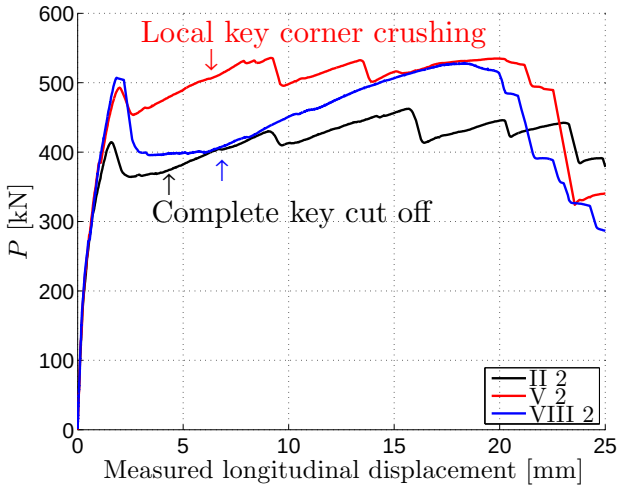

Figure 6.11: *Tested load-displacement relationships for specimens with 8 mm U-bars ('2-on-2' configuration), graph from Paper II*

magnitude of the sudden load decrease depended on the failure mode of the shear keys.

Figure 6.12 shows tested load-displacement relationships for connections reinforced with 10 mm U-bars. Both concrete and mortar were used as grout in the test series. All tests showed failure by local key corner crushing and the load-displacement relationships proved very ductile with no drop in load. The test results showed no dependency on the key length (similar

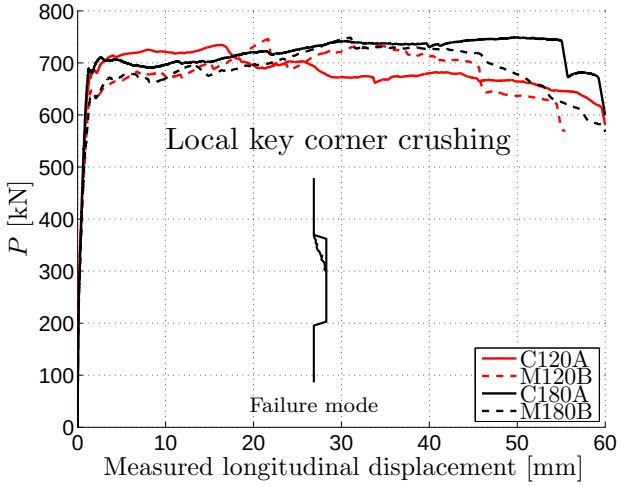

Figure 6.12: *Tested load-displacement relationships for specimens with 10 mm U-bars ('2-on-2' configuration)*

results for the three key lengths tested). In addition, the test results did not show dependency on the grout material. The mortar and concrete grouts used in the test specimens provided more or less the same capacity for the connections and a similar behavior during the tests.

In general, it can be concluded that the failure by local key corner crushing facilitates a more ductile load-displacement relationship than the failure by complete key cut off. In addition, it can be concluded that the amount of transverse reinforcement governs the residual load level after failure of the shear keys.

6.2.3 Additional Observations from Digital Image Correlation

In the following, experimental observations obtained from analysis with digital image correlation (DIC) will be presented. The analyses were performed using the software Aramis developed by GOM. Examples of DIC results were also given in the appended Papers II and III. The following examples are in line with the observations described above and they supplement the observations presented in the papers.

The comparison of the conventional design with the new design showed significant differences in the post peak load-displacement response. DIC

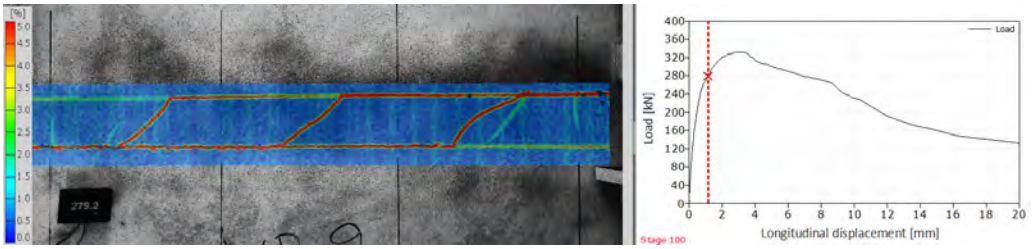

(a) Prior to peak load

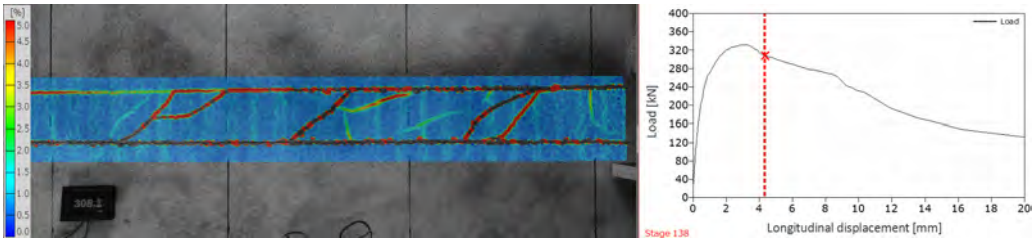

(b) Just after peak load

Figure 6.13: *DIC analysis (major principal strain) of reference Specimen R4 (U-bars pushed towards each other), showing (a) diagonal cracks prior to peak load and (b) cracks in the post peak region*

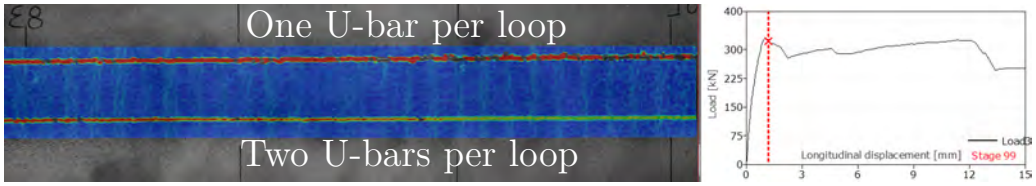

Figure 6.14: *Major principal strain recorded on the surface of Specimen P4 at the first peak load, showing no diagonal cracks (figure from Paper II)*

results clearly show that the cracking behaviors of the connections were significantly different as well. Figure 6.13(a) indicates that diagonal cracks developed for the conventional design even before reaching the peak load of the connection. Naturally, the cracking process decreased the stiffness of the connection as seen in the ascending part of the response curve (the comparison to the stiffer response curve of the new design is given in Figure 6.4). In the post peak region, when the shear keys had failed, the diagonal cracks could open widely (partly as a result of the U-bar orientation), see Figure 6.13(b). The grout therefore gradually lost the ability to maintain or increase the load level even though the U-bars were pushed towards each other (the U-bars deformed as shown in Figure 6.5(b)). In the '1-on-2' design, a different crack pattern was observed. Prior to the first peak load, diagonal cracks had not necessarily developed, see Figure 6.14. With increased shear displacement the diagonal cracks developed over one pair of shear keys, and not over several keys.

In Paper II, a crack pattern was shown for the '2-on-2' design. Less diagonal cracks were observed in the grout prior to failure of the shear keys and the observed cracks had smaller crack openings. Figure 6.15 shows the crack pattern in a late stage of the particular test. Contrary to the conventional design, where the diagonal cracks were distributed over the length of the connection, the diagonal cracks in the new design were typically located around a single pair of shear keys. This was maintained through the

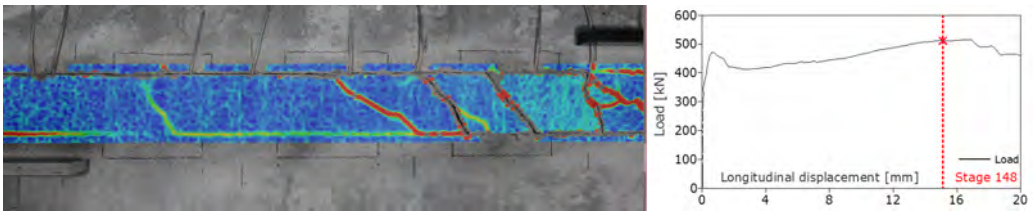

Figure 6.15: *Cracks at a late stage of the test, Specimen III2, '2-on-2' loop configuration*

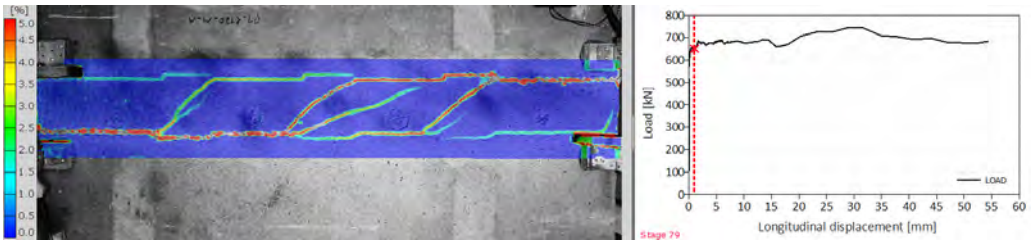

(a) M120A, L_k=120 mm

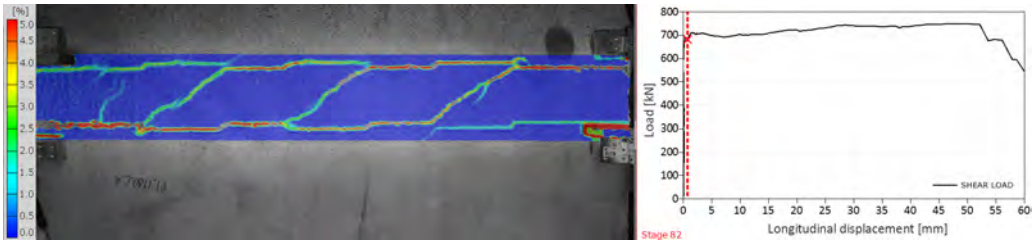

(b) C180A, L_k=180 mm

Figure 6.16: *Cracking behavior of specimens with 10 mm U-bars recorded with DIC*

test, despite the large amount of shear displacement that was imposed to the connection at that stage (approximately 15 mm). At the remaining shear keys, the displacements concentrated in the interface, where the shear keys had failed and the grout maintained the ability to carry additional load until rupture of the reinforcement. In this relation, it is beneficial that the transverse reinforcement loops were placed outside the keyed areas, i.e. in the less cracked zones.

The same crack pattern was observed for the specimens with 10 mm U-bars. Figure 6.16 shows snapshots of the crack development around the first peak load for two specimens. As can be seen, diagonal cracks between opposite keys were most dominant, while the zones where the U-bar loops overlapped were much less cracked (at least what could be observed on the surface). This can partly explain the very ductile and nearly perfect plastic behavior seen on the response curves. It should be noted that it was not only because of the position of the U-bar loops, but also the orientation of the loops, as well as the presence of the T-headed lacer bars that ensured a ductile behavior for the new design.

In Paper II and III, it was shown that the failure of a shear key can be detected by the use of DIC. In Figure 6.17, an additional example of complete key shearing at the first peak load is given (Specimen D20B). It can be seen that the crack developed where there was no previously measured strain (detected on the surface). However, the failure developed clearly as complete

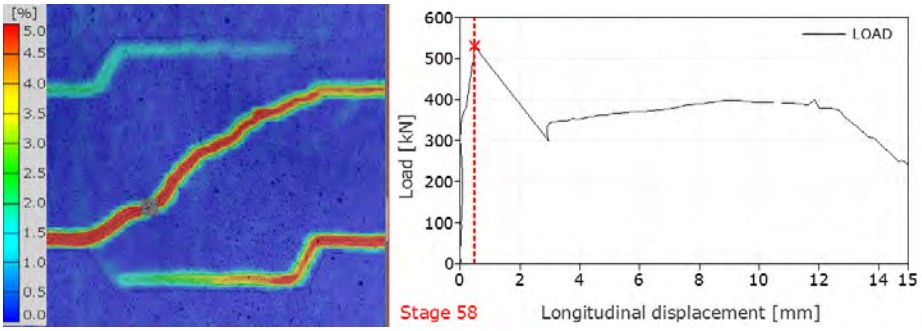

(a) Just before peak load

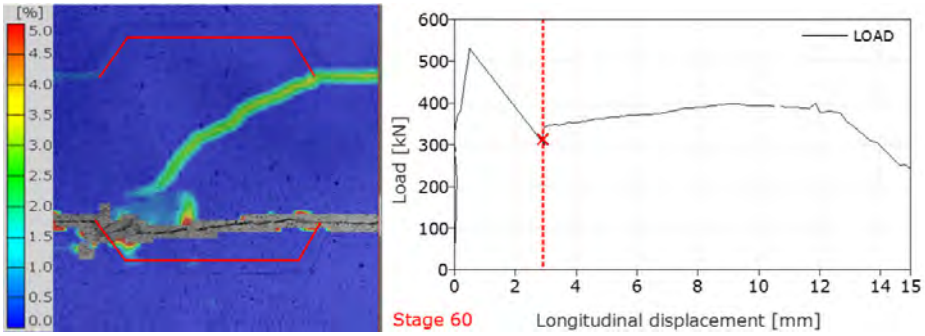

(b) Just after peak load

Figure 6.17: *Identification of key failure, Specimen D20B*

key cut off. The existing strains/openings at the interfaces and in the diagonal crack closed at the failure of the shear key. This is in accordance with the observations presented in Chapter 4. The DIC measurements confirm the jump in longitudinal displacement caused by the brittle failure of the shear key. In this relation, it can be mentioned that the crack appearance on the surface of the connection indicated that the contour of the failure plane was not completely parallel to the line of loading. This confirms that additional longitudinal displacement in the post peak regime had to be accompanied by displacement in the transverse direction. This is again similar to the results of the single key tests.

In Figure 6.18(c), a crack pattern including local key corner crushing and diagonal cracks is shown. Figure 6.18(a) and (b) show the development of a diagonal crack as the load-displacement curve enters the regime of plastic deformations (after failure of the shear keys). The small key depth (10 mm) favors a failure by local key corner crushing. In this relation, it should be mentioned that the failure by local crushing of the key corner cannot be detected as easily as the failure by complete key cut off. For this purpose, the failure of the key corner is too localized in a too narrow zone.

The local failures of the keys in combination with the diagonal cracks form the global mechanism. As discussed above, a failure of the key corners provides the most ductile load-displacement response. The specimens of the series with '2-on-2' connections with 10 mm U-bars are excellent examples of an ideal combination of key geometry (primarily in terms of key depth) and reinforcement strength that ensures an almost perfect plastic load-displacement relationship.

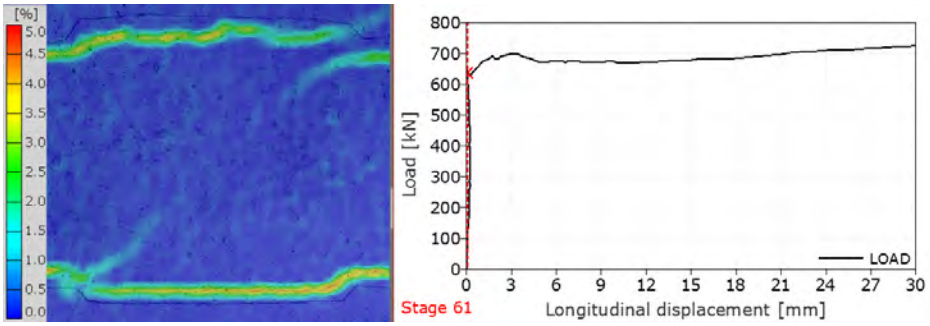

(a) Left key, before key failure

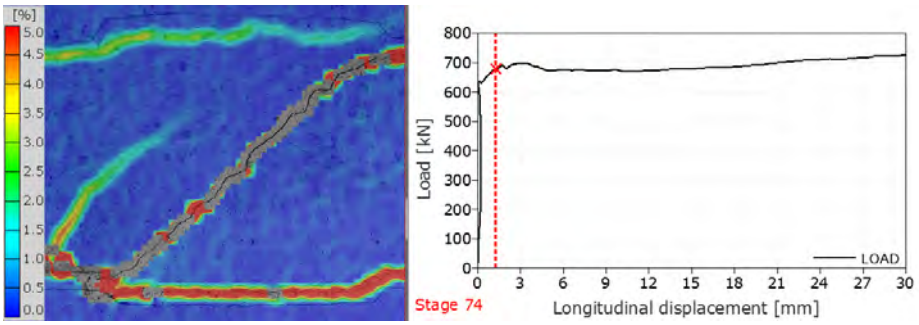

(b) Left key, after key failure

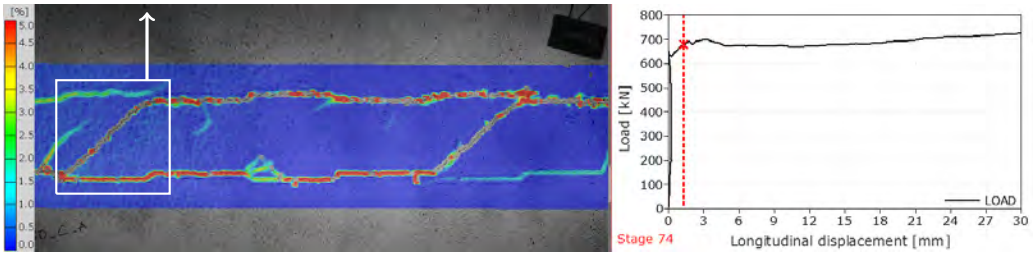

(c) Crack pattern on surface including all keys

Figure 6.18: *Identification of key failure, Specimen C150A*

6.3 Concluding Remarks

In this chapter, representative experimental results of push-off tests on shear connections, with three pairs of shear keys and four sets of reinforcement loops, were presented. The results included typical load-displacement relationships for the different test series, both for the conventional and for the new design. The recorded first peak loads, P_{FP}, and the ultimate load, P_{U}, for all the tests can be found in Appendix B. DIC analyses were performed to identify the failure modes of the shear keys and the cracking behavior of the grout. The experimental results serve as a basis for comparison to the theoretical models that will be developed in the following chapters. The main findings of the experimental tests are summarized as follows:

- ⋆ The first peak load of the keyed shear connections was governed by failure of the shear keys.
- ⋆ Two different failure modes were observed in the shear keys - complete key cut off (larger key depths) and local key corner crushing (smaller key depths).
- ⋆ Failure by local key corner crushing resulted in the most ductile behavior for the connection.
- ⋆ Diagonal cracking appeared between pairs of shear keys (i.e. diagonal crack spanning over one key) for both the conventional and the new design.
- ⋆ The orientation of the U-bars and the T-headed lacer bars in the new design for keyed shear connections ensured a ductile test response for both types of failure in the shear keys.
    - ◇ Specimens with the new layout, but without shear keys, also experienced a significant increase in capacity after initiation of plastic deformation.
    - ◇ The tests on the new design were all terminated by rupture of the reinforcement. This could not always be obtained for the conventional layout.
- ⋆ The load direction proved important for the ductility of the conventional design, whereas the response of the new design, due to the reinforcement layout, is independent of the load direction.

7 Upper Bound Solutions for Keyed Shear Connections

In this chapter, upper bound solutions for keyed shear connections will be presented and compared to the results of the experimental campaign presented in Chapter 6. The solutions have been developed and presented in the appended Paper II and they constitute so-called first-order rigid-plastic solutions. The calculations can be compared to the recorded first peak loads of the experimental tests. The solutions have been developed with inspiration from the observed crack patterns, i.e. the local failures of the shear keys and diagonal cracking are considered in the failure mechanisms. The model furnishes a simple tool to optimize the geometry of a keyed connection in order to predict the most ductile failure mode. The solutions are applicable for a variety of keyed connections, and they are not limited to the new or the conventional design. Nevertheless, the aim is primarily to compare with tests of the new design.

The upper bound method has been applied for strength prediction of keyed shear connections by a number of researchers. Jensen (1975) was the first to establish upper bound solutions and later the same basic assumptions was used by e.g. Chakrabarti et al. (1988), Abdul-Wahab and Sarsam (1991), and Christoffersen (1997). Common for all studies found in the literature is that they only consider a local failure mechanism corresponding to complete key cut off. However, several experimental investigations, including those by Hansen et al. (1976), Eriksson (1978), and Nimityongskul and Liu (1980) also reported failure by local crushing of the key corners, see Figure 7.1 for distinction between the two idealized failure modes. Since a theoretical treatment of the local key corner failure is lacking in the literature, the present work has been focused on this failure mode in the experimental campaign, in order to have a better basis for model development. In the following, the solutions, as they appear in Paper II, will also be compared to the additional test results not included in the paper. Detailed derivation of the solutions will not be repeated here.

7.1 Prediction of Capacity

When modeling the capacity of keyed shear connections, a number of assumptions has to be made in order to simplify the analysis. The following

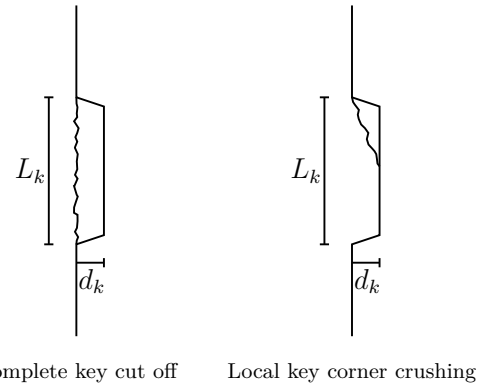

Figure 7.1: *The two local failure modes of the shear keys considered in the development of the model, see also Paper II*

must be fulfilled as a prerequisite for plastic modeling of the structural connections:

- The design of the transverse loop connections allows for tensile yielding of the U-bars (not failure of the grout)
- The precast elements possess an over-strength compared to the connections

The main theoretical assumptions include:

- Rigid-perfectly plastic material behavior
- The grout is considered as a modified Coulomb material (tensile strength neglected)
- The problem is considered as a plane strain problem

The following notations are introduced for the average shear stress, τ, the degree of transverse reinforcement, Φ, and the degree of longitudinal reinforcement, Φ_L (relating to the locking bar):

$$\tau = \frac{P_{\text{cal}}}{nA_k} \tag{7.1}$$

$$\Phi = \frac{n+1}{n}\frac{A_s f_y}{A_k f_c} \tag{7.2}$$

$$\Phi_L = \frac{A_{sL} f_{yL}}{nA_k f_c} \tag{7.3}$$

where P_{cal} is the calculated shear capacity, n is the number of shear keys in a connection, A_k is the cross sectional area of a shear key ($L_k \cdot h_k$), f_c is the compressive strength of the grout, A_s is the reinforcement area per loop

connection, f_y is the yield strength of the U-bars, A_{sL} is the cross sectional area of the locking bar, and f_{yL} is the yield strength of the locking bar.

7.1.1 Failure Mechanisms

Based on the experimental results, four basic failure mechanisms were developed and presented in Paper II. The mechanisms were developed based on two considerations. Firstly, the two failure modes of the shear keys should be reflected (see Figure 7.1). Secondly, the presence of diagonal cracking between opposite placed shear keys, see e.g. Figure 6.3, should be addressed. By use of the work equation, the closed formed solutions were developed and optimized.

Two of the basic mechanisms were based on complete key cut off, see Figure 7.2, and the remaining two basic mechanisms were based on key corner crushing, see Figure 7.3. The mechanisms can be categorized as single body mechanisms, where one rigid body displaces relatively to another rigid body. Multi-body mechanisms, including relative displacements of several rigid bodies, can also be considered. Examples of such mechanisms were given e.g. by Jørgensen et al. (2017), who studied keyed shear connections reinforced with high strength wire rope loops. For the connection design developed and tested in this study, calculations showed that the multi-body mechanisms were not critical. For this reason, they will be not considered further.

7.1.2 Complete Key Cut Off

The mechanisms with failure by complete key cut off are presented in Figure 7.2. These will be described in the following. Mechanism A involves complete shearing of all n shear keys in one side of the connection, see Figure 7.2(a). The mechanism is similar to the model of Jensen (1975). Adopting the notation for the shear stress, τ, and the reinforcement degree, Φ, the capacity and the optimal angle of displacement, α, are calculated by:

Mechanism A

$$\frac{\tau_A}{\nu f_c} = \frac{1-\sin\alpha_A}{2\cos\alpha_A} + \frac{\Phi}{\nu}\tan\alpha_A \tag{7.4}$$

$$\alpha_A = \arcsin\left(1-\frac{2\Phi}{\nu}\right), \qquad \alpha_A \geq \varphi \tag{7.5}$$

As diagonal cracking over one pair of shear keys was observed for many of the test specimens, Mechanism B with a diagonal yield line was introduced. The diagonal yield line is assumed to span over one pair of shear keys and the dissipation in this yield line is therefore influenced by the length of the

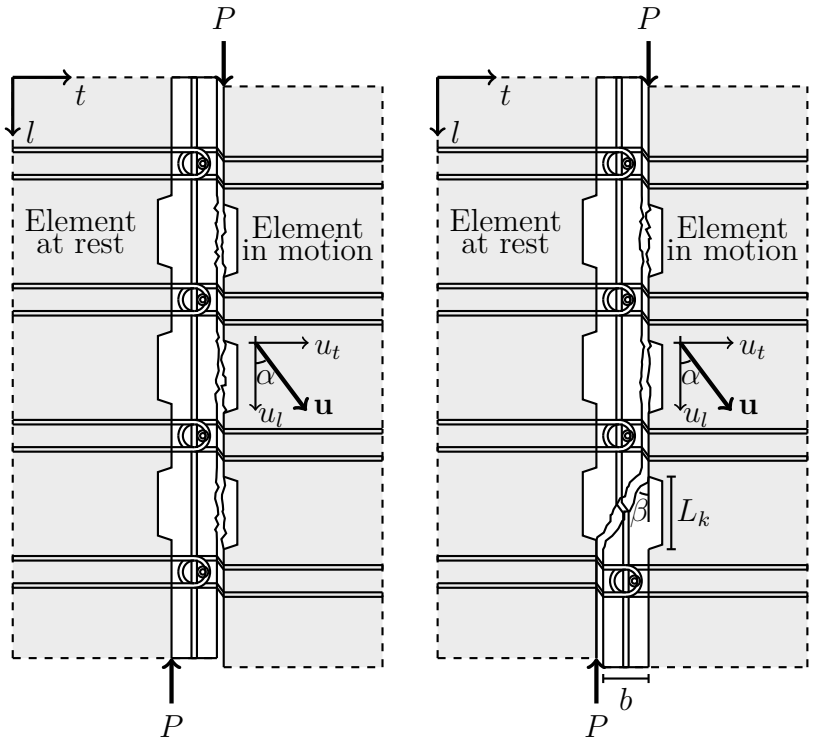

(a) Mechanism A (b) Mechanism B (and D)

Figure 7.2: *Basic failure mechanisms with complete key shearing*

keys, L_k, and the width of the joint, b. The relation is expressed by the angle $\tan\beta = b/L_k$, see Figure 7.2(b). The capacity is found by:

Mechanism B (with dissipation in diagonal yield line)

$$\frac{\tau_B}{\nu f_c} = \frac{n-1}{n}\frac{1-\sin\alpha_B}{2\cos\alpha_B} + \frac{A_d}{nA_k}\frac{1-\sin(\beta+\alpha_B)}{2\cos\alpha_B} + \frac{\Phi}{\nu}\tan\alpha_B + \frac{\Phi_L}{\nu} \tag{7.6}$$

$$\alpha_B = \arcsin\left(\frac{n-1+\dfrac{t}{h_k}-2n\dfrac{\Phi}{\nu}}{n-1+\dfrac{A_d}{A_k}}\right), \qquad \alpha_B \geq \varphi \tag{7.7}$$

where A_d is the area of the diagonal yield line, h_k is the height of the shear key (in the direction of the panel thickness), and t is the thickness of the panel. This solution appears to be more complicated than Mechanism A. However, it is still a closed form solution, which is easy to adopt for practical applications. Relating to the experimental observations, where a diagonal crack in many cases was observed before the peak load, it is argued that

the dissipation is reduced in such a diagonal crack due to the existing crack opening at the time where failure of the shear keys take place, see e.g. Figure 6.13(a). In addition, the inclination of the crack entails that the relative displacement here has a direction, which is almost perpendicular to the yield line (meaning almost no dissipation as the tensile strength of the grout is neglected). Taking these factors into account, the dissipation is deemed to be relatively small in the diagonal yield line. To simplify the calculation, this contribution is simply disregarded, when introducing Mechanism D. However, the contribution from the locking bar is still included. The mechanism appears identical to Mechanisms B, see Figure 7.2, and the capacity is calculated by:

Mechanism D (without dissipation in diagonal yield line)

$$\frac{\tau_D}{\nu f_c} = \frac{n-1}{n}\frac{1-\sin\alpha_D}{2\cos\alpha_D} + \frac{\Phi}{\nu}\tan\alpha_D + \frac{\Phi_L}{\nu} \tag{7.8}$$

$$\alpha_D = \arcsin\left(1 - \frac{2n\Phi}{(n-1)\,\nu}\right), \qquad \alpha_D \geq \varphi \tag{7.9}$$

7.1.3 Local Key Corner Crushing

For local crushing in the key corners, mechanisms with and without diagonal yield lines were likewise developed, see Figure 7.3. The upper bound solutions for these mechanisms have two optimization parameters, namely the angle of the displacement vector, α, and the inclination of the yield line to vertical, γ. The dissipation and thus the capacity are highly dependent on the combination of the two angles. If the angle γ is small, the failure will be similar to a complete key cut off mechanism. For increasing values of γ, the dissipation in the yield line will decrease; on the other hand, the reinforcement will dissipate more energy. To counteract this, α must decrease and, at some point, the restriction of the normality condition ($\alpha \geq \varphi$) is reached. As γ has to attain a certain value to deviate from complete key cut off, the restriction of the normality condition is reached for smaller degrees of transverse reinforcement as compared to Mechanisms A and B. In practical cases, the amount of transverse reinforcement provided will be sufficient to restrict α to be φ. For this reason, the assumption of $\alpha = \varphi$ is adopted, when developing the model. This reduces the problem to only contain γ as an optimization parameter.

Mechanism C is developed by assuming local key corner crushing of all n shear keys in one side, see Figure 7.3(a):

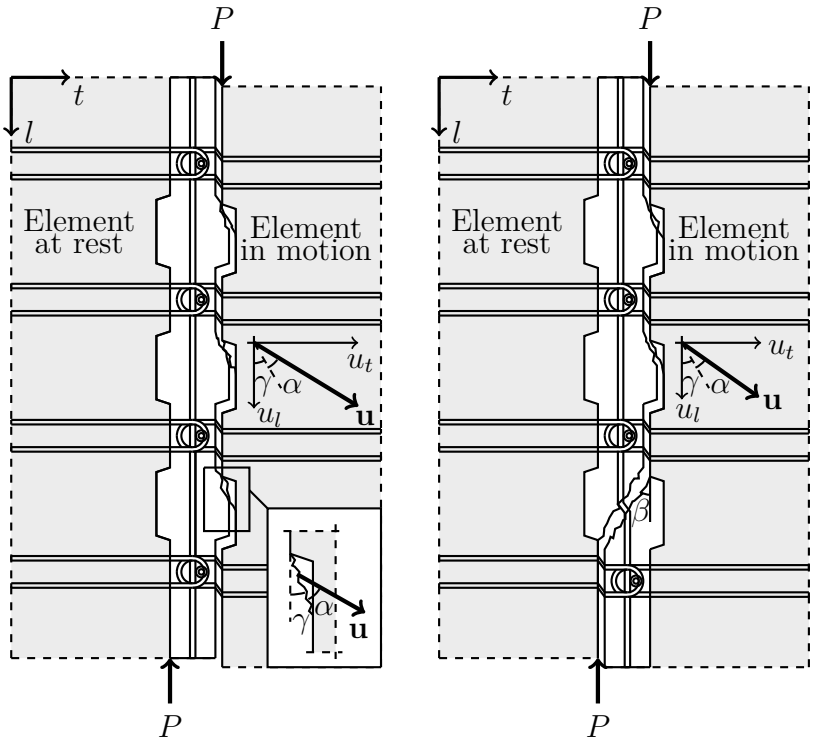

(a) Mechanism C (b) Mechanism E

Figure 7.3: *Basic failure mechanisms with key corner crushing*

Mechanism C

$$\frac{\tau_C}{\nu f_c} = \frac{d_k}{2L_k} \frac{1-\sin\varphi}{\sin\gamma_C \cos\left(\gamma_C+\varphi\right)} + \frac{\Phi}{\nu}\tan\left(\gamma_C+\varphi\right) \tag{7.10}$$

$$\gamma_C = \arctan\left(\frac{\cos\varphi}{\sin\varphi+\sqrt{1+\frac{\Phi}{\nu}\frac{2L_k}{d_k}\frac{\cos\varphi}{1-\sin\varphi}}}\right) \tag{7.11}$$

where L_k is the length of the shear key and d_k is the depth of the key (see e.g. Figure 7.1). The mechanism including a diagonal yield line is denoted Mechanism E, see Figure 7.3(b). Inspired by the simplification introduced in Mechanism D, the dissipation in the diagonal yield line is also omitted here. The contribution from the locking bar is included and the capacity can be calculated by:

Mechanism E

$$\frac{\tau_E}{\nu f_c} = \frac{n-1}{n}\frac{d_k}{2L_k}\frac{1-\sin\varphi}{\sin\gamma_E\cos\left(\gamma_E+\varphi\right)} + \frac{\Phi}{\nu}\tan\left(\gamma_E+\varphi\right) + \frac{\Phi_L}{\nu} \tag{7.12}$$

$$\gamma_E = \arctan\left(\frac{\cos\varphi}{\sin\varphi + \sqrt{1+\frac{n}{(n-1)}\frac{\Phi}{\nu}\frac{2L_k}{d_k}\frac{\cos\varphi}{1-\sin\varphi}}}\right) \tag{7.13}$$

It should here be noted that if the dissipation in the diagonal yield line is taken into account, it will no longer be possible to obtain a closed form solution for the optimal angle γ_E. The problem would in this case require an iterative procedure to solve. Results based on solutions with or without dissipation in the diagonal yield line can be seen in Figure 7.4. The calculations were performed on the basis of the geometry and the material properties of the test specimens with 6 mm U-bars, see Appendix B.3. The comparison shows that it is justified to neglect the dissipation in the diagonal yield line, when considering Mechanism E. This is due to the fact that the direction of the relative displacements is almost perpendicular to the diagonal yield line.

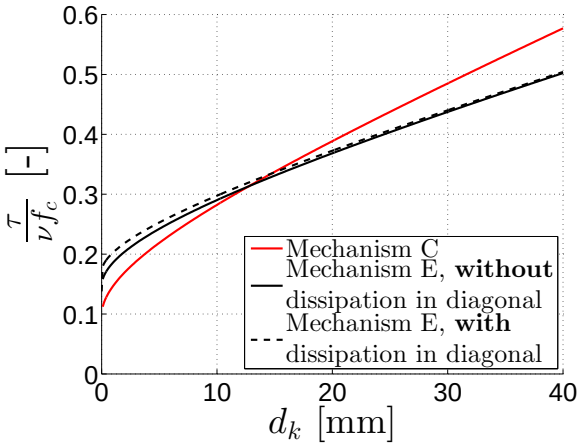

Figure 7.4: *Comparison of results based on Mechanism C and E*

For comparison, Mechanism C is also included in the figure. For this mechanism, it can be seen that in the limiting case of zero key depth, the mechanism still predicts a capacity. This is due to the assumption of a fixed angle of the displacement vector, i.e. $\alpha = \varphi$. The same capacity would in fact be found by using a shear-friction approach with a friction coefficient of $\mu = \tan\varphi$ and by neglecting the cohesion. In the limiting case of no key depth, Mechanism E results in a greater capacity than Mechanism C due to

the contribution from the locking bar. The transition between Mechanisms C and E is of course dependent on the geometry and the number of shear keys.

7.2 Comparison of Tests with Theory

In the following, results based on the presented upper bound solutions will be compared to the results of the tests presented in Chapter 6. In the comparisons, the observed failure modes of the specimens are indicated by a red symbol for local key corner crushing and a black symbol for complete key cut off. The calculated transition between the two failure modes are indicated by a dashed vertical line and the regimes are categorized with colored text. In this way, the observed failure mode can be compared with the prediction. Appendix C contains tabulated values of the tested first peak load, P_{FP}, and the calculated capacity, P_{cal}, for each specimen. The appendix also contains information on the observed and the predicted failure of the shear keys (observed and predicted failure mechanism in brackets). The calculated capacities depend highly on the values adopted for the two important parameters, namely the internal angle of friction, φ, and the effectiveness factor, ν. The values adopted in Paper II are therefore shortly repeated below.

7.2.1 Internal Angle of Friction

As the failure mechanisms are treated as plane strain problems, the choice of the internal angle of friction, φ, is important for the estimation of the capacity. In the experimental program, both concrete and mortar grouts were used to grout the connections. For normal strength concretes, a value of $\varphi = 37°$ is generally accepted (Richart et al., 1928; Johansen, 1958; Chen, 2007; Nielsen and Hoang, 2011). According to the results of the triaxial tests presented in Chapter 3, the internal angle of friction should be reduced when the maximum grain size of the mixture is smaller than 16 mm. For mortar ($d_{\max} \leq 4$ mm), a value of $\varphi = 30°$ can be adopted with reasonable accuracy, when no additional information from triaxial tests is available. These two values for the grouts used in the experimental program are adopted in the upper bound calculations presented in the following.

7.2.2 Effectiveness Factor

The effectiveness factor, adopted in Paper II originates from calibration with beam shear tests (Zhang, 1997a), and has been modified for use in structural connections (Jørgensen, 2014; Jørgensen et al., 2017). The expression is sim-

ilar to the one used for estimation of the tensile capacity of loop connections (see e.g. Chapter 5):

$$\nu = \frac{K}{\sqrt{f_c}} \left(1 + \frac{1}{\sqrt{L_k}}\right) \not> 1.0, \qquad (f_c \text{ in MPa}, \ L_k \text{ in m}) \tag{7.14}$$

As for the assessment of the tensile capacity of the loop connections, the value of K is chosen as 0.88 for a concrete grout and 0.75 for a mortar grout. To account for size effects, the characteristic length should relate to a length measured in the direction of the shear load, hence, the length of the shear key, L_k, is adopted here (while H was used for estimation of the tensile capacity in Chapter 5).

Equation (7.14) will be used throughout the following comparison with the available test results. To study their impact, the parameters included in the formula (f_c and L_k) will in addition be evaluated.

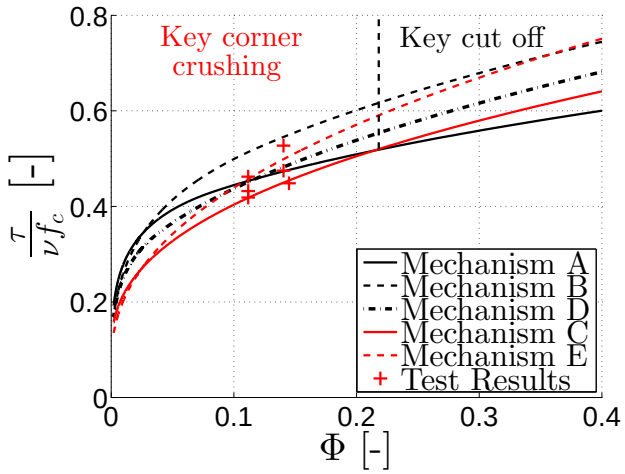

Figure 7.5: *Comparison of results from tests on the reference specimens with the upper bound solutions*

7.2.3 Reference Tests

In Figure 7.5, the developed upper bound solutions are compared to the test results for the reference specimens. The calculated capacities are also tabulated in Appendix C.1. The Mechanisms E and D are highly relevant for the conventional design as a considerable amount of diagonal cracks was observed before reaching the peak load (see e.g. Figure 6.13(a)). Nevertheless, the comparison in Figure 7.5 shows that Mechanism C without a diagonal yield line is governing the theoretical capacity. The prediction of the key failure mode is in accordance with the test observations. In general, a slight

underestimate of the capacity is found. Nevertheless, the results indicate that the developed solutions can be applied to the conventional design.

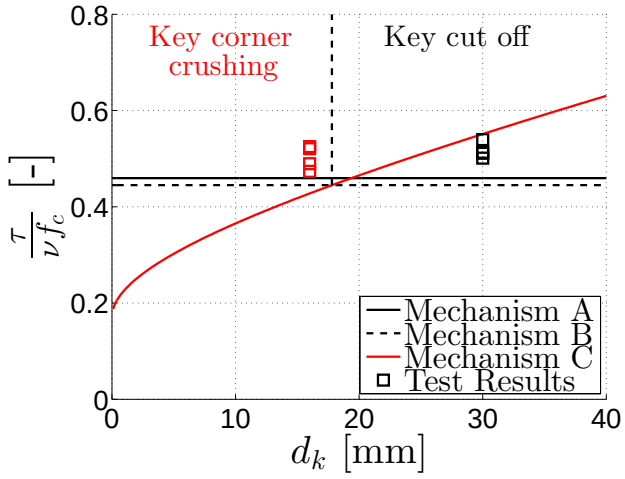

(a) 8 mm U-bars

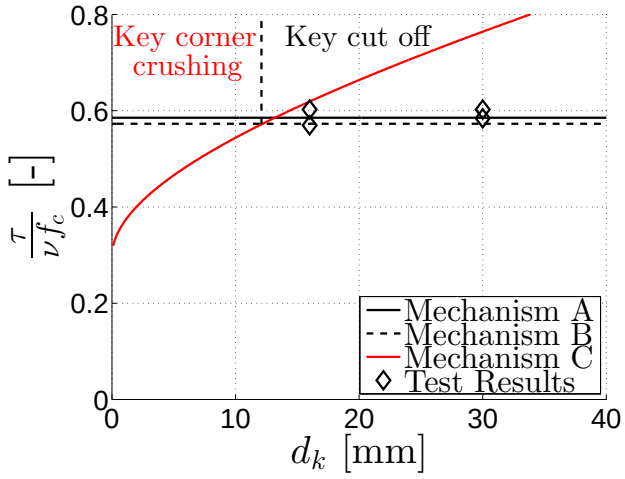

(b) 10 mm U-bars

Figure 7.6: *Comparison of results from tests on the '1-on-2' connection design with the upper bound solutions*

7.2.4 New Design '1-on-2' Configuration

Figure 7.6 shows the comparison between the upper bound solutions and the results of the '1-on-2' test series. The test results are only compared to Mechanisms A, B, and C. The reason is that diagonal cracking was observed in the tests only at the peak load level (see e.g. Figure 6.14). It appears that Mechanism A and Mechanism B lead to practically the same results.

From Figure 7.6, it can be seen that the upper bound solutions slightly underestimate the results of the specimens with 8 mm U-bars. The test results for specimens with 10 mm U-bars are predicted with much better agreement. The predicted failure modes correspond well with the experimental observations. The results of the comparison are also given in Appendix C.2.

7.2.5 New Design '2-on-2' Configuration

Figure 7.7 shows the comparison of the test results for specimens with 6 mm U-bars with the upper bound model. Generally, it is seen that the solutions underestimate the capacity of the connections. However, the tendencies of the test results are captured rather well. This implies that it is possible to obtain better agreement by choosing a different value for the effectiveness factor. The comparisons are also given in Appendix C.3.

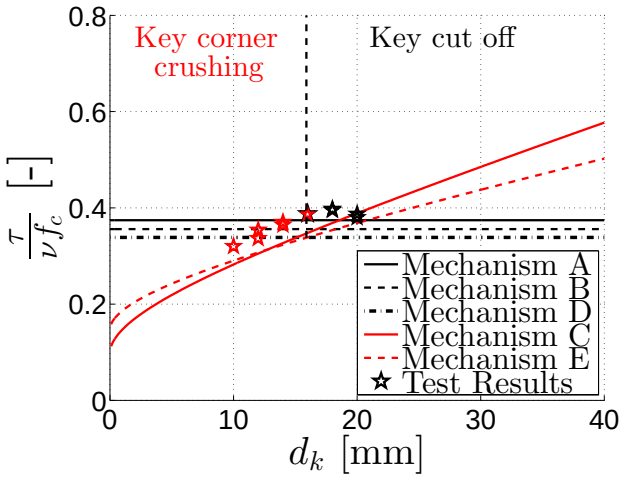

Figure 7.7: *Comparison of results from tests on the new '2-on-2' connection design (6 mm U-bars) with the upper bound solutions*

Figure 7.8 contains the results of specimens with 8 mm U-bars compared to the upper bound solutions. The results are identical to the results presented in Paper II. Appendix C.4 contains the calculated capacities. It can be seen that the theory fits the test results well and that the predicted failure modes of the shear keys are predicted relatively well.

The comparison of test results for specimens with 10 mm U-bars with the results of the upper bound solutions is shown in Figure 7.9. It can be seen that the capacity of the specimens grouted with mortar is predicted well (Figure 7.9(b)). However, the capacity of the specimens grouted with concrete is overestimated (Figure 7.9(a)). As seen in Appendix B.5, the concrete

grout and the mortar grout had practically the same compression strength. Furthermore, comparable specimens (identical geometry) had similar first peak loads regardless of the grout material. Hence, the overestimation for specimens with concrete grout must primarily be due to the different K-values adopted in the effectiveness factor, Equation (7.14). This issue will be discussed further in the Section 7.3.4.

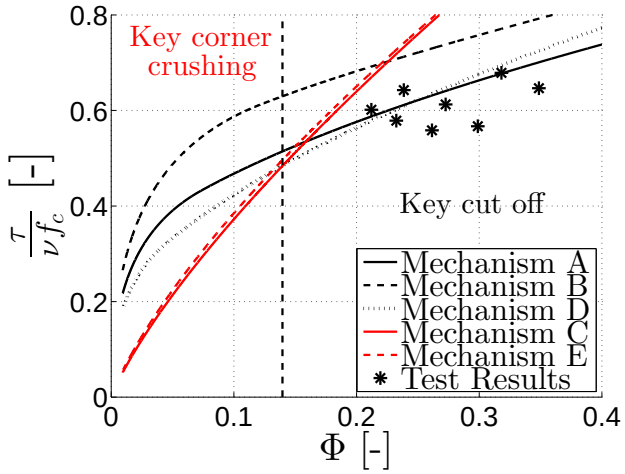

(a)

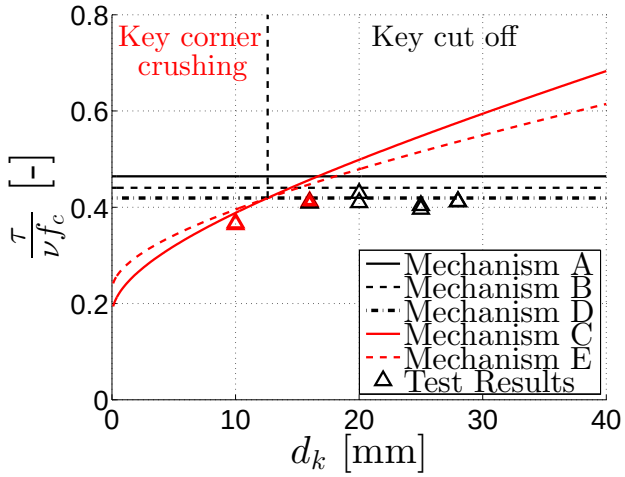

(b)

Figure 7.8: *Comparison of results from tests on the new '2-on-2' connection design (8 mm U-bars) with the upper bound solutions*

It can also be seen that the failure mode of the shear keys is not predicted correctly for all the specimens. The tests showed local key corner crushing (due to the small key depths) in all specimens and for the smaller key lengths

the theory predicts failure by complete key cut off. This can be explained by the model parameters adopted for the local mechanisms, including a size effect (in terms of the key length, L_k) incorporated in the effectiveness factor. This will be further discussed below.

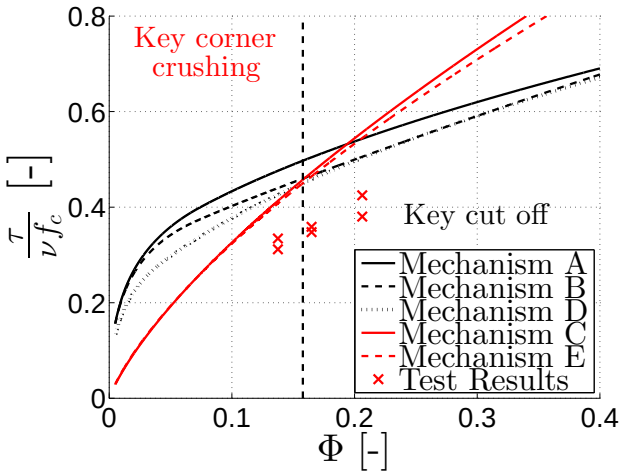

(a) Concrete grout

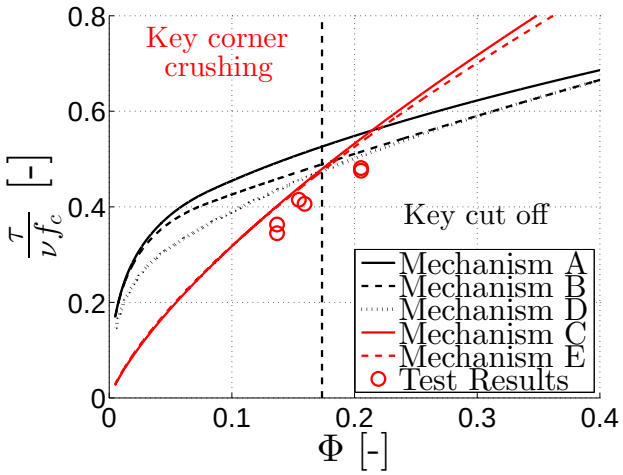

(b) Mortar grout

Figure 7.9: *Comparison of results from tests on the new '2-on-2' loop connection design (10 mm U-bars) with the upper bound solutions*

7.3 Evaluation of Model Parameters

From the comparison between the test results and the theoretical upper bound solutions, some tendencies can be observed. When considering e.g. the '2-on-2' configuration, it can be seen that the upper bound solutions fit

the test results for specimens with 8 mm U-bars very well. On the other hand, the results for specimens with 6 mm U-bars are underestimated, while the results for specimens with 10 mm U-bars are overestimated. Especially, the test results related to concrete grout are overestimated. In the following, some of the model parameters will be evaluated. The agreement between the tests and the calculations are presented as a test-to-calculation ratio based on the recorded first peak capacity, P_{FP}, and the calculated capacity for each specimen, P_{cal}. Naturally, the results are dependent on the model parameters and the choice of effectiveness factor. In the following, the influence of some of these parameters will be outlined. The results are contained in Appendix C, where the observed and the calculated local failure modes of the shear keys (corner crushing or key cut off) also are included.

7.3.1 Reinforcement Degree

In Figure 7.10, all the test-to-calculation ratios are shown versus the reinforcement degree. The results are divided into two groups corresponding to the shear key failure modes observed in the tests.

Overall, it is seen that the correlation between the test results and the calculated results is good. The mean value of the $P_{\mathrm{FP}}/P_{\mathrm{cal}}$-ratios for all the tests is 1.02 and the standard deviation amounts to 0.12. When isolating the test series, it can be seen that the test-to-calculation ratios of the series are grouped. This is indicated in the small standard deviation for the series (maximum 0.07 and generally 0.02-0.04, see Appendix C). This proves that the tendencies of the experimental results are captured well with the upper bound solutions. However, the magnitude of P_{cal} can be predicted better for some test series.

7.3.2 Connection Width

From the comparison presented in Figure 7.10(a), it is tempting to conclude that the dimension of the U-bars influences the $P_{\mathrm{FP}}/P_{\mathrm{cal}}$-ratio. A smaller rebar size seems to provide theoretical results that are lower than the test results (the capacity of specimens with 6 mm U-bars is underestimated, whereas the capacity of specimens with 10 U-bars is overestimated). This tendency can, however, also be related to the width of the connection, since smaller rebar diameters require smaller mandrel diameters and thus smaller b. Plots of the $P_{\mathrm{FP}}/P_{\mathrm{cal}}$-ratios versus the width, b, are shown in Figure 7.11. The width, b, is included as a parameter only in Mechanism B. However, as this mechanism rarely is governing, the parameter cannot be considered as fully accounted for in the upper bound solutions. The plots in Figure 7.11 clearly show that the $P_{\mathrm{FP}}/P_{\mathrm{cal}}$-ratio decreases as b increases.

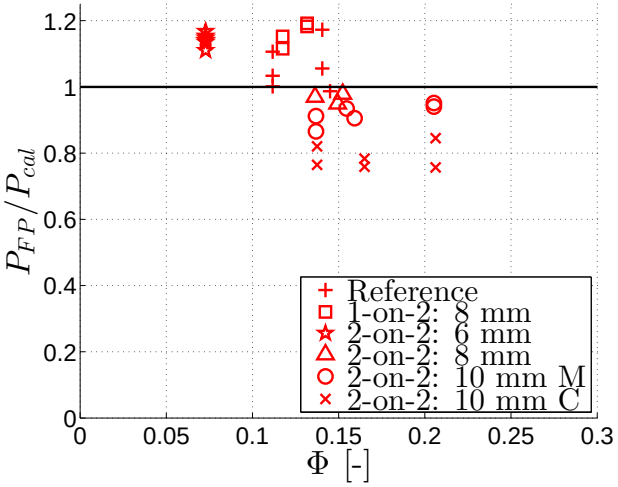

(a) Key corner crushing

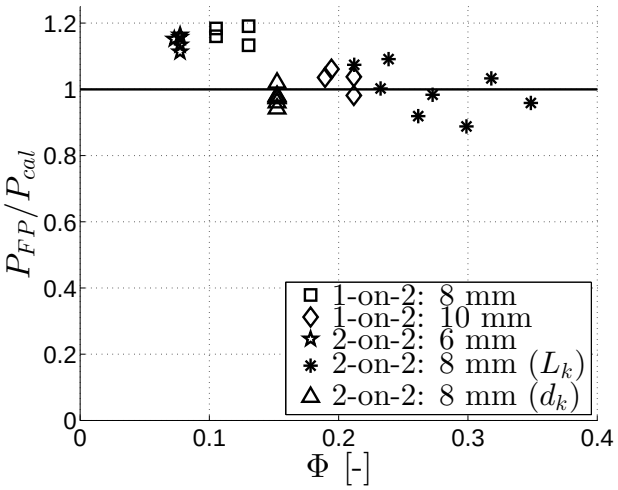

(b) Complete key cut off

Figure 7.10: *Ratio between tested and calculated peak loads versus the degree of transverse reinforcement*

Despite the overall decent agreement between the test and the calculated results, it seems that an even better agreement can be obtained by taking the connection width into account when establishing the upper bound solutions. A possibility is to incorporate an empirical relation into the formula for the effectiveness factor, as b otherwise only will be included in the solutions, if dissipation in diagonal yield lines is considered. However, the dissipation in the diagonal yield line is relatively small, confer e.g. Figure 7.4. A greater connection width entails a larger inclination of the diagonal yield line to vertical and thus smaller dissipation of energy - or a governing solution that

favors a mechanism without diagonal yield lines, i.e. no dependency of b.

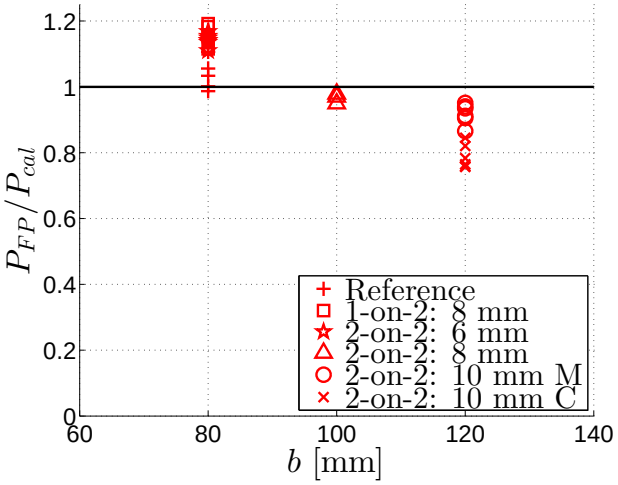

(a) Key corner crushing

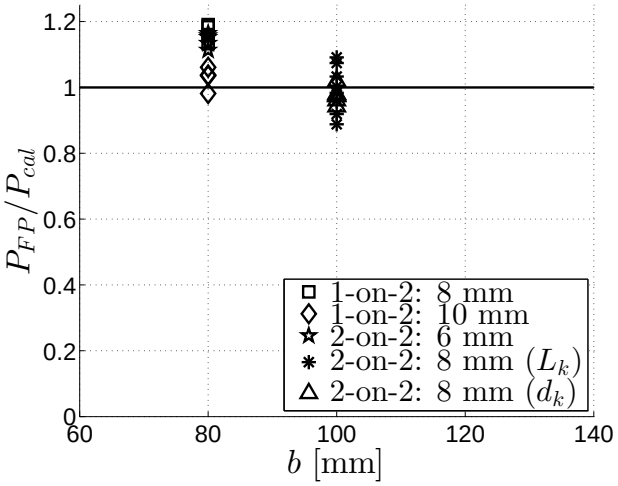

(b) Complete key cut off

Figure 7.11: *Ratio between tested and calculated peak loads versus the connection width*

7.3.3 Internal Angle of Friction

In the experimental program, two different grouts were used: concrete and mortar. As discussed above, different values for the internal angle of friction have been used in the calculations for the two materials. The value adopted for mortar resulted in good predictions for the specimens grouted with mortar, whereas the capacity for specimens grouted with concrete were

overestimated by the choice of φ. It is in this context worth mentioning that all specimens grouted with concrete had small key depths. This relatively small key depth (10 mm) is comparable to the maximum grain size of 11.2 mm in the grout mixture, where 93 % of the aggregates were smaller than 8 mm. Hence, it is practically impossible that the key corners were filled with the larger aggregates. This means that the observed shear key failure (local key corner crushing) most likely took place in a part of the matrix dominated by smaller aggregate particles. As shown in Chapter 3, the value of the internal angle of friction should be reduced even for mixtures with a maximum grain size of 8 mm. In the present case, where the failure of the key corner is highly localized in an area with mostly small aggregates, it can be argued that the local effective strength here will be similar to the case of a connection grouted with mortar. Hence, the choice of the internal angle of friction should reflect this. In the same way, the value of K can be argued to be reduced as well.

When adopting the parameters for a mortar grout, namely $\varphi = 30°$ and $K = 0.75$, for upper bound analysis of the connections grouted with concrete, better agreement between the test results and the upper bound calculations is obtained. Tests of connections with larger key depths (where failure would take place a complete key cut off) grouted with concrete most likely possess a higher capacity than similar connections grouted with mortar. Such an investigation was not performed in the current study. Based on the discussion above, the recommendation is to use $\varphi = 30°$ and $K = 0.75$ in upper bound analysis of keyed shear connections with shallow key depths grouted with concrete.

7.3.4 Parameters in the Effectiveness Factor

The comparison above indirectly evaluated the effectiveness factor. A more detailed evaluation of the effectiveness factor can be performed by assessing the two parameters currently included in the formula for ν to be used in upper bound solutions. In Equation (7.14), the compressive strength of the grout, f_c, and the length of the shear keys, L_k, are included. The evaluation of these two parameters should be divided into the two shear key failure modes. Both parameters are directly incorporated in the equations for the solutions with complete key cut off, however, from Equation (7.10) and (7.12), it is found that P_{cal} in Mechanisms C and E are independent of L_k.

Considering first the case with failure by complete key cut off, the evaluations of f_c and L_k are shown in Figure 7.12. In general, a good correlation is found. When considering the individual test series independently, it also appears that the influence of f_c and L_k is well accounted for by Equation (7.14).

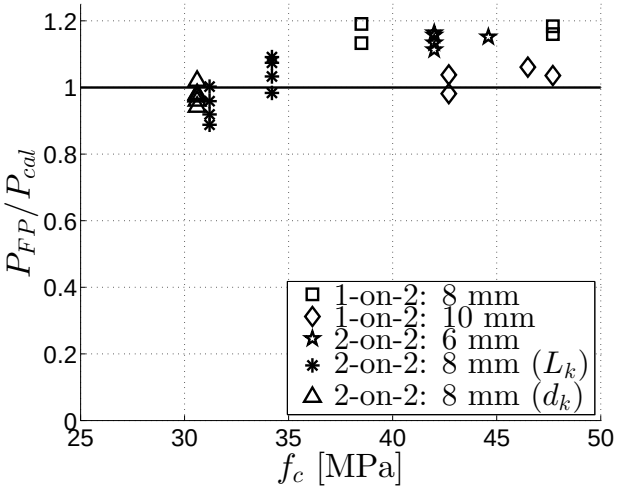

(a) Compressive strength

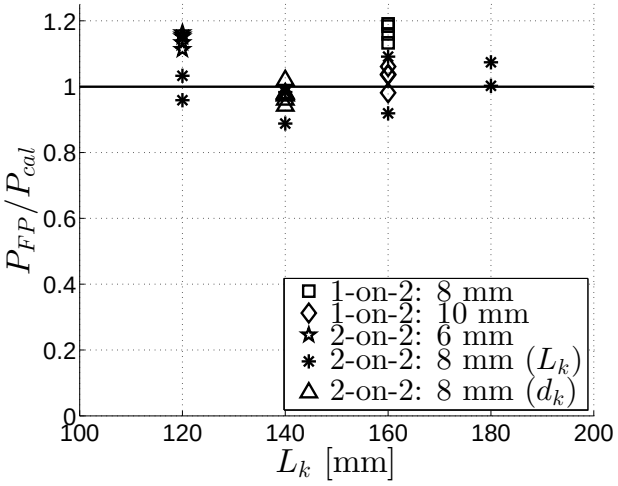

(b) Key length

Figure 7.12: *Evaluation of the parameters incorporated in the effectiveness factor for specimens suffering complete key cut off*

For the test specimens experiencing a failure by key corner crushing, it is debatable to adopt Equation (7.14) as the effectiveness factor. This is so because the factor K, as discussed above, may overestimate the effect of concrete versus mortar, and because size effects are accounted for by taking L_k as a characteristic length. The test-to-calculation ratios versus f_c and L_k are shown in Figure 7.13.

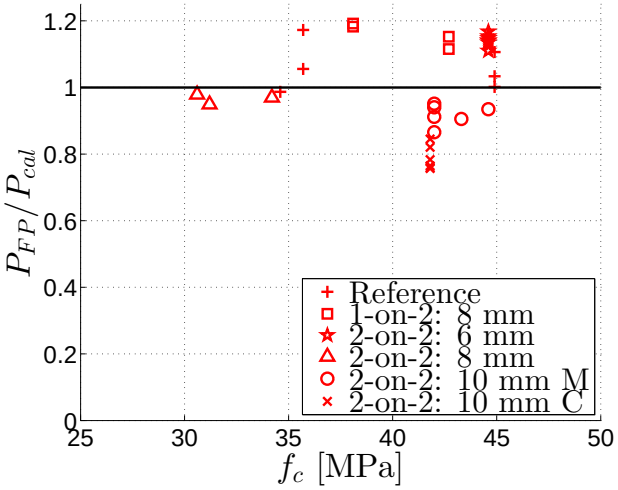

(a) Compressive strength

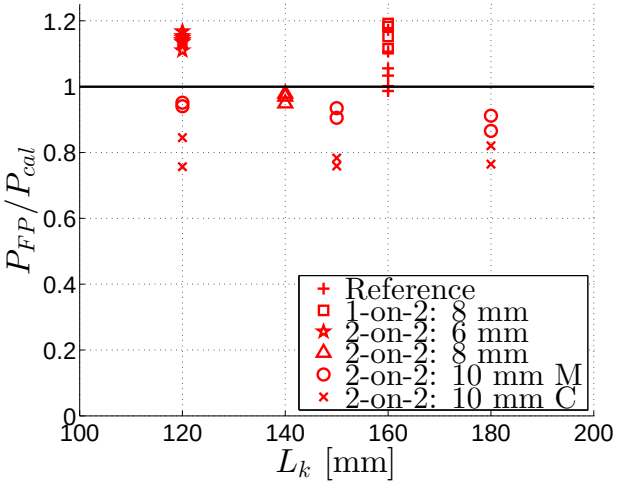

(b) Key length

Figure 7.13: *Evaluation of the parameters incorporated in the effectiveness factor for specimens suffering local key corner crushing*

For key corner crushing, the consideration of L_k as a size effect parameter is inconsistent with the actual failure, which is inclined and local. This is e.g. seen in the test results of the '2-on-2' specimens with 10 mm U-bars, which were practically unaffected by an increase in the key length from 120 mm to 180 mm. A characteristic length, if included at all, should rather reflect the length of the failure plane. This is not easy to interpret for the local failure as the direction of the failure plane does not coincide with the direction of loading. The discussion above shows that it may be relevant to establish a modified ν-expression for the case of local key corner crushing.

Nevertheless, the current test results do not seem extensively affected by the use of Equation (7.14) for prediction of P_{FP}. Only a 7 % change in ν is seen, when using $L_k = 120$ mm compared to $L_k = 180$ mm. The influence of L_k and f_c can in this case not be independently evaluated, as the size effect in the end also is related to the brittleness.

7.4 Practical Application

The comparison between the test results and the developed upper bound solutions showed an overall acceptable agreement, both in terms of predicted first peak capacity and in terms of predicted failure mode. The mechanisms including diagonal cracking proved that the upper bound solutions can be adjusted to account for boundary effects in test specimens with a limited number of shear keys. In the comparison of the calculations with the test results, the adjusted solutions proved valuable and provided a better fit for some specimens. However, for shear connections in practice, where the number of shear keys can be large, e.g. $n \geq 10$, the inclusion of the boundary effect (diagonal yield line at the end of the connection) will most likely not lead to results that deviate much from the two basic mechanisms without diagonal yield lines (i.e. Mechanisms A and C). Alternatively, $(n-1)$ shear keys can be included in the calculations to account for any boundary effect instead of a mechanism including a diagonal yield line.

The conclusion must be that for practical applications, where connections with a larger number of shear keys are to be designed, Mechanism A with complete key cut off and Mechanism C with local key corner crushing, should form the basis for the assessment of the structural capacity. In this relation, the key depth is an important factor for achieving a ductile response after failure of the shear keys. Smaller key depths favor a failure by local key corner crushing, which is the most ductile compared to complete key cut off.

Regarding the effect of the grout material, the test results showed that the use of a concrete grout for smaller key depths (less than the maximum grain size in the mixture) did not provide a greater capacity than when using a mortar. As the larger grains of a concrete mix cannot fill in the shallow keys, where a highly localized failure may take place, the crushing of the concrete in the corner corresponds to a failure in a mortar and the same material properties as for a mortar should be assumed (i.e. $\varphi = 30°$ as determined in Chapter 3 and $K = 0.75$).

The comparison between the tests and the calculations showed that the adopted effectiveness factor, Equation (7.14), provides reasonable results. It has been pointed out that the influence of the connection width is not completely accounted for in the solutions. A larger number of tests is required to establish a relation for the dependency of the connection width. In fact,

only three values of b have been tested in the experimental campaign. For practical applications, this means that the design should not deviate significantly from a tested connection geometry, if upper bound solutions are used for strength prediction. If the geometry deviates significantly from the experimental database, a more detailed analysis, than what is provided by the unsafe nature of the upper bound method, should be adopted. This can be done e.g. by use of stress fields, which will be a safe solution, where the specific geometry of the keyed connection can be taken into account in a more detailed manner (see Chapter 8).

7.5 Concluding Remarks

In this chapter, the upper bound solutions developed in Paper II have been summarized and compared to the results of the tests presented in Chapter 6. Some of the test series have also been treated in Paper II. The comparison between the test results and the calculations showed an overall good agreement, both in terms of the estimated capacity and for the predicted failure mode. However, it was also discussed that a better agreement may be obtained, if the influence of the connection width, b, is accounted for, i.e. included in the effectiveness factor. The findings of the chapter are summarized as follows:

- ⋆ The developed upper bound solutions account for the two observed failure modes of the shear keys - complete key cut off and local key corner crushing.
- ⋆ Four different failure mechanisms were presented based on the two main failure modes of the shear keys. The mechanisms were established with or without inclusion of a diagonal yield line.
- ⋆ The solutions can be used both for the conventional design and the new design ('1-on-2' and '2-on-2' loop connections were considered).
- ⋆ The effectiveness factor should include correction terms for both material brittleness and size effects.
  - ◇ For a failure by complete key cut off, the inclusion of f_c and L_k in Equation (7.14) provide reasonable results.
  - ◇ For a failure by local key corner crushing, the failure plane is small and the use of L_k to reflect any size effect is debatable.
- ⋆ The adopted ν-formula is only applicable in upper bound solutions (which in the case of keyed shear connections are not necessarily the exact solutions). However, it should be mentioned that the influence of b is not accounted for in the ν-formula or in all the mechanisms. Hence the solutions should only be used for practical applications in cases supported by experimental data.
- ⋆ For practical applications, Mechanisms A and C provide sufficient information to estimate the capacity and distinguish between the two local failure modes of the shear keys.

8 Lower Bound Solutions for Keyed Shear Connections

In this chapter, the lower bound solutions developed in Paper III will be presented and compared to the results presented in Chapter 6. The main purpose of the lower bound solutions is to supplement the upper bound solutions and thereby provide a more complete theoretical basis for practical design. The set of solutions can be used to bound the theoretically exact solution from below and above. In this relation, it should be mentioned that it remains an open question whether the effectiveness factor in the upper bound solutions, which is obtained from calibration with tests, in addition to brittleness effects also accounts for the fact that the model may not be the exact solution. Establishment of lower bound solutions, based on an independent choice of ν may provide the necessary information to evaluate the validity of the models. This discussion will be given in Chapter 9.

Development of optimal lower bound solutions for narrow connections between precast elements is complicated as the actual stress field is complex. Analytical attempts have been made previously, see e.g. Christoffersen (1997) and Nielsen and Hoang (2011), who assumed a simple stress field consisting of uniaxial struts spanning over one or more pairs of shear keys. The single-strut solution is shown in Figure 8.1, where it is assumed that the uniaxial stress field in the strut is transferred to the precast element through a nodal zone subjected to plane hydrostatic pressure (hatched in the figure). The capacity is dependent on the geometry of the connection, the compressive strength of the grout, and the strength of the transverse reinforcement (disregarding any external transverse loading). The single-strut solution often provides conservative capacities, when compared to test results.

8.1 Development of Lower Bound Solutions

The lower bound solutions developed in Paper III were inspired by the numerical finite element limit analysis method developed by Herfelt et al. (2016). The numerical approach ensures that the optimal solution for a given geometry and reinforcement degree is found. This entails that struts with different inclinations can be combined and meet in nodal zones at the key corners. As a further improvement to the single-strut model by Christof-

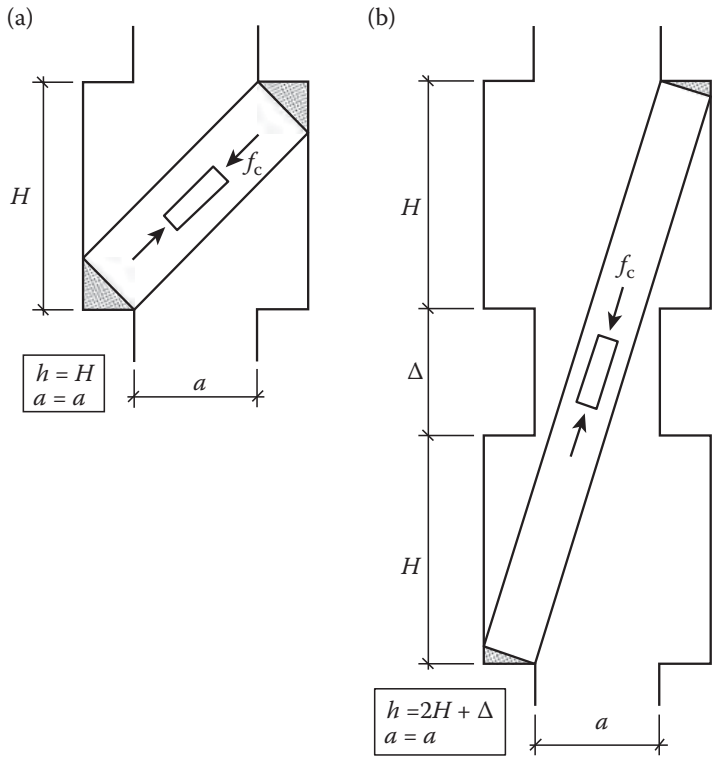

Figure 8.1: *Stress fields for the single-strut solution, showing (a) a strut over one and (b) two shear keys, illustrations from Nielsen and Hoang (2011)*

fersen (1997), the ability of the concrete-to-grout interface to transfer shear stresses by friction is utilized in the numerical model. Inclusion of friction leads to a non-hydrostatic biaxial stress state in the nodal zones. Based on the two mentioned improvements (as compared to the single-strut solution), more complex stress fields can be obtained in the joint grout.

Figure 8.2 contains examples of optimized stress distributions (obtained by finite element limit analysis) in a keyed connection subjected to shear. The analyses were based on the material properties and the geometry of the test specimens with the '2-on-2' loop configuration with 6 mm U-bars (see e.g. Appendix B.3). In the numerical model, the reinforcement is assumed continuous across the joint, which ensures that the full yield force can be utilized. The results show that an increase in key depth changes the stress field and increases the capacity of the connection. For large key depths, the optimized stress field appears similar to the single-strut solution, spanning over two pairs of shear keys. However, the capacity is increased as friction is included in the indented parts of the interface. More detailed examples of modeling with finite element limit analysis (FELA) can be found in Herfelt (2017).

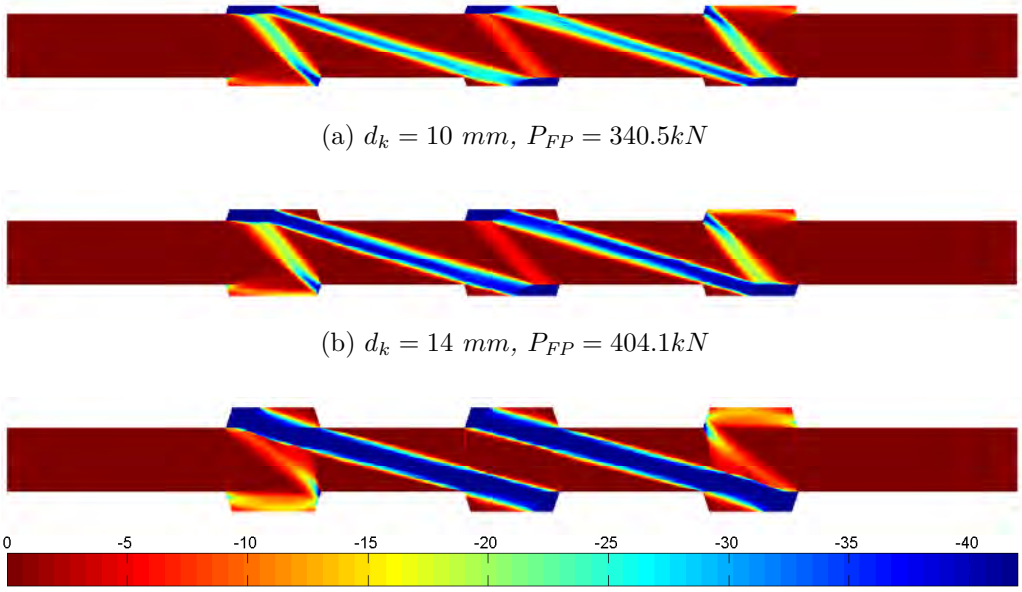

(a) $d_k = 10\ mm$, $P_{FP} = 340.5kN$

(b) $d_k = 14\ mm$, $P_{FP} = 404.1kN$

(c) $d_k = 20\ mm$, $P_{FP} = 486.1kN$

Figure 8.2: *Examples of optimized distributions of the maximum compressive stress [MPa] (tension positive), illustrations from Paper III*

8.1.1 Inclusion of Friction in Interface

For the friction between the grout and the precast concrete, a Coulomb friction criterion is assumed with a friction coefficient and a neglectable cohesion. The main argument for neglecting the cohesion is that smooth formwork was used to cast the reinforced concrete elements in the experimental campaign (smooth formwork is commonly used also in practice). Thus, any small cohesive resistance in the interface may have (partly or completely) vanished at the ultimate limit state.

Friction is only considered active in the indented areas of the interface. The main argument for this is that the normal stress required to activate friction stems from tension in the transverse reinforcement, which represents a form of passive confinement, in contrast to active confinement from an external normal force. Since the load is anticipated to be carried mainly by strut action between the shear keys, only the indented areas can transfer friction, as these are the only areas which experience compression.

For interfaces cast against smooth formwork, Eriksson (1978) modeled the sliding along the inclined interface of a key corner with a coefficient of friction of $\mu = 0.7$. Cholewicki (1971) also considered sliding in the inclined part of the key with $\mu = 0.7$. In Paper III, μ was taken as 0.75 for the smooth and untreated interfaces (relevant for the specimens with '2-on-2'

loop configurations). This value was also adopted in Nielsen and Hoang (2011) and Herfelt et al. (2016). In Paper IV, a discussion is given for the value of μ to be adopted for a greased interface. For consistency, the same value of $\mu = 0.3$ is adopted for the comparison between test results of specimens with greased interfaces (reference specimens and specimens with '1-on-2' loop configurations) and the lower bound solutions.

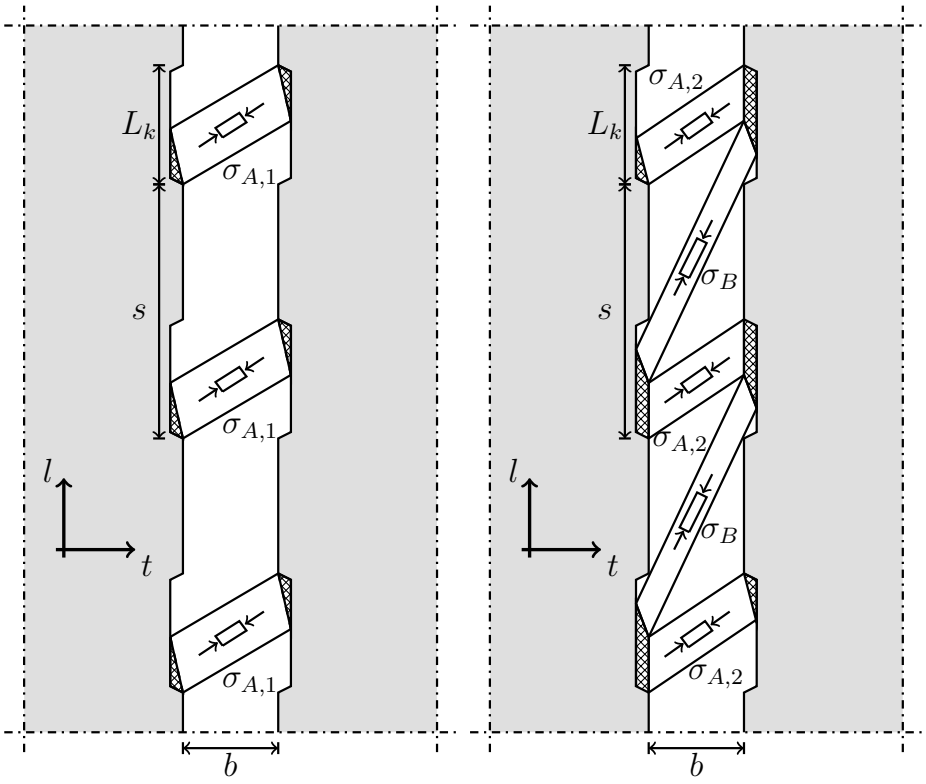

(a) Solution 1 (b) Solution 2

Figure 8.3: *The two stress fields considered, illustrations from Paper III*

8.1.2 Development of Stress Fields

In Paper III, two analytical lower bound solutions were developed. These are illustrated in Figure 8.3 for a connection with $n = 3$ shear keys. Solution 1 considers a distribution of struts with identical inclination, spanning over one pair of shear keys. This solution appears similar to the single-strut solution, however, the inclusion of friction in the interface allows for a smaller inclination of the struts as the stress state in the key corners does not have to be plane hydrostatic. The difference between the current solutions and the single-strut solutions by Christoffersen (1997) is particularly seen in

the limiting case of zero key depth ($d_k = 0$), where the single-strut solution predicts no capacity, while the current solutions predict a capacity stemming solely from friction.

A large number of combinations of uniaxial struts can be considered when developing lower bound solutions. The most simple solution is based on a combination of struts, which span over one or two shear keys, see Figure 8.3(b). This combination is denoted Solution 2. The stress states in the struts are uniaxial and the nodal zones in the key corners are stressed in biaxial compression (hatched area). At the outermost keys of the connection, the stress transfer is asymmetric in a pair of shear keys, as no strut is assumed to develop towards the end of the connection. In this relation, it should be mentioned that any potential locking bar is disregarded in the modeling.

Figure 8.4 shows the stress fields in the key corners for the two solutions. In Solution 1, the nodal zones are identical at both ends of the strut (Triangle I) due to symmetry. In Solution 2, three triangular zones can be identified. In these zones, the stress is transferred from the struts to the precast elements (see Paper III for details). A main feature of the stress field in Solution 2 is that the grout is stressed in the full length of the shear keys (see the right shear key in Figure 8.4(b)). The stress transfer in the boundary key (left shear key in Figure 8.4(b)) is identical to the stress transfer in the key corners of Solution 1.

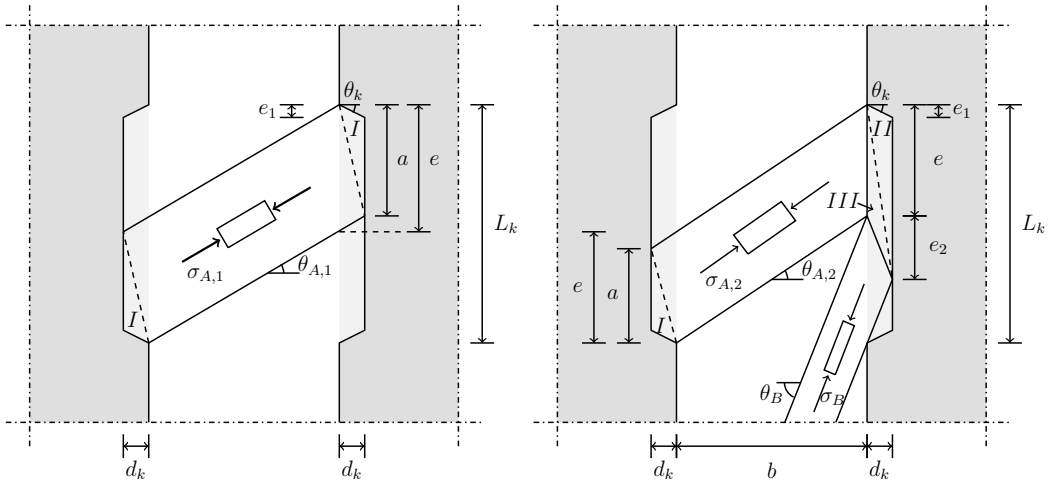

(a) Solution 1 (b) Solution 2

Figure 8.4: *Geometry of key corners and identification of the nodal zones I, II, and III in the key corners of the two solutions, illustrations from Paper III*

For both solutions, the length e is an optimization parameter and through this value, the optimal admissible stress field in the joint can be established. The optimal value of e ensures that the stress field fulfills the failure criteria of the grout and of the interface. The stresses in the key corners are modeled by the concept of homogeneous stress fields, see e.g. Nielsen (1969), Muttoni et al. (1997), and Pistoljevic and Nielsen (2009).

8.1.3 Failure Criteria

The stress field in the grout is limited by the strength of the grout. Failure criteria for uniaxial stress fields, for biaxial stress fields, and for stress transfer in the interface are considered. For the uniaxial compression (i.e. struts between the shear keys), the stress cannot exceed the effective strength:

$$\sigma_{A,i} \leq \nu f_c, \qquad \nu \leq 1, \quad i = 1, 2 \tag{8.1}$$

$$\sigma_B \leq \nu f_c, \qquad \nu \leq 1 \tag{8.2}$$

where ν is the effectiveness factor and i refers to Solution 1 or 2 (the stress σ_B is not present in Solution 1). It is in this context important to mention that the ν-factor to be adopted does not have to be the one used in Chapter 7 for the upper bound solutions, since the upper bounds, as already mentioned, are not necessarily exact solutions. In fact, to keep the lower bound results independent of the upper bound results, the adopted ν-factor should not be affected by any previous calibration with upper bound solutions. In the following, the value of ν will be taken as unity, when comparing the analytical lower bound model with numerical calculations. For comparison with test results, the value will be calculated by the following formula, which is proposed in the *fib* Model Code (fib, 2013) and primarily aimed at stress field modeling of shear related problems:

$$\nu = \left(\frac{f_{c,0}}{f_c}\right)^{1/3} \not> 1.0, \qquad (f_c \text{ in MPa}) \tag{8.3}$$

where $f_{c,0} = 30$ MPa. Originally, the formula was suggested by Muttoni (1990) using $f_{c,0} = 20$ MPa and later it was modified to the current form. The formula is considered as a qualified estimate of the effect of material brittleness. As can be seen, the formula differs slightly from the inverse square root dependency of f_c, which appears in the ν-formula determined by calibration of upper bound solutions with test results. Further discussion on the ν-factor to be used in lower bound modeling can be found in Paper III.

In the nodal zones, the grout is stressed in biaxial compression. As shown by e.g. Kupfer et al. (1969), the strength of concrete loaded in biaxial compression is greater than when loaded in uniaxial compression. The following

criteria for the stress state in the nodal zones (in terms of principal stresses, compression positive) are adopted:

$$\sigma_2 \leq cf_c, \qquad c \geq 1 \tag{8.4}$$

$$\sigma_1 \geq 0 \tag{8.5}$$

where c can be understood as a strength enhancement factor. The actual value of c is dependent on the stress state. For simplicity, a constant value of c can be adopted. The same approach is suggested in the *fib* Model Code, where an increase in strength of 10 % is allowed in regions, where significant biaxial compression exists. In the nodal zones ν can be taken as unity, also in practice.

The last criterion relates to the frictional resistance in the interface. As already mentioned, a Coulomb criterion is adopted for the interface:

$$|\tau_{nt}| \leq \mu\sigma_n \tag{8.6}$$

where τ_{nt} is the shear stress and σ_n is the normal stress acting on a interface. The criterion applies to the vertical and the inclined parts of the keyed interface, see e.g. Figure 8.5(a) for distribution of stresses on the boundaries of Triangle I. In Figure 8.5(b), the stress distributions are expressed in terms of stress resultants.

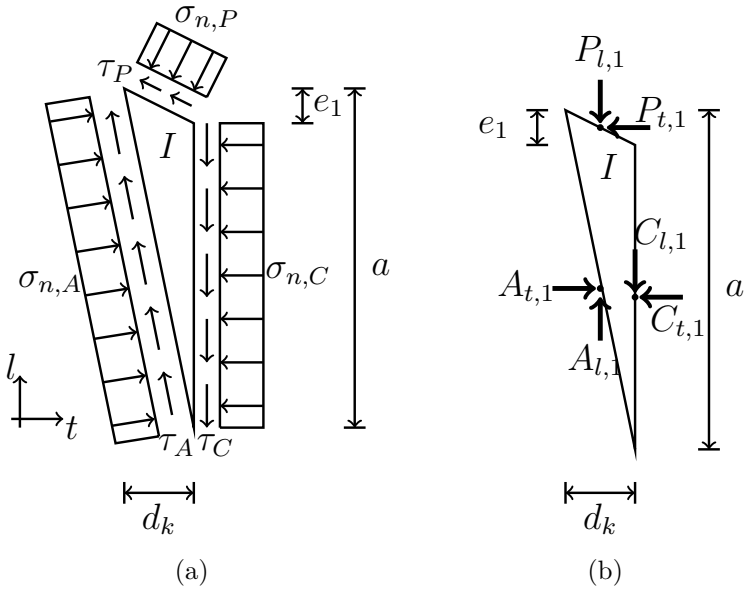

Figure 8.5: *Homogeneous stress field in the nodal zone of Solution 1, (a) Stresses along boundaries of Triangle I and (b) resultants of stresses on boundaries, illustrations from Paper III*

The criteria for the interfaces can be described in terms of stress resultants:

$$|C_{l,i}| \leq \mu C_{t,i}, \qquad i = 1, 2 \tag{8.7}$$

$$\left| \frac{P_{l,i} \sin\theta_k - P_{t,i} \cos\theta_k}{P_{t,i} \sin\theta_k + P_{l,i} \cos\theta_k} \right| \leq \mu, \qquad i = 1, 2 \tag{8.8}$$

where Equation (8.7) is valid for the vertical part of the shear key and Equation (8.8) applies to the inclined part of the shear key. The angle θ_k is the inclination of the key corner to horizontal, see Figure 8.4. It can be mentioned that when choosing traditional values of θ_k (in this relation meaning values less than 30°) and normal values of μ (≈ 0.7), the friction criterion of the inclined part of the key will not be critical. The inclination of the key corner does not affect the results, as long as it is relatively small ($\theta_k < 30°$). However, for practical applications, an inclination larger than 0° should be used to ensure adequate grouting of the key corners. A value of $\theta_k = 30°$ is adopted e.g. in Eurocode 2 (CEN, 2004) as a maximum limit to prevent sliding at the key corner.

In relation to force transfer by friction, it should be noted that when the optimized value of e entails an inclination of Strut A that fulfills the condition:

$$\tan\theta_{A,i} \leq \mu, \qquad i = 1, 2 \tag{8.9}$$

the stress from Strut A, σ_A, can be transferred by friction in the keyed interface of Triangle I and the stress state in Triangle I can be considered as uniaxial (Equation (8.1) then applies for the stress state in the nodal zone).

In addition to the failure criteria for the grout, the tensile stresses carried by the U-bars cannot exceed the yield limit:

$$\sigma_s \leq f_y \tag{8.10}$$

As the transverse loop connections should be designed to enable tensile yielding of the reinforcement (to avoid a brittle failure of the connection grout, see Chapter 5), this requirement (Equation (8.10)) ensures that the transverse capacity of the connection is not exceeded. If the full yield force cannot be activated, f_y should in Equation (8.10) be replaced by the reinforcement stress that corresponds to the tensile capacity of the connection related to grout failure. By use of force equilibrium, the requirement in Equation (8.10) can be reformulated as a constrain on the stress in the struts, see Paper III for details.

8.1.4 Optimization of Analytical Solutions

As described in Paper III, two independent parameters are available for optimization of the solution. As the statical optimization parameter, the resultant $C_{l,i}$ (which represents how much vertical force that can be transferred in the vertical interface, see e.g. Figure 8.5(b)) is chosen. An increased stress transfer leads to increased shear capacity and for this reason, the longitudinal stress transfer is chosen as large as possible. As the stress is transferred by friction, this means:

$$C_{l,i} = \mu C_{t,i}, \qquad i = 1, 2 \tag{8.11}$$

The only parameter left for optimization of the stress field is hereafter e. By varying the value of e, the stress state in the connection can be established and checked against the failure criteria.

8.2 Comparison to Finite Element Limit Analysis

The developed analytical lower bound solutions can be benchmarked against the numerical counterpart. Completely identical solutions are not expected as the numerical optimization operates with a much larger number of admissible stress fields.

Figure 8.6 shows a comparison between the numerical and analytical solutions. The calculations are performed using a geometry and a reinforcement degree, which are identical to the tests on the '2-on-2' shear connection design reinforced with 6 mm U-bars, see e.g. Appendix B.3. In the calculations, the coefficient of friction was taken as $\mu = 0.75$. The effectiveness factor and the strength enhancement factor for the mortar were taken as unity, i.e. $\nu = c = 1$. The comparison shows an almost perfect correlation between the numerical and analytical limit analysis. A small deviation is seen around the transition from Solution 1 to Solution 2, however, the overall agreement is excellent. For comparison, the results of the single-strut solution (Christoffersen, 1997) are also included. It can be seen that the developed lower bound solutions provide larger load carrying capacity than the single-strut model.

It should be noted that a benefit of the analytical solution compared to the current numerical solution is that the different zones in the joint grout can be assigned different strengths, depending on the stress state. In the numerical optimization, the same failure criteria must be assumed for all zones of the grout. This is the reason for choosing $\nu = 1$ and $c = 1$ when comparing the models. In the following comparisons, the nominal shear

stress, τ, has been determined as in Equation 7.1. For consistency, P is adopted for the shear load in the lower bound calculations as it was in the upper bound solutions. The notation deviates from Paper III, where V was used for the shear force, however, the symbols express the same load. For the degree of transverse reinforcement, Φ is calculated as in Equation (7.2).

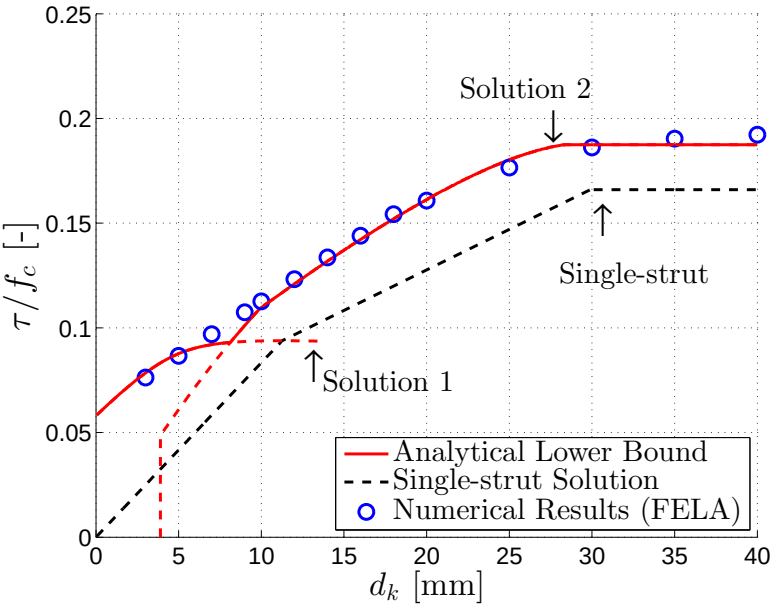

Figure 8.6: *Comparison between numerical and analytical lower bound modeling, illustration from Paper III*

8.3 Comparison of Tests with Theory

In the following, the analytical lower bound solutions will be compared to the test results presented in Chapter 6. In the comparison, $c = 1.15$ and $\nu = 1$ are adopted for the local strength in the key corners (similar to how compression nodes in strut-and-tie models are treated) and the effectiveness factor for the compression struts is calculated by Equation (8.3). The coefficients of friction are chosen as discussed in Section 8.1.1. In the figures, an experimentally observed key failure by local key corner crushing is indicated with a red symbol while failure by complete cut off is indicated with a black symbol. The calculated capacities are tabulated in Appendix D along with the tested first peak capacities. In the appendix, information about which stress component that is governing is also included.

8.3.1 Reference Tests

Figure 8.7 shows the comparison between the two analytical solutions and the reference tests (conventional design). The theoretical results are generated by a variation of f_c. The lower bound model predicts capacities that are lower than the test results. From the calculations (see also Table D.1), it is found that Solution 1 is governing and that the maximum compressive stress in Triangle I is the limiting stress component. The underestimation of the capacity (an average of 30 % underestimation) would be smaller, if a larger value of μ was used for the greased interface.

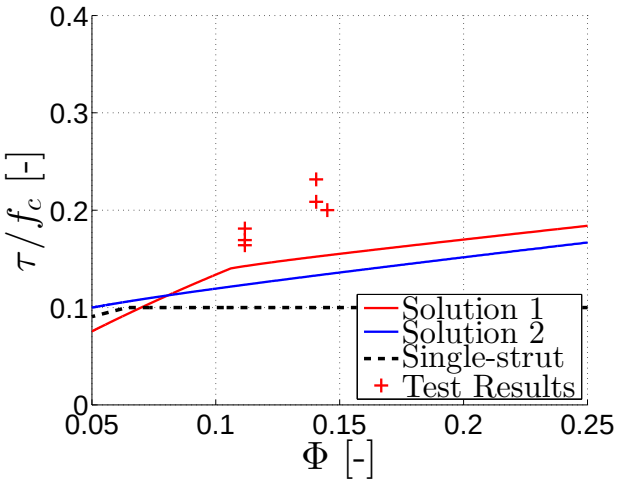

Figure 8.7: *Comparison of results from tests on the reference specimens with the lower bound solutions ($\mu = 0.3$)*

8.3.2 New Design '1-on-2' Configuration

In Figure 8.8, the lower bound solutions are compared to the test results of the new design with a '1-on-2' loop configuration. The plots show capacity versus key depth. It can be seen that Solution 1 is governing for smaller key depths, whereas Solution 2 becomes governing for larger key depths. This is as expected. The model captures the test results reasonable well. The calculations (see Table D.2) show that different stress components are governing for the theoretical prediction of the capacity.

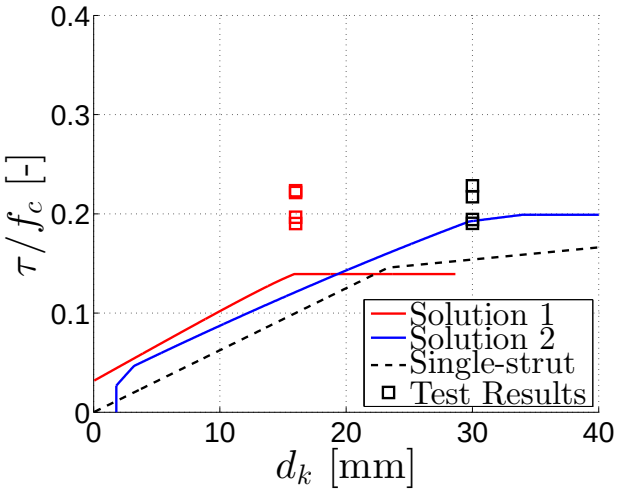

(a) 8 mm U-bars

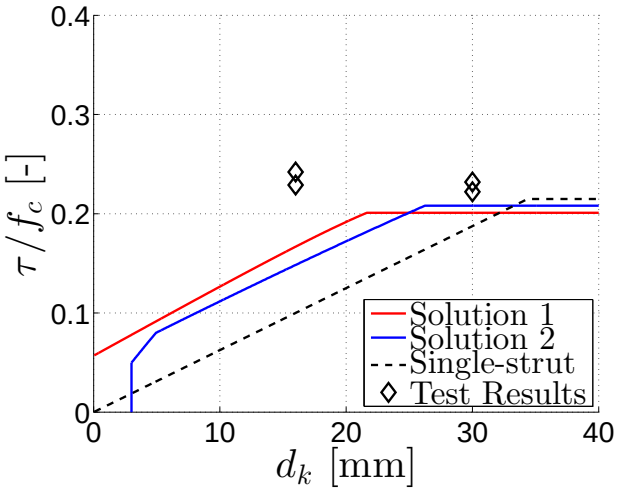

(b) 10 mm U-bars

Figure 8.8: *Comparison of results from tests on the '1-on-2' connection design with the lower bound solutions ($\mu = 0.3$)*

8.3.3 New Design '2-on-2' Configuration

The comparison of lower bound calculations with test results for the new design with 6 mm U-bars are included in Paper III and repeated in Figure 8.9. Generally, a good fit between tests and theory is found. It is seen that the capacity is predicted by Solution 2 for all tests. It should be mentioned that for a key depth of approximately 16 mm, the lower bound solutions predict a change in the governing stress component. In the tests, both failure modes (corner crushing and complete key cut off) were observed for this key depth. However, the change in failure mode cannot be directly interpreted from the change in the governing stress component.

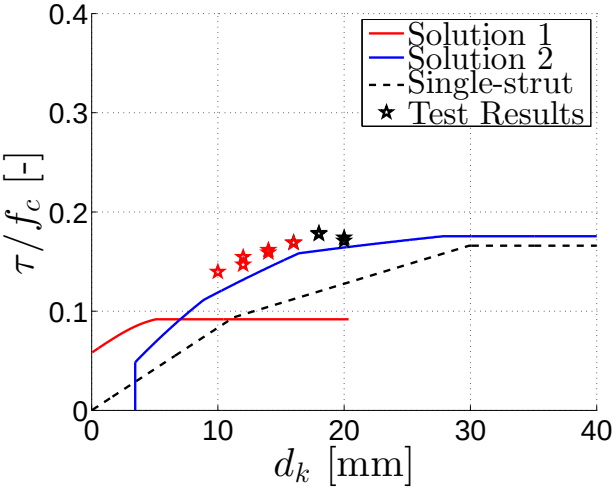

Figure 8.9: *Comparison of results from tests on the new '2-on-2' connection design (6 mm U-bars) with the lower bound solutions ($\mu = 0.75$)*

In Figure 8.10, the test results of the new design reinforced with 8 mm U-bars are compared to the lower bound model. For the series with varying key length (Specimens I-IV, see Table B.4), the results are generated by a variation of the key length. The remaining specimens had different key depths (Specimens V-IX, see Table B.5), which is why the capacity for these tests has been plotted as a function of d_k. In general, the lower bound model agrees reasonable well with the test results. For the series with varying key length, the correlation is rather good and only a noticeable deviation is seen for the smallest key length (120 mm). The reason for the apparent decrease in capacity with increasing key length is due to the fact that the area of the shear key is used in the definition of the shear stress, τ. A greater key length results in a steeper inclination of the struts and thereby a higher capacity. In Appendix D.4 increasing values of P_{cal} is reported for increasing key lengths.

For the series with varying key depths, it is noted that some of the test results with larger key depths (Figure 8.10(b)) fall below the lower bound prediction. This is not expected from the extremum theorems of plastic theory. However, this may be due to the adopted effectiveness factor. For a compression strength around 30 MPa (the strength of the grout was 30.6 MPa for the test specimens with large key depths), Equation (8.3) predicts practically no reduction of the compressive strength due to brittleness. In reality, the average plastic strength of the mortar should most likely be reduced, even for f_c lower than 30 MPa.

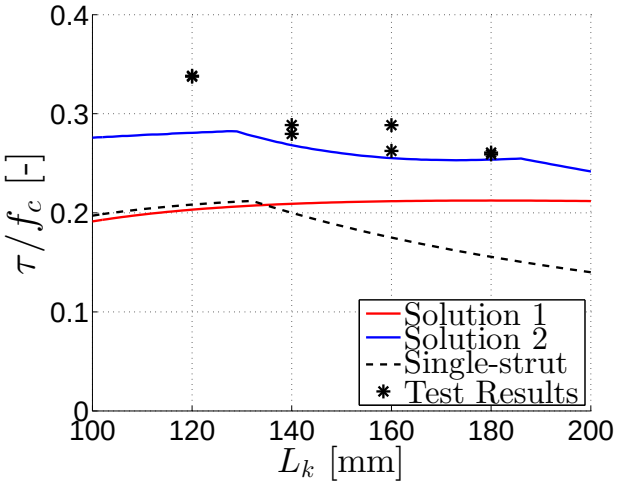

(a) 8 mm U-bars, varying key length

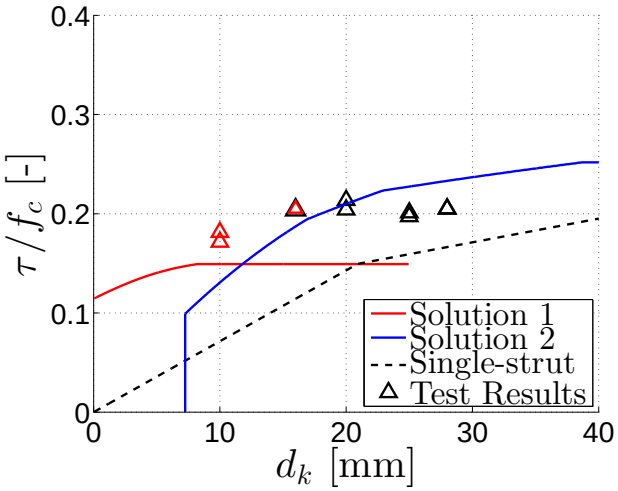

(b) 8 mm U-bars, varying key depth

Figure 8.10: *Comparison of results from tests on the new '2-on-2' connection design (8 mm U-bars) with the lower bound solutions ($\mu = 0.75$)*

For the '2-on-2' test series with 10 mm U-bars, both concrete and mortar were used as grouts. As the same relations for the effectiveness factor, ν, and the strength enhancement factor, c, are adopted for the two materials, the calculations predict the same capacity for the two grouts. The comparison can be seen in Figure 8.11. It is found that for all specimens, the capacity is governed by Solution 1, i.e. struts spanning over one pair of shear keys. This is due to the small key depth used in the tests. Furthermore, it is seen that the calculations predict the test results better for the longer key lengths. Again, this is a combination of the small key depth and the length of the keys (inclination of the struts).

As a concluding remark on the comparison of the lower bound calculations with test results, it is noted that the developed lower bound model in all cases provides results that fit the test results better than the single-strut solution. Higher capacities can be obtained by inclusion of the locking bar in the model. This extension to the model has not been incorporated in the current study.

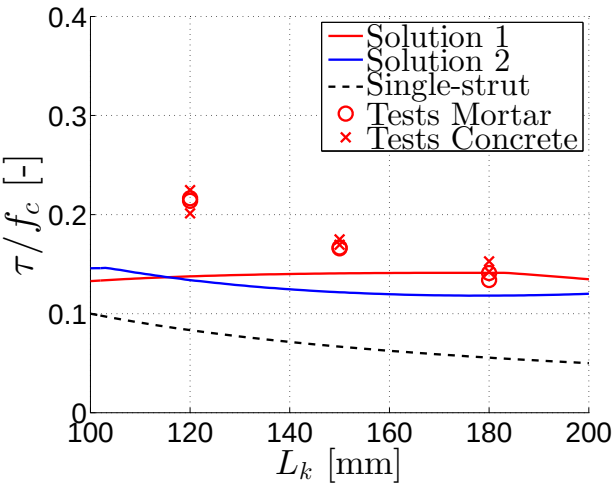

Figure 8.11: *Comparison of results from tests on the new '2-on-2' connection design (10 mm U-bars) with the lower bound solutions ($\mu = 0.75$)*

8.4 Evaluation of Model Parameters

Based on the comparisons between calculations and test results, the performance of the lower bound solutions can be evaluated. Figure 8.12(a) shows the test-to-calculation ratios versus the reinforcement degree. It can be seen that most of the capacities are predicted below the tested capacity, which is to be expected from a lower bound model. The mean value of the $P_{\mathrm{FP}}/P_{\mathrm{cal}}$-ratio for all the tests is 1.17 and the standard deviation amounts to 0.18.

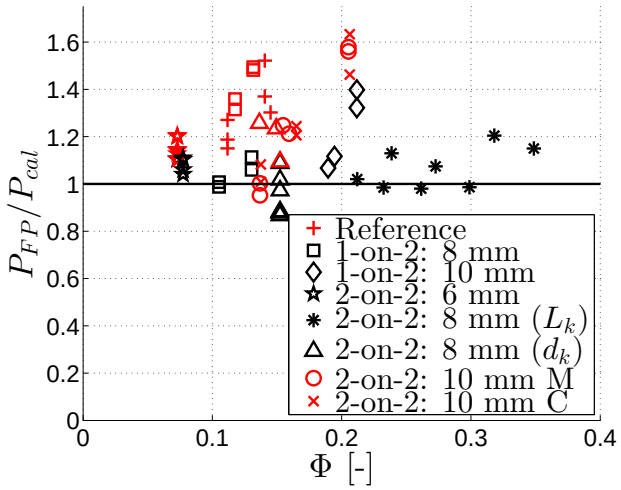

(a)

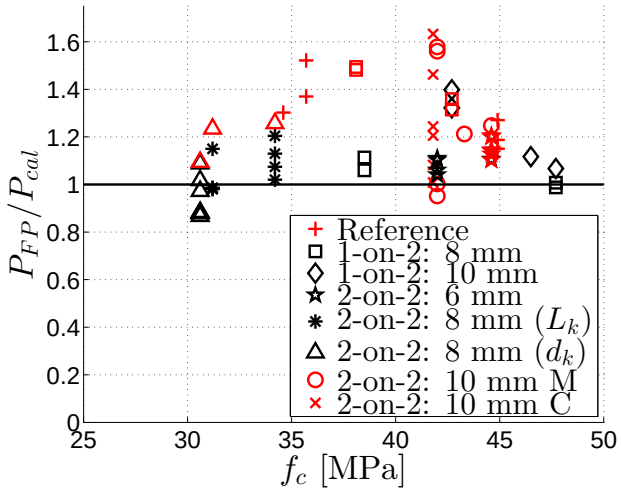

(b)

Figure 8.12: *Ratio between tested and calculated peak loads versus (a) the reinforcement degree, Φ, and (b) the compressive strength, f_c*

In Figure 8.12(b), the correlation can be seen in a $P_{\mathrm{FP}}/P_{\mathrm{cal}}$ versus f_c plot. This comparison is relevant as the effectiveness factor for each test is calculated based on the tested compression strength. The values of ν varied between 0.86 and 0.99. From a lower bound point of view, the solutions compare reasonably well with the test results. It appears that the adopted values of ν and c do not lead to overestimation of the capacity. It should be noted that the predicted capacity is not always limited by the same failure criterion and therefore, it is not possible to evaluate the parameters directly when comparing to all the test results. Nevertheless, the combination of the two parameters dictates which of stress components that is governing, thus the overall comparison constitutes a basis for evaluation of the combination of the two parameters.

8.4.1 Key Depth and Width of Connection

In Figure 8.13, the influence of two essential geometric parameters is evaluated. As mentioned earlier, the test series were designed with a particular interest in the key depth. It is therefore of interest to study how the lower bound model agrees with tests as d_k varies. This is shown in Figure 8.13(a). A general tendency which is valid for all test series cannot be observed. For some series, it seems that the theory overestimates the capacity more for smaller key depths than for the larger key depths. This can probably be explained partly by the fact that the simple stress field assumed in the model consists of narrow struts, when the key depth is small. Where the stress is transferred to the elements, the real stress state locally in the key corner might be described better by a triaxial stress state than the biaxial stress state assumed in the solutions. As the key depth increases, the width of the struts increases as well (see e.g. Figure 8.2). In this case, the stress concentrations may lead to a smaller strength increase than for the smaller key depths. A more accurate failure criterion for the stress state might capture the results better for all key depths, however, it is not possible to capture effects of a triaxial stress state by the simple relation using a constant c factor.

As shown in Chapter 7, the connection width, b, affected the agreement between tests and the upper bound solutions, most probably because b is not properly accounted for in the model. In the lower bound solutions on the other hand, b plays an important role for the stress field. The influence of b on the calculated capacity should therefore be reflected better in the lower bound solutions. This seems in fact to be the case, when comparing the plot in Figure 8.13(b) with its counterpart in Figure 7.11. The strong declining tendency in Figure 7.11 is not observed in Figure 8.13(b), which suggests that the mean value of the $P_{\mathrm{FP}}/P_{\mathrm{cal}}$-ratios, for fixed values of b is

less affected by b, when using the lower bound solutions.

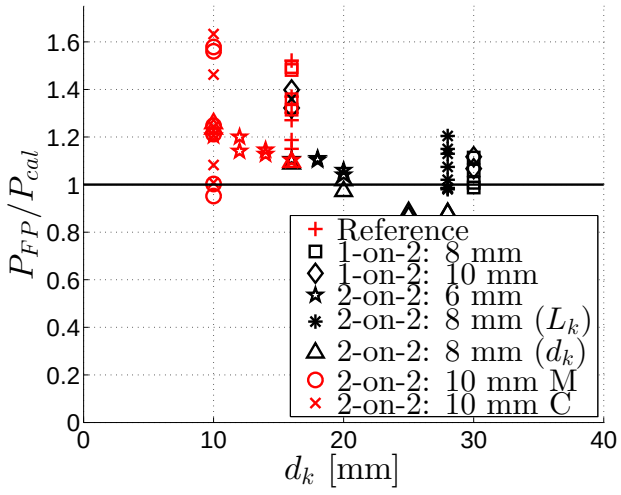

(a)

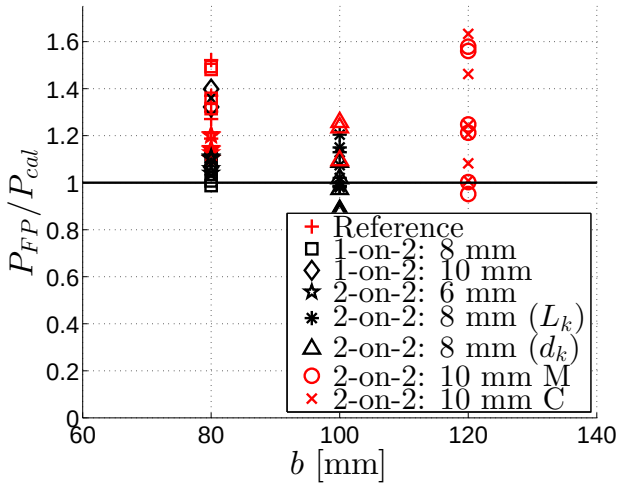

(b)

Figure 8.13: *Ratio between tested and calculated peak loads versus (a) key depth, d_k, and (b) connection width, b*

8.5 Concluding Remarks

In this chapter, the lower bound model developed in Paper III was compared to the test results presented in Chapter 6. One of the test series has also been treated in Paper III. The developed model leads to two solutions: Solution 1 with struts spanning over one pair of shear keys and Solution 2 with a combination of struts with different inclinations. The local stress states in the key corners were assessed by the concept of homogeneous stress fields. A number of other solutions can be developed, however, these two solutions captured the tendencies of the experimental results reasonable well. The main results and findings of the chapter are summarized as follows:

- ⋆ Inclusion of interface friction increases the calculated shear capacity of the keyed connections compared to the previously developed single-strut solution.
- ⋆ Introduction of local strength parameters allows for assessment of different stress states in the grout:
  - ◇ For the uniaxial compression struts, an effective strength of νf_c was adopted. The ν-factor of the model primarily accounts for material brittleness.
  - ◇ For the nodal zones stressed in biaxial compression, an enhancement factor, c, was introduced to allow for an increase of the maximum compressive principal stress.
- ⋆ The influence of the connection width on the calculated capacity is better accounted for by the lower bound solutions than its upper bound counterparts.

9 Comparison of Upper and Lower Bound Solutions

In the previous chapters, upper and lower bound solutions for the ultimate capacity of shear connections have been presented and compared to the test results, presented in Chapter 6. One of the main purposes for developing both types of models is to narrow the range of expected test results. Identical upper and lower bound solutions are not possible to obtain as the basic assumptions adopted for development of the solutions are not identical. For the upper bound model, plane strain conditions are usually assumed for analysis of the failure mechanism in the narrow connection zone. For the lower bound solutions, on the other hand, plane stress conditions are assumed. Nevertheless, the comparison of the two methods provides information on the expected capacity of a keyed shear connection.

In the following, the upper as well as the lower bound model will be compared to the test results. In the lower bound calculations, the strength parameters adopted in Chapter 8 will be used. This includes the coefficients of friction ($\mu = 0.3$ or 0.75) as well as the strength enhancement factor $c = 1.15$. For the upper bound solutions, the same effectiveness factor as used in the lower bound calculations will be adopted (Equation (8.3)). This value of ν accounts only for material brittleness and hence, the influence of the model assumptions (plane strain versus plane stress) can be visualized while at the same time, any effect related to calibration with upper bound solutions is avoided.

9.1 Expected Range of Results

Figure 9.1 shows the calculated upper and lower bound results compared to the test results for the reference specimens (conventional design). The expected range of results is shaded in grey and bounded by the upper bound solutions from above and by the lower bound solutions from below. It is found that the test results lie well within the expected range. The difference between the upper and lower bound increases with increased reinforcement degree. Only the result of Mechanism C is included in the graph as this mechanism was governing in the upper bound calculations. The failure mode observed in tests also reflected this mechanism (local key corner crushing, indicated with red symbols).

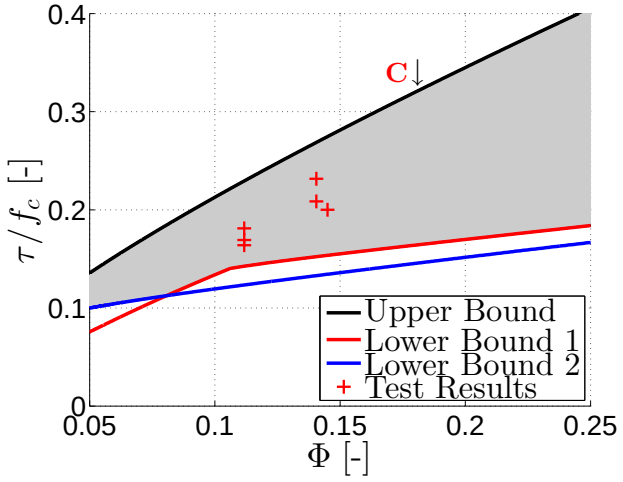

Figure 9.1: *Expected range of results predicted by the upper and lower bound solutions, compared with test results of reference specimens (conventional design)*

The plots of the expected range of results for the tests with a '1-on-2' loop configuration are shown in Figure 9.2. In this case, the governing upper bound solutions correspond to Mechanism B (key cut off, indicated with black color) and Mechanism C (local key corner crushing, indicated with red color). It is found that the test results for both dimensions of U-bars fall within the predictions of the upper and lower bound solutions. It can be mentioned that a greater range is predicted for calculations with 10 mm U-bars (Figure 9.2(b)). The failure modes predicted by the upper bound solutions for specimens reinforced with 8 mm U-bars reflect the observed failure modes, when using the chosen ν-factor. The transition between the two failure modes (according to the upper bound solutions) is indicated in the figures. For the specimens reinforced with 10 mm U-bars, correct prediction of the key failure mode is only obtained for two tests.

Figure 9.3 shows the expected range of results together with test results for the '2-on-2' configuration with 6 mm U-bars. The results of Mechanism D represent the capacity related to complete key cut off and both Mechanism C (solid line) and Mechanism E (dashed line) are included for the failure by key corner crushing. The models provide a very narrow range of expected results, within which the test results are actually found.

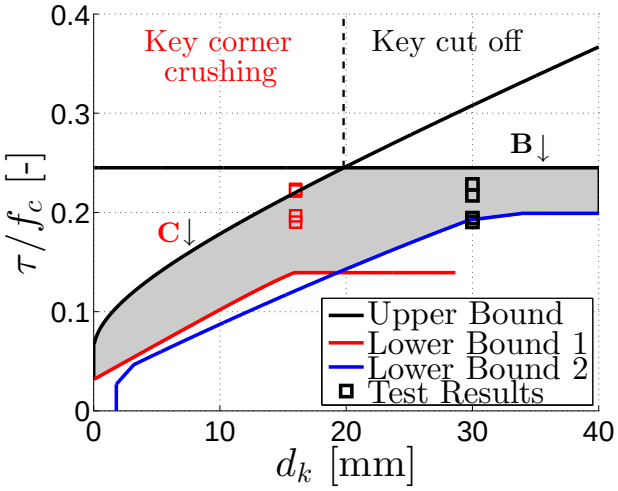

(a) 8 mm U-bars

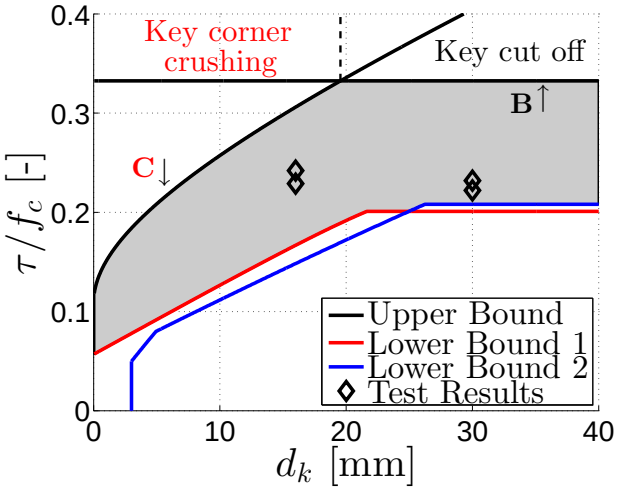

(b) 10 mm U-bars

Figure 9.2: *Expected range of results predicted by the upper and lower bound solutions, compared with test results of the '1-on-2' loop configuration*

It should be noted that for very small key depths, the lower bound model (Solution 1) provides capacities that are greater than the upper bound solution (Mechanism C with local crushing of the key corners). This is inconsistent with the extremum theorems of plasticity theory. To obtain results consistent with the extremum theorems, the upper bound calculations should be modified to include the friction criterion for the interface and at the same time fulfill the normality condition at the interface. This would change the lower limit for α from $\varphi = 30°$ (adopted for a mortar) to $\varphi = \arctan \mu = 37°$ ($\mu = 0.75$). There will be no extra dissipation of energy in the upper bound

solution as the dissipation along the interface is zero, when the normality condition is imposed on a friction criterion without cohesion. In this case, the upper and lower bound solutions will be identical for $d_k = 0$. This is not relevant for practical applications, however, consistent with the extremum theorems.

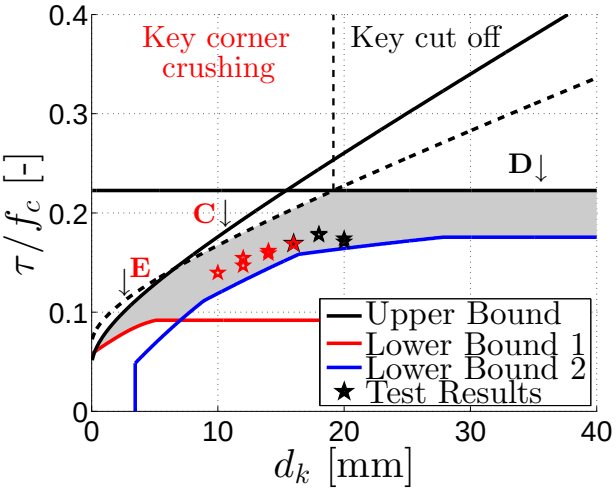

Figure 9.3: *Expected range of results predicted by the upper and lower bound solutions, compared with the test results of the '2-on-2' loop configuration with 6 mm U-bars*

Figure 9.4 contains the expected range of results for the tests on the '2-on-2' loop configuration with 8 mm U-bars. For the tests with varying key length, both the upper and the lower bound model captures the observed tendency well, i.e. increasing τ / f_c for decreasing L_k. The reason for the apparent decrease in τ is explained in Chapter 8. For the series with varying key depth, the models provide a reasonable range of expected results. However, the test results for specimens with larger key depths lie below the lower bound prediction. A smaller value of ν would provide a better correlation for both the upper and lower bound model. This was also discussed for the lower bound model in Chapter 8.

Figure 9.5 shows the expected range of results for the tests on the '2-on-2' loop configuration with 10 mm U-bars. Only the mechanisms corresponding to local crushing of the key corners are included, as this was the observed failure mode in the tests. The internal angle of friction adopted in the upper bound calculations is the one suggested for mortar, i.e. $\varphi = 30°$. It can be seen that the test results lie well within the range of model predictions. It is found that the difference between the upper and the lower bound models increases with decreasing key length. The upper bound model predicts the

experimental tendency better than the lower bound model. On the other hand, the lower bound model provides a better fit when the key length is large. This is due to the inclinations of the struts, which are steeper for larger key lengths and thereby a larger capacity can be predicted.

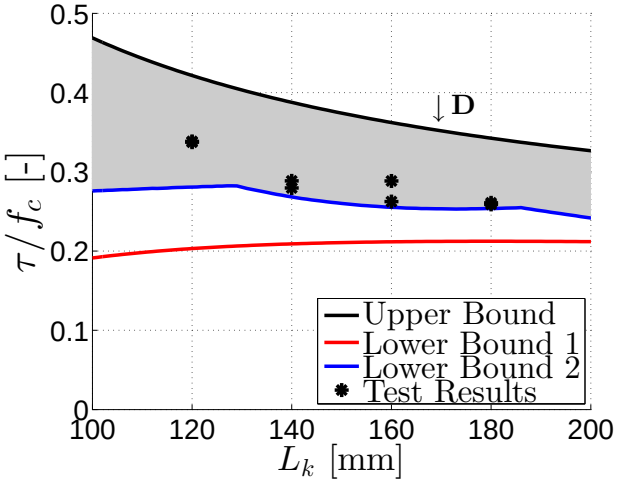

(a) 8 mm U-bars, varying key length

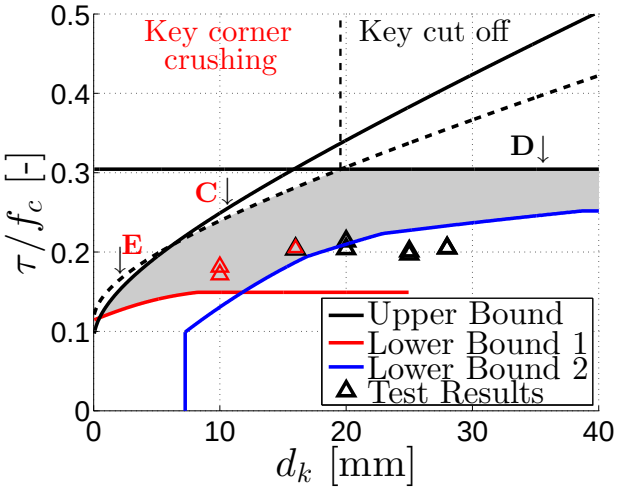

(b) 8 mm U-bars, varying key depth

Figure 9.4: *Expected range of results predicted by the upper and lower bound solutions, compared with test results of the '2-on-2' loop configuration with 8 mm U-bars*

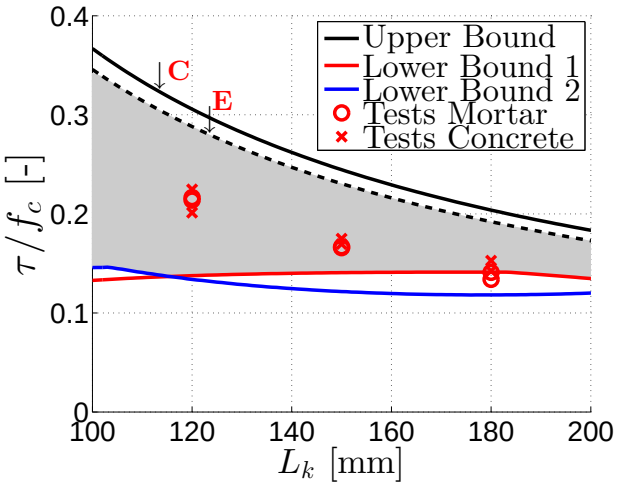

Figure 9.5: *Expected range of results predicted by the upper and lower bound solutions, compared with test results of the '2-on-2' loop configuration with 10 mm U-bars*

9.2 Evaluation of the Models

The models have been used to determine the range of expected results bounded from above by the upper bound solutions and from below by the lower bound solutions. The calculations were based on the best estimate of model parameters (including the chosen value of ν) and showed that neither the upper bound solutions, nor the lower bound solutions, can be regarded as the exact solution for the problem considered. Nevertheless, for the relevant geometrical parameters, the upper and lower bound models display the same tendencies, i.e. increase or decrease in capacity by a variation of the investigated parameter. This is for example seen in the calculations, where the key depth varies, see e.g. Figure 9.3. At some characteristic key depth, the upper bound model predicts a transition from local key corner crushing to complete key cut off (no further increase in capacity from an increase in key depth). The lower bound model also predicts a change in capacity with increasing key depth (the governing stress component changes). However, the failure mode related to the governing stress state cannot be determined from the lower bound model. Nevertheless, the calculations based on the two approaches do not contradict each other.

In this relation, it should be noted that the upper bound model considering local key corner crushing and the detailed lower bound model including friction and accounting for the local stress states (with different strengths) constitute models that provide better predictions than the previously devel-

oped models. In the previous models only complete key cut off and single-strut action were considered. Benchmarked against the previous models, the developed models constitute an improvement, not only in relation to the prediction of the capacity, but also regarding estimation of the failure mode of the shear keys. Relating to the test results presented in Chapter 6, an accurate prediction of the failure mode is beneficial when a ductile load-displacement relationship is required.

9.3 Practical Relevance

The practical relevance of the upper and lower bound models can be discussed based on the conducted comparison between model calculations and test results. The primary merit of the upper bound model lies in the simplicity (closed-form equations). However, the effectiveness factor to be adopted, i.e. Equation (7.14), must be calibrated with tests in order to compensate for the fact that the solutions are not exact and thereby unsafe. The lower bound solutions, on the other hand, provide safe results, but are more complicated to develop. The most accurate stress condition in a shear connection is most likely somewhere in between the assumptions adopted for the two approaches (i.e. plane strain versus plane stress). It might be too optimistic to expect that a solution closer to the exact one can be developed and at the same time appears as user-friendly as the closed-form upper bound solutions. Therefore the upper bound solutions will still have preference from a practical point of view, even though they have to be used in conjunction with an effectiveness factor that not only accounts for the material behavior, but also functions as an adjustment parameter to compensate for the unsafe nature of upper bound solutions. Awareness of this is important when applying the upper bound solutions to practical cases, which deviate significantly from the experimentally tested configurations. This also means that the lower bound model should be applied in situations, where the design of keyed connections deviates significantly from tested designs.

In relation to the practical application of the upper bound solutions, realistic material properties should also be used in conjunction with the proper effectiveness factor. The results of the triaxial tests presented in Chapter 3 proved that mortar does not possess the same material properties as concrete. This is especially evident, when comparing the values of φ indicated in the triaxial tests. Ideally, detailed information on the internal angle of friction for the grout should be provided in the design process. As this requires extensive testing, the suggested parameter, namely $\varphi = 30°$ for mortar, should be adopted. As discussed in Chapter 7, a value of $\varphi = 30°$ can also be used in the upper bound solutions, when concrete is used to grout shallow indentations.

As a final remark, it should also be noted that the adopted enhancement factor in the biaxially compressed key corners has been estimated based on tests on concrete. For the comparison to test results, the value of $c = 1.15$ does not seem to be unrealistic. However, additional biaxial testing on mortar would provide further information about this material property to be adopted in lower bound modeling. This has not been carried out in relation to this study.

9.4 Concluding Remarks

In this chapter, the upper bound model, developed in Paper II and presented in Chapter 7, have been used together with the lower bound model, developed in Paper III and presented in Chapter 8, to establish an expected range of results. The expected range was compared to the test results presented in Chapter 6. The calculations were performed by use of an effectiveness factor, which accounts only for material brittleness and without any previous calibration with the upper bound solutions. The comparisons showed that the first peak loads obtained from tests generally were within the predicted range. The models have been evaluated based on the comparisons and the practical relevance of the solutions has been discussed. The findings of the chapter are summarized as follows:

- ⋆ The upper and lower bound models are not based on the same assumptions and hence, no exact solution can be obtained from the developed models.
- ⋆ In most cases, the upper and lower bound models provide a reasonable narrow range of expected results. The upper and lower bound models show the same tendencies.
- ⋆ An exact analytical model would be very difficult to develop as the conditions in the grout cannot be described as plane stress nor plane strain.
- ⋆ The effectiveness factor to be adopted in the upper bound solutions must account for the material brittleness as well as compensating for the unsafe nature of the solutions.
- ⋆ For practical applications, the upper bound solutions (closed-form equations) are easy to use. However, care must be taken when the solutions are used in situations that deviate significantly from tested configurations.
- ⋆ The lower bound solutions should be applied, when test results are not available.

10 Dowel and Catenary Action in Rebars Crossing a Shear Joint

In this chapter, the second-order plasticity model developed in Paper IV for modeling of the load-displacement response of a two-sided dowel joint will be presented. In the preceding chapters, first-order plastic solutions were developed to model the load-carrying capacity of keyed shear connections. When comparing with tests, the first-order calculations (upper and lower bound) refer to the first peak load, which in Chapter 6 was shown to be the capacity related to failure of the shear keys. The new design for keyed shear connections displayed a significant ductile response with a pronounced deformation capacity. Examples of load-displacement relationships are given in Figure 10.1(a), where a higher ultimate load, P_{U}, was reached at larger displacements, than the first peak load, P_{FP}, recorded at small displacements. The relationships show that the amount of dissipated energy (i.e. area below the response curve) is significantly greater than that of the conventional design. If this ductile response is to be utilized in an assessment of the overall robustness for the structural system, the load-displacement relationship beyond the first peak capacity should be modeled accurately. In order to do so within the framework of the theory of rigid-plasticity, second-order modeling, where change of structural geometry is taken into account, must be adopted. Examples of large deformation modeling have been demonstrated by e.g. Calladine (1968), Bræstrup (1980), and Belenkiy (2007). If such a model is to be developed for keyed shear connections, inspiration can be found in observations retrieved during and after tests, see e.g. Figure 10.1(b), where the permanent deformations of a U-bar observed after a test (Specimen P12, '1-on-2' design with 10 mm U-bars) can be seen.

In Paper IV, a second-order plasticity model was developed, where the case of a casting joint crossed by rebar(s) and exposed to pure shear was considered. The load carrying mechanism consists in this case of a combination of dowel and catenary action in the rebars. The combination of the two actions can be related to the imposed shear displacements through the kinematical conditions of the dowel and the normality condition of plastic theory. The comparisons between the model and the test results presented in Paper IV showed good agreements and reasonable estimates of the available

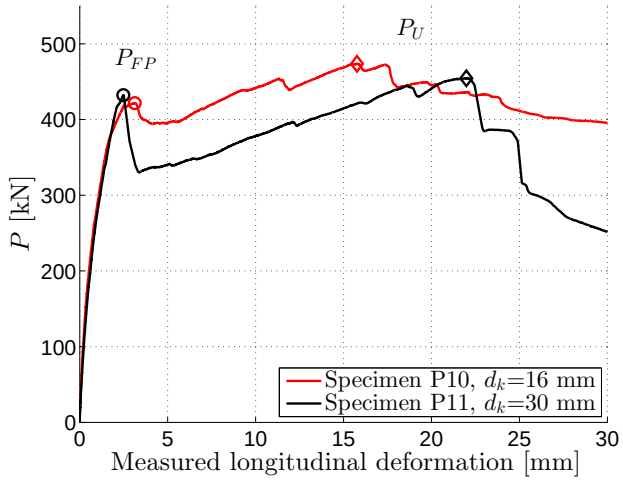

(a) Load-displacement relationship

(b) U-bar deformation

Figure 10.1: *Examples of (a) load-displacement relationships where the ultimate load, P_U, is larger than the first peak load P_{FP} and (b) U-bar deformation after test (Specimen P12)*

plastic energy can be obtained from the calculations. However, the model, in its present form, does not provide the means to perform a complete analysis of the load-displacement relationship for the keyed shear connections tested. This is partly because the failure of shear keys is not included in the model and partly because the displacement field assumed is too simple compared to the experimental observations on the keyed shear connections. Chapter 4 showed an example of the displacement field for the failure of a mortar shear key by complete key cut off, see Figure 4.10. It was found that the failure process of the key includes transverse displacement over the crack and furthermore that the angle of the relative displacements varied with increasing shear displacement. Nevertheless, the second-order model developed in Paper IV assesses a basic problem, where the capacity is increased due to change of structural geometry. The model can be considered as an introduction to a simple approach, which has potential for practical assessment of system robustness, e.g. in structural connections of precast concrete components.

In this chapter, the general considerations and methods adopted for the second-order modeling will be presented. As the final results are not as self-explaining as the solutions obtained from first-order modeling, the formulas from Paper IV will be repeated in the following. However, only a few comparisons between the model and test results from the paper will be replicated. Instead, the model will be compared to the test results of a shear connection

with a '1-on-2' loop configuration without indentations (Specimens S4, see Appendix B.2 for details on the specimen). Based on the comparison, a discussion will be given on possible extensions of the model that should be incorporated to account for more complex displacement fields.

10.1 Second-Order Plastic Modeling

The developed second-order plasticity model describes the problem of a rebar crossing a casting joint loaded in shear. The first phase of the load transfer mechanism will be dominated by dowel action in the rebar. This was first treated by Friberg (1938), who modeled the dowel as a linear elastic beam transversely supported on elastic springs. The obvious shortcoming of this approach is the linear elastic assumption for material behavior. Due to the non-linear material behavior, a model based on the theory of plasticity seems more appropriate to apply for dowel action in the ultimate limit state. This was done by Rasmussen (1963), who established a first-order plastic solution for one-sided dowel action (a rebar with part of its length embedded in a concrete block and loaded transversely at the free end). Rasmussen assumed yielding of the rebar simultaneously with crushing of the concrete underneath the dowel.

A joint is called a two-sided dowel joint, when the rebar has both ends fully embedded in concrete, as shown schematically in Figure 10.2. The first phase of the load-displacement relationship is, also in this case, gov-

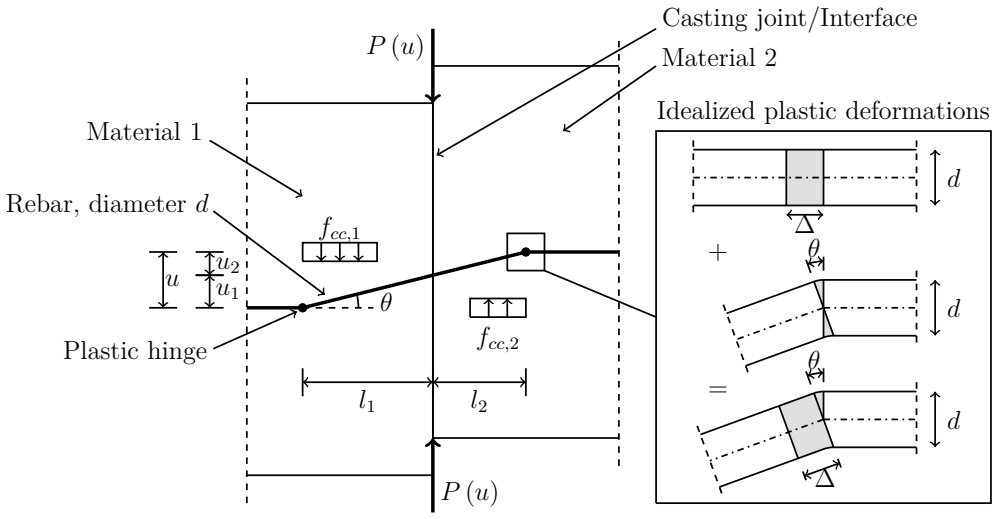

Figure 10.2: *Joint between concretes cast at different times, crossed by a rebar and subjected to shear displacements, figure from Paper IV*

erned by development of pure dowel action (plastic hinges and crushing of the concrete in both blocks, see e.g. Nielsen and Hoang (2011)). However, with increasing shear displacements, the bending in the rebar is accompanied by tension. Eventually, when further shear displacements are imposed, the extent of tension increases and in the final stage, the dowel action is completely replaced by catenary action in the rebar. The development of pure catenary action requires relatively large shear displacements and it is evident that the change of structural geometry must be taken into account, when the capacity in this phase is to be modeled.

In the model, the rates of plastic deformations can be determined by establishing the kinematic relationship for the assumed mechanism. Then, by imposing the normality condition of plastic theory on the yield condition for the rebar and by applying the work equation for increments of displacement, the necessary equations to determine the load, P, as a function of displacement, u, can be derived. For in-depth details, the reader is referred to Paper IV.

10.1.1 Assumptions for Second-Order Modeling

As in the first-order plastic models, a number of assumptions have to be made for the material behavior. The concrete as well as the reinforcing steel are treated as rigid-plastic materials. However, contrary to the first-order models, the finite deformation capacity of the materials is taken into account. Due to the rigid-plastic assumption, the displacements are the sole results of accumulated plastic deformations. The relative displacement, u, between the two blocks of concrete is assumed to be parallel to the interface. The model will be established for the general case, where the casting joint constitutes the interface between two concretes cast at different times. The materials on each side of the interface are allowed to have different strengths and properties when loaded in triaxial compression (e.g. mortar cast against concrete). The problem is modeled as a displacement-controlled problem with a monotonically increasing shear displacement. A simple relation for the time dependent displacement is assumed (a displacement velocity equal to unity):

$$u(t) = t \tag{10.1}$$

Only the case with rebars placed perpendicular to the interface is considered.

10.1.2 Formation of Mechanism

To establish the starting point for the model, a mechanism must be assumed. The mechanism is shown in Figure 10.2. When exposed to shear displace-

ments, two plastic hinges must develop in the rebar to accommodate the displacement. The plastic hinges are developed at the distances l_1 and l_2, respectively, from the interface. The magnitudes of l_1 and l_2 depend on the moment capacity of the dowel and on the local concrete strength on each side of the interface. In order to comply with compatibility requirements, the plastic hinges must undergo plastic elongation as well as rotation, θ, when the shear displacement is increased. Since rigid-plastic material behavior has been assumed, it is convenient to consider the elongation as a plastic extension, Δ, concentrated in the plastic hinges. The plastic deformations are calculated by:

$$\tan\theta = \frac{u}{l_1 + l_2} = \frac{u_1}{l_1} = \frac{u_2}{l_2} \tag{10.2}$$

$$\Delta = -\frac{l_1 + l_2}{2} + \frac{l_1 + l_2}{2}\sqrt{1 + \left(\frac{u}{l_1 + l_2}\right)^2} \tag{10.3}$$

where $u = u_1 + u_2$, see e.g. Figure 10.2. The plastic deformations can be regarded as the general strains that correspond to the bending moment, M, and normal force, N, acting in the plastic hinges.

The positions of the plastic hinges can be estimated based on equilibrium considerations (similar to the approach of Rasmussen (1963)). The assumed displacement field for the rebar implies that local crushing of the concrete must take place. The actual stress distribution in the concrete is complex and it is not possible, in this context, to determine the details of the entire stress distribution. As a simplification, an enhanced average strength, f_{cc}, is assumed for the triaxial stress condition of the type developed in the concrete at the contact zone between the rebar and the concrete:

$$f_{cc,i} = c_i f_{c,i}, \qquad c_i \geq 1 \tag{10.4}$$

where c expresses the enhancement factor for the concrete strength and f_c is the uniaxial compression strength. Index i equals 1 or 2 and refers to the material on the two sides of the interface. The stress distributions locally in the concrete at the rebar are assumed to be uniform, see Figure 10.3. In the undeformed state, i.e. the starting point of the model, the distances l_1 and l_2 can be calculated from vertical force equilibrium and moment equilibrium. The results are given in Equation (10.5) and (10.6):

$$l_1 = \sqrt{\frac{2}{3}}\frac{d}{\sqrt{1 + \frac{f_{cc,1}}{f_{cc,2}}}}\sqrt{\frac{f_y}{f_{cc,1}}} \tag{10.5}$$

$$l_2 = \sqrt{\frac{2}{3}}\frac{d}{\sqrt{1 + \frac{f_{cc,2}}{f_{cc,1}}}}\sqrt{\frac{f_y}{f_{cc,2}}} \tag{10.6}$$

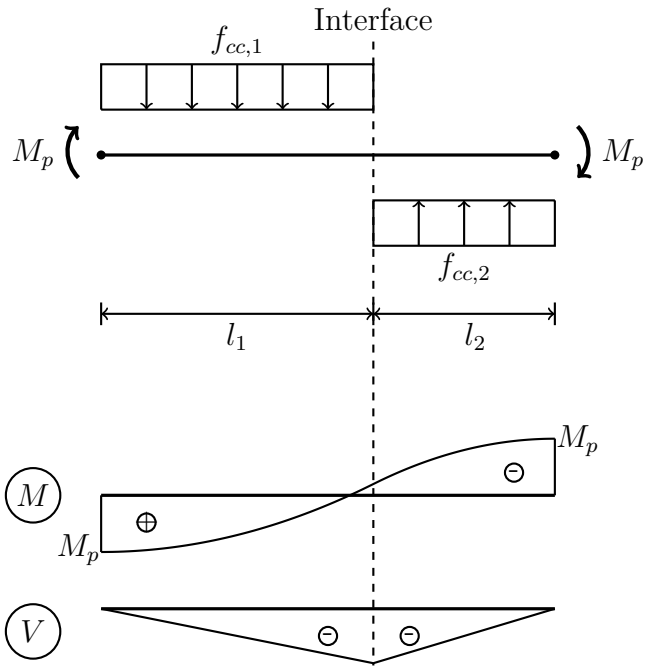

Figure 10.3: *Position of plastic hinges and distribution of contact pressure at initiation of pure dowel action, illustration from Paper IV*

where d is the diameter of the rebar and f_y is the yield strength of the rebar. It should be noted that to fulfill moment equilibrium, the moment in the rebar at the position of the interface is not zero, when the strengths of the two materials are different, see moment diagram in Figure 10.3. Hence, to maintain equilibrium, when $f_{cc,1} \neq f_{cc,2}$ and when the external action corresponds to pure shear, tension must develop in the rebar, which eventually leads to a distribution of so-called clamping stresses in the interface. The tension force in combination with the clamping stresses will then be able to outbalance the (small) bending moment in the rebar at the interface cross section. Therefore, the assumption of uniformly distributed contact pressure is not able to fulfill all equilibrium requirements at $u = 0$ (i.e. initiation of pure dowel action), when $f_{cc,1} \neq f_{cc,2}$. This is, however, acceptable since the assumption of uniformly distributed concrete stresses primarily was motivated by the aim of obtaining a simple estimate of the position of the plastic hinges. In reality, the rebar will probably experience a combination of tension and bending, already in the elastic range. When having the same material on both sides of the interface, i.e. $f_{cc,1} = f_{cc,2}$, Equations (10.5) and (10.6) are identical with the expression obtained by Rasmussen (1963).

At this point, the mechanism has been established and the positions of the plastic hinges have been estimated. It should here be mentioned, that the positions of the plastic hinges are assumed to be fixed as the joint is

exposed to shear displacements. The rates of the plastic deformations in the plastic hinges can be calculated by:

$$\dot{\theta} = \frac{d\theta}{dt} = \frac{d\theta}{du}\frac{du}{dt} = \frac{l_1 + l_2}{(l_1 + l_2)^2 + u^2} \tag{10.7}$$

$$\dot{\Delta} = \frac{d\Delta}{dt} = \frac{d\Delta}{du}\frac{du}{dt} = \frac{u}{2\sqrt{(l_1 + l_2)^2 + u^2}} \tag{10.8}$$

Finally, by use of Equations (10.7) and (10.8), the following condensed expression for the kinematical condition of the rebar can be established:

$$\frac{\dot{\Delta}}{\dot{\theta}} = \frac{u}{2}\sqrt{1 + \left(\frac{u}{l_1 + l_2}\right)^2} \tag{10.9}$$

10.1.3 Yield Condition of Rebar

As rigid-plastic material behavior is assumed, plastic deformations in the rebar are only possible, when the entire cross section is stressed to yielding. In case of pure tension, the plastic tensile capacity is N_p. In case of pure bending, the plastic moment capacity is M_p. The plastic sectional capacities for a circular cross section are given by:

$$N_p = \frac{\pi}{4} d^2 f_y \tag{10.10}$$

$$M_p = \frac{1}{6} d^3 f_y \tag{10.11}$$

For combinations of bending and axial tension, plastic deformation may initiate when the yield condition for the rebar is fulfilled, i.e. $f(M, N) = 0$. In previous investigations of dowel action, a number of researchers have recognized that the presence of axial tension reduces the bending capacity of the dowel. These includes e.g. Dulácska (1972), Millard and Johnson (1984), Engström (1990), and Randl and Wicke (2000). Most often, the simple MN-interaction diagram for a rectangular cross section has been used to account for the combination of moment and bending:

$$f(M, N) = \frac{M}{M_p} + \left(\frac{N}{N_p}\right)^2 - 1 = 0 \tag{10.12}$$

This yield condition is easy to implement in analytical calculations, however, it is not the correct yield condition for a circular rebar. The MN-interaction diagram for a circular cross section can be established based on the stress distribution shown in Figure 10.4.

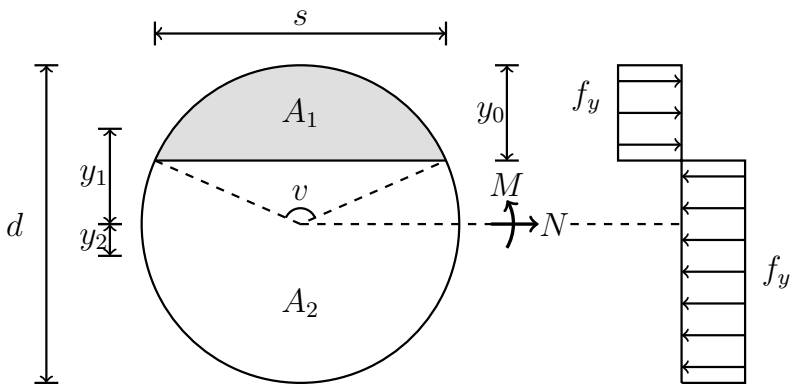

Figure 10.4: *Full plastic stress distribution in a circular cross section when subjected to the sectional forces M and N, illustration from Paper IV*

The MN-interaction diagram can be calculated by requiring static equivalence between the normal stresses and the sectional forces. The result can be formulated as follows:

$$f\left(M,N\right)=\frac{N}{N_p}+\frac{2}{\pi}\left(\arcsin\left(\left(\frac{M}{M_p}\right)^{\frac{1}{3}}\right)-\left(\frac{M}{M_p}\right)^{\frac{1}{3}}\sqrt{1-\left(\frac{M}{M_p}\right)^{\frac{2}{3}}}\right)-1=0 \tag{10.13}$$

Figure 10.5 shows the yield conditions of a rectangular and a circular cross section. It can be seen that the two yield conditions do not deviate significantly. This means that the yield condition for a rectangular cross section (when adopting the plastic capacities of a circular cross section) will be a good approximation for a circular cross section and will only be a slightly conservative choice. As the shapes of the yield conditions are roughly similar, the strain vector, $\bar{\varepsilon}$, will have nearly the same direction, when imposing the normality condition.

In the following, the yield condition of a circular cross section will be adopted, as this constitutes a more precise description of the combinations of sectional forces that leads to yielding in the rebar. In addition, it can be mentioned that calculations show a more smooth transition from a combination of tension and bending to pure catenary action on the load-displacement curve, when Equation (10.13) is used compared to the use of Equation (10.12).

From the yield condition of the rebar, the rates of plastic deformations

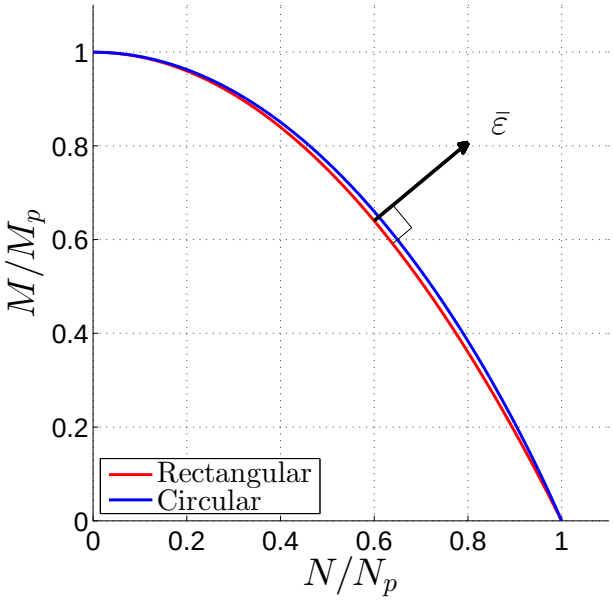

Figure 10.5: *Comparison of yield conditions for a rectangular and a circular cross section, including indication of a strain vector fulfilling the normality condition*

can be calculated by imposing the normality condition of plastic theory:

$$\dot{\theta} = \lambda \frac{\partial f}{\partial M} = \lambda \frac{8}{\pi d^3 f_y} \frac{1}{\sqrt{1 - \left(\frac{M}{M_p}\right)^{2/3}}} \tag{10.14}$$

$$\dot{\Delta} = \lambda \frac{\partial f}{\partial N} = \lambda \frac{4}{\pi d^2 f_y} \tag{10.15}$$

where λ is a positive constant proportional to the displacement velocity. When the ratio between the rates of plastic deformation, $\dot{\Delta}/\dot{\theta}$, is established, λ cancels out. The condensed expression is given by:

$$\frac{\dot{\Delta}}{\dot{\theta}} = \frac{d}{2} \sqrt{1 - \left(\frac{M}{M_p}\right)^{2/3}} \tag{10.16}$$

10.1.4 Sectional Forces in Plastic Hinges

Based on the rates of plastic deformations established above, a link can be made between the shear displacement, u, and the sectional forces of the rebar. It is found that the ratio of plastic deformation rates obtained from the kinematic relations, Equation (10.9), provides information related

to the material strengths and the shear displacements. From the rates of plastic deformations given by the constitutive relations, Equation (10.16), a relation to the sectional forces of the rebar is obtained. Combining these two expressions, Equations (10.9) and (10.16), the sectional forces in the rebar as a function of the shear displacement can be established. The bending moment in the rebar can be calculated by:

$$\frac{M\left(u\right)}{M_p} = \left(1 - \left(\frac{u}{d}\right)^2 \left(1 + \left(\frac{u}{l_1 + l_2}\right)^2\right)\right)^{3/2} \not< 0 \tag{10.17}$$

It can be seen that for zero shear displacement, $u = 0$, the bending moment, $M\left(u\right)$, equals the plastic bending moment, M_p, and the load transfer mechanism corresponds to pure dowel action (the first-order solution). Using the yield condition for the rebar, Equation (10.13), the tension force in the rebar, $N\left(u\right)$, can be obtained:

$$\frac{N\left(u\right)}{N_p} = 1 - \frac{2}{\pi}\left(\arcsin\left(\left(\frac{M\left(u\right)}{M_p}\right)^{\frac{1}{3}}\right) - \left(\frac{M\left(u\right)}{M_p}\right)^{\frac{1}{3}} \sqrt{1 - \left(\frac{M\left(u\right)}{M_p}\right)^{\frac{2}{3}}}\right) \not> 1 \tag{10.18}$$

According to Equation (10.18), tension develops in the rebar as soon as $u > 0$. At a certain shear displacement, the normal force reaches the tensile capacity, N_p, and the regime of pure catenary action is reached. The displacement at the transition to pure catenary action can be calculated by equating the right hand side of Equation (10.17) with zero.

10.1.5 Displacement Capacity

In plastic theory, the materials are normally assumed to have unlimited deformation capacity. In reality, the capacity is limited and for a second-order model where the load keeps on increasing with increasing deformations, the range of the model should be restricted by accounting for the capacity of the materials. The deformation capacity can be evaluated for concrete and for the reinforcement.

Starting with the concrete, which is the least rigid-plastic material of the two, the material experiences softening after reaching the peak strength. The local pressure in the concrete reduces, when the concrete experiences too large compressive strains. The displacement, u, may become so large that the concrete near the joint interface spalls off which leaves a zone to be stress free. With increased shear displacement, this zone will expand

from the position of the interface and into the concrete blocks. Due to the assumed material properties, redistribution of the contact pressure will take place as u increases. In addition to this, the redistribution of stresses must take place in such a way that equilibrium can be maintained, when catenary action starts to develop in the rebar. In the modeling, the effect of softening (and spalling of concrete) will indirectly be taken into account by introducing effective lengths, $l_{1,\text{ef}}$ and $l_{2,\text{ef}}$, over which the contact pressures, $f_{cc,1}$ and $f_{cc,2}$, are assumed to act uniformly, see Figure 10.6.

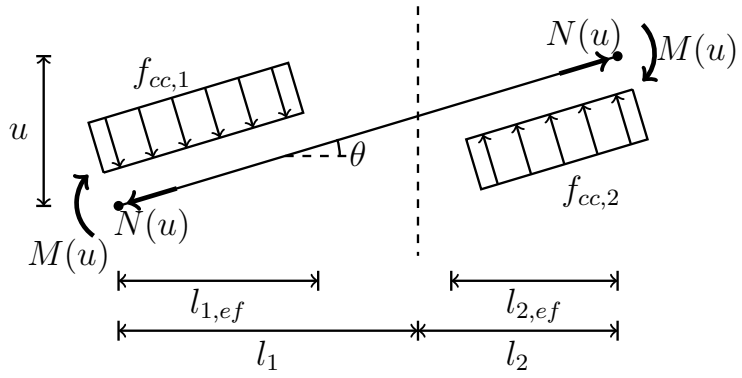

Figure 10.6: *Distribution of contact pressures at combined dowel action and catenary action, illustration from Paper IV*

This may be interpreted as an assumption of rigid-plastic behavior with finite deformation capacity, although there is actually no real information about the deformation capacity of the concrete, when it is subjected to contact pressures by the dowel. The following relationship between u and the effective lengths, $l_{1,\text{ef}}$ and $l_{2,\text{ef}}$, can be established from equilibrium considerations in the deformed state:

$$l_{i,\text{ef}} = l_i \left(1 - \sqrt{1 - \frac{M\left(u\right)}{M_p + \left(\frac{u}{2}\right)^2 d \frac{f_{cc,1} f_{cc,2}}{f_{cc,1} + f_{cc,2}}}} \right) \not< 0 \tag{10.19}$$

It appears that the effective lengths are identical to the initial lengths, l_1 and l_2, when $u = 0$. Furthermore, when u has reached a value that makes $M\left(u\right) = 0$ the effective lengths reduce to zero. It can be interpreted as a situation, where the rebar will no longer experience contact pressures between the two hinges, but instead acts as a tie.

Regarding the reinforcing steel, the deformation capacity is also limited, even though the assumption of rigid-plastic material behavior fits much better for the reinforcing steel than for concrete. When exposed to tension, the

elongation of the rebar is uniformly distributed over the length. At a certain point, concentrated local strains develop, also referred to as necking. Shortly after, failure by rupture will initiate. The ability to carry tension will remain until rupture of the rebar and the local deformations in the necking zone will be relatively large.

The deformation capacity of the rebar can be implemented in the model as a maximum elongation, $\Delta_{\max}$, that can be allowed in the plastic hinges. To facilitate this, the elongation capacity in the necking region of a rebar must be studied. In Figure 10.7(a), four examples of experimentally obtained stress-elongation relationships are presented. Figure 10.7(b) shows the strains in the rebar and the position of the necking region. The measurements were possible by use of DIC. This detailed information cannot be obtained from the standard methods for measuring the nominal maximum strain in rebars. In the case of dowel and catenary action, the plastic hinges can be interpreted as the necking zone of a rebar exposed to tension as plastic strains accumulate in the hinges.

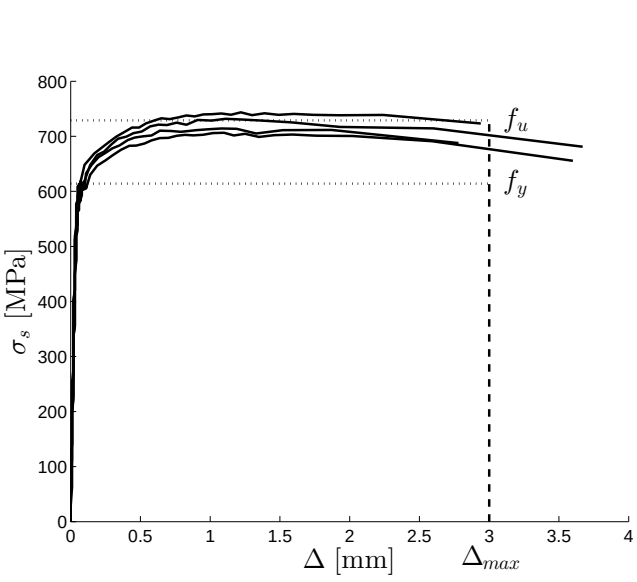

(a) Stress-elongation relation

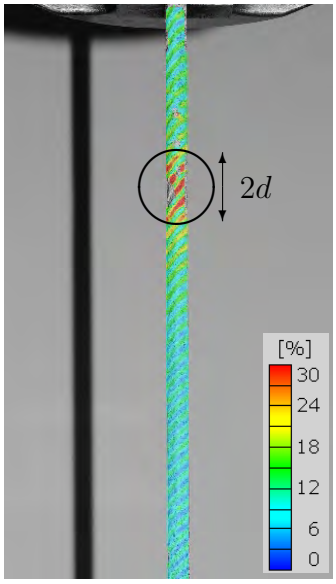

(b) Aramis results at necking (major principal strain)

Figure 10.7: *Local stress-elongation relationship for rebars and indication of the measurement length spanning the zone where necking occurs, figures from Paper IV*

10.1.6 Load Displacement Relationship

Based on the obtained results, it is now possible to determine the load-displacement response of a perfectly smooth two-sided dowel joint by use of the work equation. For this purpose, a stationary situation with displacement, u, and load, $P(u)$, is used as the starting point from which an increment of displacement, δu, is considered. The external work, W_E, is given by:

$$W_E = P(u)\,\delta u \tag{10.20}$$

The internal work, W_I, has contributions from the energy dissipated in the plastic hinges during deformation as well as the energy absorbed, when the concrete crushes at the rebar. As the strengths and properties of the two materials on each side of the interface may be different, the contributions from the two sides are included separately. The internal work can be calculated by:

$$\begin{aligned} W_I = f_{cc,1} l_{1,\mathrm{ef}} d \left(\frac{1}{2} \frac{l_{1,\mathrm{ef}}}{l_1} \delta u_1 \right) + f_{cc,2} l_{2,\mathrm{ef}} d \left(\frac{1}{2} \frac{l_{2,\mathrm{ef}}}{l_2} \delta u_2 \right) \\ +2N(u)\,\delta\Delta + 2M(u)\,\delta\theta \end{aligned} \tag{10.21}$$

The incremental displacement and deformation quantities, δu_1, δu_2, $\delta\Delta$, and $\delta\theta$, can be expressed in terms of δu through the following relationships (where $\delta t = \delta u$):

$$\delta\theta = \dot{\theta}\delta u \tag{10.22}$$

$$\delta\Delta = \dot{\Delta}\delta u \tag{10.23}$$

$$\delta u_1 = \frac{l_1}{l_1 + l_2}\delta u \tag{10.24}$$

$$\delta u_2 = \frac{l_2}{l_1 + l_2}\delta u \tag{10.25}$$

By setting up the work equation, an expression for the shear load, P, as a function of the shear displacement, u, can be derived. The result is given in Equation (10.26):

$$P_{\mathrm{s}}(u) = \begin{cases} \dfrac{1}{2} f_{cc,1} d \dfrac{l_{1,\mathrm{ef}}^2}{l_1 + l_2} + \dfrac{1}{2} f_{cc,2} d \dfrac{l_{2,\mathrm{ef}}^2}{l_1 + l_2} + 2N(u)\,\dot{\Delta} + 2M(u)\,\dot{\theta} & \text{(10.26a)} \\ 2N_p\dot{\Delta} & \text{(10.26b)} \end{cases}$$

The two parts of the equation reflect the two regimes of the load transfer mechanism. Equation (10.26a) is valid for $N(u) < N_p$, i.e. a combination of dowel and catenary action and Equation (10.26b) is valid for $N(u) = N_p$, where the capacity stems from catenary action (i.e. pure tension in the rebar). For $u = 0$, the capacity stems solely from dowel action.

10.1.7 Inclusion of Friction

Equation (10.26) is established for the case of a perfectly smooth interface, where there is no resistance from friction. In reality, a casting joint is never frictionless. From Equation (10.18), it was found that tension develops in the rebar, when $u > 0$. The tension force causes compressive normal stresses to develop in the interface (so-called clamping stresses). From simple shear-friction considerations, the resistance stemming from friction can be estimated by Equation (10.27), assuming a coefficient of friction, μ, which is independent of the shear displacement:

$$P_{\mathrm{f}}(u) = \mu N(u) \cos\theta \tag{10.27}$$

The value of μ must reflect the properties of the interface. In the literature, several suggestions have been made for the coefficient of friction to be applied in different situations. Birkeland and Birkeland (1966) suggested $\mu = 1.7$ for monolithic concrete and $\mu = 0.8 - 1.0$ for ordinary construction joints. These values reflect calculation models where all the shear capacity stems from friction without consideration of dowel action (bending in the dowel). Other suggestions have been made for a combination of actions. Engström (1990) introduced a model, where friction is combined with dowel action using a coefficient of friction of $\mu = 0.3-0.6$ for a concrete-to-concrete interface. Randl and Wicke (2000) also considered a combination of tension and bending in the rebar with interface friction using $\mu = 0.5$ for smooth interfaces. However, the mentioned works did not provide a link between the shear displacement and the sectional forces in the rebar. When this link is established, the coefficient of friction should reflect the properties of the interface alone. This is the same property that was sought in Paper III, where $\mu = 0.75$ was used for the smooth (and untreated) joints. For tests with greased interfaces, $\mu = 0.3$ was adopted in Paper IV.

10.1.8 Load-displacement Response

The total load-displacement response, including the combination of dowel and catenary action as well as friction in the interface can be obtained by addition of Equations (10.26) and (10.27):

$$P_{\mathrm{total}}(u) = P_{\mathrm{s}}(u) + P_{\mathrm{f}}(u) \tag{10.28}$$

An example of model results is given in Figure 10.8, see Paper IV for details. The results clearly show the two displacement regimes (transition indicated by a plus sign), where the first phase is governed by a combination of bending and tension in the rebar and the late phase is governed by catenary

action in the rebar. The inclusion of friction raises the load-displacement response as the tension force in the rebar increases. It is also found that the contribution from friction does not influence the first-order solution at $u = 0$. In the following, a few comparisons with the experimental results presented in Paper IV will be repeated and in addition, a comparison to the results of a shear connection test on a specimen without shear keys will be given.

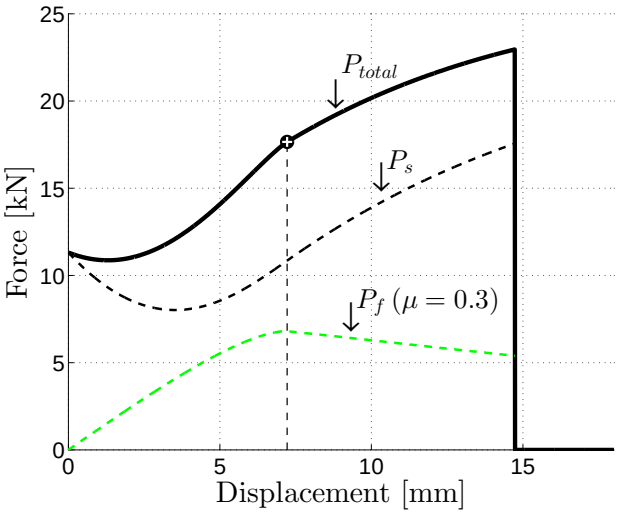

Figure 10.8: *Load-displacement relation for a rebar crossing a casting joint loaded in shear, illustration from Paper IV*

10.2 Comparison of Model with Test Results

When the model is compared to test results, only a few model parameters have to be determined, namely the coefficient of friction and the enhancement factors for the concrete materials. For the smooth and greased interface, $\mu = 0.3$ is adopted. Regarding the enhancement factors, c_i, Rasmussen (1963) calibrated his model with test results and found values in the range of $3.7 - 5.4$ for concrete. In case of a two-sided dowel joint, the c-factors can also be calibrated with tests, however, it requires tests, where the same material is used on both sides of the interface. The calibration with test results should be performed at the onset of plastic deformations, e.g. when the first-order solution is reached, as the model response at $u = 0$ is independent of the contribution from friction, see e.g. Figure 10.8.

In Paper IV, reasonable agreement between tests and the model was

found when a value of $c = 5$ was used for concrete (also suggested by Vintzeleou and Tassios (1986)) and $c = 4$ was used for mortar. It is argued to use a smaller enhancement factor in the case of mortar, as mortar normally has a relatively more brittle compression failure compared to concrete. An estimate of the local enhancement factor cannot be obtained from the triaxial tests presented in Chapter 3. However, it was evident from the triaxial tests that the increase in strength for mortar was less than that for concrete, when loaded in triaxial compression. Based on this observation it is justified to adopt a smaller value of c for mortar than for concrete.

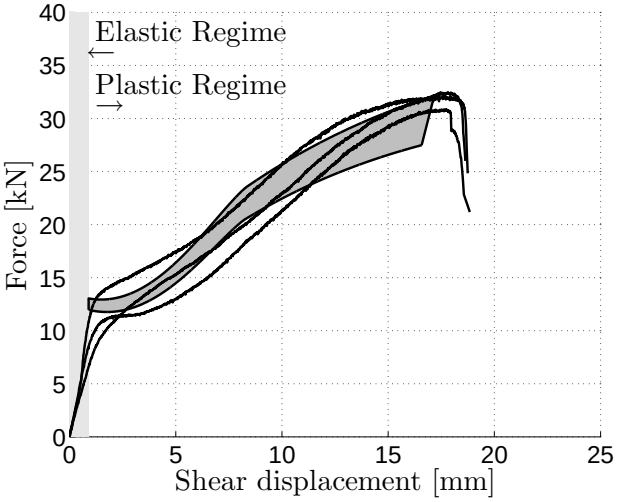

(a) 1 rebar

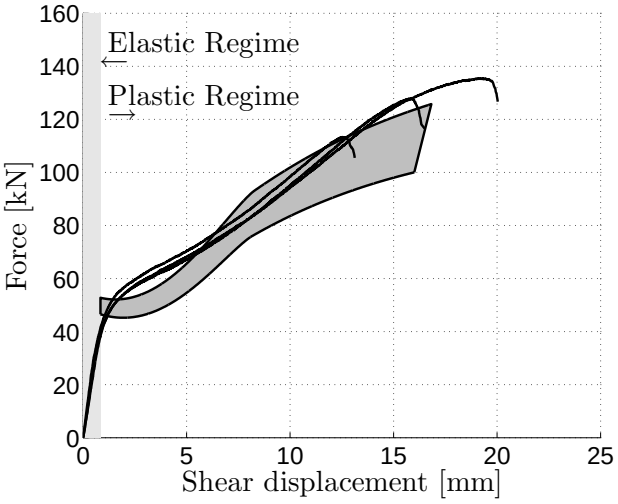

(b) 4 rebars

Figure 10.9: *Comparison of second-order model with test results (a) with one rebar and (b) with four rebars, graphs from Paper IV*

Figure 10.9 shows the comparison between the model and results from tests, where concrete was used on one side of the interface and mortar was cast on the other side (concrete-to-mortar interface). For details on material properties and test setup, see Paper IV. It is seen that reasonable agreement is obtained in the entire displacement regime and that the load level at the onset of plastic deformations is predicted fairly well. In the figure, calculations of an upper and lower limit for the expected test results are included. The lower limit is calculated by use of the yield strength of the reinforcement, f_y, as this strength governs the onset of plastic deformations. However, as can be seen in Figure 10.7(a) the reinforcement hardens already at relatively small strains/elongations. For this reason the calculations based on the ultimate strength of the reinforcement, f_u, is also included as an upper limit. Such reasoning was also made by Mirzaei (2010) and Fernández Ruiz et al. (2013) for the post-punching behavior of flat slabs. In the comparisons, an estimate of the elastic displacements has also been included (represented as a horizontal shift of the plastic load-displacement curve). The calculations were performed based on the analogy of a beam on an elastic foundation with a constant stiffness, see Paper IV for details.

From the comparison, it is also seen that the estimate for the maximum displacement, i.e. $u_{\max}$, which depends on the experimentally determined $\Delta_{\max}$, corresponds fairly well with the maximum displacement obtained in tests. In the calculations $\Delta_{\max} = 3$ mm was used. Paper IV contains additional comparisons between the model and test results. The tests comprised specimens with 1, 2, and 4 rebars crossing the interface. The tests showed that the position of the rebars provided results that were proportional to each other, i.e. there were no interaction between the crushed zones of the

(a) Local crushing of mortar/concrete (b) Rupture of rebar

Figure 10.10: *(a) Local crushing at rebars at the casting joint and (b) deflected shape of ruptured rebar, illustrations from Paper IV*

concrete. This can be seen in Figure 10.10(a), where the concrete clearly was crushed and, to some extent, had spalled off at the interface. Moreover, Figure 10.10(b) shows an extracted rebar after a test. From these observations, it appears that the model assumptions of concrete crushing and formation of plastic hinges in the rebar are fair assumptions.

As a general remark, it should be noted that a higher compressive strength of the materials leads to a higher load at the transition to the non-linear behavior, i.e. at full dowel action. However, a higher compressive strength also leads to a decrease in displacement capacity. Therefore, a lower compressive strength of the concrete/mortar is beneficial for catenary action, because this requires plastic deformation over a longer length of the rebar and at the same time makes it easier for the rebar to cut its way through the concrete/mortar.

10.2.1 Comparison to Test Results for Shear Connections without Indentations

In Chapter 6, results of tests on shear connections without shear keys were presented, see Figure 6.8. The specimens were reinforced transversely by loop connections with the new design in a '1-on-2' configuration. The developed second-order model can be compared to these test results, as the displacements primarily consisted of sliding along the interfaces without a noticeable dilatation. As the reinforcement degree was smaller in one side of the connection, the displacements were primarily concentrated in this interface. However, it was observed that the displacements were not limited to the interface with the smallest amount of reinforcement. Figure 10.11 shows results of a DIC analysis of Specimen S4. It can be seen that strains are also localized in the interface with the largest amount of reinforcement. To establish test results that are comparable with the displacements assumed in the model, the displacements (measured in the longitudinal direction of the shear connection) over the interface with the smallest amount of re-

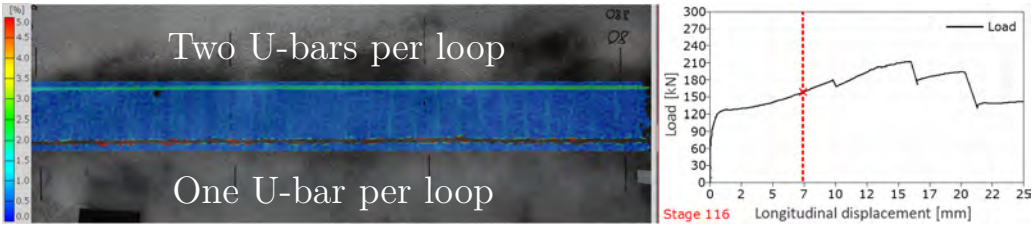

Figure 10.11: *Major principal strain during test and representation of shear displacement in the weak side of the connection, Specimen S4*

inforcement have been isolated (see right hand side of Figure 10.11). It appears that the difference to the response curve, where the displacements are measured over the entire width of the connection (see Figure 6.8), is not great. At the time of rupture of the first rebar ($u \approx 15$ mm), the difference amounts to approximately 3.5 mm. When comparing the DIC measured displacements to the second-order model, the same parameters as adopted in Paper IV can be used. The interface/joint had a precast concrete element on one side ($c_1 = 5$) and an in-situ cast mortar on the other side ($c_2 = 4$). In addition, the interface was greased before casting the connection grout ($\mu = 0.3$). The connection grout was tested to a compressive strength of $f_{c,2} = 43.0$ MPa. Unfortunately, the compressive strength of the precast element was not tested in the experimental campaign. Therefore, the strength has been estimated, and a value of $f_{c,1} = 50$ MPa was used in the calculations. The comparison between the extracted load-displacement relationship of the weakest side of the shear connection, where 8 rebars crossed the casting joint, and the model, can be seen in Figure 10.12(a).

The model underestimates the load carrying capacity at the onset of plastic deformations (i.e. the first-order solution). However, the development after transition to pure catenary action is captured surprisingly well, including the estimate of the displacement capacity, $u_{\max}$, ($\Delta_{\max} = 3$ mm was adopted in the calculations). In Figure 10.12(b), the DIC measured transverse displacements across the interface are presented. For correlation between the measured displacements, some characteristic points have been indicated in the figures. On an overall level, it can be concluded that the assumption of pure shear displacement is a relatively good model assumption in this particular case (only a maximum of 0.3 mm transverse displacement compared to longitudinal displacements of 10 mm at the same instance). However, it is found that as the in-elastic displacement regime is entered, the shear displacement is accompanied by an increase in transverse displacement. The transverse displacements would be far more pronounced in the case of keyed shear connections, when shear displacements are imposed after failure of the shear keys.

Although the model does not agree with the test results in all aspects, the model furnishes a simple tool for robustness assessment. In this relation, the underestimation seen at small shear displacements in Figure 10.12 is not decisive in a robustness consideration, as the main concern is the amount of dissipated energy, i.e. the area under the curve. In this respect, the model seems to be able to provide a reasonable estimate of the available plastic energy.

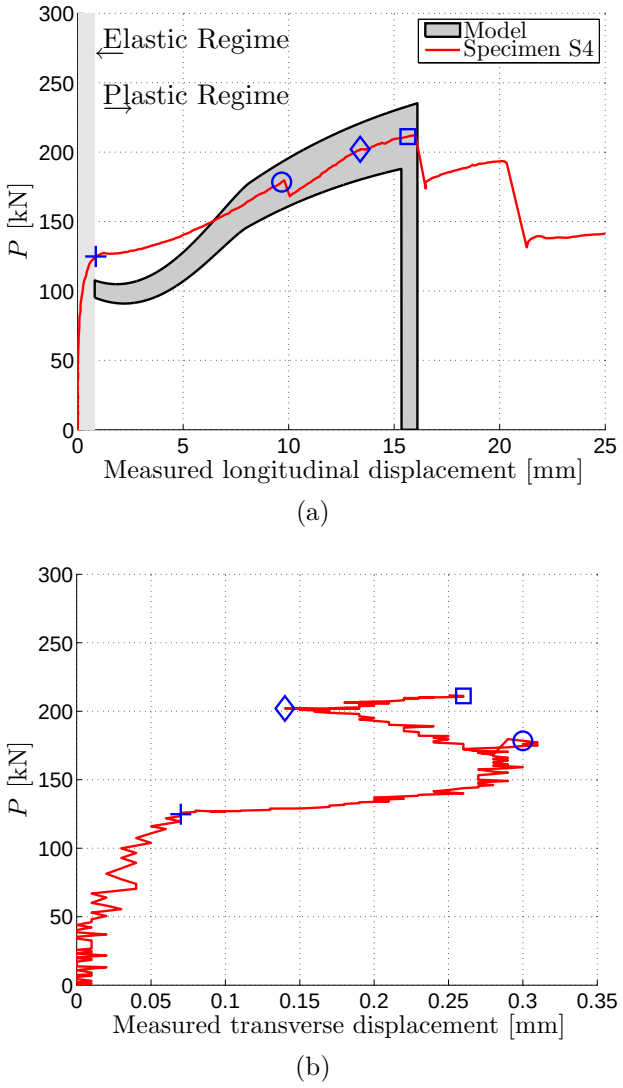

Figure 10.12: *(a) Comparison of second-order model with test results obtained from DIC and (b) DIC measured transverse displacements, Specimen S4*

10.3 Considerations for Model Extensions

As mentioned above, the model cannot directly be used to predict the load-displacement relationship of keyed shear connections. This is because the model assumes displacements parallel to the interface, whereas the presence of shear keys in the interface entails that large shear displacements will be associated with transverse displacements. Examples of transverse displacements were given in Figures 4.10 and 6.10, which showed that the

magnitude of transverse displacements cannot be neglected in the modeling. It would be possible in future works to extend the model to account for dilatation. In this relation, it should be noted that the failure mode of the shear keys (local key corner crushing versus complete key cut off) influences the load-displacement relationship. This is e.g. seen in Figure 10.1(a), where the failure of Specimen P10 was characterized by local key corner crushing, whereas Specimen P11 suffered complete key cut off.

The starting point (first-order solution) of the current model assumes pure dowel action (pure bending in rebar). However, in the first-order solution for the capacity of a keyed connection, the reinforcement is assumed to be stressed to tensile yielding. The transition from the failure of the shear keys to new equilibrium conditions after failure of the shear keys must be considered. The tests showed that the failure of the shear keys may lead to a brittle drop in load (see e.g. Figure 6.9) before equilibrium is reestablished and an increase in load can be facilitated. The problem is here to establish the level of tension in the rebar, N_0, at the new equilibrium state. In addition, the yield condition has to be established for the sectional forces in the rebar under these new conditions. The simplest way to extend the current model to cover this case is to replace the MN-diagram with a ΔMΔN-diagram describing the possible combinations of tension and bending in a plastic hinge, when N_0 is subtracted. With this reduced interaction diagram and the assumption of the associated flow rule, the sectional forces in the dowel can be established as a function of the shear displacement in a similar way as shown above.

Once the starting point is fixed, the nature of the displacement field must be considered, i.e. dilatation must be accounted for in the model. Such a mechanism is depicted in Figure 10.13, where the displacement, v, can be described by the components u and t related by the angle ω. From this mechanism, the kinematic relations of the problem can be established as in the current model. The angle of the displacement will be dependent on the roughness of the failure surface and most likely, the direction of the displacements will change with increased shear displacement. When the mechanism includes dilatation, the rate of the plastic elongation, $\dot{\Delta}$, in the hinges will be larger than in the current model and as a result, the displacement capacity, $u_{\max}$, of the joint will be smaller. However, the load carrying capacity will be greater as tension is introduced earlier and the transition to catenary action, which constitutes the regime where the highest capacity is calculated, takes place at a smaller shear displacement.

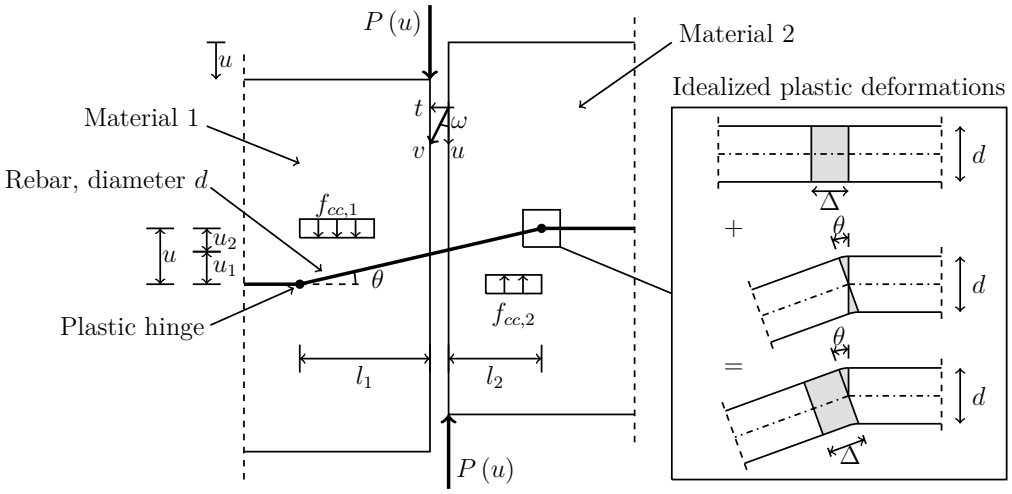

Figure 10.13: *Mechanism including dilatation in a casting joint*

10.4 Concluding Remarks

In this chapter, the second-order plasticity model developed in Paper IV for assessment of dowel and catenary action in rebars crossing a shear joint has been described. The model provides an estimate of the in-elastic load-displacement relationship for smooth joints exposed to large shear displacements. The model has, in addition to the comparisons with test results presented in Paper IV, been compared to DIC results of a '1-on-2' shear connection with a smooth and greased interface without shear keys. The comparison was performed using the same model parameters as established in Paper IV and a satisfactory agreement was found. The findings of the chapter are summarized as follows:

- ⋆ The kinematic relations for the mechanism and the normality condition of plastic theory were combined to establish a unique link between the shear displacements and the sectional forces in the rebar.
- ⋆ The yield condition of a circular cross section was used for the rebar. This constitutes an improvement compared to the use of the yield condition of a rectangular cross section.
- ⋆ The work equation was used to establish an expression for calculation of the load-displacement relationship for the case of a rebar crossing a casting joint (Equation (10.28)). The materials on each side of the interface were allowed to have different strengths.
- ⋆ The calculation of tension in the rebar provided the necessary information to include friction in the interface in a consistent manner.
- ⋆ As an estimate of the displacement capacity of the joint, the local deformation capacity of a rebar was determined from uniaxial tension tests and incorporated in the model as a limit for elongation in the plastic hinges of the rebar.
- ⋆ Despite the simplicity of the model and the relatively small number of required input parameters, the developed second-order plasticity model has the potential for assessment of structural robustness.

11 Conclusions

This thesis presented a study of structural joints in precast concrete structures. The main part of the study focused on keyed shear connections between shear wall panels. The study comprised a large experimental program as well as development of calculation models based on limit analysis. The theoretical work consisted of first-order models for assessment of structural capacity and a second-order plastic model for prediction of the load-displacement relationship of a shear joint.

The overall objectives of the thesis were to develop a solution for structural connections that improves the on-site construction phase, provides structural continuity, and ensures a ductile behavior. The requirements were met by a modification of the conventional design for keyed shear connections. The traditional orientation of the U-bar loops was changed and the transverse reinforcement (lacer bars) took the form of double T-headed rebars. The results of tests on the new configuration were very promising, and in terms of ductility the new design was superior to the conventional design. In the following, the main conclusions for the different topics of the study will be outlined.

Main Research Topics

The thesis treated a number of aspects concerning material properties and basic mechanisms that led to a detailed investigation of the keyed shear connections. The main topics and their findings can be summarized as:

- ⋆ **The material properties of mortar** were studied, as mortar is the primary grout material for connections between precast concrete elements in buildings. From triaxial tests on both concrete and mortar it was found that a smaller maximum grain size of a mixture led to a decrease in triaxial strength. The experimental results showed that for a mortar ($d_{\max} \leq 4$ mm) the internal angle of friction can with reasonable accuracy be taken as $\varphi = 30°$ (corresponding to $k = 3$).

- ⋆ **The failure of a mortar shear key** was studied in push-off tests and the results were analyzed by use of digital image correlation. The results showed that the recorded peak load corresponded to failure of the shear key. Analysis of the displacement field, measured over

the governing crack, showed that the shearing of a mortar key was associated with dilatation.

⋆ **The tensile capacity of loop connections** was experimentally studied. Upper bound plasticity models were developed to estimate the amount of lacer reinforcement required to obtain yielding of the U-bars (avoiding the more brittle failure of the grout), when the connection is loaded in tension. The models can be used for concrete as well as mortar and comparison to test results showed reasonable agreement. The comparison revealed the importance of using the correct material parameters for the grout.

⋆ **Tests on shear connections** were performed. The experimental campaign comprised tests on the conventional design and the new design with varying U-bar diameters and key geometries. The tests showed that the first peak load on the load-displacement curve was associated with failure of the shear keys, either as complete key cut off or as key corner crushing. The new design displayed a ductile response, where the ultimate load recorded at large shear displacements could be larger than the first peak load.

⋆ **Upper bound solutions** were developed for prediction of the first peak load recorded in the tests. The developed model accounts for the local failure of the shear keys and the formation of diagonal cracks between opposite placed shear keys. The local failures of the keys were either complete key cut off or crushing of the key corner. Overall good agreement between tests and calculations were obtained, when using an effectiveness factor which in the literature was calibrated with tests of similar problems.

⋆ **Lower bound solutions** were developed as the counterpart to the upper bound solutions. The essentials of the developed model were the possibility to combine struts with different inclinations and the inclusion of friction in the indented interfaces. The solutions constitute improvements to the previous developed single-strut model and better agreement with test results was obtained.

⋆ **The set of the upper and lower bound solutions** provided a range of expected results. It was not possible to obtain the theoretical exact solution, as the assumptions for the models were not completely identical. The comparison of the models emphasized that in practice, the effectiveness factors to be used in the two models should not necessarily be identical. In the upper bound solutions, the ν-factor should account for brittleness effects as well as the model assumptions

in order to address the unsafe nature of upper bound solutions. For practical situations, the upper bound solutions are easier to adopt, however, the solutions should only be used, when the ν-factor can be calibrated with test results. Where experimental results are not available, the lower bound solutions can safely be used for prediction of the structural capacity of the keyed connections.

⋆ **Second-order modeling of dowel and catenary action in rebars** was performed to establish the load-displacement relationship for a rebar crossing a casting joint loaded in pure shear. The kinematical conditions of the two-sided dowel joint and the normality condition of plastic theory were used to establish a unique link between the shear displacement and the sectional forces in the rebar.

The model furnishes a simple tool to estimate the amount of plastic energy available in the joint. Comparison with a test on a shear connection without shear keys provided promising results. However, the model considers only shear displacements parallel to the interface and for this reason, it is not directly applicable for analysis of the load-displacement relationship of keyed shear connections. A few extensions should be incorporated in the current model to make it applicable for keyed shear connections.

In conclusion, the test results on the new design for keyed shear connections were very promising. Regarding ductility, the new design is superior to the conventional design. The developed theoretical models showed an overall satisfying agreement with the test results and it can be concluded that the models furnish a sound theoretical basis for assessment of the ultimate behavior of keyed shear connections. Due to the large load carrying capacity and the ductile behavior that can be obtained by the new design, the connection type has potential for use in high rises and other heavily loaded structures build by the precast method.

Bibliography

Abdul-Wahab, H. M. S. and Sarsam, S. Y. H. (1991). Prediction of Ultimate Shear Strength of Vertical Joints in Large Panel Structures. *ACI Structural Journal*, 88(2):204–213.

Abrams, D. A. (1919). *Design of Concrete Mixtures*. Bulletin No. 1, Structural Materials Research Laboratory, Lewis Institute, Chicago.

Bakhoum, M. M. (1991). *Shear Behavior and Design of Joints in Precast Concrete Segmental Bridges*. PhD thesis, Department of Civil Engineering, Massachusetts Institute of Technology.

Balmer, G. (1952). A General Analytic Solution for Mohr's Envelope. *Proceedings ASTM*, 52:1260–1271.

Belenkiy, L. M. (2007). Upper-Bound Solutions for Rigid-Plastic Beams and Plates of Large Deflections by Variation Principles. *Journal of Engineering Mechanics*, 133(1):98–105.

Birkeland, P. W. and Birkeland, H. W. (1966). Connections in Precast Concrete Construction. *Journal of the American Concrete Institute*, 63(3):345–368.

Bongers, J. P. W. and Rutten, H. S. (1998). Concrete in multiaxial compression - a multilevel analysis. *Heron*, 43(3):159–180.

Bræstrup, M. W. (1980). Dome Effect in RC Slabs: Rigid-Plastic Analysis. *Journal of the Structural Division - ASCE*, 106(6):1237–1253.

Calladine, C. R. (1968). Simple Ideas in the Large-Deflection Plastic Theory of Plates and Slabs. In Heyman, J. and Leckie, F. A., editors, *International Conference on the Applications of Plastic Theory in Engineering Design*, pages 93–127, Cambridge, UK.

CEN (2004). *EN 1992-1-1 Eurocode 2: Design of Concrete Structures - Part 1-1: General Rules and Rules for Buildings*. European Committee for Standardization, Brussels, 3rd edition.

Chakrabarti, S. C., Nayak, G. C., and Paul, D. K. (1988). Shear Characteristics of Cast-in-Place Vertical Joints in Story-High Precast Wall Assembly. *ACI Structural Journal*, 85(1):30–45.

Chen, W.-F. (2007). *Plasticity in Reinforced Concrete*. J. Ross Publishing, Fort Lauderdale.

Cholewicki, A. (1971). Loadbearing Capacity and Deformability of Vertical Joints in Structural Walls of Large Panel Buildings. *Building Science*, 6(4):163–184.

Christoffersen, J. (1997). *Ultimate Capacity of Joints in Precast Large Panel Concrete Buildings, Series R No 25*. PhD thesis, Department of Structural Engineering and Materials, Technical University of Denmark, Lyngby.

Coulomb, C. A. (1776). Essai sur une application des règles de maximis & minimis à quelques problèmes de statique, relatifs à l'Architecture (English: Note on an application of the rules of maximum and minimum to some statical problems, relevant to architecture, Heyman (1997)). *Mémoires de Mathèmatique & de Physique, présentés à l'Academie Royale des Sciences*, 7:343–382.

Dahl, K. K. B. (1992a). *A Constitutive Model for Normal and High Strength Concrete, Series R No 287*. PhD thesis, Department of Structural Engineering, Technical University of Denmark, Lyngby.

Dahl, K. K. B. (1992b). *A Failure Criterion for normal and High Strength Concrete, Series R No 286*. PhD thesis, Department of Structural Engineering, Technical University of Denmark, Lyngby.

Dahl, K. K. B. (1992c). *The Calibration and Use of a Triaxial Cell, Series R No 285*. PhD thesis, Department of Structural Engineering, Technical University of Denmark, Lyngby.

Dahl, K. K. B. (2014). Bella Sky Hotel - taking precast concrete to the limit. *Structural Concrete*, 15(4):441–447.

Drucker, D. C. (1950). Some Implications of Work Hardening and Ideal Plasticity. *Quarterly of Applied Mathematics*, 7(4):411–418.

Drucker, D. C. and Prager, W. (1952). Soil Mechanics and Plastic Analysis or Limit Design. *Quarterly of Applied Mathematics*, 10(2):157–165.

Drucker, D. C., Prager, W., and Greenberg, H. J. (1952). Extended Limit Design Theorems for Continuous Media. *Quarterly of Applied Mathematics*, 9(4):381–389.

Dulácska, H. (1972). Dowel Action of Reinforcement Crossing Cracks in Concrete. *ACI Journal*, 69(12):754–757.

Engström, B. (1990). Combined Effects of Dowel Action and Friction in Bolted Connections. *Nordic Concrete Research*, 9:14–33.

Eriksson, A. (1978). *Structural behaviour of vertical joints in large panel buildings*. PhD thesis, Division of Structural Design, Chalmers University of Technology, Göteborg.

Fauchart, J. and Cortini, P. (1972). *Étude expérimentale de joints horizonraux entre panneaux préfabriqués pour murs de batiments*. Annales de L'institut Technique du Batiment et Des Travaux Publics, Paris.

Fernández Ruiz, M., Mirzaei, Y., and Muttoni, A. (2013). Post-Punching Behavior of Flat Slabs. *ACI Structural Journal*, 110(5):801–812.

fib (2008). *Bulletin 43: Structural Connections for Precast Concrete Buildings*. fédération international du béton, Lausanne, Switzerland.

fib (2013). *fib Model Code for Concrete Structures 2010*. Wilhelm Ernst & Sohn, Berlin, Germany.

fib (2014). *Bulletin 74: Planning and Design Handbook on Precast Building Structures*. fédération international du béton, Lausanne, Switzerland.

Friberg, B. F. (1938). Design of Dowels in Transverse Joints of Concrete Pavements. *American Society of Civil Engineers*, 64(9):1809–1828.

Gvozdev, A. (1960). The determination of the value of the collapse load for statically indeterminate systems undergoing plastic deformation. *International Journal of Mechanical Sciences*, 1(4):322–335.

Halasz, R. and Tantow, G. (1966). Schubfestigkeit der Vertikalfugen im Grosstafelbau. In *Berichte aus der Bauforschung, Heft 39*. Verlag Wilhelm Ernst & Sohn. Berlin.

Hansen, K., Kavyrchine, M., Melhorn, G., Olesen, S. Ø., Pume, D., and Schwing, H. (1976). SBI-report 97: Keyed shear joints. Technical report, Danish Building Research Institute, Copenhagen.

Hansen, T. C. (1995). *Triaxial Tests with Concrete and Cement Paste, Series R No 319*. PhD thesis, Department of Structural Engineering, Technical University of Denmark, Lyngby.

Herfelt, M. A. (2017). *Numerical limit analysis of precast concrete structures - A framework for efficient design and analysis*. PhD thesis, Department of Civil Engineering, Technical University of Denmark, Lyngby.

Herfelt, M. A., Poulsen, P. N., Hoang, L. C., and Jensen, J. F. (2016). Numerical limit analysis of keyed shear joints in concrete structures. *Structural Concrete*, 17(3):481–490.

Hilsdorf, H. K., Lorman, W. R., and Monfore, G. (1973). Triaxial Testing of Nonreinforced Concrete Specimens. *Journal of Testing and Evaluation*, 1(4):330–335.

Hobbs, D. (1971). Strength of Concrete under Combined Stress. *Cement and Concrete Research*, 1(1):41–56.

Imran, I. and Pantazopoulou, S. J. (1996). Experimental Study of Plain Concrete under Triaxial Stress. *ACI Materials Journal*, 93(6):589–601.

Ingerslev, A. (1921). Om en elementær beregningsmetode af krydsarmerede plader (English: On an Elementary Method of Calculation for Two-way Slabs). *Ingeniøren*, 30(69):507–515.

Ingerslev, A. (1923). The Strength of Rectangular Slabs. *The Structural Engineer*, 1(1):3–14.

Issa, M. A. and Abdalla, H. A. (2007). Structural Behavior of Single Key Joints in Precast Concrete Segmental Bridges. *Journal of Bridge Engineering*, 12(3):315–324.

Jensen, B. C. (1975). On the Ultimate Load of Vertical, Keyed Shear Joints in Large Panel Buildings. Technical report, Institute of Building Design, Report No 108, Technical University of Denmark, Lyngby.

Jensen, B. C. (1976). *Nogle plasticitetsteoretiske beregninger af beton og jernbeton (English: Some Applications of Plastic Analysis to Plain and Reinforced Concrete)*. Report no 111, Institute of Building Design, Technical University of Denmark, Lyngby.

Johansen, K. W. (1931). Beregning af krydsarmerede jernbetonpladers brudmoment (English: Calculation of the Rupture Moment of Two-way Slabs). *Proceedings of the Danish Society for Structural Science and Engineering*, 3(1):1–18.

Johansen, K. W. (1943). *Brudlinieteorier (English: Yield Line Theory, Cement and Concrete Association, London, 1962)*. Jul. Gjellerups Forlag, Copenhagen.

Johansen, K. W. (1958). Brudbetingelser for sten og beton (English: Failure Criteria of Rock and Concrete). *Proceedings of the Danish Society for Structural Science and Engineering*, 29(2):25–44.

Jørgensen, H. B. (2014). *Strength of Loop Connections between Precast Concrete Elements*. PhD thesis, Department of Technnology and Innovation, University of Southern Denmark, Odense.

Jørgensen, H. B. and Hoang, L. (2015a). Strength of Loop Connections between Precast Bridge Decks Loaded in Combined Tension and Bending. *Structural Engineering International*, 25(1):71–80.

Jørgensen, H. B. and Hoang, L. C. (2013). Tests and limit analysis of loop connections between precast concrete elements loaded in tension. *Engineering Structures*, 52:558–569.

Jørgensen, H. B. and Hoang, L. C. (2015b). Load Carrying Capacity of Keyed Joints Reinforced with High Strength Wire Rope Loops. In *Concrete - Innovation and Design, fib Symposium*, Copenhagen.

Jørgensen, H. B., Hoang, L. C., and Hagsten, L. G. (2017). Strength of precast concrete shear joints reinforced with high-strength wire ropes. *Proceedings of the Institution of Civil Engineers. Structures and Buildings*, 170(3):1–12.

Jørgensen, K. F. (2015). Bella Sky Hotel - exploring the potential in precast concrete design. *Structural Concrete*, 16(4):449–457.

Kaneko, Y., Connor, J. J., Triantafillou, T. C., and Leung, C. K. (1993a). Fracture Mechanics Approach for Failure of Concrete Shear Keys. I: Theory. *Journal of Engineering Mechanics*, 119(4):681–700.

Kaneko, Y., Connor, J. J., Triantafillou, T. C., and Leung, C. K. (1993b). Fracture Mechanics Approach for Failure of Concrete Shear Keys. II: Verification. *Journal of Engineering Mechanics*, 119(4):701–719.

Karihaloo, B. L. (1995). *Fracture Mechanics and Structural Concrete*. Longman Scientific & Technical, Harlow.

Kjærbye, P. and Mork, P. (1998). *Precast Buildings - Design and Implementation of the Precast Method*. CIDB, Singapore.

Kupfer, H., Hilsdorf, H. K., and Rusch, H. (1969). Behavior of Concrete Under Biaxial Stresses. *ACI Journal*, 66(8):656–666.

Leonhardt, F., Walther, R., and Dieterle, H. (1973). *Versuche zur Ermittlung der Tragfähigkeit von Zugschlaufenstößen*. Deutscher Ausschuss für Stahlbeton, Bulletin No. 226, Berlin, Germany.

Malecot, Y., Daudeville, L., Dupray, F., Poinard, C., and Buzaud, E. (2010). Strength and damage of concrete under high triaxial loading. *European Journal of Environmental and Civil Engineering*, 14(6):777–803.

Mattock, A. H. and Hawkins, N. M. (1972). Shear transfer in reinforced concrete - recent research. *PCI Journal*, 17(2):55–75.

Millard, S. G. and Johnson, R. P. (1984). Shear Transfer Across Cracks in Reinforced Concrete due to Aggregate Interlock and to Dowel Action. *Magazine of Concrete Research*, 36(126):9–21.

Mirzaei, Y. (2010). *Post-Punching Behavior of Reinforced Concrete Slabs*. PhD thesis, Á la Faculté Environnement Naturel, Architectural et Construit, École Polytechnique Fédérale de Lausanne, Lausanne.

Mises, R. v. (1928). Mechanik der plastischen Formänderung von Kristallen. *Zeitschrift für Angewandte Mathematik und Mechanik*, 8(3):161–185.

Muttoni, A. (1990). *Die Anwendbarkeit der Plastizitätstheorie in der Bemessung von Stahlbeton*. PhD thesis, Bericht Nr. 176, Institut für Baustatik und Konstruktion, ETH Zürich.

Muttoni, A., Joseph Schwartz, and Bruno Thürlimann (1997). *Design of Concrete Structures with Stress Fields*. Birkhäuser Verlag, Basel, Switzerland.

Nielsen, C. V. (1998). Triaxial Behavior of High-Strength Concrete and Mortar. *ACI Materials Journal*, 95(2):144–151.

Nielsen, M. P. (1969). *Om jernbetonskivers styrke (English: On the strength of reinforced concrete discs)*. Polyteknisk Forlag, Lyngby.

Nielsen, M. P., Bræstrup, M. W., Jensen, B. C., and Bach, F. (1978). *Concrete Plasticity, Beam Shear - Shear in Joints - Punching Shear*. Special Publication, Danish Society for Structural Science and Engineering, Lyngby.

Nielsen, M. P. and Hoang, L. C. (2011). *Limit Analysis and Concrete Plasticity*. CRC Press, Taylor & Francis Group, Boca Raton, 3rd edition.

Nimityongskul, P. and Liu, H. Y. (1980). Vertical Shear Strength of Joints in Prefabricated Loadbearing Walls. *Housing Science*, 4(2):137–157.

Ottosen, N. S. (1977). A Failure Criterion for Concrete. *Journal of the Engineering Mechanics Division*, No. EM4:527–535.

Palaniswamy, R. and Shah, S. P. (1974). Fracture and Stress-Strain Relationship of Concrete under Triaxial Compression. *Journal of the Structural Division - ASCE*, 100(No. ST5):901–916.

Pistoljevic, N. and Nielsen, M. P. (2009). HSTO-metoden. Plasticitetsteori for armerede betonskiver. Anvendelse af homogene spændingstilstande i trekantformede områder. *Proceedings of the Danish Society for Structural Science and Engineering*, 80(2):19–54.

Pommeret, M. (1972). Le comportement sous charges ou déformations répétées alternées des joints verticaux entre panneaux préfabriqués. Technical report, Centre expérimental de recherches et d'études du batiment et des travaux publics, Saint Remy les Chevreuxe.

Randl, N. and Wicke, M. (2000). Schubübertragung zwischen Alt- und Neubeton. *Beton- und Stahlbetonbau*, 95(Heft 8):461–473.

Rasmussen, B. H. (1963). Betonindstøbte tværbelastede boltes og dornes bæreevne (English: Resistance of Embedded Bolts and Dowels Loaded in Shear). *Proceedings of the Danish Society for Structural Science and Engineering*, 34(2):39–55.

Richart, F., Brandtzaeg, A., and Brown, R. L. (1928). A Study of the Failure of Concrete under Combined Compressive Stresses. *University of Illinois Bulletin No. 185*, 26(12):1–104.

Smee, D. J. (1967). The effect of Aggregate Size and Concrete Strength on the Failure of Concrete under Triaxial Compression. *Civil Engineering Transactions, The Institution of Engineers, Australia*, 9(2):339–344.

Sørensen, J. H., Herfelt, M. A., Hoang, L. C., and Muttoni, A. (2018). Test and lower bound modeling of keyed shear connections in RC shear walls. *Engineering Structures*, 155:115–126.

Sørensen, J. H., Hoang, L. C., Olesen, J. F., and Fischer, G. (2017a). Tensile capacity of loop connections grouted with concrete or mortar. *Magazine of Concrete Research*, 69(17):892–904.

Sørensen, J. H., Hoang, L. C., Olesen, J. F., and Fischer, G. (2017b). Test and analysis of a new ductile shear connection design for RC shear walls. *Structural Concrete*, 18(1):189–204.

Sørensen, J. H., Hoang, L. C., Olesen, J. F., and Fischer, G. (2017c). Testing and modeling dowel and catenary action in rebars crossing shear joints in RC. *Engineering Structures*, 145:234–245.

St John, D. A., Poole, A. W., and Sims, I. (1998). *Concrete Petrography - A handbook of investigative techniques*. Arnold, London.

Vintzeleou, E. N. and Tassios, T. P. (1986). Mathematical Models for Dowel Action under Monotonic and Cyclic Conditions. *Magazine of Concrete Research*, 38(134):13–22.

Walker, S. and Bloem, C. L. (1960). Effects of Aggregate Size on Properties of Concrete. *Journal of the American Concrete Institute*, 57(9):283–298.

Walraven, J. C. and Reinhardt, H. W. (1981). Theory and Experiments on the Mechanical Behaviour of Cracks in Plain and Reinforced Concrete Subjected to Shear Loading. *Heron*, 26(1A):1–68.

Willam, K. J. and Warnke, E. P. (1975). Constitutive model for the triaxial behaviour of concrete. *Proceedings, International Association for Bridge and Structural Engineering, Seminar on Concrete Structures Subjected to Triaxial Stresses, Bergamo, Italy*, 19(1):1–30.

Zhang, J.-P. (1997a). Diagonal cracking and shear strength of reinforced concrete beams. *Magazine of Concrete Research*, 49(178):55–65.

Zhang, J.-P. (1997b). *Strengh of Cracked Concrete: Part 2 - Micromechanical Modelling of Shear Failure in Cement Paste and in Concrete, Series R No 17*. PhD thesis, Department of Structural Engineering and Materials, Technical University of Denmark, Lyngby.

Zhou, X., Mickleborough, N., and Li, Z. (2005). Shear Strength of Joints in Precast Concrete Segmental Bridges. *ACI Structural Journal*, 102(1):3–11.

Appendix A

Results of Triaxial Tests

A.1 Series C16a

Table A.1: *Mixture C16a,* $d_{max} = 16$ *mm,* $f_c = 30.8$ *MPa*

σ_1 [MPa]	σ_3 [MPa]	$\frac{\sigma_1}{f_c}$ [-]	$\frac{\sigma_3}{f_c}$ [-]
14.28	90.97	0.46	2.95
24.23	123.28	0.79	4.00
33.78	162.60	1.10	5.28
43.63	192.32	1.42	6.24
53.38	219.53	1.73	7.13
63.42	256.61	2.06	8.33
72.48	280.86	2.35	9.12
82.53	302.13	2.68	9.81
92.47	325.87	3.00	10.58

A.2 Series C8a

Table A.2: *Mixture C8a, $d_{max} = 8$ mm, $f_c = 41.2$ MPa*

σ_1 [MPa]	σ_3 [MPa]	$\frac{\sigma_1}{f_c}$ [-]	$\frac{\sigma_3}{f_c}$ [-]
9.45	67.15	0.23	1.63
14.48	88.38	0.35	2.15
19.20	103.80	0.47	2.52
24.32	121.32	0.59	2.94
34.07	153.47	0.83	3.73
42.25	175.15	1.03	4.25
53.57	211.77	1.30	5.14
63.03	224.13	1.53	5.44
72.68	240.68	1.76	5.84
82.62	246.62	2.01	5.99

A.3 Series C4a

Table A.3: *Mixture C4a, $d_{max} = 4$ mm, $f_c = 44.2$ MPa*

σ_1 [MPa]	σ_3 [MPa]	$\frac{\sigma_1}{f_c}$ [-]	$\frac{\sigma_3}{f_c}$ [-]
9.65	66.36	0.22	1.50
14.57	86.42	0.33	1.95
19.40	104.57	0.44	2.37
24.23	117.05	0.55	2.65
34.17	137.48	0.77	3.11
43.23	153.63	0.98	3.48
53.97	164.77	1.22	3.73
72.78	180.68	1.65	4.09
82.33	187.93	1.86	4.25

A.4 Series C2a

Table A.4: *Mixture C2a,* $d_{max} = 2$ *mm,* $f_c = 37.7$ *MPa*

σ_1 [MPa]	σ_3 [MPa]	$\frac{\sigma_1}{f_c}$ [-]	$\frac{\sigma_3}{f_c}$ [-]
7.04	50.77	0.19	1.35
9.60	61.80	0.25	1.64
11.87	69.12	0.31	1.83
14.43	82.08	0.38	2.18
19.30	95.31	0.51	2.53
24.13	112.85	0.64	2.99
34.09	142.15	0.90	3.77
43.45	155.36	1.15	4.12
53.28	164.46	1.41	4.36
62.68	173.90	1.66	4.61
72.78	184.58	1.93	4.90
82.33	189.83	2.18	5.04

A.5 Series C16b

Table A.5: *Mixture C16b, $d_{max} = 16$ mm, $f_c = 29.8$ MPa*

σ_1 [MPa]	σ_3 [MPa]	$\frac{\sigma_1}{f_c}$ [-]	$\frac{\sigma_3}{f_c}$ [-]
5.11	53.06	0.17	1.78
8.05	64.92	0.27	2.18
11.12	79.19	0.37	2.66
15.08	91.72	0.51	3.08
20.14	105.79	0.68	3.55
25.61	116.51	0.86	3.91
30.32	130.36	1.02	4.38
34.98	146.49	1.17	4.92
40.34	160.07	1.35	5.37
45.02	170.23	1.51	5.71
50.10	184.96	1.68	6.07
55.37	201.87	1.86	6.48
60.18	212.36	2.02	6.81
70.05	225.88	2.35	7.51
80.24	257.80	2.69	8.11

A.6 Series C8b

Table A.6: *Mixture C8b,* $d_{max} = 8$ *mm,* $f_c = 26.3$ *MPa*

σ_1 [MPa]	σ_3 [MPa]	$\frac{\sigma_1}{f_c}$ [-]	$\frac{\sigma_3}{f_c}$ [-]
5.13	42.07	0.19	1.60
7.97	55.29	0.30	2.10
10.27	62.35	0.39	2.37
11.00	63.34	0.42	2.41
15.08	75.70	0.57	2.88
20.08	87.50	0.76	3.33
25.12	99.25	0.95	3.77
30.41	110.67	1.16	4.21
35.16	118.02	1.34	4.49
40.12	134.21	1.52	5.10
45.16	139.37	1.72	5.30
50.11	150.01	1.90	5.70
56.51	159.13	2.15	6.05
60.51	169.61	2.30	6.45
70.15	180.93	2.67	6.88

A.7 Series C4b

Table A.7: *Mixture C4b, $d_{max} = 4$ mm, $f_c = 27.4$ MPa*

σ_1 [MPa]	σ_3 [MPa]	$\frac{\sigma_1}{f_c}$ [-]	$\frac{\sigma_3}{f_c}$ [-]
5.18	40.97	0.19	1.50
8.01	52.12	0.29	1.91
10.95	60.95	0.40	2.23
15.03	68.06	0.55	2.49
20.12	85.55	0.74	3.13
25.05	92.78	0.92	3.39
30.11	106.43	1.10	3.89
35.18	112.11	1.29	4.10
39.99	118.03	1.46	4.31
45.23	124.51	1.65	4.55
50.42	134.54	1.84	4.92
54.95	142.07	2.01	5.19
60.10	148.00	2.20	5.41

Appendix B

Summary of Push-off Tests on Shear Connections

Figure B.1 shows the layout of the test specimens, including definition of geometric parameters and the three different loop configurations tested.

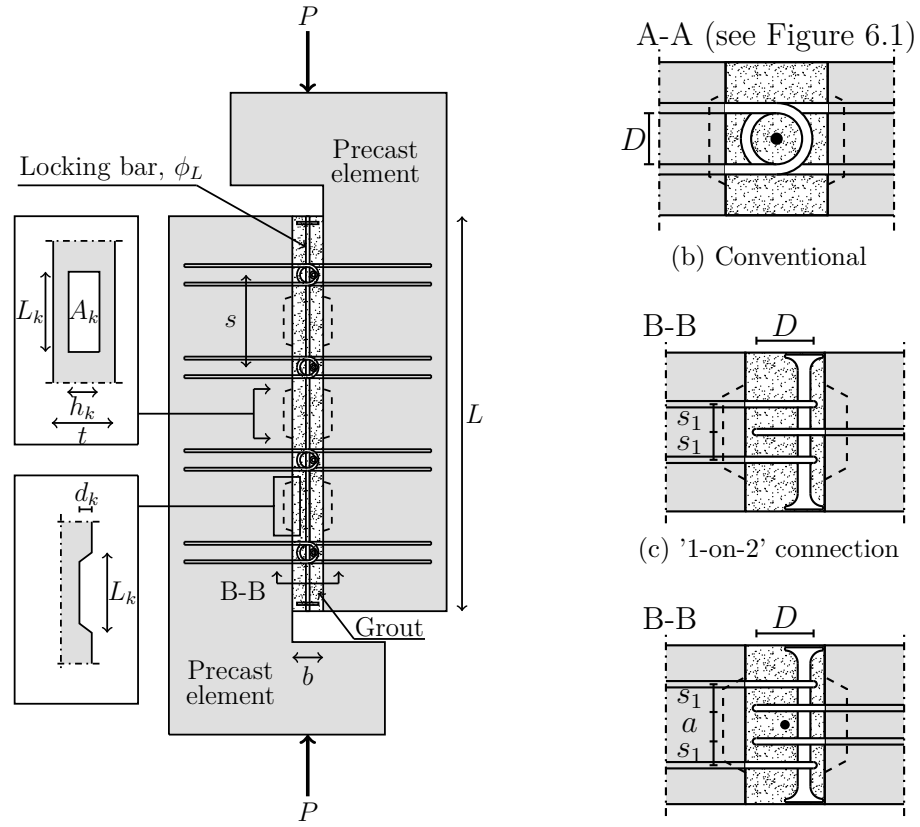

(a) Test setup (loop layout of new design)

(b) Conventional

(c) '1-on-2' connection

(d) '2-on-2' connection

Figure B.1: *General layout of the push-off specimens*

In Figure B.2(a) the test arrangement is schematically presented. The piston applied load to one of the precast elements, and the other precast element was supported by a steel cylinder (pinned support). The setup consisted of a steel frame build with U-profiles on a strong floor.

In Figure B.2(b) a picture of a specimen placed in the test arrangement is shown. In the picture the position of the displacement pins can be seen. Four LVDT's were used to measure the longitudinal and transverse displacements in each end of the connection. In addition, the position of the digital camera used for collection of data for the digital image correlation analysis can be seen.

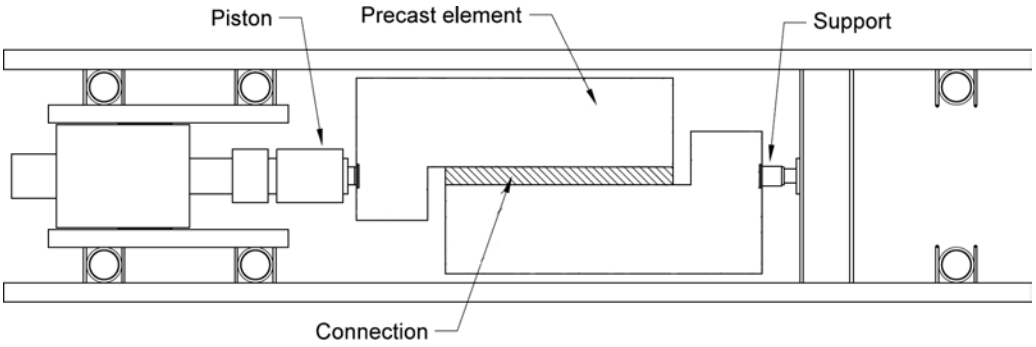

(a) Schematic view of test setup

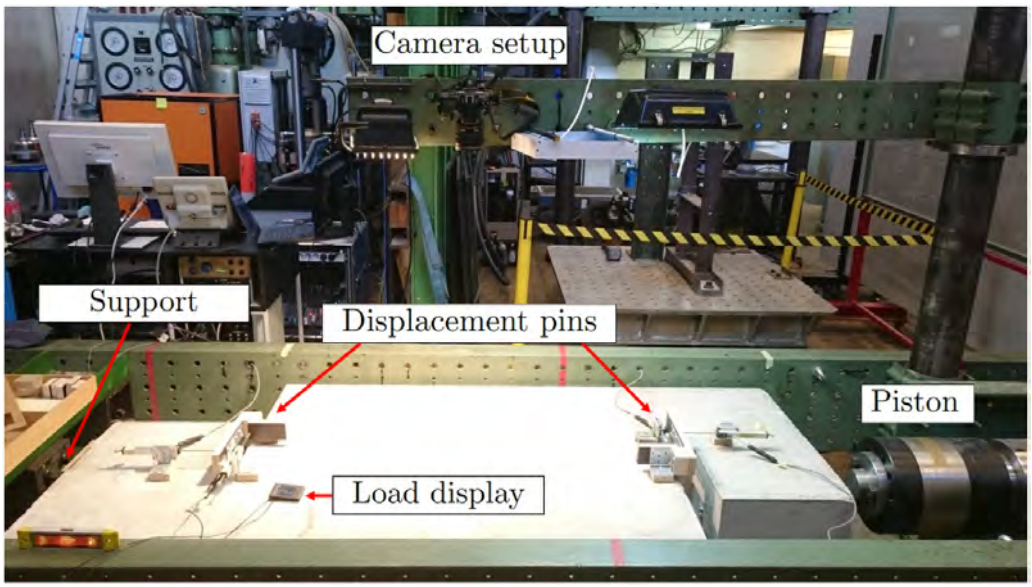

(b) Specimen placed in test setup before test

Figure B.2: *Test setup with (a) schematic view of the test arrangement and (b) picture of a specimen placed in the test setup before testing*

B.1 Reference Specimens

The specimens had a thickness of $t = 150$ mm and contained three shear keys and four U-bars loop connections. The U-bars in the loop connections were placed closely together with the conventional layout, see Figure B.1(b). The U-bars had an internal bend diameter of $D = 60$ mm and the loop connections were placed outside the indentations with a mutual distance of $s = 300$ mm. Specimens R1, R2, and R3 were included in Paper II. The strengths of the reinforcement were:

- 8 mm U-bars: $f_y = 509$ MPa and $f_u = 650$ MPa
- 12 mm locking bar: $f_{yL} = 596$ MPa and $f_{uL} = 697$ MPa

The connections had a width of $b = 80$ mm, a total length of $L = 1280$ mm, a key length of $L_k = 160$ mm, and a key height of $h_k = 85$ mm. The interfaces were greased before casting the joint grout. The tests were conducted in relation to student project *e*.

Table B.1: *Tests on reference specimens, conventional design ('1-on-1' configuration)*

ID	ϕ [mm]	f_c [MPa]	d_k [mm]	Φ [-]	Φ_L [-]	P_{FP} [kN]	P_{U} [kN]
R1	8	34.6	16	0.145	0.048	282.43	-
R2	8	35.7	16	0.140	0.046	303.80	-
R3	8	35.7	16	0.140	0.046	337.42	-
R4	8	44.9	16	0.117	0.037	331.75	-
R5	8	44.9	16	0.117	0.037	300.36	-
R6	8	44.9	16	0.117	0.037	310.02	-

B.2 Pilot Specimens ('1-on-2' configuration)

The specimens had a thickness of $t = 200$ mm and contained three shear keys and four U-bar loop connections. The U-bars in the loop connections were arranged as a '1-on-2' configuration using the new design, see Figure B.1(c). The U-bars had an internal bend diameter of $D = 60$ mm and the distance between the U-bars was $s_1 = 35$ mm. In the longitudinal direction, the loop connections were placed with a mutual distance of $s = 300$ mm. Tests were performed using both 8 and 10 mm U-bars. Specimens P1-P4 were included in Paper II.

The strengths of the reinforcement were:

- 8 mm U-bars: $f_y = 509$ MPa and $f_u = 650$ MPa
- 10 mm U-bars: $f_y = 587$ MPa and $f_u = 678$ MPa
- 12 mm double T-headed lacer bar: $f_{y,Lacer} = 552$ MPa

The connections had a width of $b = 80$ mm, a total length of $L = 1280$ mm, a key length of $L_k = 160$ mm, and a key height of $h_k = 85$ mm. The interfaces were greased before casting the joint grout. The tests were conducted in relation to student project *e*.

Table B.2: *Tests on the new design, '1-on-2' configuration*

ID	ϕ [mm]	f_c [MPa]	d_k [mm]	Φ [-]	Φ_L [-]	P_{FP} [kN]	P_{U} [kN]
S1	8	38.1	-	-	-	134.24	221.72
S2	8	38.1	-	-	-	140.88	234.15
S3	8	43.0	-	-	-	129.96	243.29
S4	8	43.0	-	-	-	127.43	212.06
P1	8	38.1	16	0.132	-	344.24	357.45
P2	8	38.1	16	0.132	-	347.04	368.12
P3	8	42.7	16	0.117	-	342.49	339.97
P4	8	42.7	16	0.117	-	331.42	324.49
P5	8	38.5	30	0.130	-	341.15	324.71
P6	8	38.5	30	0.130	-	358.52	315.93
P7	8	47.7	30	0.105	-	378.09	320.97
P8	8	47.7	30	0.105	-	370.63	300.09
P9	10	42.7	16	0.212	-	398.78	489.66
P10	10	42.7	16	0.212	-	421.68	473.54
P11	10	47.7	30	0.190	-	432.20	454.42
P12	10	46.5	30	0.194	-	439.96	471.37

B.3 New Design - 6 mm U-bars

The specimens had a thickness of $t = 200$ mm and contained three shear keys and four U-bar loop connections. The U-bars in the loop connections had a diameter of 6 mm and were arranged as a '2-on-2' configuration using the new design, see Figure B.1(d). The U-bars had an internal bend diameter of $D = 45$ mm, the distance between the outermost U-bars was $s_1 = 30$ mm and the distance between the innermost U-bars was $a = 40$ mm. In the longitudinal direction, the loop connections were placed with a mutual distance of $s = 300$ mm. Details on the test specimens can also be found in Paper III. The strengths of the reinforcement were:

- 6 mm U-bars: $f_y = 517$ MPa and $f_u = 622$ MPa
- 12 mm locking bar: $f_{yL} = 599$ MPa and $f_{uL} = 689$ MPa
- 12 mm double T-headed lacer bar: $f_{y,Lacer} = 552$ MPa

The connections had a width of $b = 80$ mm, a total length of $L = 1280$ mm, a key length of $L_k = 120$ mm, and a key height of $h_k = 200$ mm (equal to the thickness of the panel). The interfaces were not treated before casting the joint grout. The tests were conducted in relation to student project f.

Table B.3: *Tests on the new design, '2-on-2' configuration with 6 mm U-bars*

ID	ϕ [mm]	f_c [MPa]	d_k [mm]	Φ [-]	Φ_L [-]	P_{FP} [kN]	P_{U} [kN]
D10A	6	44.6	10	0.073	0.084	448.56	417.38
D10B	6	44.6	10	0.073	0.084	448.62	417.24
D12A	6	44.6	12	0.073	0.084	471.74	437.98
D12B	6	44.6	12	0.073	0.084	496.36	452.90
D14A	6	44.6	14	0.073	0.084	510.91	449.09
D14B	6	44.6	14	0.073	0.084	519.16	462.70
D16A	6	44.6	16	0.073	0.084	543.30	421.02
D16B	6	44.6	16	0.073	0.084	541.57	452.24
D18A	6	42.0	18	0.077	0.090	540.73	380.72
D18B	6	42.0	18	0.077	0.090	537.50	412.51
D20A	6	42.0	20	0.077	0.090	526.62	431.17
D20B	6	42.0	20	0.077	0.090	517.03	398.51

B.4 New Design - 8 mm U-bars

The specimens had a thickness of $t = 200$ mm and contained three shear keys and four U-bar loop connections. The U-bars in the loop connections had a diameter of 8 mm and were arranged as a '2-on-2' configuration using the new design, see Figure B.1(d). The U-bars had an internal bend diameter of $D = 60$ mm, the distance between the outermost U-bars was $s_1 = 30$ mm and the distance between the innermost U-bars was $a = 42$ mm. In the longitudinal direction, the loop connections were placed with a mutual distance of $s = 300$ mm. Details on the test specimens can also be found in Paper II. The strength parameters of the reinforcement were:

- 8 mm U-bars: $f_y = 487$ MPa and $f_u = 569$ MPa
- 12 mm locking bar: $f_{yL} = 584$ MPa and $f_{uL} = 689$ MPa
- 16 mm double T-headed lacer bar: $f_{y,Lacer} = 563$ MPa

The connections had a width of $b = 100$ mm and a total length of $L = 1280$ mm. The interfaces were not treated before casting the joint grout.

Table B.4 contains a test series where the key length was varied. The key height was $h_k = 100$ mm and the key depth was $d_k = 28$ mm. The tests were conducted in relation to student project *c*.

Table B.4: *Tests on the new design, '2-on-2' configuration with 8 mm U-bars and with a varying key length*

ID	ϕ [mm]	f_c [MPa]	L_k [mm]	Φ [-]	Φ_L [-]	P_{FP} [kN]	P_{U} [kN]
I1	8	31.2	120	0.349	0.059	379.02	441.21
I2	8	34.2	120	0.318	0.054	416.59	472.92
II1	8	31.2	140	0.299	0.050	366.40	463.79
II2	8	34.2	140	0.273	0.046	414.46	462.48
III1	8	31.2	160	0.262	0.044	393.04	494.70
III2	8	34.2	160	0.239	0.040	473.52	514.87
IV1	8	31.2	180	0.232	0.039	439.44	470.89
IV2	8	34.2	180	0.212	0.036	478.17	515.31

Table B.4 contains a test series where the key depth was varied. The key length was $L_k = 140$ mm and the key height was $h_k = 200$ mm (equal to the thickness of the panel). The tests were conducted in relation to student project *d*.

Table B.5: *Tests on the new design, '2-on-2' configuration with 8 mm U-bars and with a varying key depth*

ID	ϕ [mm]	f_c [MPa]	d_k [mm]	Φ [-]	Φ_L [-]	P_{FP} [kN]	P_{U} [kN]
V1	8	31.2	10	0.149	0.025	475.24	488.97
V2	8	34.2	10	0.136	0.023	492.86	535.61
VI1	8	30.6	16	0.152	0.026	527.09	502.55
VI2	8	30.6	16	0.152	0.026	523.82	550.98
VII1	8	30.6	20	0.152	0.026	549.17	451.58
VII2	8	30.6	20	0.152	0.026	524.46	527.85
VIII1	8	30.6	25	0.152	0.026	507.05	528.67
VIII2	8	30.6	25	0.152	0.026	516.97	545.33
IX1	8	30.6	28	0.152	0.026	526.53	534.19
IX2	8	30.6	28	0.152	0.026	527.59	527.07

B.5 New Design - 10 mm U-bars

The specimens had a thickness of $t = 200$ mm and contained three shear keys and four U-bar loop connections. The U-bars in the loop connections had a diameter of 10 mm and were arranged as a '2-on-2' configuration using the new design, see Figure B.1(d). The U-bars had an internal bend diameter of $D = 75$ mm, the distance between the outermost U-bars was $s_1 = 30$ mm and the distance between the innermost U-bars was $a = 40$ mm. In the longitudinal direction, the loop connections were placed with a mutual distance of $s = 320$ mm. The strength parameters of the reinforcement were:

- 10 mm U-bars: $f_y = 494$ MPa and $f_u = 610$ MPa
- 12 mm locking bar: $f_{yL} = 599$ MPa and $f_{uL} = 689$ MPa
- 20 mm double T-headed lacer bar: $f_{y,Lacer} = 564$ MPa

The connections had a width of $b = 120$ mm, a total length of $L = 1340$ mm, a key depth of $d_k = 10$ mm, and a key height of $h_k = 200$ mm. Half the specimens were cast with a mortar (denoted M) and the remaining were cast with concrete (denoted C). The interfaces were not treated before casting the joint grout. The tests were conducted in relation to student project *g*.

Table B.6: *Tests on the new design, '2-on-2' configuration, 10 mm U-bars*

ID	ϕ [mm]	f_c [MPa]	L_k [mm]	Φ [-]	Φ_L [-]	P_{FP} [kN]	P_{U} [kN]
M120A	10	42.0	120	0.205	0.022	654.51	745.23
M120B	10	42.0	120	0.205	0.022	646.88	745.98
M150A	10	43.3	150	0.159	0.017	646.43	757.01
M150B	10	44.6	150	0.155	0.017	669.62	752.28
M180A	10	42.0	180	0.137	0.015	607.25	720.64
M180B	10	42.0	180	0.137	0.015	639.55	748.52
C120A	10	41.8	120	0.206	0.023	605.52	689.11
C120B	10	41.8	120	0.206	0.023	676.15	734.61
C150A	10	41.8	150	0.165	0.018	637.77	736.94
C150B	10	41.8	150	0.165	0.018	658.19	733.13
C180A	10	41.8	180	0.138	0.015	689.76	749.10
C180B	10	41.8	180	0.138	0.015	642.81	686.82

Appendix C

Upper Bound Calculations for Shear Connections

C.1 Reference Specimens

Table C.1: *Test and upper bound results, reference specimens designed with the conventional design*

ID	P_{FP} [kN]	P_{cal} [kN]	$\frac{P_{\mathrm{FP}}}{P_{\mathrm{cal}}}$	ν	Key failure mode Observed/Predicted
R1	282.43	286.20	0.99	0.45	Corner (E)/Corner (C)
R2	303.80	287.78	1.06	0.44	Corner (E)/Corner (C)
R3	337.42	287.78	1.17	0.44	Corner (E)/Corner (C)
R4	331.75	299.90	1.11	0.39	Corner (E)/Corner (C)
R5	300.36	299.90	1.00	0.39	Corner (E)/Corner (C)
R6	310.02	299.90	1.03	0.39	Corner (E)/Corner (C)
Mean			1.06		
Standard deviation			0.07		

C.2 Pilot Specimens ('1-on-2' configuration)

It should be noted that the test results were only compared to the calculations of Mechanisms A, B, and C.

Table C.2: *Test and upper bound results, new design with '1-on-2' loop configuration*

ID	P_{FP} [kN]	P_{cal} [kN]	$\frac{P_{FP}}{P_{cal}}$	ν	Key failure mode Observed/Predicted
P1	344.24	291.12	1.18	0.43	Corner (C)/Corner (C)
P2	347.04	291.12	1.19	0.43	Corner (C)/Corner (C)
P3	342.49	297.16	1.15	0.40	Corner (C)/Corner (C)
P4	331.42	297.16	1.12	0.40	Corner (C)/Corner (C)
P5	341.15	301.06	1.13	0.42	Cut off (B)/Cut off (B)
P6	358.52	301.06	1.19	0.42	Cut off (B)/Cut off (B)
P7	378.09	319.40	1.18	0.38	Cut off (B)/Cut off (B)
P8	370.63	319.40	1.16	0.38	Cut off (B)/Cut off (B)
Mean			1.16		
Standard deviation			0.03		
P9	398.78	406.26	0.98	0.40	Cut off (B)/Cut off (B)
P10	421.68	406.26	1.04	0.40	Cut off (B)/Cut off (B)
P11	432.20	417.27	1.04	0.38	Cut off (B)/Cut off (B)
P12	439.96	414.68	1.06	0.38	Cut off (B)/Cut off (B)
Mean			1.03		
Standard deviation			0.03		

C.3 New Design with '2-on-2' Configuration - 6 mm U-bars

Table C.3: *Test and upper bound results, new design with '2-on-2' loop configuration and 6 mm U-bars*

ID	P_{FP} [kN]	P_{cal} [kN]	$\frac{P_{\mathrm{FP}}}{P_{\mathrm{cal}}}$	ν	Key failure mode Observed/Predicted
D10A	448.56	393.34	1.14	0.44	Corner (E)/Corner (C)
D10B	448.62	393.34	1.14	0.44	Corner (E)/Corner (C)
D12A	471.74	425.08	1.11	0.44	Corner (E)/Corner (C)
D12B	496.36	425.08	1.17	0.44	Corner (E)/Corner (C)
D14A	510.91	450.16	1.13	0.44	Corner (E)/Corner (E)
D14B	519.16	450.16	1.15	0.44	Corner (E)/Corner (E)
D16A	543.30	471.83	1.15	0.44	Cut off (B or D)/Corner (E)
D16B	541.57	471.83	1.15	0.44	Corner (E)/Corner (E)
D18A	540.73	464.55	1.16	0.45	Cut off (B or D)/Cut off (D)
D18B	537.50	464.55	1.16	0.45	Cut off (B or D)/Cut off (D)
D20A	526.62	464.55	1.13	0.45	Cut off (B or D)/Cut off (D)
D20B	517.03	464.55	1.11	0.45	Cut off (B or D)/Cut off (D)
Mean			1.14		
Standard deviation			0.02		

C.4 New Design with '2-on-2' Configuration - 8 mm U-bars

Table C.4: *Test and upper bound results, new design with '2-on-2' loop configuration and 8 mm U-bars*

ID	P_{FP} [kN]	P_{cal} [kN]	$\frac{P_{FP}}{P_{cal}}$	ν	Key failure mode Observed/Predicted
I1	379.02	395.34	0.96	0.52	Cut off (B or D)/Cut off (A)
I2	416.59	403.29	1.03	0.50	Cut off (B or D)/Cut off (A)
II1	366.40	412.67	0.89	0.49	Cut off (B or D)/Cut off (A)
II2	414.46	421.43	0.98	0.47	Cut off (B or D)/Cut off (A)
III1	393.04	427.62	0.92	0.47	Cut off (B or D)/Cut off (D)
III2	473.52	433.99	1.09	0.45	Cut off (B or D)/Cut off (D)
IV1	439.44	438.33	1.00	0.45	Cut off (B or D)/Cut off (D)
IV2	478.17	455.20	1.07	0.43	Cut off (B or D)/Cut off (D)
Mean			0.99		
Standard deviation			0.07		
V1	475.24	500.73	0.95	0.49	Corner (E)/Corner (C)
V2	492.86	508.21	0.97	0.47	Corner (E)/Corner (C)
VI1	527.09	538.21	0.98	0.50	Corner (E)/Cut off (D)
VI2	523.82	538.50	0.97	0.50	Cut off (B or D)/Cut off (D)
VII1	549.17	538.50	1.02	0.50	Cut off (B or D)/Cut off (D)
VII2	524.46	538.50	0.97	0.50	Cut off (B or D)/Cut off (D)
VIII1	507.05	538.50	0.94	0.50	Cut off (B or D)/Cut off (D)
VIII2	516.97	538.50	0.96	0.50	Cut off (B or D)/Cut off (D)
IX1	526.53	538.50	0.98	0.50	Cut off (B or D)/Cut off (D)
IX2	527.59	538.50	0.98	0.50	Cut off (B or D)/Cut off (D)
Mean			0.97		
Standard deviation			0.02		

C.5 New Design with '2-on-2' Configuration - 10 mm U-bars

Table C.5: *Test and upper bound results, new design with '2-on-2' loop configuration and 10 mm U-bars*

ID	P_{FP} [kN]	P_{cal} [kN]	$\frac{P_{FP}}{P_{cal}}$	ν	Key failure mode Observed/Predicted
M120A	654.51	687.92	0.95	0.45	Corner (E)/Cut off (D)
M120B	646.88	687.92	0.94	0.45	Corner (E)/Cut off (D)
M150A	646.43	713.93	0.91	0.41	Corner (E)/Corner (E)
M150B	669.62	716.30	0.93	0.40	Corner (E)/Corner (E)
M180A	607.25	701.43	0.87	0.39	Corner (E)/Corner (E)
M180B	639.55	701.43	0.91	0.39	Corner (E)/Corner (E)
Mean			0.92		
Standard deviation			0.03		
C120A	605.52	800.14	0.76	0.53	Corner (E)/Cut off (D)
C120B	676.15	800.14	0.85	0.53	Corner (E)/Cut off (D)
C150A	637.77	840.36	0.76	0.49	Corner (E)/Cut off (D)
C150B	658.19	840.36	0.78	0.49	Corner (E)/Cut off (D)
C180A	689.76	840.68	0.82	0.46	Corner (E)/Corner (E)
C180B	642.81	840.68	0.76	0.46	Corner (E)/Corner (E)
Mean			0.79		
Standard deviation			0.04		

Appendix D

Lower Bound Calculations for Shear Connections

D.1 Reference Specimens

Table D.1: *Test and lower bound results, reference specimens designed with the conventional design*

ID	P_{FP} [kN]	$P_{\mathrm{cal},1}$ [kN]	$P_{\mathrm{cal},2}$ [kN]	$\frac{P_{\mathrm{FP}}}{P_{\mathrm{cal}}}$	Stress component
R1	282.43	216.88	189.76	1.30	$\sigma_{2,I}$
R2	303.80	221.76	193.70	1.37	$\sigma_{2,I}$
R3	337.42	221.76	193.70	1.52	$\sigma_{2,I}$
R4	331.75	261.08	226.20	1.27	$\sigma_{2,I}$
R5	300.36	261.08	226.20	1.15	$\sigma_{2,I}$
R6	310.02	261.08	226.20	1.19	$\sigma_{2,I}$
Mean				1.30	
Standard deviation				0.13	

D.2 Pilot Specimens ('1-on-2' configuration)

Table D.2: *Test and lower bound results, new design with '1-on-2' loop configuration*

ID	P_{FP} [kN]	$P_{\mathrm{cal},1}$ [kN]	$P_{\mathrm{cal},2}$ [kN]	$\frac{P_{\mathrm{FP}}}{P_{\mathrm{cal}}}$	Stress component
P1	344.24	232.31	202.25	1.48	$\sigma_{2,I}$
P2	347.04	232.31	202.25	1.49	$\sigma_{2,I}$
P3	342.49	252.01	218.49	1.36	$\sigma_{2,I}$
P4	331.42	252.01	218.49	1.31	$\sigma_{2,I}$
P5	341.15	258.75	321.93	1.06	$\sigma_{2,II}$
P6	358.52	258.75	321.93	1.11	$\sigma_{2,II}$
P7	378.09	271.01	375.18	1.01	σ_B
P8	370.63	271.01	375.18	0.99	σ_B
Mean				1.23	
Standard deviation				0.21	
P9	398.78	301.65	270.53	1.32	$\sigma_{A,1}$
P10	421.68	301.65	270.53	1.40	$\sigma_{A,1}$
P11	432.20	391.06	404.99	1.07	$\sigma_{2,II}$
P12	439.96	388.01	393.93	1.12	$\sigma_{2,II}$
Mean				1.23	
Standard deviation				0.16	

D.3 New Design with '2-on-2' Configuration - 6 mm U-bars

Table D.3: *Test and lower bound results, new design with '2-on-2' loop configuration and 6 mm U-bars*

ID	P_{FP} [kN]	$P_{\mathrm{cal,1}}$ [kN]	$P_{\mathrm{cal,2}}$ [kN]	$\frac{P_{\mathrm{FP}}}{P_{\mathrm{cal}}}$	Stress component
D10A	448.56	279.90	372.35	1.20	$\sigma_{2,II}$
D10B	448.62	279.90	372.35	1.20	$\sigma_{2,II}$
D12A	471.74	279.90	413.55	1.14	$\sigma_{2,II}$
D12B	496.36	279.90	413.55	1.20	$\sigma_{2,II}$
D14A	510.91	279.90	453.22	1.13	$\sigma_{2,II}$
D14B	519.16	279.90	453.22	1.15	$\sigma_{2,II}$
D16A	543.30	279.90	491.21	1.11	$\sigma_{2,II}$
D16B	541.57	279.90	491.21	1.10	$\sigma_{2,II}$
D18A	540.73	277.69	487.25	1.11	σ_B
D18B	537.50	277.69	487.25	1.10	σ_B
D20A	526.62	277.69	496.94	1.06	σ_B
D20B	517.03	277.69	496.94	1.04	σ_B
Mean				1.13	
Standard deviation				0.05	

D.4 New Design with '2-on-2' Configuration - 8 mm U-bars

Table D.4: *Test and lower bound results, new design with '2-on-2' loop configuration and 8 mm U-bars*

ID	P_{FP} [kN]	$P_{\mathrm{cal},1}$ [kN]	$P_{\mathrm{cal},2}$ [kN]	$\frac{P_{\mathrm{FP}}}{P_{\mathrm{cal}}}$	Stress component
I1	379.02	241.05	329.60	1.15	σ_B
I2	416.59	250.12	345.90	1.20	σ_B
II1	366.40	290.77	371.53	0.99	σ_B
II2	414.46	300.32	385.73	1.07	σ_B
III1	393.04	337.40	400.94	0.98	σ_B
III2	473.52	347.52	419.16	1.13	σ_B
IV1	439.44	381.45	446.18	0.98	σ_B
IV2	478.17	392.20	468.64	1.02	σ_B
Mean				1.07	
Standard deviation				0.09	
V1	475.24	385.06	341.04	1.23	$\sigma_{A,1}$
V2	492.86	392.01	366.08	1.26	$\sigma_{A,1}$
VI1	527.09	383.57	481.51	1.09	$\sigma_{2,III}$
VI2	523.82	383.57	481.51	1.09	$\sigma_{2,III}$
VII1	549.17	383.57	539.51	1.02	$\sigma_{2,II}$
VII2	524.46	383.57	539.51	0.97	$\sigma_{2,II}$
VIII1	507.05	383.57	584.82	0.87	σ_B
VIII2	516.97	383.57	584.82	0.88	σ_B
IX1	526.53	383.57	599.54	0.88	σ_B
IX2	527.59	383.57	599.54	0.88	σ_B
Mean				1.02	
Standard deviation				0.15	

D.5 New Design with '2-on-2' Configuration - 10 mm U-bars

Table D.5: *Test and lower bound results, new design with '2-on-2' loop configuration and 10 mm U-bars*

ID	P_{FP} [kN]	$P_{\mathrm{cal},1}$ [kN]	$P_{\mathrm{cal},2}$ [kN]	$\frac{P_{\mathrm{FP}}}{P_{\mathrm{cal}}}$	Stress component
M120A	654.51	414.62	404.82	1.58	$\sigma_{A,1}$
M120B	646.88	414.62	404.82	1.56	$\sigma_{A,1}$
M150A	646.43	533.22	470.63	1.21	$\sigma_{A,1}$
M150B	669.62	536.65	481.82	1.25	$\sigma_{A,1}$
M180A	607.25	638.02	535.78	0.95	$\sigma_{A,1}$
M180B	639.55	638.02	535.78	1.00	$\sigma_{A,1}$
Mean				1.26	
Standard deviation				0.27	
C120A	605.52	414.12	403.35	1.46	$\sigma_{A,1}$
C120B	676.15	414.12	403.35	1.63	$\sigma_{A,1}$
C150A	637.77	529.07	457.67	1.21	$\sigma_{A,1}$
C150B	658.19	529.07	457.67	1.24	$\sigma_{A,1}$
C180A	689.76	637.38	533.72	1.08	$\sigma_{A,1}$
C180B	642.81	637.38	533.72	1.01	$\sigma_{A,1}$
Mean				1.27	
Standard deviation				0.24	

Appended Papers

Paper I

"Tensile capacity of loop connections grouted with concrete or mortar"

Jesper H. Sørensen, Linh C. Hoang, John F. Olsen, Gregor Fischer

Published in: *Magazine of Concrete Research (2017), 69(17):892-904*

Magazine of Concrete Research
Volume 69 Issue 17

Tensile capacity of loop connections grouted with concrete or mortar
Sørensen, Hoang, Olesen and Fischer

Magazine of Concrete Research, 2017, **69**(17), 892–904
http://dx.doi.org/10.1680/jmacr.16.00466
Paper 1600466
Received 31/10/2016; revised 18/01/2017; accepted 02/03/2017
Published online ahead of print 06/04/2017
Keywords: joints/precast concrete/testing, structural elements

ice
Institution of Civil Engineers
publishing

Tensile capacity of loop connections grouted with concrete or mortar

Jesper Harrild Sørensen
PhD student, Department of Civil Engineering, Technical University of Denmark, Kongens Lyngby, Denmark

Linh Cao Hoang
Professor, Department of Civil Engineering, Technical University of Denmark, Kongens Lyngby, Denmark

John Forbes Olesen
Associate Professor, Department of Civil Engineering, Technical University of Denmark, Kongens Lyngby, Denmark

Gregor Fischer
Associate Professor, Department of Civil Engineering, Technical University of Denmark, Kongens Lyngby, Denmark

This paper presents a study of grout failure in symmetric U-bar loop connections loaded in tension, with focus on the performance of two grouting materials – concrete and mortar. The study contains an experimental investigation as well as a rigid-plastic modelling of the tensile capacity. The test specimens consisted of symmetric '2-on-2' loop connections transversely reinforced with a double T-headed rebar. The amount of transverse reinforcement was varied, including the limiting cases of specimens with no transverse reinforcement, as well as connections with sufficient transverse reinforcement to allow yielding of the U-bars. The experimental work showed that connections grouted with concrete performed better than the connections grouted with mortar. In the theoretical models, the difference in tested capacity is explained by the difference in the internal angle of friction and in the softening behaviour of concrete as compared with mortar.

Notation

A_c	circular area of U-bar overlap
A_I	area of failure plane in U-bar overlap
A_i	area of failure plane
A_l	area of tensile failure plane
A_s	reinforcement area of U-bars
A_{sL}	reinforcement area of lacer bar
A_t	area of tensile failure plane
a	distance between innermost loops
a/c	ratio between aggregates and cement
b	width of joint
D	internal bend diameter of U-bar
d_{max}	maximum aggregate size
f_c	compression strength of grout
f_{cm}	mean compression strength of grout
f_t	tensile strength of grout
f_u	ultimate strength of reinforcement
f_y	yield strength of reinforcement
f_{yL}	yield strength of lacer reinforcement
H	overlapping length of U-bars
K	factor influencing v
l	relation between f_t and f_c
m	relation between f_t and f_c
N	tensile load on loop connection
N_u	ultimate capacity of loop connection
N_y	yielding capacity of U-bars
N_0	cracking load of loop connection
s	distance between U-bars
$\boldsymbol{u}_a$	displacement vector of segment II_a
$\boldsymbol{u}_b$	displacement vector of segment II_b
u_l	displacement in the l-direction
u_t	displacement in the t-direction
V	shear load
W_E	rate of external work
W_I^C	rate of internal work from concrete
W_I^S	rate of internal work from steel
w/c	ratio between water and cement
α	angle between u and yield line
β	inclination of yield line to vertical
v	effectiveness factor, concrete in compression
v_t	effectiveness factor, concrete in tension
σ_c	concrete stress
Φ_L	reinforcement degree, lacer bar
ϕ	diameter of reinforcement
ϕ_L	diameter of lacer bar
φ	internal angle of friction

Introduction

This paper presents an investigation into the structural behaviour of so-called '2-on-2' loop connections between precast concrete elements loaded in tension. The investigation includes rigid-plastic modelling of the tensile capacity as well as experimental tests.

The paper has been prepared as a self-contained research article on the topic of loop connections loaded in tension. However, there is a strong correlation with the development of construction-friendly and ductile shear joints for connection of precast shear wall elements. A new design of keyed shear wall connections has recently been tested by the authors (Sørensen *et al.*, 2017). The principle of the design is illustrated in Figure 1(a), which shows two precast wall elements with indented interfaces connected by a joint grouted with either concrete or mortar. The significance of the new design is the orientation of the overlapping U-bar loops, which are placed

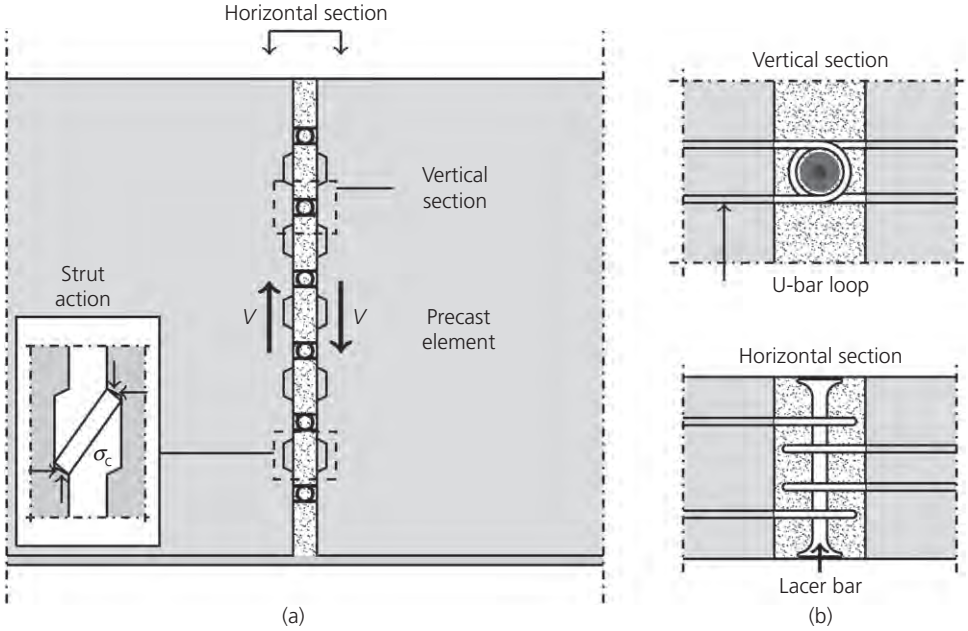

Figure 1. Keyed joint between shear wall elements (see Sørensen *et al*. (2017)) with '2-on-2' symmetrical loop connections

in the same plane as that of the wall elements. This is different from the classical design (fib, 2008; Hansen *et al*., 1974) where the plane of the loops is perpendicular to the plane of the wall elements. As shown in Figure 1(b), each loop connection in the shear joint is reinforced transversely with a double T-headed rebar (in the following, termed a lacer bar), in order to enhance the ability of the overlapping U-bars to transfer tension between the precast elements. As indicated in Figure 1(a), the ability to transfer tension is in fact a prerequisite for the joint to transfer shear by way of interlock action in the keys (the horizontal component of the diagonal compressive struts formed in the grout between opposite keys must be balanced by horizontal tension transfer in the U-bar loops). The test results reported by Sørensen *et al*. (2017) showed that this new design is able to carry larger shear loads and performs in a much more ductile manner than the classical solution, provided that the U-bars are stressed to yielding. Therefore, in order to ensure ductile shear behaviour of the new joint design, it is necessary to develop a method regarding how to detail the layout of the U-bar loop connections, so that the core of grout becomes strong enough to enable tensile yielding of U-bars and prevent premature concrete/mortar failure.

To develop such designs, it is essential to carry out tests on specimens where concrete/mortar failure actually takes place, and to develop models that can estimate the tensile capacity related to failure of the grout materials. It is in this broader context that the present experimental programme and the theoretical study should be viewed. However, the design method is not limited to application in shear walls only. A number of tensile connections in structural concrete can be designed according to the principles presented, the main benefits being the narrow connection zone required and the ability to estimate the capacity of the grout, leading to a ductile design governed by yielding of the reinforcement.

This study focuses on two main design variables: (*a*) the dimension of the transverse reinforcement placed in the loops and (*b*) the composition of the grout material (concrete and mortar). Ideally, concrete should be used in practice; however, for the narrow joints typically found in building structures, mortar can be a more practical and construction-friendly solution. The behaviour of connections grouted with mortar must therefore be studied as well.

Previous investigations on loop connections

Regarding tensile action in loop connections, Gordon (2006) introduced the term symmetric unit to describe a connection where the main reinforcement is placed symmetrically about the longitudinal axis. Gordon tested symmetric '4-on-3' connections as well as non-symmetric connections, and concluded that the non-symmetric specimens tended to experience rotations of the joint concrete and to fail at a load level lower than expected. Therefore, when loop connections are used to transfer tensile action, the symmetry condition should be fulfilled. Leonhardt *et al*. (1973) were the first to publish results of tension tests of symmetric '2-on-2' loop connections (i.e. two U-bars overlapping two other U-bars). In their programme, the overlapping U-bars were placed closely together with no spacing in between. The specimens were cast in one sequence without casting joints, and transverse reinforcement was not

provided. The influence of the overlapping area of the U-bar loops on the failure load was investigated. To obtain yielding of the U-bars, Leonhardt *et al.* (1973) suggested a design where the overlapping concrete area is larger than a circular area with a diameter of 15ϕ. The design proposal included transverse reinforcement placed inside the overlapping area.

Hao (2004) and Ong *et al.* (2006) also tested symmetric designs. Their experimental programme consisted of '2-on-1' designs, and their calculations were based on a strut-and-tie model. However, they concluded that the model was only applicable for similar '2-on-1' designs, as the model was calibrated with these tests only. Jørgensen and Hoang (2013) tested '3-on-2' symmetric specimens to investigate the influence of a number of factors, including the spacing of the overlapping U-bars. They proposed an upper bound plasticity model for the tensile capacity of the connection, and later the solution was extended to include a combination of tension and bending action (Jørgensen and Hoang, 2015).

Regarding requirements for transverse reinforcement in the joint, Gordon (2006) also examined the use of fibre-reinforced concrete as replacement for conventional reinforced concrete. He concluded that the fibre-reinforced material could not replace steel reinforcement as some ductility was lost. Also Araújo *et al.* (2014) tested loop connections with fibre-reinforced concrete as replacement for steel reinforcement; however, they only tested a non-symmetric '1-on-1' connection design.

A comparative study of the tension behaviour of symmetric '2-on-2' loop connections grouted with concrete and with mortar, as presented in the following, has to the best of the authors' knowledge, not been previously published in the literature. A further advance, compared to earlier tension tests on loop connections, is the use of a double T-headed bar as transverse reinforcement. The bar provides increased anchorage (DeVries *et al.*, 1999; Ghali and Youakim, 2005; Thompson *et al.*, 2006), even in cracked concrete (Brantschen *et al.*, 2016), which is required as the joint is rather narrow.

Experimental programme

The experimental programme comprised 32 specimens, each consisting of two precast concrete elements joined by a symmetric '2-on-2' loop connection, see Figure 2. The overlapping area was transversely reinforced with lacer reinforcement in the shape of a double T-headed bar. Three series with different compositions of grouting material were investigated, see Table 1. The connections in series C were grouted with concrete (maximum aggregate size, $d_{max} = 16$ mm) while in series M and T, mortars with $d_{max} = 2$ mm and 4 mm, respectively, were used. Table 2 provides the relative proportions of the concrete and mortar mixtures. It should be noted that the batches of mortar in series M were produced simply by removing the content of the larger aggregates from the concrete recipe of series C, without considering the cement to aggregate ratio. In series C and M, the lacer bar was placed in the centre of the circle formed by the overlapping U-bars, see Figures 2 and 3(a). In series T, as an alternative, the lacer bar was fixed to the looped end of the outermost U-bars, as illustrated in Figure 3(b). The idea behind this was to consider the circular core of mortar inside the connection as a small beam subjected to four-point bending, having the lacer bar as a fully anchored tension reinforcement.

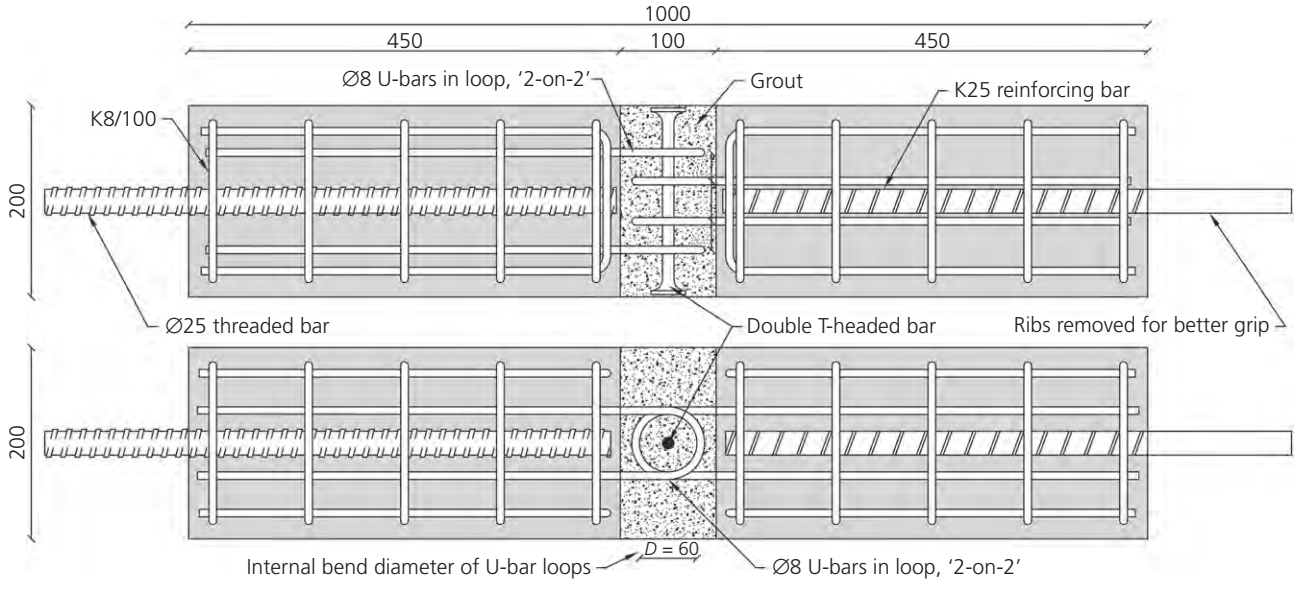

Figure 2. General geometry of test specimen, including reinforcement details (dimensions: mm)

The diameter of the lacer bars ranged from 12 to 20 mm, see Figure 3(c). Some specimens were also tested without a lacer bar. The cross-sectional diameter (8 mm) and the internal bend diameter (60 mm) of the U-bars were kept constant throughout all three series. The yield strength of the U-bars was tested in uniaxial tension to an average of $f_y = 550$ MPa. The average ultimate strength was found to be $f_u = 677$ MPa. Table 3 contains the remaining properties of each specimen. For statistical reasons, three replicates of each connection design were cast. However, some unsuccessful castings had to be omitted because the lacer bars accidentally moved out of position during casting and ended in a position with eccentricity to the axial system line of the specimen. The number (0, 12, 14, 16 and 20) adjoining the series letter (C, M and T) refers to the diameter of the lacer reinforcement, while 'a', 'b' and 'c' denote the replicates.

Table 1. Test series in experimental programme

Series	No. of specimens	Grout material	Max aggregate size, d_{max}: mm
C	13	Concrete	16
M	10	Mortar	2
T	9	Mortar	4

Table 2. Mixture proportions (kg) used in the three series

	Series C	Series M	Series T
Cement	340	340	375
Water	180	180	170
Aggregate 0–2 mm	0	884	0
Aggregate 0–4 mm	884	0	1400
Aggregate 4–8 mm	244	0	0
Aggregate 8–16 mm	738	0	0
Fly ash	0	0	28·5
Plasticiser	0	0	1·0
Water-to-cement ratio, *w/c*	0·53	0·53	0·45
Aggregate-to-cement ratio, *a/c*	5·49	2·60	3·73

Test set-up and testing procedure

The precast elements were designed with a reinforcement bar centrally placed in the axial direction. In one element, ordinary ribbed reinforcement was used, where the ribs on the part protruding from the element were removed for a better grip in the testing machine, see Figure 2. In the other element, a threaded steel rod was used in combination with a specially designed load application device, see Figure 4. The tensile load was applied through a spherical nut.

The tests were performed as quasi-static deformation controlled tests in a servo-controlled hydraulic testing machine with a capacity of 500 kN. The loading rate was 0·5 mm piston movement per minute. The relative displacements across the connection were measured on all four surfaces using linear variable differential transducers (LVDTs). The measured relative axial displacements were thereby related to the behaviour of the grouted connection.

Experimental results and observations

The test results are presented as load–displacement relationships, where the displacement is taken as the average elongation of the connection measured by the LVDTs. The ultimate load, N_u, of the connection is taken as the maximum load observed within the test range of 0–10 mm relative axial displacement. Table 3 contains the recorded N_u for all test specimens.

Figure 5 shows the tested load–displacement curves for the specimens in series C and M. One single specimen in series C14 experienced unloading due to an interruption of hydraulic

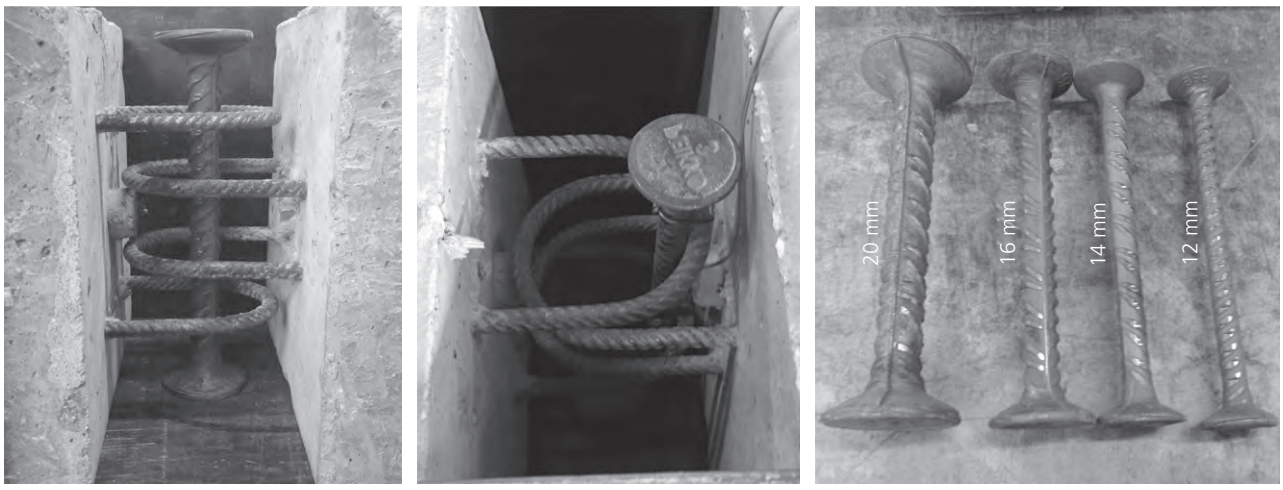

(a) (b) (c)

Figure 3. Positioning of lacer reinforcement before casting of grout (a) and (b) and diameter of lacer bars (c): (a) series C and M; (b) series T; (c) lacer bars

Table 3. Material properties and reinforcement details of test specimens

		Grout			Lacer		
Specimens		Material	f_c: MPa	d_{max}: mm	ϕ_L: mm	f_{yL}: MPa	N_u: kN
C0	a	Concrete	44·1	16	—	—	68·7
	b						62·4
	c						66·8
C12	a	Concrete	44·1	16	12	552	97·6
	b						89·2
	c						95·1
C14	a	Concrete	39·9	16	14	562	108·8
	b						101·1
	c						109·1
C16	a	Concrete	41·3	16	16	563	112·5
	b						103·1
C20	a	Concrete	41·3	16	20	564	129·6
	b						126·7
M0	a	Mortar	36·6	2	—	—	47·7
	b						48·9
	c						43·4
M12	a	Mortar	36·6	2	12	552	76·3
	b						77·9
M14	a	Mortar	39·5	2	14	562	79·3
M16	a	Mortar	37·4	2	16	563	82·3
M20	a	Mortar	37·4	2	20	564	108·6
	b						116·0
	c						96·5
T12	a	Mortar	39·5	4	12	552	73·6
	b						77·6
	c						78·4
T14	a	Mortar	39·5	4	14	562	76·4
	b						79·2
	c						88·0
T16	a	Mortar	39·5	4	16	563	88·2
	b						97·2
	c						103·8

pressure during the test. As the test was resumed, the specimen continued the expected load path of an uninterrupted test. From the plots in Figure 5 it can be clearly seen that connections grouted with concrete in general were able to carry a higher ultimate load than a similar connection (i.e. with the same lacer bar configuration) grouted with mortar. It can also be observed that only the specimens grouted with concrete and reinforced transversely with a 20 mm lacer bar behaved in a significantly ductile manner. For these particular specimens, the ultimate load was governed by yielding of the 8 mm U-bars. The remaining specimens experienced failure of the grout material without yielding of the U-bars.

For specimens without transverse reinforcement (i.e. no lacer bar in series C0 and M0) the load-carrying capacity was governed by cracking of the grout material, and the load–displacement curves displayed significant softening in the post-peak regime. For specimens with transverse reinforcement, on the other hand, cracking of the grout material activated the lacer bar, which enabled further increase of the load and the post-peak softening behaviour was less pronounced than observed for specimens without lacer bars.

The test results revealed that the choice of grout material influenced the behaviour significantly: see, for example, Figure 5. The grout material with larger aggregate content and larger aggregate sizes leads to a stiffer response after crack initiation and a higher ultimate capacity compared to the grouts with smaller aggregates. Furthermore, the concrete grout has a slightly better ability to sustain the load after peak compared to the mortar material.

For both grout materials, the connections were uncracked and behaved elastically at low load levels. At a load level corresponding to the capacity of a connection without lacer bar, a crack became visible on the surface of the connection. The crack typically developed in the axial direction – see Figure 6(a) – and appeared between the innermost U-bars. The appearance of this crack on the surface was, however, not representative for the crack pattern throughout the thickness of the connection, as the cracking behaviour was governed by a complex state of stress between the U-bars. In some tests, the crack parallel to the axial direction was accompanied by inclined cracks on the same surface. The cracks were followed by an opening of the interface between the joint grout and the precast element

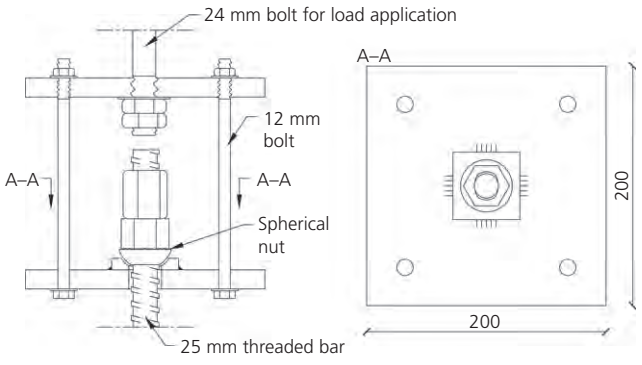

(a)

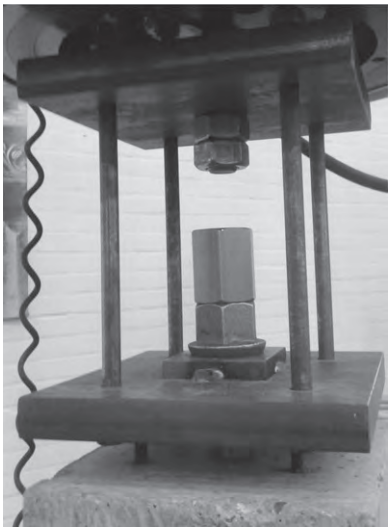

(b)

Figure 4. (a) Geometry of load application device (dimensions: mm) and (b) device with specimen mounted before test initiation

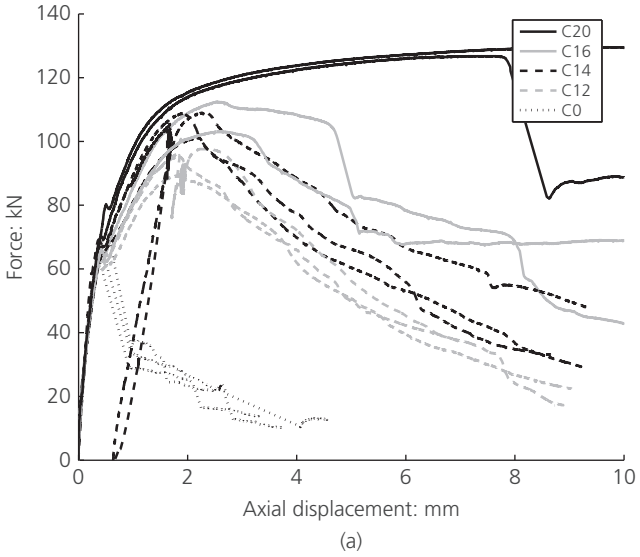

(a)

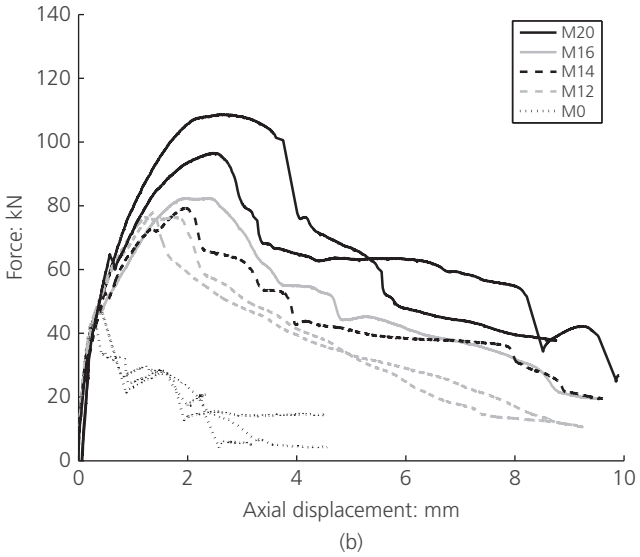

(b)

Figure 5. Tested load–displacement curves: (a) series C (concrete grout); (b) series M (mortar grout)

which contained the innermost U-bars, see Figure 6(b). The opening was greatest at the edges of the surface and smallest at the location of the axial crack in the centre, indicating a slight rotation of the grout cover. For a further increase of displacement into the post-peak region, the grout cover broke off and revealed cracks between the U-bar loops. Figure 7 shows the typical crack pattern inside the grout at the level of the loop reinforcement. Two inclined cracks developed between the tips of the U-bars. These cracks were supplemented by a straight crack between the tips of the innermost U-bars and two cracks originating at the tip of the outermost U-bars. The crack pattern near the heads of the lacer bar indicates that the head has been utilised for anchorage once the lacer reinforcement was activated after cracking of the grout material.

From the test results of series M and T, it was also found that the tensile capacity of the connections did not depend particularly on whether the lacer bar was positioned in the centre of the circular loop, Figure 3(a), or fixed to the looped end of the outermost U-bars, Figure 3(b). It seems more important that the lacer bars are placed correctly in the line of loading. This was indicated by trial tests performed on the above-mentioned unsuccessful castings (specimens with lacer bar positioned with eccentricity to the line of loading), which showed lower capacity.

Failure mechanisms and upper bound solutions

In this section, an upper bound model for prediction of the load-carrying capacity related to the failure in the grout material is developed. For this purpose, the grout materials will be treated as rigid-plastic, modified Coulomb materials, obeying the associated flow rule, and the reinforcement

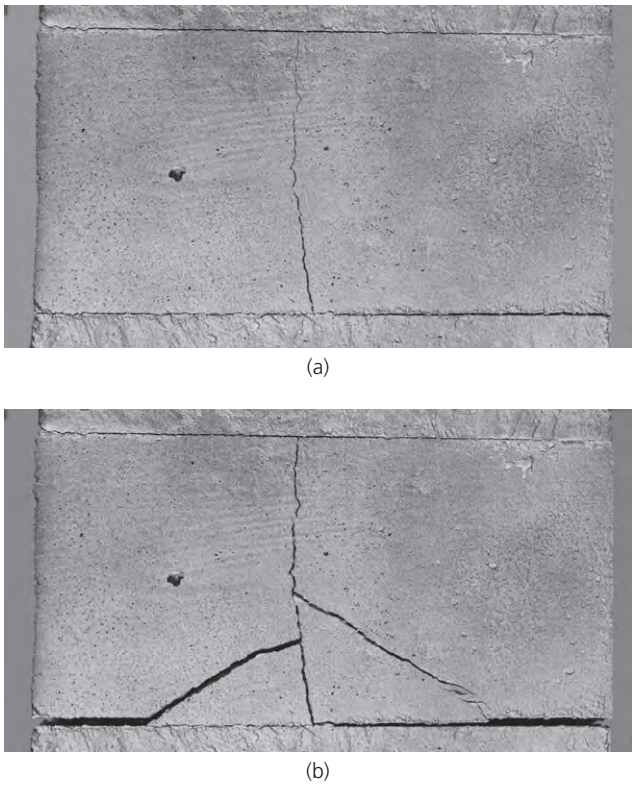

(a)

(b)

Figure 6. Crack patterns on surface of specimen T12a: (a) crack in axial direction; (b) development of inclined cracks on surface

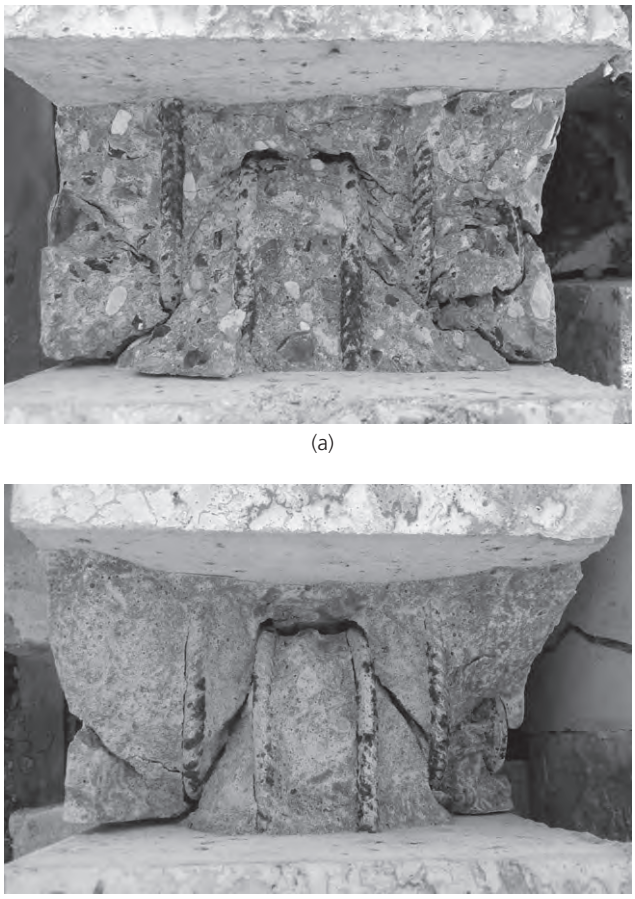

(a)

(b)

Figure 7. Examples of failed specimens after test: (a) concrete grout (b) mortar grout

bars are assumed to be rigid-plastic and only capable of carrying axial loads. A kinematically admissible failure mechanism is shown in Figure 8, where the experimental observations described in the previous section 'Experimental results and observations' are captured in a simplified representation inspired by the work of Jørgensen and Hoang (2013). The failure surfaces formed in the grout material are simplified as plane surfaces, which may be represented by the yield lines indicated in Figure 8(a). The geometries of the actual failure surfaces are three-dimensional as a result of the complex stress state between the loop bars of the connection, see Figure 7. However, the simplifications introduced are necessary in order to develop analytical solutions suitable for practical use.

In rigid-plastic limit analysis of problems in structural concrete, the tensile strength of concrete is usually neglected. This can be justified by the fact that the (rather small) tensile strength of concrete will normally have vanished almost completely when the reinforcement enters the state of yielding. This is a fair assumption for the test specimens with lacer bars, where cracking activates the lacer bars, which eventually reach yielding at the ultimate state. However, for the specimens in series C0 and M0 without lacer reinforcement, the cracking load is also the ultimate load and, for this reason, it is necessary to take the tensile strength into account when modelling the load-carrying capacity in such cases. Therefore, in the following, two solutions are developed. The first one concerns the failure of a connection with lacer reinforcement where the tensile strength of the grout material is neglected. The second solution is developed for connections without lacer reinforcement and therefore includes the tensile strength of concrete/mortar. The second solution can be considered as a lower limit for the tensile capacity of connections containing transverse reinforcement. This will be further discussed in the following.

Upper bound solutions for connections with lacer reinforcement

Figure 8 illustrates a failure mechanism for specimens with lacer reinforcement. The displacement field in the grout is idealised as rigid body motions of the three segments, III, II_a and II_b relative to segment I. The determination of the relative displacements between adjacent segments is inspired by the work of Jørgensen and Hoang (see Jørgensen and Hoang (2013) for an in-depth description), and adjusted to the geometry of the tested '2-on-2' symmetrical connection. As illustrated in Figure 8(b) the relative displacements in each yield line can be determined as follows. Segment II_a is displaced

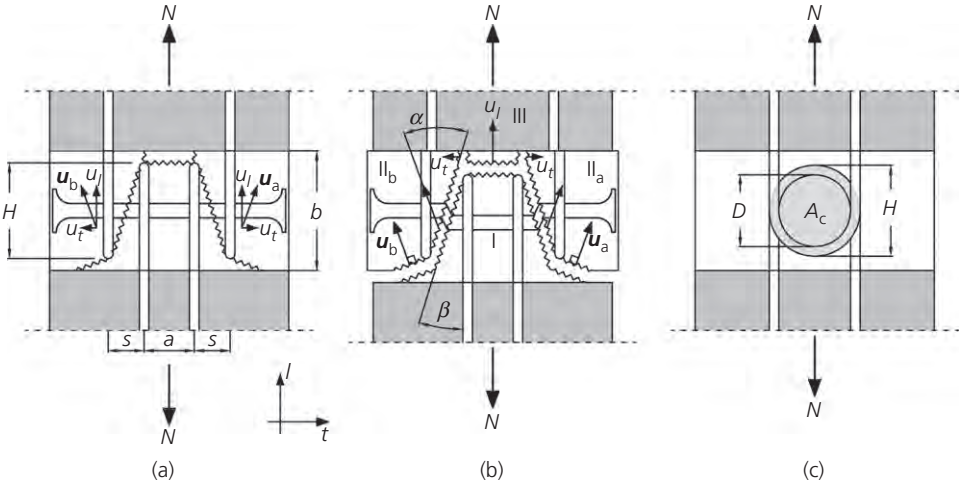

Figure 8. (a) Failure mechanism, (b) relative displacements and (c) overlapping loop area considered for grout failure

with the displacement vector $\boldsymbol{u}_a$ relative to segment I

$$\boldsymbol{u}_a = \begin{pmatrix} u_l \\ u_t \end{pmatrix} \tag{1}$$

where u_l is the component parallel to the longitudinal direction, l, and u_t is the component in the transverse direction, t. The displacement vector, $\boldsymbol{u}_b$, which describes the relative motion of segment II_b relative to segment I is $\boldsymbol{u}_a$ mirrored about the l-axis. This is due to the symmetric conditions and for this reason, $|\boldsymbol{u}| = |\boldsymbol{u}_a| = |\boldsymbol{u}_b|$, can be introduced. Segment III is displaced by u_l relative to segment I. Finally, the two segments II_a and II_b are also moving transversely and relative to segment III by the displacement u_t. The components of the relative displacements are related in the following way

$$u_l = |\boldsymbol{u}| \cos(\alpha - \beta) \tag{2}$$

$$u_t = |\boldsymbol{u}| \sin(\alpha - \beta) \tag{3}$$

where α is the angle between the displacement vector and the inclined yield line running between the tips of the U-bars, and β is the inclination of the yield line to the l-axis

$$\tan\beta = \frac{s}{H} \tag{4}$$

The rate of external work performed by the load, N, is given by

$$W_E = N u_l \tag{5}$$

The rate of internal work consists of contributions from the lacer bar and the grout material. The contribution from the lacer reinforcement (which is stressed to yielding at the two points where it crosses the inclined yield lines) is given by

$$W_I^S = 2A_{sL} f_{yL} u_t \tag{6}$$

A formula for the dissipation in a plane of discontinuity formed in a modified Coulomb material was established by Jensen (1976). When the tensile strength is neglected and the normality condition is fulfilled, the dissipation is found by Nielsen and Hoang (2011)

$$W_I^C = \frac{1}{2} v f_c A_i (1 - \sin\alpha)|\boldsymbol{u}|, \quad \alpha \geq \varphi \tag{7}$$

where A_i is the area of the plane of failure (i.e. length of the yield line times its width) and φ is the internal angle of friction for the grout material. In order to account for the fact that neither concrete nor mortar are perfectly plastic materials, an effectiveness factor, v, is introduced (Nielsen and Hoang, 2011). The effectiveness factor depends on a number of factors such as softening effects and effects of cracking. For a loop connection loaded in tension and grouted with concrete, Jørgensen and Hoang (2013) discussed in depth the choice of effectiveness factor. In the following, a modification of the equation used in Jørgensen and Hoang (2013) is adopted. The modification, which is similar to the findings of Jørgensen (2014) and Jørgensen and Hoang (2015), is introduced to account for the fact that the softening effect in mortar deviates from that of concrete

$$v = \frac{K}{\sqrt{f_c}} \left(1 + \frac{1}{\sqrt{H}}\right) \tag{8}$$

where f_c is given in MPa and H is given in m. Here the factor K depends on the grout material, and H expresses a characteristic length of the sliding failure/yield line, see Figure 8(c).

In order to determine the rate of internal work performed in the grout material, the areas of the respective failure surfaces must be determined. From Figure 8(b) it can be seen that only the two inclined yield lines running between the tips of the U-bars are relevant for this solution, as the remaining yield lines are separation yield lines with zero dissipation (the tensile strength is disregarded). The areas of the inclined yield lines are calculated as

$$9. \quad A_I = \frac{A_c}{\cos\beta} = \frac{\pi}{4}\frac{H^2}{\cos\beta} = \frac{\pi(D+2\phi)^2}{4\cos\beta}$$

where A_c is the circular area delimited by the overlapping U-bars (see Figures 8(b) and 8(c)). It appears that A_I has the shape of an elliptical surface. The adaptation of Equation 9 entails that the grout outside the overlapping U-bars is neglected. This is primarily justified by the fact that the grout cover more or less spalled off during testing, leaving only the grout core inside the loops to carry the tensile load. A similar way of determining the area of the inclined yield lines was suggested by Jørgensen and Hoang (2013).

The solution for the load-carrying capacity in the case of grout failure is influenced by the geometry of the loop connection, the s/H ratio, see Figure 8(a), and the internal angle of friction for the grout material. Owing to the normality condition, the angle of displacement will always be larger than or equal to the internal angle of friction. Furthermore, the angle of displacement cannot be smaller than the inclination of the yield line, β, as an inwards displacement of segment II_a/II_b towards segment III is not possible. The requirements are summarised in Equation 13, which describes the tensile capacity of the loop connection including lacer reinforcement and disregarding the tensile strength of the grout material (α is calculated by Equation 12 and β is calculated by Equation 4).

From Equation 13 it can be seen that the internal angle of friction, φ, is an essential parameter for the tensile capacity of the joint. This parameter is dependent on the properties of the grout material, and especially on the aggregate content and aggregate sizes of the mixture. It should be noted, that the solution presented by Jørgensen and Hoang (2013), with the exception of a factor of 2, can be reproduced by Equation 13 when inserting the internal angle of friction for normal strength concrete, $\tan\varphi = 3/4$.

$$13. \quad \frac{N}{\nu f_c A_c} = \begin{cases} \sqrt{\left(\frac{s}{H}\right)^2 + \frac{4\Phi_L}{\nu}\left(1-\frac{\Phi_L}{\nu}\right)} - \frac{s}{H} & \text{for } \alpha \geq \varphi \text{ and } \varphi \geq \beta \\ \frac{[1+(s/H)^2][(1/\cos\varphi)-\tan\varphi] + 2\Phi_L/\nu[\tan\varphi - (s/H)]}{1+(s/H)\tan\varphi} & \text{for } \alpha < \varphi \text{ and } \varphi > \beta \\ \sqrt{1+\left(\frac{s}{H}\right)^2} - \frac{s}{H} & \text{for } \alpha < \beta \text{ and } \varphi \leq \beta \end{cases}$$

From the work equation, an upper bound solution for the tensile capacity of the connection is found as

$$10. \quad \frac{N}{\nu f_c A_c} = \frac{1-\sin\alpha}{\cos\beta\cos(\alpha-\beta)} + 2\frac{\Phi_L}{\nu}\tan(\alpha-\beta), \quad \alpha \geq \varphi$$

where Φ_L is the mechanical reinforcement degree of the lacer reinforcement, defined as

$$11. \quad \Phi_L = \frac{A_{sL} f_{yL}}{A_c f_c}$$

The optimal upper bound solution is found by minimising Equation 10 with respect to the angle of displacement, α. It can be shown that the optimal angle of displacement is given as

$$12. \quad \alpha = \beta + \arcsin\left[\frac{1-2(\Phi_L/\nu)}{\sqrt{1+(s/H)^2}}\right], \quad \alpha \geq \varphi$$

It can be seen that the tensile capacity according to Equation 13 approaches zero when $\Phi_L \to 0$. Hence, for very small values of Φ_L, it may happen that Equation 13 predicts a capacity that is lower than the capacity calculated for a similar connection without lacer bar, but taking into account the tensile strength of concrete/mortar (see next section). In such a situation, the solution that accounts for the tensile strength should of course be taken as the capacity – and the connection should then be classified as being under-reinforced with respect to transverse reinforcement.

Upper bound solutions for connections without lacer reinforcement

For connections without transverse reinforcement, the capacity depends on the tensile strength of the grout. The dissipation in a concrete/mortar yield line when the tensile strength, f_t, is included, is given by Nielsen and Hoang (2011)

$$14. \quad W_I^C = \frac{1}{2}\nu f_c A_i (l - m\sin\alpha)|\boldsymbol{u}|, \quad \alpha \geq \varphi$$

where the effectiveness factor, v, is still estimated according to Equation 8 and the parameters l and m are given as

$$15. \quad l = 1 - 2\frac{v_t f_t}{v f_c}\frac{\sin\varphi}{1-\sin\varphi}$$

$$16. \quad m = 1 - 2\frac{v_t f_t}{v f_c}\frac{1}{1-\sin\varphi}$$

The tensile strength of the grout may, for example, be estimated by the following formula given by Nielsen and Hoang (2011)

$$17. \quad f_t = 0{\cdot}26 f_{cm}^{2/3}$$

The mean compression strength of the grout, f_{cm}, is in this study taken as the average value found from compression tests on cylinders. In Equations 15 and 16, v_t denotes the effectiveness factor for concrete in tension. This factor is, with inspiration from Nielsen and Hoang (2011), taken as

$$18. \quad v_t = 0{\cdot}6\left(\frac{H}{0{\cdot}1}\right)^{-0{\cdot}3}$$

Again, H is a characteristic dimension, see Figure 9. Considering the failure mechanism in Figure 8, the rate of internal work consists of contributions from five separation yield lines and two sliding yield lines inclined with the angle β to the l-direction. For that particular failure mechanism, the optimal angle of displacement cannot be given explicitly when the tensile strength of the grout is included. However, for the slightly simplified failure mechanism introduced in Figure 9, the solution can be optimised explicitly.

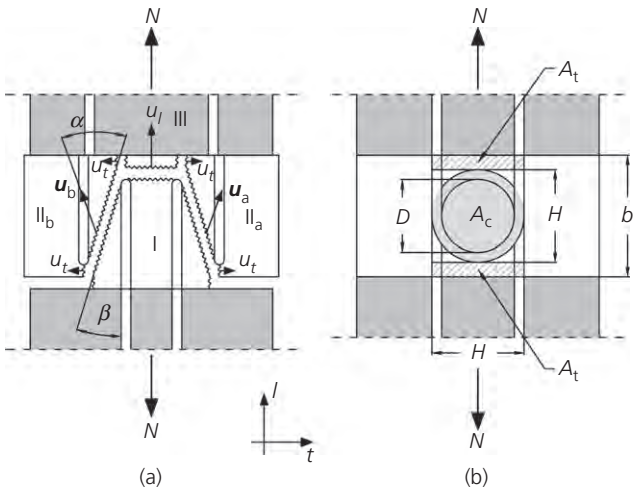

Figure 9. Simplified failure mechanism for connection without lacer bar: (a) relative movements; (b) areas considered for grout failure

This failure mechanism consists of contributions from seven yield lines, namely two inclined sliding yield lines running between the loop bars, two separation yield lines in the l-direction at the tip of the outer loops with an area of A_t, two separation yield lines in the l-direction at the tip of the inner loops with an area of A_t, and one separation yield line in the t-direction between the inner loops with an area of A_l. The areas of the four separation yield lines formed in the axial direction, referring to Figure 9(b), are considered equal. Again the cover is ignored, which constitutes a conservative choice. The areas of the yield lines are estimated as follows

$$19. \quad A_t = \frac{1}{2}H(b-H)$$

$$20. \quad A_l = aH$$

The area of the inclined sliding yield line may also in this case be determined by Equation 9. It should be noted that H appears as a characteristic dimension in all the considered areas. When solving the work equation, using the external work introduced in Equation 5, the internal work in Equation 14 and with the areas given in Equations 9, 19 and 20, the following solution for the tensile capacity, N_0, without lacer reinforcement, is found

$$21. \quad \frac{N_0}{v f_c A_c} = \frac{l - m\sin\alpha}{\cos\beta\cos(\alpha-\beta)} + 4\frac{v_t f_t A_t}{v f_c A_c}\tan(\alpha-\beta) + \frac{v_t f_t A_l}{v f_c A_t}$$

The optimal angle of displacement is found as

$$22. \quad \alpha = \beta + \arcsin\left[\left(\frac{m}{l} - \frac{4}{l}\frac{v_t f_t A_t}{v f_c A_c}\right)\frac{1}{\sqrt{(s/H)^2+1}}\right], \quad \alpha \geq \varphi$$

Again the same restrictions are imposed on the angle of displacement, $\alpha \geq \varphi$ and $\alpha \geq \beta$. It should be noted that the solution is different from that of Jørgensen and Hoang (2015), as more separation yield lines are included in this model.

Tensile capacity of loop connection

The solutions developed above are valid when failure in the grout material is governing. Naturally, these solutions cannot be used if the yield capacity of the U-bars renders a smaller load. Hence, the true tensile capacity of the connection is the minimum of the capacity of the grout material and the yield

capacity of the U-bar loops. As discussed, the capacity calculated by inclusion of the tensile strength of the grout and without any transverse reinforcement constitutes a lower limit for the capacity of the joint. The true shift between the two theoretical solutions, Equations 13 and 21, is governed by a transition phase where the U-bars are yielding and the grout at the same time contributes with a small, residual strength. As a conservative and simplistic approach, Equation 21 is introduced simply as the lower limit of the capacity. The complete solution for the tensile capacity of the loop connection is thereby given as

$$23. \quad N_u = \min \begin{cases} N = \max \begin{cases} N & \text{Equation 13} \\ N_0 & \text{Equation 21} \end{cases} \\ \text{Failure in grout material} \\ N_y = 4A_s f_y \quad \text{Yielding of U} - \text{bars} \end{cases}$$

Comparison of tests with theory and discussion

Besides the geometry and the parameters that were experimentally determined in this study (strength of materials), the tensile capacity of the loop connection (Equation 23) is governed by two parameters, the factor K in the v-factor, Equation 8, and the internal angle of friction, φ, which was not explicitly determined in this study. However, the experimental results suggest a variation in these factors for the different grout materials tested. Jørgensen and Hoang (2013) proposed the factor K to be taken as 0·88 for concrete, whereas for mortar they suggested a factor of $K = 0{\cdot}75$ based on shear tests on keyed shear joints reinforced with wire-rope loops and grouted with mortar (Jørgensen and Hoang, 2015). In the following, these two suggestions are adopted. The difference in this factor is mainly attributed to the difference in the maximum aggregate size.

Regarding the internal angle of friction, φ, the aggregate content as well as the maximum size of the aggregate influence this parameter. For normal strength concrete, a value of $\varphi = 37°$ is usually adopted (Dahl, 1992; Nielsen and Hoang, 2011), but only few investigations of the internal angle of friction of mortar have been conducted. For mortars, Nielsen (1998) reported tests indicating an internal angle of friction of approximately 30°. In the following comparison of tests with calculations, a value of $\varphi = 37°$ is chosen for test series C, $\varphi = 32°$ for series M and $\varphi = 34°$ for series T. A higher value is chosen for series T compared to series M because the maximum aggregate size as well as the aggregate-to-cement ratio (a/c) is larger in series T than in series M.

The comparison of test results with calculations can be seen in Figures 10(a)–10(c). The theoretical results are generated using the average values of the strengths given in Table 3, and the test results are normalised with the actual strength parameters of

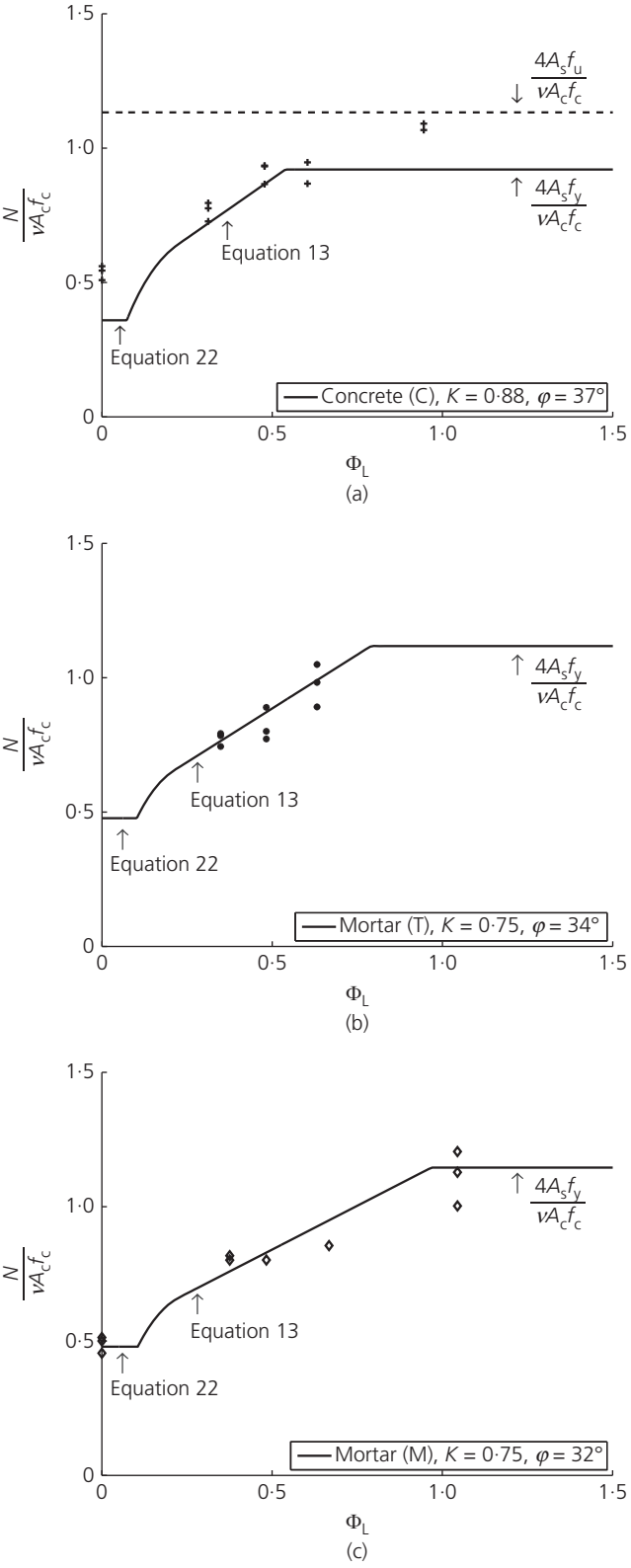

Figure 10. Comparison of models with test results: (a) Series C; (b) Series T; (c) Series M

each specimen. Equation 23 accounts for initiation of yielding in the U-bars. However, when the concrete core is sufficiently strong, the U-bars may develop hardening with increased displacement. The load corresponding to the rupture of the U-bars has therefore been added in Figure 10(a) for comparison with the results of specimens C20, where the reinforcement loops yielded and hardened before termination of the test, see Figure 5(a).

In general, the models capture the experimental results well and predict the tensile capacity of the connections. The test results revealed a difference in the capacity depending on the material properties. These differences are accounted for in the choice of internal angle of friction for the grout material and in a reduction of the effectiveness factor for the mortar grout compared to concrete. This is justified by the more brittle behaviour of mortar compared to concrete, which is evidently a result of the difference in the maximum aggregate size as the effect of aggregate interlock is smaller in mortar. In addition, it can be discussed whether the aggregate-to-cement ratio influenced the parameters as well.

From Figures 10(a) and 10(c), it can be seen that the solution for connections without transverse reinforcement estimates the test results of series M0 well and gives a slight underestimate of the results of series C0. The solution accounts for the contribution of the grout outside the overlapping area of the U-bars, which fails at the same time as the overlapping area between the U-bars. However, the side cover is not included, see Figure 9(c), as the complex crack pattern in this region cannot be simplified by a simple failure plane. Besides the geometry, it is recognised from Equation 21 that the capacity without transverse reinforcement is governed by the tensile strength of the grout. The effective tensile strength has, owing to lack of investigations of mortars, been calculated by the same formulas (Equations 17 and 18) for both mortar and concrete. This, however, is not necessarily accurate, but has been judged to be an acceptable approximation. The solution may be used to establish the transition from under-reinforced to normally reinforced connections. In practice, connections should always be designed with a sufficient amount of lacer reinforcement in order to satisfy the condition for normally reinforced connections.

As a concluding remark on the practical aspects, connections should in addition always be designed to obtain yielding of the U-bars. The models presented in this paper provide a method to determine the necessary combination of geometry, U-bar strength and dimension with the amount of lacer bar reinforcement required to avoid grout failure. Naturally, yielding of the U-bars preserves the highest ductility, both when the loop connection is loaded in tension and in the case of a shear wall, where an intact grout material improves the conditions for a ductile response in the ultimate limit state.

Conclusions

Tensile tests on symmetric '2-on-2' loop connections have been performed. The overall aim of the study was to compare the performance of connections grouted with concrete and with mortar, and on this basis develop models to predict the load related to failure in the grout material. Special attention was given to the maximum aggregate size of the grout matrix, and the amount of transverse reinforcement (lacer reinforcement). An upper bound solution based on the theory of plasticity was established for estimation of the tensile capacity of the loop connection. The following main conclusions can be drawn.

- Connections with concrete grout with a maximum aggregate size of 16 mm performed better (in terms of ultimate load as well as ductility) than similar connections grouted with mortar containing a maximum aggregate size of 2 mm and 4 mm and with similar compression strengths.
- The tested capacity of connections without lacer reinforcement corresponds to the cracking load of connections with lacer reinforcement.
- Transverse reinforcement prevented brittle failure.
- The capacity of the joint increased with increasing amount of lacer reinforcement.
- The developed rigid-plastic upper bound solutions revealed that the internal angle of friction for the grout material is an essential parameter for the capacity.
- With reasonably selected effectiveness factors and estimates of the internal angle of friction, it is possible to calculate the capacity of the connections.

The comparison with test results shows that the models provide a tool that identifies the transition between failure of the grout material and yielding of the U-bars. Connections in practice should always be designed for yielding of the U-bars, as this first of all provides a significant ductile response when loaded in tension and also constitutes the basis for a ductile response when the loop connections are used as part of a shear-resisting structural element. Based on the experimental results and the theoretical analysis, some aspects need to be further investigated in more detail. These include

- internal angle of friction for grout material
- effectiveness factor for grout material.

Acknowledgements

The experimental research presented in this paper was financially supported by the Danish Association for Precast Concrete Elements and the COWI Foundation. The test elements were produced at CRH Concrete and testing of Series T was conducted with support from MSc Jacob Svejgaard and MSc Lasse Øvrelid. The authors gratefully acknowledge these valuable contributions.

REFERENCES

Araújo DDL, Curado MC and Rodrigues PF (2014) Loop connection with fibre-reinforced precast concrete components in tension. *Engineering Structures* **72**: 140–151.

Brantschen F, Faria DMV, Ruiz MF and Muttoni A (2016) Bond behaviour of straight, hooked, U-shaped and headed bars in cracked concrete. *Structural Concrete* **17(5)**: 799–810.

Dahl KKB (1992) *A Failure Criterion for Normal and High Strength Concrete*. PhD thesis, Technical University of Denmark, Lyngby, Denmark, Report No. 286.

DeVries RA, Jirsa JO and Bashandy T (1999) Anchorage capacity in concrete of headed reinforcement with shallow embedments. *ACI Structural Journal* **96(5)**: 728–736.

fib (Fédération International du Béton) (2008) *Bulletin 43: Structural Connections for Precast Concrete Buildings*. fib, Lausanne, Switzerland.

Ghali A and Youakim SA (2005) Headed studs in concrete: state of the art. *ACI Structural Journal* **102(5)**: 657–667.

Gordon SR (2006) *Joints for Precast Decks in Steel Concrete Composite Bridges*. PhD thesis, Heriot Watt University, Edinburgh, UK.

Hansen K, Kavyrchine M, Melhorn G *et al.* (1974) Design of vertical keyed shear joints in large panel buildings. *Building Research and Practice* **2(4)**: 202–215.

Hao J (2004) *Structural Behaviour of Precast Component Joints with Loop Connection*. PhD thesis, National University of Singapore, Singapore.

Jensen BC (1976) *Nogle Plasticitetsteoretiske Beregninger af Beton og Jernbeton*. PhD thesis, Technical University of Denmark, Lyngby, Denmark, Report No. 111 (in Danish).

Jørgensen HB (2014) *Strength of Loop Connections between Precast Concrete Elements*. PhD thesis, Department of Technology and Innovation, University of Southern Denmark, Odense, Denmark.

Jørgensen HB and Hoang LC (2013) Tests and limit analysis of loop connections between precast concrete elements loaded in tension. *Engineering Structures* **52**: 558–569.

Jørgensen HB and Hoang LC (2015) Load carrying capacity of keyed joints reinforced with high strength wire rope loops. *Concrete – Innovation and Design, Proceedings of fib Symposium, Copenhagen, Denmark*, pp. 1–13.

Leonhardt F, Walther R and Dieterle H (1973) *Versuche zur Ermittlung der Tragfähigkeit von Zugschlaufenstößen*. Deutscher Ausschuss für Stahlbeton, Berlin, Germany, Bulletin No. 226 (in German).

Nielsen CV (1998) Triaxial behavior of high-strength concrete and mortar. *ACI Material Journal* **95(2)**: 144–151.

Nielsen MP and Hoang LC (2011) *Limit Analysis and Concrete Plasticity*, 3rd edn. CRC Press, Taylor & Francis Group, Boca Raton, FL, USA.

Ong KCG, Hao JB and Paramasivam P (2006) A strut-and-tie model for ultimate loads of precast concrete joints with loop connections in tension. *Construction and Building Materials* **20(3)**: 169–176.

Sørensen JH, Hoang LC, Olesen JF and Fischer G (2017) Test and analysis of a new ductile shear connection design for RC shear walls. *Structural Concrete* **18(1)**: 189–204.

Thompson MK, Jirsa JO and Breen JE (2006) Behavior and capacity of headed reinforcement. *ACI Structural Journal* **103(4)**: 522–530.

Paper II

"Test and analysis of a new ductile shear connection design for RC shear walls"

Jesper H. Sørensen, Linh C. Hoang, John F. Olsen, Gregor Fischer

Published in: *Structural Concrete (2017), 18(1):189-204*

Received: 22 March 2016 | Revised: 27 May 2016 | Accepted: 30 May 2016

DOI 10.1002/suco.201600056

WILEY fib

TECHNICAL PAPER

Test and analysis of a new ductile shear connection design for RC shear walls

Jesper Harrild Sørensen | Linh Cao Hoang | John Forbes Olesen | Gregor Fischer

Department of Civil Engineering, Technical University of Denmark, Lyngby, Denmark

Correspondence
Jesper Harrild Sørensen, Department of Civil Engineering, Technical University of Denmark, Brovej, Bygning 118, 2800 Kgs. Lyngby, Denmark.
Email: jhaso@byg.dtu.dk

Funding information
Danish Association for Precast Concrete Elements; COWI Foundation.

This paper presents a new and construction-friendly shear connection for the assembly of precast reinforced concrete shear wall elements. In the proposed design, the precast elements have indented interfaces and are connected by a narrow zone grouted with mortar and reinforced with overlapping U-bar loops. Contrary to conventional shear connections, the planes of the U-bar loops are here parallel to the plane of the wall elements. This feature enables a construction-friendly installation of the elements without the risk of rebars clashing. The core of mortar inside each U-bar loop is reinforced with a transverse double T-headed bar to ensure transfer of tension between the overlapping U-bars. Push-off tests show that a significantly ductile load–displacement response can be obtained by the new solution as compared to the performance of the conventional keyed shear connection design. The influence of the interface indentation geometry was investigated experimentally and the failure modes in the push-off tests were identified by use of digital image correlation (DIC). For strength prediction, rigid plastic upper-bound models have been developed with inspiration from the observed failure mechanisms. Satisfactory agreement between tests and calculations has been obtained.

KEYWORDS
concrete plasticity, digital image correlation, ductility, keyed shear connections, robustness

1 | INTRODUCTION

Structural solutions based on precast concrete elements are often more economically feasible than in situ cast solutions, because precast technology enables a reduction of construction time as well as labor cost. When using precast solutions, the on-site work mostly consists of assembling and connecting the precast elements into an integrated structural system. Hence, connection designs that are construction-friendly play an important role for the overall cost reduction. It is, however, a challenge to design connections that are easy to construct and at the same time have structural performance (in terms of strength and ductility) which can be compared with that of in situ cast solutions. In cases with unusual structural geometry, it may be necessary to supplement the advantages of precast construction with in situ cast solutions in selected zones. An example of how current precast solutions have been pushed to the limit can be studied in References 1 and 2 that report on the design and construction of a landmark building in Copenhagen, Denmark. The leaning characteristic of the building imposed serious challenges to the design of the shear connections between the precast panels for insurance of overall structural stability.

Currently, structural continuity between precast shear panels is established by use of narrow keyed connections containing overlapping U-bars and grouted with mortar (see Figure 1). However, with this conventional solution, which has been used since the 1960s, it is difficult to obtain full structural continuity because the strength and ductility of

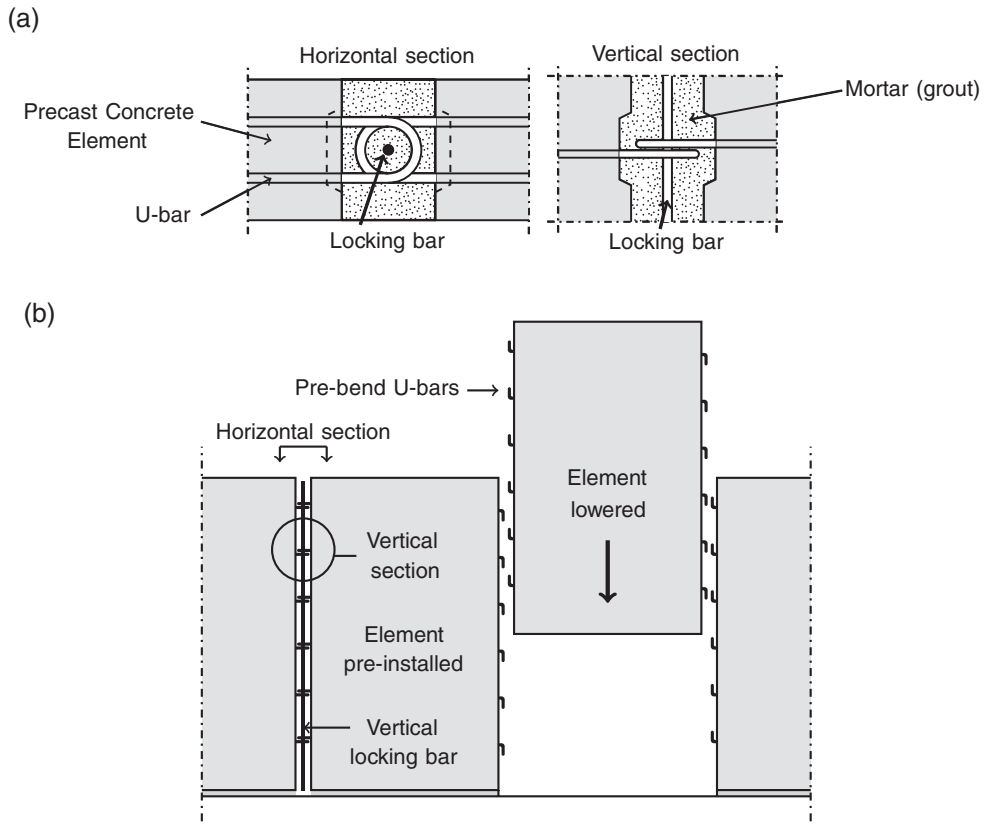

FIGURE 1 (a) Conventional shear connection design and (b) illustration of procedure for assembling of precast elements.

these connections will normally be less than that of the precast elements.[3,4] In addition, the construction sequence is influenced by the design. To avoid rebar-clashing when assembling the precast panels (Figure 1b), the U-bars protruding from the precast panels have to be bent up (prior to installation of panel) and subsequently straightened again once the panel has been placed in position. This procedure imposes a limit on the cross-sectional diameter of the U-bars and hence limits the strength of the connection (normally bars with diameter 6–8 mm are used). The conventional shear connection is therefore not feasible for use, for example, in shear walls of tall buildings where considerable horizontal loads have to be carried.

This paper presents a new solution for the connection of precast shear wall elements. The aim of the new design is to ease the construction challenges and at the same time improve the structural performance compared to the conventional solution. Figure 2 schematically illustrates the new connection design, which differs from the conventional solution in the way the U-bar loops are oriented and in the way structural continuity is ensured in the U-bar overlaps. The joint interfaces are keyed as in the conventional solution. As illustrated in Figure 2, the loop orientation in the new solution allows for a construction-friendly installation (vertical lowering) of the precast panels, without clashing of rebars and thus without the need to pre-bend and post-straighten the U-bars, which enables U-bars with diameters larger than 8 mm to be used. In addition to a single longitudinal locking bar, the new design also includes the use of transverse locking bars (in the following called lacer bars) in the form of a double T-headed rebar placed inside the U-bar loops. The idea here is to utilize the double-headed rebar together with the core of mortar inside the loop as a transverse dowel that enables transfer of tension between the overlapping U-bars. Tension in the U-bars across the connection is required to ensure equilibrium when diagonal compression struts develop between the keyed joint interfaces as a result of shear loading. The double T-headed rebar is chosen because the heads provide increased anchorage of the short lacer reinforcement, which otherwise cannot be ensured using regular straight reinforcement.

To investigate the structural performance of the new connection design, an experimental program was conducted. The investigation showed that the load–displacement response of the new design is significantly more ductile than that of the conventional solution. Furthermore, the tests indicated that it is possible to obtain higher load-carrying capacities with the new design. In addition to the experimental work, this paper also presents upper-bound rigid plastic models for prediction of the critical failure mode as well as the load-carrying capacity of the new connection design. The models furnish a simple tool to optimize the geometry of the keyed joint interfaces in order to enhance the ductile behavior of the connection.

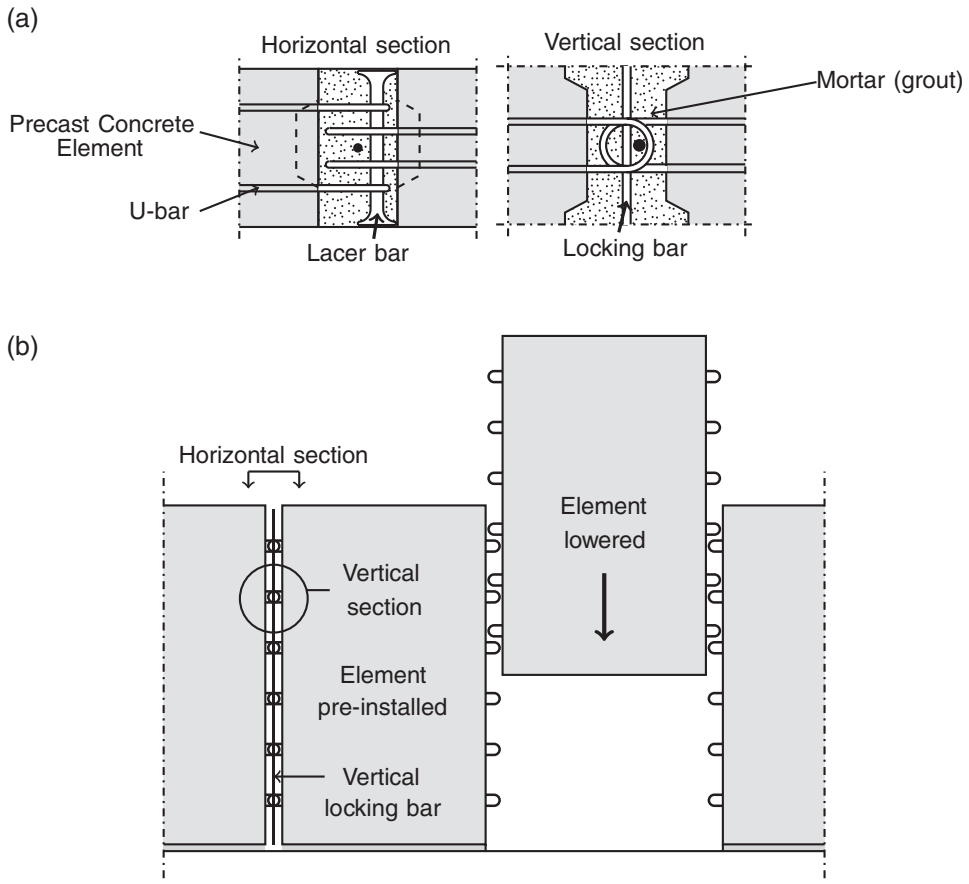

FIGURE 2 (a) New construction-friendly connection design and (b) illustration of procedure for assembling of precast elements.

2 | PREVIOUS INVESTIGATIONS ON SHEAR CONNECTIONS

With the introduction of precast element construction, the design and performance of on-site cast connections became a matter of special interest. Since the 1960s, the conventional keyed shear connection has been experimentally investigated, with the main interests being the behavior of the connection during loading, the ultimate load-carrying capacity, and the design aspects of the joint configuration. Hansen et al.[4] summarized the early work on this topic in a report, which constitutes the work of the CIB commission W23A. The experimental programs that served as basis for the commission's report include the work of Halasz and Tantow, Cholewicki, Pommeret, and Fauchart and Cortini,[5–8] who used similar test setups as the one used in the present study. Shear tests with other test setups to investigate factors that influence the load-carrying capacity have also been published.[9–14] In all investigations, regardless of testing method, it was recognized that the ultimate capacity was influenced by a number of factors, including the number of shear keys, the cross-sectional area of the keys, the strength of the grout mortar, the degree of transverse reinforcement, and the magnitude of external transverse confinement stresses.

Based on the experimental findings, a number of semi-empirical formulas were suggested for the prediction of the ultimate load-carrying capacity. Current design provisions for joints between concrete cast at different times are based on the shear friction hypothesis (see, for example, the *fib* guide to good practice[3] and the European code of practice[15]). However, other approaches can also be used. Kaneko et al.[16,17] proposed a fracture mechanics approach to predict the crack formation in indented shear joints. They identified two main fracture mechanisms for shearing of keys, based on an experimental program that included plain and fiber-reinforced concrete joints. The test results were supplemented with nonlinear finite element calculations. Later, Kaneko and Mihashi[18] extended the investigation by presenting an analytical model for determination of the transition between the two mechanisms. However, variations in key dimensions such as length and depth were not included in the experimental investigation.

Theoretical works based on the theory of rigid plasticity have also been proposed. Jensen[19] was the first to establish an upper-bound solution for the load-carrying capacity of keyed shear joints by assuming complete shearing of the key area. These findings were later the basis for several simplified formulas, which incorporate empirical factors to fit theory with test results. This includes the

formulas by Chakrabarti et al.[20] and Abdul-Wahab and Sarsam.[21] Later Christoffersen[22] expanded the application of plasticity theory to include both upper- and lower-bound solutions for the shear capacity of keyed joints. Recently, Jørgensen and Hoang[23] developed an upper-bound model for the failure of keyed shear joints reinforced with high-strength wire rope loops by accounting for diagonal cracks between the shear keys. Jensen, Christoffersen as well as Jørgensen and Hoang considered only a global failure mechanism with complete shearing of the keyed area. A local failure mode that involves key corner crushing has been observed by several authors. However, the problem has not been treated in depth, nor has an analytical solution been proposed.

3 | EXPERIMENTAL PROGRAM

The experimental program contained a total of 25 push-off tests. The program included a preliminary investigation of seven specimens where the performance of the conventional design, as a reference, was compared with the new design with identical geometrical joint properties. The remaining 18 specimens, Series I–IX, were subdivided into two investigations related to the geometry of the key indentation (see Figure 3). The tests were carried out in quasi-static deformation control.

3.1 | Specimens and geometry

The general geometry of the push-off test specimens can be seen in Figure 3 and details of geometrical and material properties are given in Table 1. Series R refers to reference specimens designed with a conventional reinforcement layout as illustrated in Figure 1a (however, in the reference specimens, the loops were placed outside the keyed area). Series P refers to pilot specimens designed with "2-on-1" vertical loop connections. This refers to a design similar to the principles shown in Figure 2a, however, in the pilot specimens, there was (for each looped connection) only one centrally placed U-bar that protruded from the precast element to the right. The cross-sectional area of this single U-bar is referred to as A_s in Table 1. The reinforcement area in the weak side, A_s, as well as the geometry of the shear keys were identical for all specimens in Series R and P. The joints in Series P were not provided with longitudinal locking bars. For specimens type I–IX, "2-on-2" vertical loop connections were used (see Figure 2a). For these specimens, the area A_s listed in Table 1 should be understood as the cross-sectional area of two U-bars. In order to eliminate the edge effect, anchorage plates were mounted at each end of the longitudinal locking bar in Series I–IX. In eight specimens (Series I–IV), the length of the keys, L_k, was varied, while the key height, h_k, was kept constant to half of the panel thickness, t. In the remaining

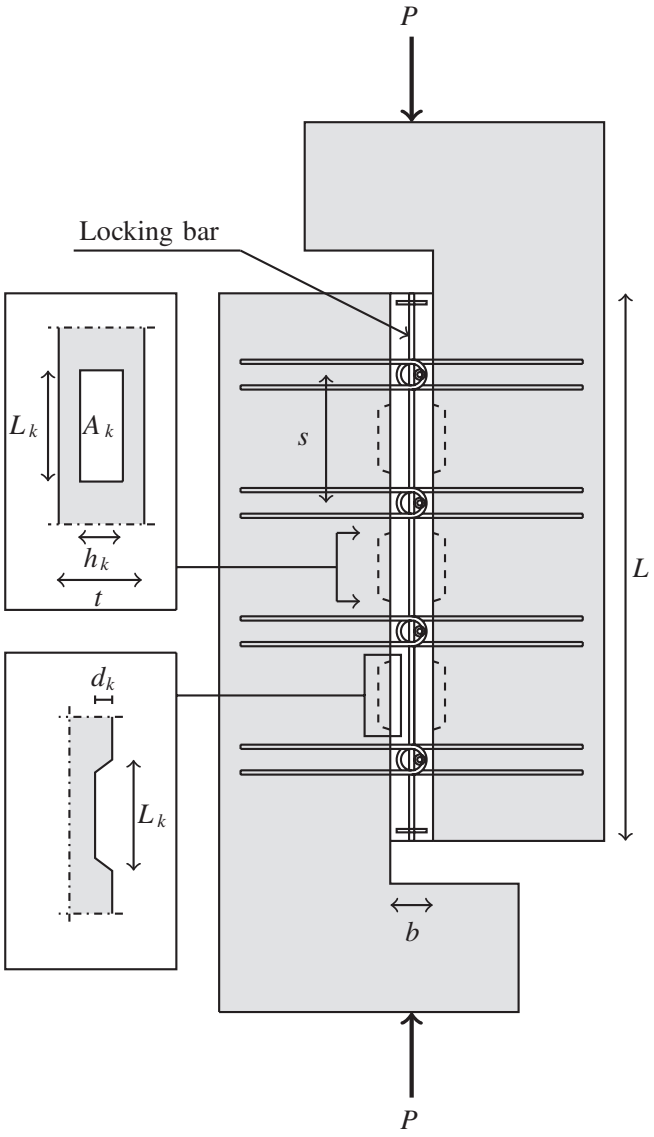

FIGURE 3 General layout of push-off test specimens, thickness equals 200 mm (reinforcement in precast element not shown).

ten specimens (Series V–IX), the depth of the key indentation, d_k, was varied, while the key length and the key height were kept constant, $L_k = 140$ mm and $h_k = 200$ mm. Table 2 contains parameters and material properties for Series I–IX. The diameter of the lacer bar was carefully designed so that the tensile capacity of the overlapping loops would be governed by yielding of the U-bars and not crushing of the mortar. For this purpose, the calculation model for tensile capacity of U-bar loop connections developed by Jørgensen and Hoang[24] was used. The double T-headed lacer bar in each loop was positioned as shown in Figure 2a to make it function as tension reinforcement in the small transverse circular mortar dowel, which ensures transfer of tension between the overlapping U-bars. Each design was tested with two replicates and the material properties were found as average values obtained from tensile tests of the steel reinforcement and compression tests of $\phi 100 \times 200$ mm cylinders of the mortar used for casting the joints.

TABLE 1 Geometrical parameters and strength properties of the joints in the experimental program, bold numbers indicating the specifics of the specimen

	No.	f_c[a] [MPa]	h_k [mm]	L_k [mm]	A_k [mm^2]	d_k [mm]	A_s [mm^2]	P_{FP} [kN]	P_U [kN]	D_I [-]
R	1	34.6	85	160	13,600	16	**101**	282.43	–	0.42[b]
	2	35.7	85	160	13,600	16	**101**	303.80	–	0.59[b]
	3	35.7	85	160	13,600	16	**101**	337.42	–	0.70[b]
P	1	38.1	85	160	13,600	16	**101**	344.24	357.45	1.00[b]
	2	38.1	85	160	13,600	16	**101**	347.04	368.12	0.97[b]
	3	42.7	85	160	13,600	16	**101**	342.49	339.97	0.87[b]
	4	42.7	85	160	13,600	16	**101**	331.42	324.49	0.95[b]
I	1	31.2	100	**120**	12,000	28	201	379.02	441.21	1.03[c]
	2	34.2	100	**120**	12,000	28	201	416.59	472.92	1.00[c]
II	1	31.2	100	**140**	14,000	28	201	366.40	463.78	1.06[c]
	2	34.2	100	**140**	14,000	28	201	414.46	462.48	1.00[c]
III	1	31.2	100	**160**	16,000	28	201	393.04	494.70	1.07[c]
	2	34.2	100	**160**	16,000	28	201	473.52	514.87	0.98[c]
IV	1	31.2	100	**180**	18,000	28	201	439.44	470.89	0.94[c]
	2	34.2	100	**180**	18,000	28	201	478.17	515.31	0.96[c]
V	1	31.2	200	140	28,000	**10**	201	475.24	488.97	0.97[c]
	2	34.2	200	140	28,000	**10**	201	492.86	535.61	1.04[c]
VI	1	30.6	200	140	28,000	**16**	201	527.09	502.55	0.89[c]
	2	30.6	200	140	28,000	**16**	201	523.82	550.98	0.90[c]
VII	1	30.6	200	140	28,000	**20**	201	549.17	451.58	0.78[c]
	2	30.6	200	140	28,000	**20**	201	524.46	527.85	0.87[c]
VIII	1	30.6	200	140	28,000	**25**	201	507.05	528.67	0.92[c]
	2	30.6	200	140	28,000	**25**	201	516.97	545.33	0.92[c]
IX	1	30.6	200	140	28,000	**28**	201	526.53	534.19	0.93[c]
	2	30.6	200	140	28,000	**28**	201	527.59	527.07	0.88[c]

[a] Compression strength of mortar.

[b] Calculated using $\delta_{max} = 13$ mm.

[c] Calculated using $\delta_{max} = 20$ mm.

TABLE 2 Parameters kept constant for Series I–IX

Description	Symbol	Value
U-bar diameter	ϕ	8 mm
Yield strength of U-bar	f_y	487 MPa
Lacer bar diameter	ϕ_{Lacer}	16 mm
Yield strength of lacer bar	$f_{y,Lacer}$	563 MPa
Diameter of locking bar	ϕ_L	12 mm
Yield strength of locking bar	f_{yL}	584 MPa
Panel thickness	t	200 mm
Internal bend diameter of loops	D	60 mm
Width of joint	b	100 mm
Distance between loops	s	300 mm
Total length of joint	L	1,280 mm
Strength of precast concrete	$f_{c,element}$	49.6 MPa
Maximum aggregate size in mortar	d_{max}	4 mm

3.2 | Digital image correlation

In the present investigation, digital image correlation (DIC) was used to study the relative displacements on the surface of the shear connection, including development of cracks in the joint mortar. The analysis was performed with the program Aramis.[25] An example of application of the same software has been described by Pereira et al.,[26] who studied the cracking behavior of cement paste, mortar, concrete, and fiber-reinforced concrete. In the present study, the analysis was performed as a two-dimensional analysis using images taken with a 36.3-megapixel digital camera. The surface of the connection was spray painted with a white base layer, followed by black dots sprayed randomly to create a unique and recognizable pattern on the surface. The area covered by the Aramis analysis corresponds approximately to the area of the joint, namely $L \cdot (b + 2d_k)$ (see Figure 3). The results include the overall response of the shear connection, failure of the joint mortar between the precast elements, and also local failure of the shear keys. The results were dependent on the quality of the sprayed pattern, the light settings, and the care taken in the adjustment of the camera. The results covered only the development of cracks on the surface of the joint, however, the analysis provided invaluable information on joint behavior during loading.

3.3 | Test results

Figure 4 presents the general characteristics of the load–displacement response of the different tested connections.

The measured displacements are relative displacements (in the longitudinal direction of the connection) between the two precast elements. Figure 4a can be used as a direct comparison between Series R and P, where the behavior of the reference specimens complies with previous investigations, for example, as described in detail by Hansen et al.[4] The first peak also appears to be the global peak, which is immediately followed by a softening branch as the shear displacement increases. It should be noted that the response curve of specimen R1 represents a test in which the U-bar loops are pushed away from each other, whereas for specimens R2 and R3, the U-bars are pushed toward each other as the shear displacement increases. This indicates a very unfortunate property of the conventional design because the postpeak response is apparently dependent on the loading direction. It may very well be due to this fact that the postpeak behavior of the conventional design in the literature is reported both as brittle and as ductile.

Figure 4a clearly illustrates the main difference between the two designs. The loads corresponding to the first peak are comparable for specimens having identical A_s (as given in Table 1) and identical key configuration. However, the postpeak behavior differs significantly as the new design exhibits a pronounced ductile behavior. It should be noted that the reference design (Series R), with limited ductility, can be classified as a 1-on-1 connection. The total amount of looped reinforcement in the connection may have influenced the test results (when comparing the ductility of 1-on-1 connections with the ductility of 1-on-2 and 2-on-2 connections). However, the most dominant influence on the test results is most probably due to the orientation of the U-bar loops and the presence of the transverse double-headed lacer bars. This ductile behavior is especially observed for the 2-on-2 connections, see Figure 4b, which presents examples of the main findings of the test Series I–IX. Before cracking, the joint behaves with a stiffness similar to that of a monolithic wall. At a relatively small load level, cracks develop at the interface between the joint mortar and the precast element, slightly reducing the stiffness. At a higher load level, diagonal cracks between the corners of each pair of opposite shear keys start to emerge on the surface, as indications of diagonal strut action. After diagonal cracking, the stiffness of the joint decreases until the first peak on the load–displacement curve is reached, which corresponds to the value of P_{FP}, given in Table 1. For the new design, a drop in the response is observed after the first peak. However, as the displacement increases, the load increases again and reaches approximately the same level as the first peak. The relation between the first peak load and the ultimate load depends on the key design, which turns out to be one of the main parameters that control the failure mechanism. Rupture of the U-bars starts to take place at a displacement in the range of 12–20 mm, depending on the reinforcement configuration. The ultimate load of the joint, indicated as P_U in Table 1, is typically found at large displacements. The load level in Figure 4b is higher than the load level in Figure 4a due to the difference in the reinforcement area, A_s, per loop connection.

The first peak capacity, P_{FP}, is governed by several factors, as identified in the above-mentioned literature. In the present study, where the tensile capacity of the loop connections was designed to be governed by U-bar yielding, the magnitude of P_{FP} is influenced by the geometry of the shear keys. A larger key area generally results in a higher first peak capacity. Specimen II2 has a smaller key area compared with V2 and VIII2. This explains the lower first peak capacity for II2, however, the response after first peak shows the same tendencies as that of specimen VIII2 because both specimens had identical loop reinforcement configuration (see Figure 4b). Furthermore, it is seen that the first peak capacities of V2 and VIII2 are rather similar

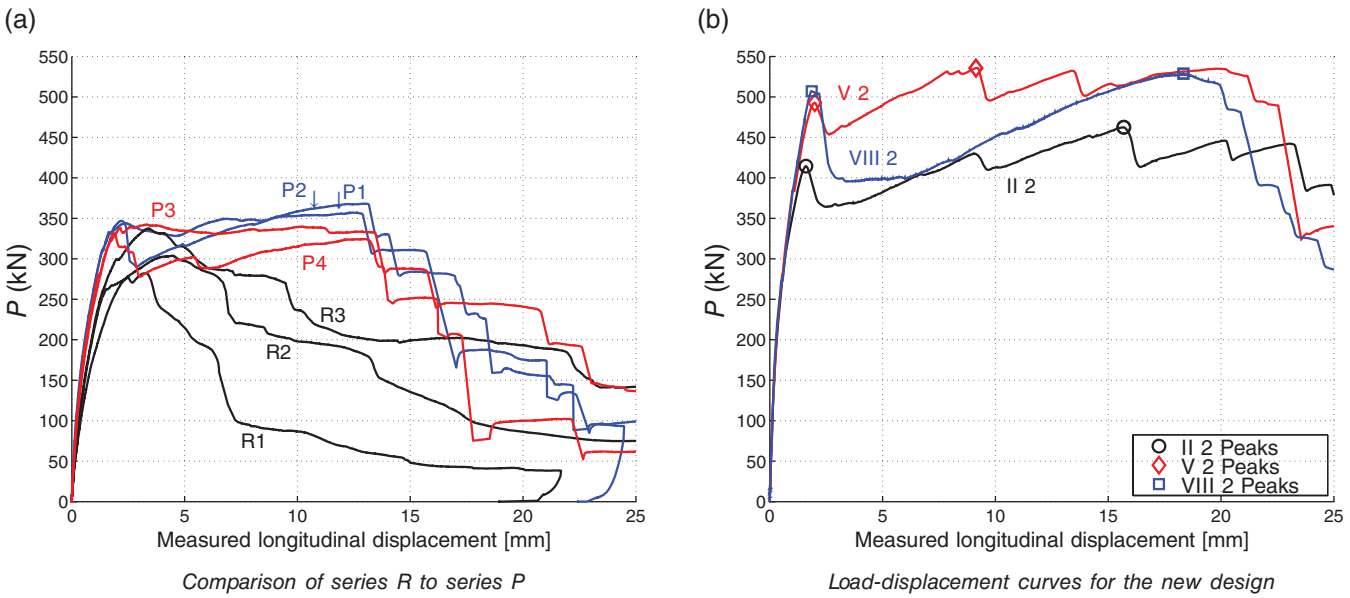

Comparison of series R to series P

Load-displacement curves for the new design

FIGURE 4 Examples of performance of tested shear keyed joints.

as the key areas are identical. However, after the first peak, the two specimens behave differently as the governing failure mechanisms are different (referring to Mechanisms B and C introduced in Figure 7). The small key depth, d_k, of specimen V2 favors shearing of the key corners, whereas the larger key depth of specimen VIII2 results in complete shearing of the key. These partly or complete key shearing failure mechanisms are in agreement with the findings for the conventional keyed joint described by Hansen et al.[4] Nimityongskul and Liu[9] also observed these failure mechanisms, and they interpreted the failure with partial shearing of the key corners as a consequence of an increase of the key area. A correlation between this failure mode and the depth of the shear keys has not been investigated until now.

3.4 | Detection of failure mechanisms

As DIC was used to monitor the cracking process on the surface of the specimen, the experimental failure mechanisms could be detected. For specimens with keys hidden in the joint, that is, Series I–IV, where $h_k < t$, failure of the keys was only observed indirectly as displacements at the casting joint and as diagonal cracking in the joint mortar (also see Figure 9). For specimens with keys having $h_k = t$, cracking of the keyed area was clear and visible when it occurred. Figure 5 shows an example of a complete shearing of a single key, where it is also observed that the pre-existing diagonal crack closes almost completely as the key is sheared off. From the load–displacement response of the specimen, it appears that the observed first peak capacity was related to the shear failure of the keys. On this basis, it seems reasonable to conclude that failure of the shear keys also governs the first peak capacity of the specimens with keys hidden in the joint ($h_k < t$). DIC measurements of the cracking/failure patterns have served as inspiration when developing collapse mechanisms used in the upper-bound calculations of the first peak capacity, P_{FP}, (see Section 4).

3.5 | Ductility of connections

It appears from the test results that a much more ductile load–displacement response can be obtained by the new design compared to the conventional solution. To quantify the ductility of a shear joint, the concept of relative strain energy described by Engström[27] may be considered. Engström compared the maximum resistance with the average force that can be resisted by the connection during the entire displacement spectrum. This results in an average-to-peak ratio less than or equal to unity, where unity is the ideal rigid plastic behavior. In order to refine this measure, a ductility index as defined in Equation 1 is introduced:

$$D_I = \frac{1}{\delta_{max} - \delta_{FP}} \int_{\delta_{FP}}^{\delta_{max}} \frac{P(\delta)}{P_{FP}} d\delta \quad (1)$$

The idea here is to evaluate the ability of the joint to dissipate energy in the displacement regime $\delta_{FP} - \delta_{max}$, where δ_{FP} corresponds to the shear displacement at the occurrence of the first peak capacity, while δ_{max} is the maximum shear displacement capacity of the connection. The displacement capacity, δ_{max}, can be defined as the displacement where rupture of U-bars initiates or taken as a fixed predefined value. The index, D_I, is the ratio between the dissipated energy (see the filled area in Figure 6), and the value $P_{FP} \cdot (\delta_{max} - \delta_{FP})$, which reflects the energy of a perfectly plastic connection having the capacity P_{FP} (see the hatched area in Figure 6). The ductility index may attain a value larger than unity. An index $D_I > 1.0$ indicates that the joint has a robust behavior because it will be able to absorb the potential energy released when, for example, gravitational loads (applied in a load-controlled manner) reach the first peak capacity, P_{FP}. The ductility index is highly dependent on the total shear area of the keys, A_k, as the first peak capacity increases with increasing A_k. Table 1 contains calculated values of D_I for the tested joints. The maximum shear displacement is chosen as 13 mm for 2-on-1 connections and 20 mm for the 2-on-2 design as rupture of the reinforcement loops was observed around this magnitude of displacement. In general, the new design has a much higher D_I index than the conventional design. The most important factor for obtaining a high ductility index is the governing failure mechanism. For practical application, it should be noted that a mechanism with key corner shearing leads to the most ductile and robust response. This issue will be further addressed in Section 4.

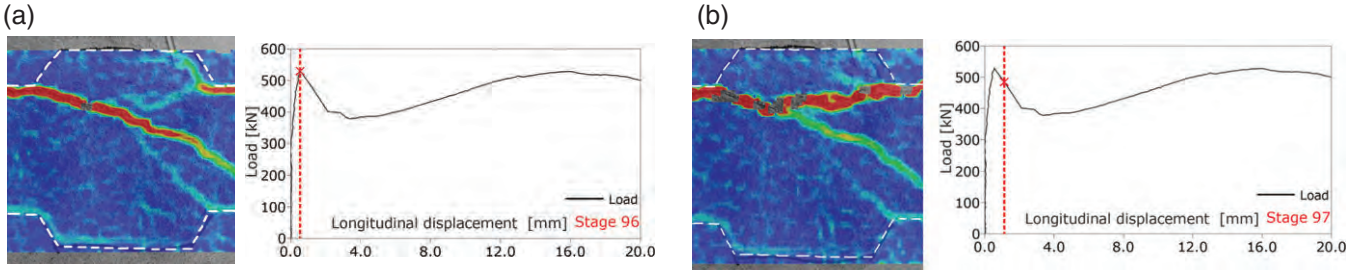

FIGURE 5 Example of complete key shearing (keys indicated with dashed lines) at first peak load, P_{FP}, specimen IX2, $dk = 28$ mm .

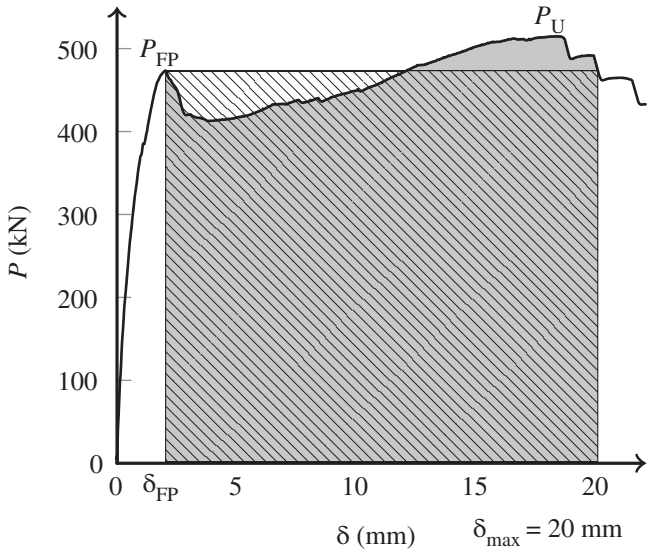

FIGURE 6 Example of calculation of the ductility index, D_I, for specimen III2, $D_I = 0.98$.

4 | FAILURE MECHANISMS AND UPPER-BOUND SOLUTIONS

As demonstrated by the DIC analysis (see Section 3.4), the first peak load, P_{FP}, is governed by failure of the shear keys. In this paper, so-called first-order rigid plastic upper-bound models will be developed to predict P_{FP}. The ultimate load, P_U, of the joints is associated with large displacements and cannot be modeled in the same simple manner. Analytical modeling of P_U would require second-order plastic analyses accounting for the change of geometry. The theoretical treatment of P_U is not a part of this paper. In the following, concrete, mortar, and reinforcing steel are assumed to be rigid perfectly plastic materials obeying the associated flow rule. Concrete and mortar are considered as modified Coulomb materials with zero tensile strength. For plain strain problems, the energy dissipated per unit area of a failure surface (yield line) may be determined as follows:[28,29]

$$W_A = \frac{1}{2}\nu f_c(1-\sin\alpha)|\mathbf{u}|,\ \alpha \geq \varphi \tag{2}$$

where α is the angle of the displacement vector with the yield line and φ is the internal angle of friction. The internal angle of friction is a material property, which depends partly on the aggregate sizes and partly on the aggregate content of the matrix.[29] Triaxial tests by Dahl[30] indicate that φ also depends on the confinement pressure. However, for normal strength concrete and low confinement pressures, the internal angle of friction is normally taken to be $\varphi = 37°$. For normal strength mortar with confinement pressures less than the uniaxial compressive strength of the mortar, Nielsen[31] reported tests indicating an internal angle of friction around 30°. In this study, it is assumed that $\varphi = 30°$ for the mortar material used to grout the joints. As neither concrete nor mortar is a perfectly plastic material, an effectiveness factor ν is introduced into the theoretical solutions.[29] The ν-factor depends on the type of problem and is usually found by calibration with tests. For keyed joints transversely reinforced with high-strength wire loops, Jørgensen and Hoang[23,32] suggest to adopt a ν-formula similar to the one used for beam shear problems,[33] but modified to the geometric layout of the keyed shear joint. Furthermore, the factor was adjusted to fit the shear capacity of joints cast with mortar. The ν-factor for mortar joints proposed by Jørgensen and Hoang is adopted in this work:

$$\nu = \frac{0.75}{\sqrt{f_c}}\left(1+\frac{1}{\sqrt{L_k}}\right) \geq 1.0 \quad (f_c \text{ in MPa and } L_k \text{ in m}) \tag{3}$$

It should be noted that the dependency of ν on f_c and L_k basically reflects softening effects and size effects, which in the end is also due to softening. According to Equation 3, a decrease in key length will increase the effectiveness factor, which explains why identical key areas may lead to different tested load-carrying capacities, depending on the L_k/h_k ratio. In the test Series I–IX, the effectiveness factor ranges from 0.43 to 0.52.

4.1 | Failure mechanisms

The load-carrying capacity, P_{cal}, related to a specific failure mechanism is found by solving the work equation, in which the rate of work performed by the external loads must equal the rate of internal work dissipated in the yield lines. Figure 7 shows the three basic failure Mechanisms A, B, and C considered in this study. The mechanisms have been identified partly on the basis of theoretical reasoning and partly with inspiration from the experimentally observed failure modes. For all three failure mechanisms, it is assumed that the precast element on the right-hand side experiences a rigid body motion described by the displacement vector **u**:

$$\mathbf{u} = \begin{pmatrix} u_t \\ u_l \end{pmatrix} \tag{4}$$

The rate of external work is then given by:

$$W_E = P_{cal} u_l \tag{5}$$

For Mechanisms A and B, it is more convenient to express the components of **u** by $|\mathbf{u}|$ and the angle α as follows (see Figure 7):

$$u_l = |\mathbf{u}|\cos\alpha \tag{6}$$

$$u_t = |\mathbf{u}|\sin\alpha \tag{7}$$

The rate of internal work, W_I, for the three mechanisms may in general be written as:

$$W_I = W_{I,j}^c + W_I^s + W_I^{sL} \tag{8}$$

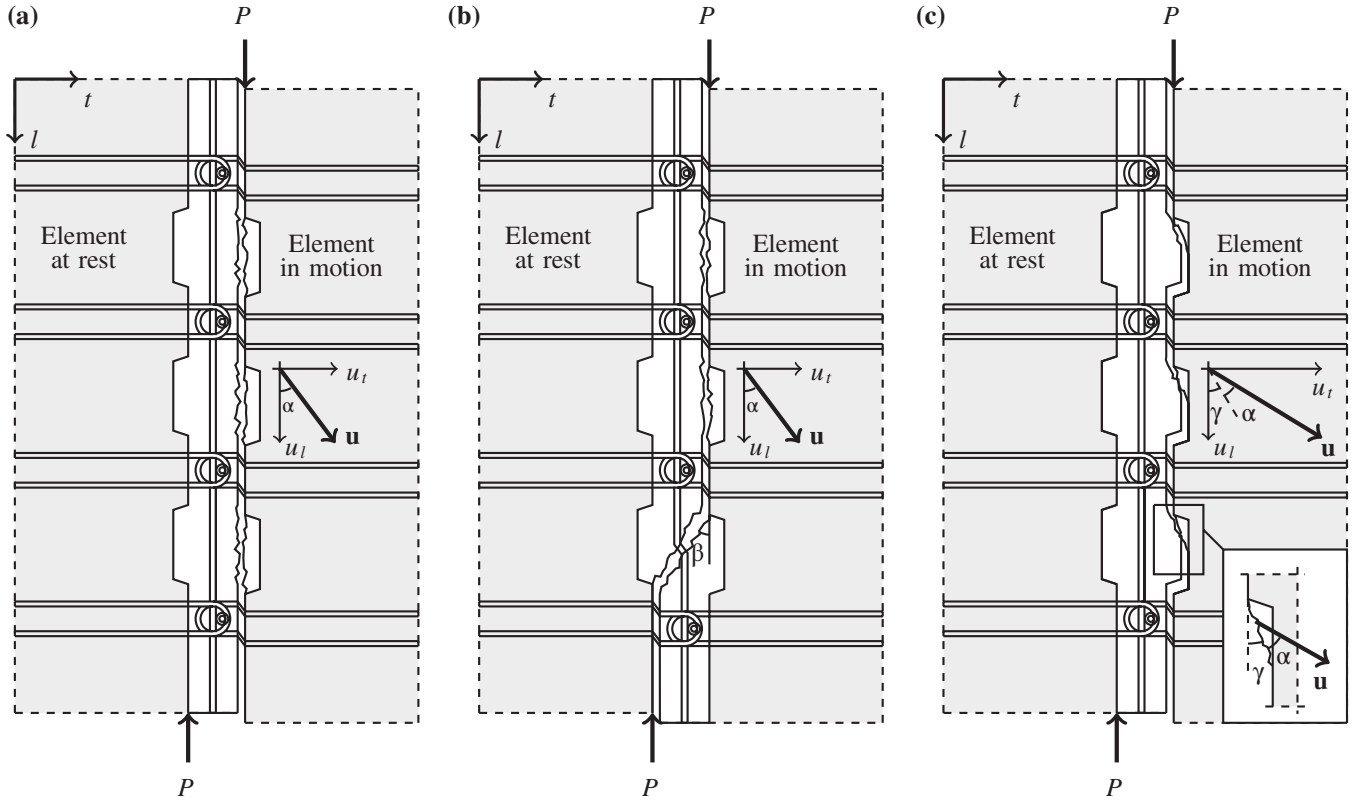

FIGURE 7 Basic failure mechanisms.

$$W_{I,j}^{c} = W_A A_j \tag{9}$$

$$W_I^s = A_s f_y u_t \tag{10}$$

$$W_I^{sL} = A_{sL} f_{yL} u_l \tag{11}$$

where $W_{I,j}^{c}$ is the contribution from a concrete/mortar yield line with the area A_j, W_I^s is the contribution from the U-bars, and W_I^{sL} is the contribution from the locking bar. Yielding of the locking bar is only required in Mechanism B.

For a general description, the following parameters are introduced and explained in Table 3:

$$A_k = L_k h_k,\ A_d = t\sqrt{b^2 + L_k^2},\ A_i = h_k \frac{d_k}{\sin\gamma},$$

$$\tan\beta = \frac{b}{L_k}, \Phi = \frac{n+1}{n}\frac{A_s f_y}{A_k f_c}, \Phi_L = \frac{A_{sL} f_{yL}}{n A_k f_c}$$

The parameters introduced make it easier to derive general formulas for calculation of a joint with n shear keys and $(n + 1)$ pairs of U-bar loops crossing the joint interface. It is convenient to define the shear capacity of the joint by an average shear stress, τ, which is related to the total area of the shear keys:

$$\frac{\tau}{\nu f_c} = \frac{P_{\text{cal}}}{n A_k \nu f_c} \tag{12}$$

4.2 | Mechanism A: Key cut off

To solve the work equation for Mechanism A, the rate of internal work is found as the sum of contributions from n shear keys being sheared off (using $A_j = A_k$) and the contribution from $(n + 1)$ reinforcement loops stressed to yielding:

$$W_I = n\frac{1}{2}\nu f_c(1-\sin\alpha)A_k|\mathbf{u}| + (n+1)A_s f_y u_t \tag{13}$$

An upper-bound solution is established from $W_E = W_I$:

$$\frac{\tau}{\nu f_c} = \frac{1-\sin\alpha}{2\cos\alpha} + \frac{\Phi}{\nu}\tan\alpha \tag{14}$$

TABLE 3 Symbols used in the theoretical determination of the first peak capacity

Symbol	Definition
A_s	Reinforcement area per loop connection $4\frac{\pi}{4}\phi^2$ for 2-on-2 connections $2\frac{\pi}{4}\phi^2$ for 2-on-1 connections
A_k	Area of one shear key
A_d	Area of diagonal yield line
A_i	Area of inclined yield line in a shear key
Φ	Reinforcement degree of loop connection
Φ_L	Reinforcement degree of locking bar
β	Slope of diagonal yield line
γ	Slope of inclined yield line in a shear key

The optimal solution is found by minimizing the expression with respect to the angle of displacement, α. The optimal solution is found when:

$$\alpha = \arcsin\left(1 - \frac{2\Phi}{\nu}\right), \quad \alpha \geq \varphi \tag{15}$$

From Equation 15, it is implicitly given that the key area influences the optimal angle of displacement and thereby the capacity of the shear connection. It should be noted that the expression, with only slight change of notation, is similar to the findings of Jensen[19] and Christoffersen.[22]

4.3 | Mechanism B: One diagonal yield line

For Mechanism B, the rate of internal work consists of the following contributions: $(n-1)$ times $W^c_{I,j}$ with $A_j = A_k$, one time $W^c_{I,j}$ with $A_j = A_d$, $(n+1)$ reinforcement loops stressed to yielding, and one contribution from the locking bar stressed to yielding. The upper-bound solution is found to be:

$$\frac{\tau}{\nu f_c} = \frac{n-1}{2n}\frac{1-\sin\alpha}{\cos\alpha} + \frac{A_d}{2nA_k}\frac{1-\sin(\beta+\alpha)}{\cos\alpha} + \frac{\Phi}{\nu}\tan\alpha + \frac{\Phi_L}{\nu} \tag{16}$$

which has a minimum when the angle of displacement is:

$$\alpha = \arcsin\left(\frac{n-1+\frac{t}{h_k}-2n\frac{\Phi}{\nu}}{n-1+\frac{A_d}{A_k}}\right), \quad \alpha \geq \varphi \tag{17}$$

From Equation 17 it can be seen that the ratio between the height of the key and the thickness of the connection influences the optimal solution for this particular failure mechanism.

4.4 | Mechanism C: Inclined key cut off

For Mechanism C, the rate of internal work is found as n times $W^c_{I,j}$ (with $A_j = A_i$) plus the contribution from $(n+1)$ reinforcement loops. In this mechanism, the angle between the l-axis and the inclined yield line is γ (see Figure 7c). The components of the displacement vector are given by:

$$u_l = |\mathbf{u}|\cos(\gamma+\alpha) \tag{18}$$

$$u_t = |\mathbf{u}|\sin(\gamma+\alpha) \tag{19}$$

As the relationship between the transverse and the longitudinal displacement is dependent on the sum of γ and α, the lower limit of the condition $\alpha \geq \varphi$ is reached at lower degrees of reinforcement for this mechanism compared with Mechanisms A and B. Therefore (and to simplify), it is for this particular mechanism assumed that $\alpha = \varphi = 30°$. The optimization of the upper-bound solution is then reduced to an optimization problem involving only the angle γ, which is governed by the key dimensions and the internal angle of friction φ. The load-carrying capacity is given by:

$$\frac{\tau}{\nu f_c} = \frac{d_k}{2L_k}\frac{1-\sin\varphi}{\sin\gamma\cos(\gamma+\varphi)} + \frac{\Phi}{\nu}\tan(\gamma+\varphi) \tag{20}$$

The critical angle of the inclined yield line is found as:

$$\gamma = \arctan\left(\frac{\cos\varphi}{\sin\varphi + \sqrt{1+\frac{\Phi}{\nu}\frac{2L_k}{d_k}\frac{\cos\varphi}{1-\sin\varphi}}}\right) \tag{21}$$

It appears that the internal angle of friction of the joint mortar influences the capacity significantly and to a large extent dictates, in combination with the key length to depth ratio (L_k/d_k), which of the failure mechanisms (A, B, or C) that constitutes the critical mechanism.

5 | INFLUENCE OF KEY GEOMETRY ON FAILURE MODE

From the derived expressions for the load-carrying capacity (Equations 14, 16, and 20) and the corresponding optimal angles of displacement, it is evident that the geometry of the joint and, in particular, the geometry of the keys, plays an important role in defining the governing failure mechanism. Figure 8 contains the results of a theoretical comparison of the load-carrying capacity related to the three basic failure mechanisms. The calculations have been performed by assuming a reinforcement arrangement similar to the one used in the experimental program Series I–IX. Figure 8a demonstrates the influence of the key height, h_k, and it appears that a higher relative key height, h_k/t, favors Mechanism B compared with a small relative key height that favors Mechanism A. Figure 8b demonstrates the influence of the key depth on the failure mechanism of a joint configuration similar to the test specimens of Series V–IX, where the relative key height $h_k/t = 1$. As expected, the smaller key depths favor Mechanism C.

The transition point (in Figure 8b) between the failure mechanisms is of particular interest because the deformation characteristics of the joint depend on the governing failure mechanism. As shown in Figure 4b, shearing of the key corners (specimen VII) results in a pronounced ductile behavior, which in turn leads to a high ductility index. In this context, it should be noted that the internal angle of friction for mortar is of significant interest because the transition point (see Figure 8b) partly depends on the magnitude of φ. Aramis recordings of the relative displacements at the first peak load indicate that $\varphi = 30°$ is an appropriate choice for the material used in this study, and furthermore, it is in accordance with the investigations by Nielsen.[31] The recorded relative displacements were compared with the theoretical relative displacements for test specimens where the angle of displacement was predicted to be $\alpha = \varphi$.

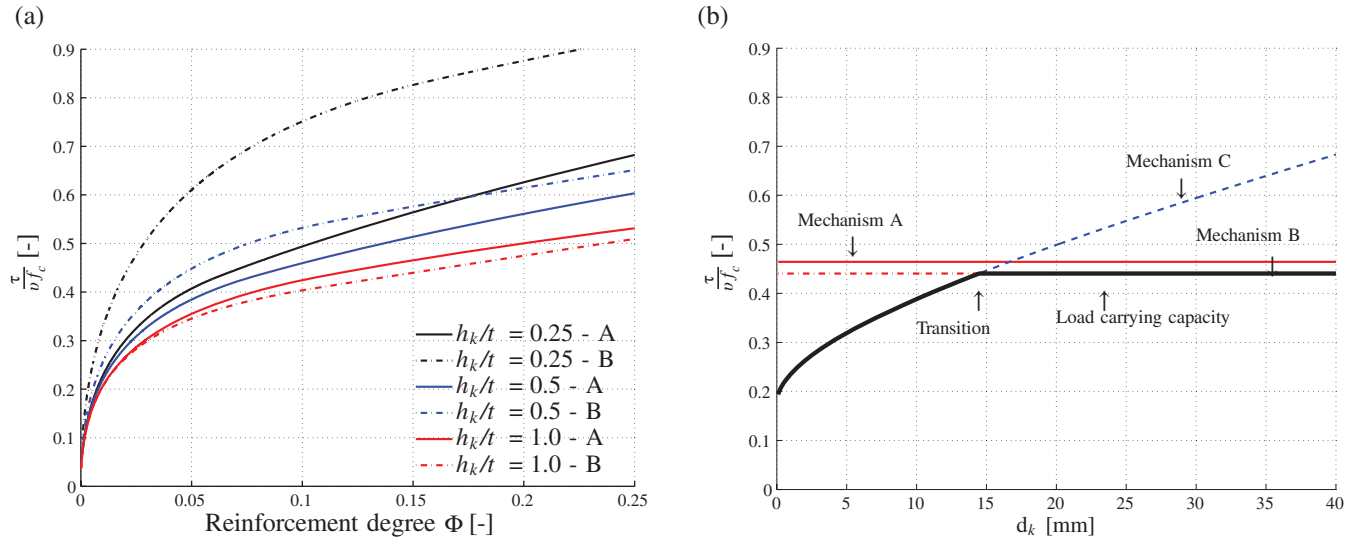

Load carrying capacity for varying relative height of key, h_k/t, f_c = 31 MPa

Load carrying capacity for varying key depth, f_c = 31 MPa, L_k = 0.140 m, h_k = 0.200 m, Φ = 0.15

FIGURE 8 Illustrations of change in failure mechanism when changing geometry of the shear keys.

6 | FAILURE MECHANISMS BASED ON EXPERIMENTAL OBSERVATIONS

Based on the experimental observations, the theoretical failure mechanisms for Series I–IX are evaluated. DIC measurements have shown that a failure mechanism similar to Mechanism B, but with a relatively large crack opening in one diagonal crack prior to the first peak load, governs independently of the height of the key. Figure 9 shows Aramis recordings of the cracking process of specimen III2, which according to the theoretical calculations should reach the first peak load-carrying capacity by development of Mechanism A. It appears that diagonal cracks develop even before the first peak (see Figure 9a), and the relative displacements during failure take place in one of the existing diagonal cracks (see development from b to c in Figure 9). The crack opening of the diagonal cracks prior to first peak can be determined from Aramis measurements. Figure 10 shows examples of recorded crack opening of the largest diagonal crack (crack opening only in the longitudinal direction of the joint is shown). It appears that the crack opening before first peak load, P_{FP}, is approximately 0.4 mm, which is relatively large for mortar. This observation leads to the conclusion that the dissipation in the diagonal yield line (i.e., the mortar contribution) must be significantly reduced and thereby making a mechanism which is similar to Mechanism B more critical than Mechanism A.

In the following, two additional failure mechanisms are introduced, namely Mechanism D similar to Mechanism B (see Figure 7b), but omitting the mortar contribution from the diagonal yield line when calculating the rate of internal work, and Mechanism E based on Mechanism C, however, introducing a diagonal yield line (see Figure 11) and omitting the mortar contribution from the diagonal yield line in the calculation. For both cases, the contribution from the longitudinal locking bar is considered.

In practice, the length of a shear wall connection will at least be equal to the height of one storey, and for this reason, there will be many more shear keys in these connections as compared with the connections investigated in this study. When many shear keys are present, the significance of Mechanisms D and E will be limited. However, for the limited geometry of the test specimens, the influence of the boundary effect included in these mechanisms is relevant. The load-carrying capacity of Mechanism D is found to be:

$$\frac{\tau}{\nu f_c} = \frac{n-1}{2n}\frac{1-\sin\alpha}{\cos\alpha} + \frac{\Phi}{\nu}\tan\alpha + \frac{\Phi_L}{\nu} \tag{22}$$

The optimal angle of displacement is given as:

$$\alpha = \arcsin\left(1 - \frac{2n\Phi}{(n-1)\nu}\right), \quad \alpha \geq \varphi \tag{23}$$

For Mechanism E (see Figure 11), the load-carrying capacity, assuming $\alpha = \varphi$, is:

$$\frac{\tau}{\nu f_c} = \frac{n-1}{2n}\frac{d_k}{L_k}\frac{1-\sin\varphi}{\sin\gamma\cos(\gamma+\varphi)} + \frac{\Phi}{\nu}\tan(\gamma+\varphi) + \frac{\Phi_L}{\nu} \tag{24}$$

The critical angle, γ, of the inclined yield line in the keys is found as:

$$\gamma = \arctan\left(\frac{\cos\varphi}{\sin\varphi + \sqrt{1 + \frac{n}{(n-1)}\frac{\Phi}{\nu}\frac{2L_k}{d_k}\frac{\cos\varphi}{1-\sin\varphi}}}\right) \tag{25}$$

It should be noted, that Mechanisms B/D and E are only relevant for test Series I–IV, where the specimens had 2-on-2 loop connections. For specimens in Series P with 2-on-1 connections, the asymmetric reinforcement arrangement favors Mechanism A or C. This can be seen in Figure 12,

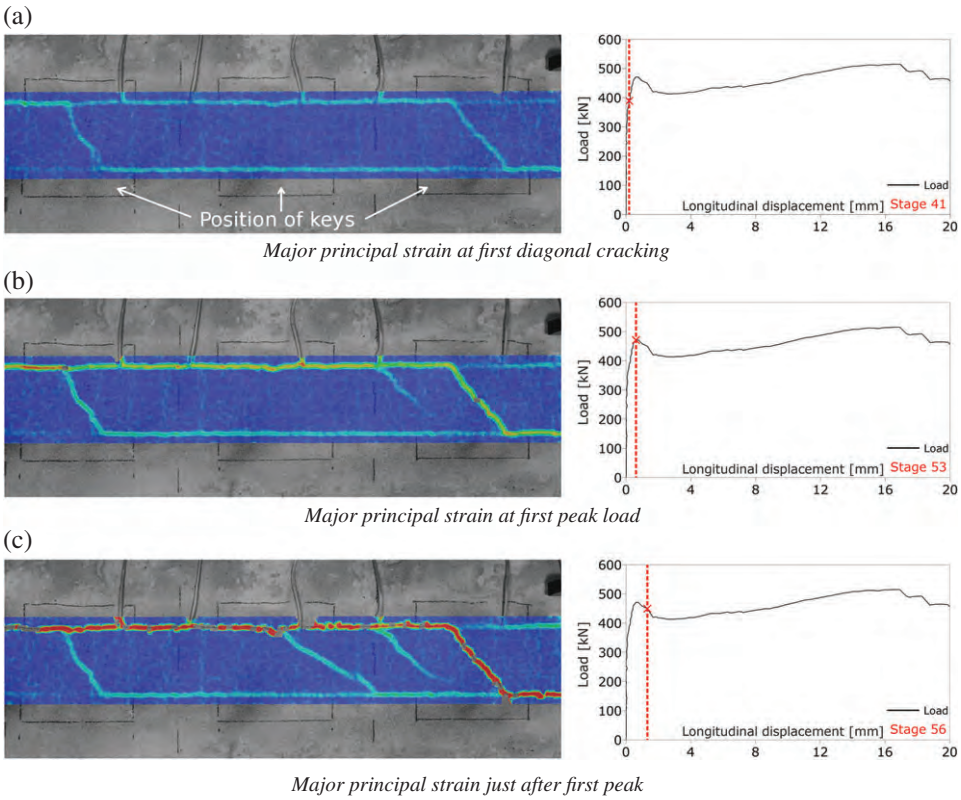

FIGURE 9 Aramis record of strain localization and cracking behavior of shear connection around first peak load, specimen III2.

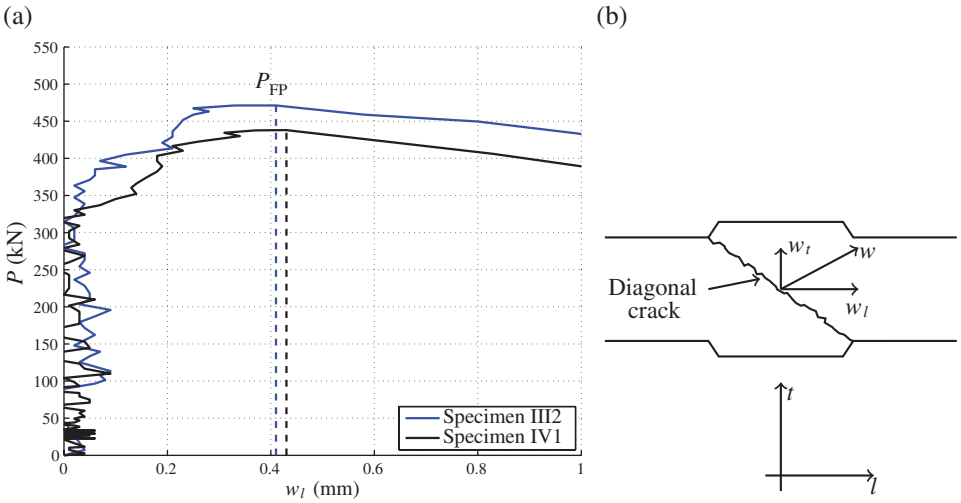

FIGURE 10 (a) Measured longitudinal crack opening in diagonal crack between shear keys and (b) definition of crack opening.

where Aramis recordings show that no diagonal cracks were present just after the first peak load.

7 | COMPARISON OF TESTS WITH THEORY

Table 4 shows the obtained experimental first peak loads as well as the theoretical determined values. For test specimens in Series I–IX, the theoretical capacity has been determined as the minimum value predicted from the five presented failure mechanisms. For specimens in Series P, only Mechanisms A and C are of interest. The yield strength of the reinforcement loops in Series P was $f_y = 509$ MPa, the width of the joint was $b = 80$ mm, and the remaining properties are given in Tables 1 and 2.

Figures 13 and 14 show a graphical comparison where the governing failure mechanisms are identified. The

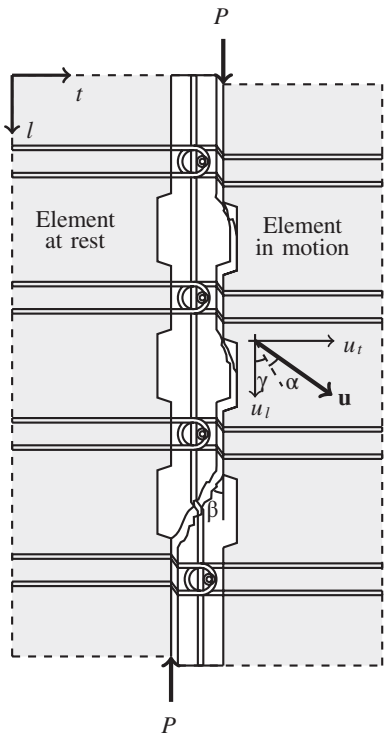

FIGURE 11 Mechanism E, based on experimental observations.

calculations are performed using the average compression strength of the grout mortar and the reinforcement strengths given in Table 2. Figure 13 shows a comparison in which the length of the shear keys, L_k, is varied and the height is kept constant at half the panel thickness. The results thereby compare with Series I–IV (Mechanism C is not critical). Figure 14 shows the comparison for varying key depths with constant key area, that is, a comparison for Series V–IX. It can be seen that the refined Mechanism D captures the behavior and predicts the load-carrying capacity of the specimens with large key depths. It can also be seen that Mechanism E explains the cracking behavior of the specimens with small key depths before Mechanism D becomes the governing mechanism for larger key depths. Table 4 also contains a summary of the observed as well as predicted failure mechanisms. If a failure mode including a diagonal crack was observed, the failure is regarded as B for the key cut off and E for the inclined key cut off. Mechanism D cannot be observed experimentally, but in fact an observed Mechanism B might relate to a theoretical Mechanism D. It can be seen from Table 4 that both Mechanisms B and E were observed in test Series VI. It should be noted

TABLE 4 Comparison of test results with theoretical values

	No.	P_{FP} [kN]	P_{cal} [kN]	$\frac{P_{FP}}{P_{cal}}$ [-]	Failure mechanism (Observed/Predicted)
P	1	344.24	291.12	1.18	C/C
	2	347.04	291.12	1.19	C/C
	3	342.49	297.16	1.15	C/C
	4	331.42	297.16	1.12	C/C
I	1	379.02	395.34	0.96	B/A
	2	416.59	403.29	1.03	B/A
II	1	366.40	412.67	0.89	B/A
	2	414.46	421.43	0.98	B/A
III	1	393.04	427.62	0.92	B/D
	2	473.52	433.99	1.09	B/D
IV	1	439.44	438.33	1.00	B/D
	2	478.17	455.20	1.07	B/D
V	1	475.24	500.73	0.95	E/E
	2	492.86	508.21	0.97	E/E
VI	1	527.09	538.50	0.98	E/D
	2	523.82	538.50	0.97	B/D
VII	1	549.17	538.50	1.02	B/D
	2	524.46	538.50	0.97	B/D
VIII	1	507.05	538.50	0.94	B/D
	2	516.97	538.50	0.96	B/D
IX	1	526.53	538.50	0.98	B/D
	2	527.59	538.50	0.98	B/D
Mean				1.01	
Standard deviation				0.08	

that a smaller value of φ changes the transition point toward a larger key depth. However, an in-depth study of the internal angle of friction for mortar is needed to clarify the property and perhaps also the validity of the normality condition for mortar materials.

Figure 13 shows the key area as the ratio between the area of a single key compared with the joint area, A_t. The joint area is calculated using the center distance of the reinforcement loops, given as s in Figure 3, and the height of the specimen, t. It can be seen that the average shear stress can be higher for a smaller relative key area, as expected considering softening effects in the mortar material. Generally, good agreement is found between the test results and the calculations. In Figures 13 and 14, the capacity as predicted by the Eurocode 2 formula for indented interfaces using average material strengths (tensile strength of concrete calculated by use of the EC2 method), without partial safety

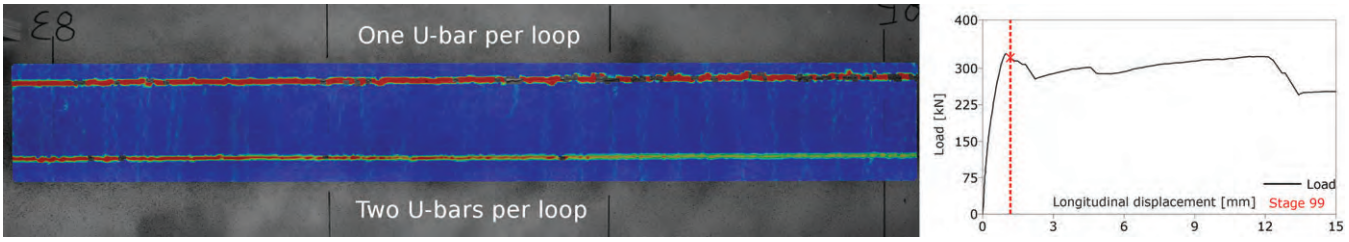

FIGURE 12 Major principal strain distribution just after first peak load, P_{FP}, of '2-on-1' specimen (specimen P4) from pilot test series.

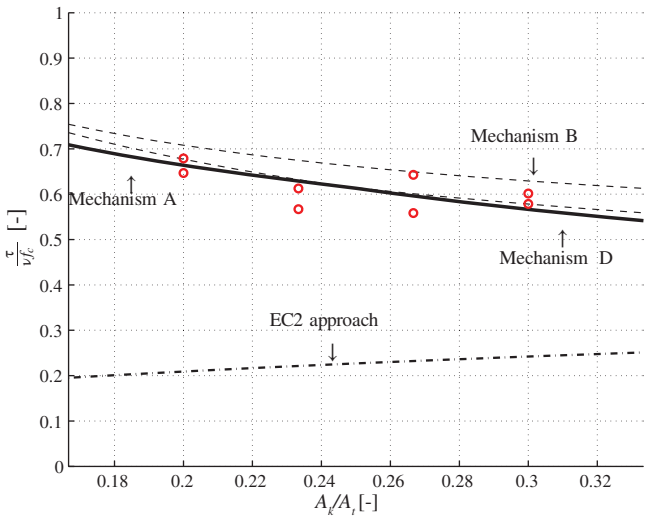

FIGURE 13 Comparison of theory with results for series I-IV, f_c, average = 33.0 MPa.

factors has been included as well. It is clearly seen that the empirical formula of Eurocode 2 is too conservative when applied to the new connection design. In this context, it should be noted that the Eurocode 2 method does not take into account the specific key geometry.

8 | CONCLUSIONS

A new and construction-friendly loop connection for the assembly of precast shear wall panels has been developed and tested. The structural performance of the new connection, in terms of ductility, is superior to that of the conventional design. A ductility index has been introduced in order to evaluate and compare the performance of the developed design with that of the conventional design. For the tested designs, the first peak on the response curve has been identified as the load that causes failure of the shear keys. Theoretical failure mechanisms have been established and used to derive upper-bound plasticity solutions to calculate the first peak capacity. The failure mechanisms for the tested connections have been refined based on observations from the experiments and the results of DIC analysis.

The significance of the key dimensions has been addressed and the influence of the key height and depth on the failure mode has been outlined. The developed models predict the transition point between the two main failure mechanisms, in terms of key depth: complete key cutoff or inclined key cutoff (see Figure 14). The refined Mechanisms D and E, relevant for the limited geometry tested, captured, and explained the experimental observations. For the design of longer connections, as those found in practice, the theoretical basic Mechanisms A, B, and C presented in Figure 7, will be sufficient.

It can be concluded that the new connection design is a feasible and promising practical solution that should be subjected to further investigation with the perspective of replacing the conventional solution. To adapt the new design for practical use, it is necessary to clarify a number of issues, including:

- Detailed characterization of the properties of grout mortar
- Test of a wider range of U-bar diameters and possibly a variation of the geometry of the U-bars
- Test of the tensile capacity of the connection
- Test of anchorage properties of the lacer reinforcement
- Investigation and modeling of the increase in load-carrying capacity after the first peak

ACKNOWLEDGMENTS

The experimental program was financially supported by the Danish Association for Precast Concrete Elements and the

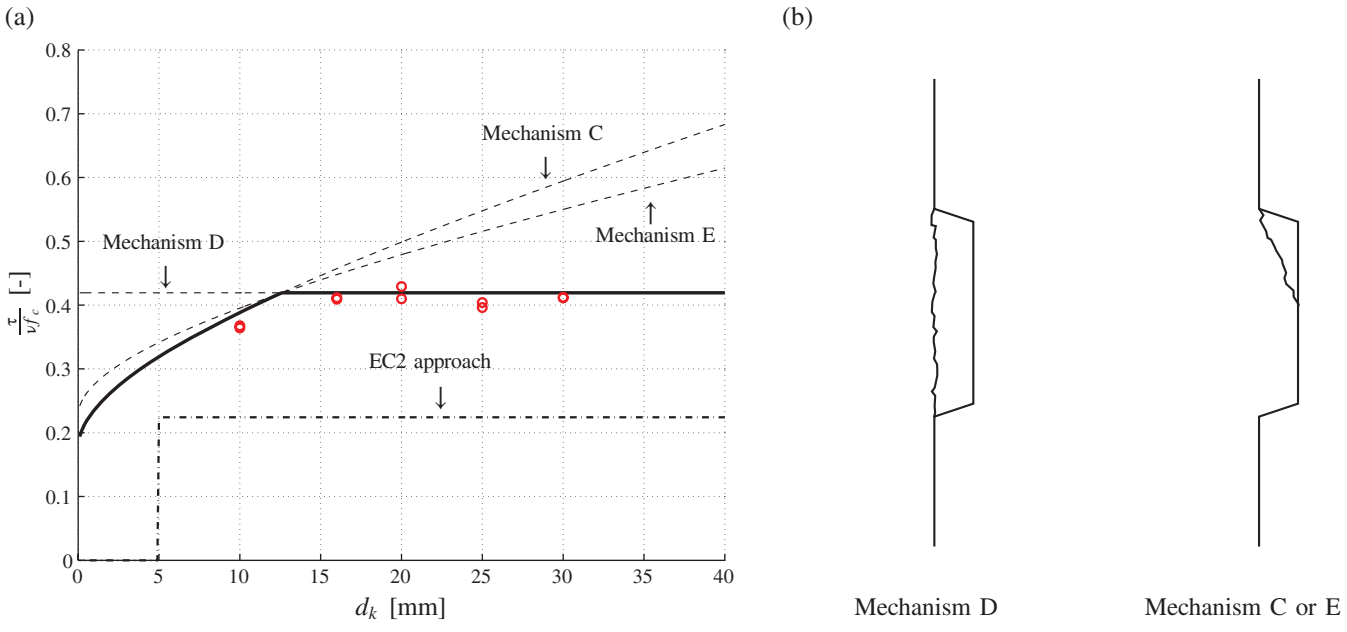

FIGURE 14 (a) Comparison of theory with results for series V-IX, f_c, average = 31.0 MPa, and (b) main failure modes.

COWI Foundation. The test elements were produced at CRH Concrete and the experimental work was conducted with support from students at DTU Civil Engineering. Rune Pedersen, B.Eng., and Mads Herløv, B.Eng., contributed with test Series R and P in their bachelor thesis, J. Svejgaard, M.Sc., contributed with test Series I–IV, and L. Øvrelid, M.Sc., contributed with test Series V–IX in their master theses. Finally, the use of double-headed studs as lacer bars instead of conventional stirrups was suggested by Tim Gudmand-Høyer, Ph.D. The authors gratefully acknowledge these valuable contributions.

NOTATIONS

A_d	area of diagonal yield line
A_i	area of inclined yield line in a shear key
A_j	area of yield line
A_k	area of one shear key
A_s	reinforcement area per loop
A_{sL}	reinforcement area of locking bar
A_t	area of joint
b	width of joint
D	internal bend diameter of loops
D_I	ductility index
d_k	depth of shear key
$d_{\max}$	maximum aggregate size in mortar
f_c	compression strength
f_y	yield strength of U-bar
$f_{y,\text{Lacer}}$	yield strength of lacer bar
f_{yL}	yield strength of locking bar
h_k	height of shear key
L	total length of joint
L_k	length of shear key
n	number of shear keys
P	shear load
P_{cal}	theoretically calculated shear capacity
P_{FP}	first peak load
P_{U}	ultimate load
s	distance between loops
t	panel thickness
u	displacement vector
u_l	longitudinal component of **u**
u_t	transverse component of **u**
w	crack opening
w_l	longitudinal crack opening
w_t	transverse crack opening
W_E	rate of external work
W_I	rate of internal work
W_I^C	rate of internal work from concrete
W_I^s	rate of internal work from U-bars
W_I^{sL}	rate of internal work from locking bar
α	angle of displacement vector
β	slope of diagonal yield line
δ	longitudinal displacement
$\delta_{\max}$	displacement capacity
δ_{FP}	displacement at first peak
γ	slope of inclined yield line in a shear key
ϕ	U-bar diameter
ϕ_{Lacer}	lacer bar diameter
ϕ_L	locking bar diameter
φ	internal angle of friction
Φ	reinforcement degree of loop connection
Φ_L	reinforcement degree of locking bar
ν	effectiveness factor
τ	shear stress

REFERENCES

1. Dahl KKB. Bella Sky Hotel: taking precast concrete to the limit. *Struct Concr*. 2014;15(4):441-447.
2. Flindt Jørgensen K. Bella Sky Hotel: exploring the potential in precast concrete design. *Struct Concr*. 2015;16(4):449-457.
3. *fib* Bulletin 43. Structural connections for precast concrete buildings, fédération international du béton (*fib*), 2008.
4. Hansen K, Kavyrchine M, Melhorn G, Olesen SØ, Pume D, Schwing H. *Keyed shear joints: SBI rapport 97, Technical report*. Danish Building Research Institute, Copenhagen; 1976.
5. Halasz R, Tantow G. Schubfestigkeit der Vertikalfugen im Grosstafelbau. In: *Berichte aus der Bauforschung, H. 39*. Berlin, Germany: Verlag Wilhelm Ernst & Sohn, Berlin; 1966.
6. Cholewicki A. Loadbearing capacity and deformability of vertical joints in structural walls of large panel buildings. *Build Sci*. 1971;6(9):163-184.
7. Pommeret M. Le comportement sous charges ou déformations répétées alternées des joints verticaux entre panneaux préfabriqués. Technical Report. Saint Remy les Chevreuxe, Centre expérimental de recherches et d'études du batiment et des travaux publics; 1972.
8. Fauchart J, Cortini P. Étude expérimentale de joints horizonraux entre panneaux préfabriqués pour murs de batiments. Annales de L´Institut Technique du Batiment et Des Travaux Publics, Paris, 1972.
9. Nimityongskul P, Liu HY. Vertical shear strength of joints in prefabricated loadbearing walls. *Hous Sci*. 1980;4(2):137-157.
10. Chakrabarti SC, Bhise NN, Sharma KN. Failure criterion of vertical shear key joints in prefabricated wall panels. *Indian Concr J*. 1981;55(3):63-67.
11. Abdul-Wahab HM. An experimental investigation of vertical castellated joints between large concrete panels. *Struct Eng*. 1986;64B(4):93-99.
12. Serrette RL, Rizkalla SH, Heuvel JS. Multiple shear key connections for load-bearing shear wall panels. *PCI J*. 1989;34(2):104-120.
13. Rossley N, Aziz F, Chew H, Farzadnia N. Behaviour of vertical loop bar connection in precast wall subjected to shear load. *Aust J Basic Appl Sci*. 2014;8(1):370-380.
14. Vaghei R, Hejazi F, Taheri H, Jaafar MS, Ali A. Evaluate performance of precast concrete wall to wall connection, APCBEE Procedia 9 (ICBEE 2013); 2014;9:285–290.
15. CEN. *EN1992-1-1 Eurocode 2: Design of Concrete Structures – Part 1–1: General Rules and Rules for Buildings*. 3rd ed. European Committee for Standardization, Brussels, 2004.
16. Kaneko Y, Connor JJ, Triantafillou TC, Leung CK. Fracture mechanics approach for failure of concrete shear keys. I: Theory. *J Eng Mech*. 1993;119(4):681-700.
17. Kaneko Y, Connor JJ, Triantafillou TC, Leung CK. Fracture mechanics approach for failure of concrete shear keys. II: Verification. *J Eng Mech*. 1993;119(4):701-719.
18. Kaneko Y, Mihashi H. Analytical study on the cracking transition of concrete shear key. *Mater Struct*. 1999;32(217):196-202.
19. Jensen BC. *On the Ultimate Load of Vertical, Keyed Shear Joints in Large Panel Buildings. Technical Report*. Lyngby, Denmark: Institute of Building Design, Technical University of Denmark, Lyngby; 1975.
20. Chakrabarti SC, Nayak GC, Paul DK. Shear characteristics of cast-in-place vertical joints in story-high precast wall assembly. *ACI Struct J*. 1988;85(1):30-45.
21. Abdul-Wahab HM, Sarsam SYH. Prediction of ultimate shear strength of vertical joints in large panel structures. *ACI Struct J*. 1991;88(2):204-213.

22. Christoffersen J, *Ultimate Capacity of Joints in Precast Large Panel Concrete Buldings, Series R No. 25* [Ph.D. thesis]. Lyngby: Technical University of Denmark, Department of Structural Engineering and Materials, Technical University of Denmark, Lyngby; 1997.
23. Jørgensen HB, Hoang LC. *Load Carrying Capacity of Keyed Joints Reinforced with High Strength Wire Rope Loops*. Proceedings of fib symposium: Concrete - Innovation and Design, Copenhagen; 2015.
24. Jørgensen HB, Hoang LC. Tests and limit analysis of loop connections between precast concrete elements loaded in tension. *Eng Struct*. 2013;52:558-569.
25. GOM: *Aramis User Manual - Software v6.1 and higher*. Braunschweig: GOM Optical Measuring Techniques; 2009.
26. Pereira EB, Fischer G, Barros JAO. Image-based detection and analysis of crack propagation in cementitious composites. In: Leung C, Wan KT, eds. Paper presented at: Proceedings of the International RILEM Conference on Advances in Construction Materials Through Science and Engineering; 2011; 1–8; HongKong, China.
27. Engström B. *Ductility of Tie Connections in Precast Structures* [Ph.D. thesis]. Goteborg: Chalmers University of Technology; 1992.
28. Jensen BC. *Nogle plasticitetsteoretiske beregninger af beton og jernbeton (English: Some Applications of Plastic Analysis to Plain and Reinforced Concrete), Report 111* [Ph.D. thesis]. Copenhagen, Denmark: Technical University of Denmark, Lyngby; 1976.
29. Nielsen MP, Hoang LC. *Limit Analysis and Concrete Plasticity*. 3rd ed. CRC Press, Taylor & Francis Group, Boca Raton, Florida, US; 2011.
30. Dahl KKB. *A Failure Criterion for normal and High Strength Concrete, Technical Report*. Lyngby, Denmark: Technical University of Denmark; 1992.
31. Nielsen CV. Triaxial behavior of high-strength concrete and mortar. *ACI Mater J*. 1998;95(2):144-151.
32. Jørgensen HB. *Strength of Loop Connections between Precast Concrete Elements* [Ph.D. thesis]. Denmark: University of Southern Denmark, Department of Technology and Innovation, Odense; 2014.
33. Zhang J-P. Diagonal cracking and shear strength of reinforced concrete beams. *Mag Concr Res*. 1997;49(178):55-65.

AUTHOR'S BIOGRAPHIES

Jesper Harrild Sørensen
M.Sc., PhD student
Department of Civil Engineering
Technical University of Denmark
Brovej, Building 118
2800 Kgs. Lyngby,
Denmark
jhaso@byg.dtu.dk

Linh Cao Hoang
Professor, PhD
Department of Civil Engineering
Technical University of Denmark
Brovej, Building 118
2800 Kgs. Lyngby,
Denmark
linho@byg.dtu.dk

John Forbes Olesen
Associate Professor, PhD
Department of Civil Engineering
Technical University of Denmark
Brovej, Building 118
2800 Kgs. Lyngby,
Denmark
jfo@byg.dtu.dk

Gregor Fischer
Associate Professor, PhD
Department of Civil Engineering
Technical University of Denmark
Brovej, Building 118
2800 Kgs. Lyngby,
Denmark
gf@byg.dtu.dk

How to cite this article: Sørensen JH, Hoang LC, Olesen JF, Fischer G. Test and analysis of a new ductile shear connection design for RC shear walls. *Structural Concrete*. 2017;18:189–204. https://doi.org/10.1002/suco.201600056

Paper III

"Test and lower bound modeling of keyed shear connections in RC shear walls"

Jesper H. Sørensen, Morten A. Herfelt, Linh C. Hoang, Aurelio Muttoni

Published in: *Engineering Structures (2018), 155:115-126*

Engineering Structures 155 (2018) 115–126

Contents lists available at ScienceDirect

Engineering Structures

journal homepage: www.elsevier.com/locate/engstruct

Test and lower bound modeling of keyed shear connections in RC shear walls

Jesper Harrild Sørensen[a,*], Morten Andersen Herfelt[a,b], Linh Cao Hoang[a], Aurelio Muttoni[c]

[a] Technical University of Denmark, Department of Civil Engineering, Brovej, Bygning 118, 2800 Kgs. Lyngby, Denmark
[b] Niras A/S, Sortemosevej 19, 3450 Allerød, Denmark
[c] École Polytechnique Fédérale de Lausanne, ENAC, Station 18, CH-1015 Lausanne, Switzerland

ARTICLE INFO

Keywords:
Keyed shear connections
Precast concrete
Push-off tests
Rigid-plasticity
Lower bound solutions

ABSTRACT

This paper presents an investigation into the ultimate behavior of a recently developed design for keyed shear connections. The influence of the key depth on the failure mode and ductility of the connection has been studied by push-off tests. The tests showed that connections with larger key indentations failed by complete key cut-off. In contrast, connections with smaller key indentations were more prone to suffer local crushing failure at the key corners. The local key corner crushing has an effect on the load-displacement response, which is relatively more ductile. In addition to the tests, the paper also presents lower bound modeling of the load carrying capacity of the connections. The main purpose of the lower bound model is to supplement an already published upper bound model of the same problem and thereby provide a more complete theoretical basis for practical design. The two models display the same overall tendencies although identical results are not possible to obtain, due to differences in the basic assumptions usually made for upper and lower bound analysis of connections. It is found that the test results, consistent with the extremum theorems of plasticity, are all lying within the gap between the upper and the lower bound solution. The obtained results finally lead to a discussion of how the two models can be used in practice. The primary merit of the upper bound model lies in its simplicity (a closed-form equation). On the other hand, the lower bound model provides safe results, but is more complicated to apply. It is therefore argued that the upper bound model may be used in cases, where calibration with tests has been carried out. The lower bound model should be applied in situations, where the design deviates significantly from the configurations of the available tests.

1. Introduction

A new design for keyed shear connections between precast wall elements has recently been proposed and the structural performance has been experimentally investigated [1]. The conceptual layout of the design can be seen in Fig. 1. Unlike the conventional solution, where the overlapping U-bars are looped in the horizontal plane [2,3], this new layout consists of U-bars looped in vertical planes. The solution contains double T-headed bars (lacer bars) placed perpendicular to the plane of the wall elements to ensure efficient transfer of tension between the U-bars [4]. It is also possible to add a vertical locking bar similar to the conventional design of keyed shear connections. As shown in [1], the new design has a much more ductile shear behavior than the conventional solution and can in addition be more construction-friendly in case of vertically lowered panels. Thus, the new design has the potential to be used in e.g. high-rise buildings in cases where in situ walls are replaced by precast concrete elements.

The experimental results reported in [1] showed that the geometry of the shear keys, and in particular the depth of the keys, plays an important role for the ductility of the connection. In addition, the ability of the U-bars to develop yielding is decisive for a desirable behavior of the connection in the ultimate limit state. Inspired by experimental observations, rigid-plastic upper bound solutions have been developed for prediction of the capacity of the connection [1].

The aim of this paper is twofold. First and foremost, there is a need for additional tests to explore the behavior of the new design and in details study the influence of the key depth. Therefore, an in-depth experimental investigation of the failure of the shear keys has been carried out. To widen the experimental database (not only with respect to the number of tests but also with respect to parameter variations) U-bar diameters smaller than those used in the first test campaign have been investigated. Secondly, from an analytical point of view, there is a need to establish lower bound solutions for the shear capacity of the connections in order to evaluate the already developed upper bound

* Corresponding author.
E-mail address: jhaso@byg.dtu.dk (J.H. Sørensen).

https://doi.org/10.1016/j.engstruct.2017.11.004
Received 13 June 2017; Received in revised form 3 November 2017; Accepted 6 November 2017

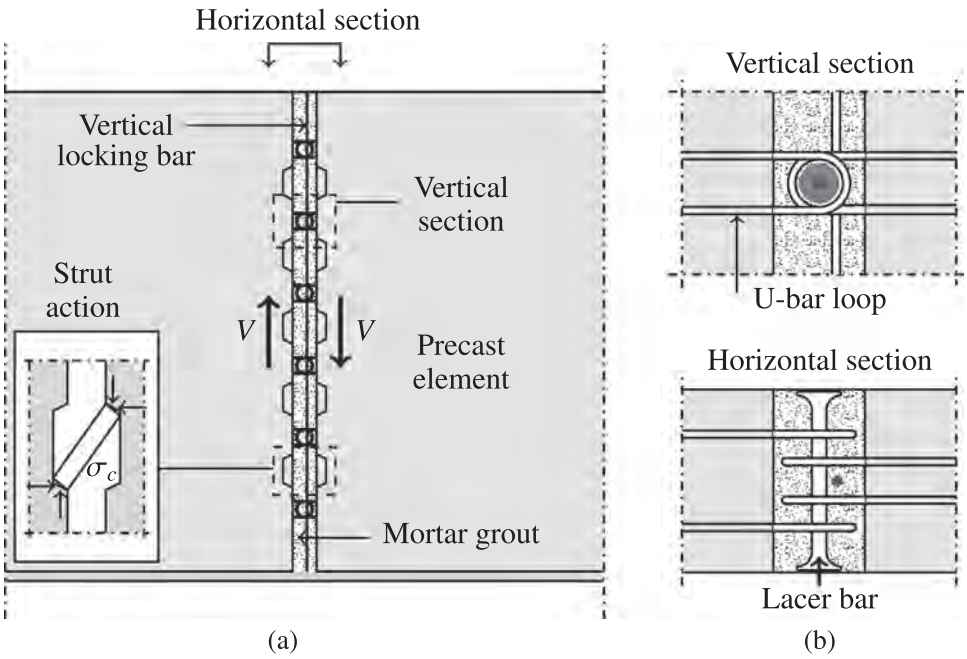

Fig. 1. (a) Shear connection between RC precast wall elements and (b) conceptual design of new connection solution (illustrations from [4]).

solutions [1]. The set of solutions can be used to bracket the theoretically exact solution from below and above, which is extremely useful for practice.

For looped connections, upper bound solutions are relatively straight forward to establish when based on observed failure modes [1,5,6], while optimal lower bound solutions are more difficult to develop. Simple lower bound solutions for keyed shear connections have e.g. been proposed by Christoffersen [7] and further developed in Nielsen and Hoang [8]. However, the models contain only single uniaxial strut action and are in many cases too conservative. Recently, Herfelt et al. [9] presented a numerical framework for obtaining optimal lower bound solutions based on finite element limit analysis (FELA). The numerical tool calculates the optimal stress distribution and the corresponding failure mechanism in the joint mortar. In this paper the results obtained by FELA will be used as inspiration to establish analytical lower bound solutions.

Compared to the single strut solution [7], the following numerical and analytical models utilize combinations of struts with different inclinations to optimize the theoretical load carrying capacity. In addition, the ability of the grout-to-panel interface to transfer shear stresses is utilized which eventually leads to non-hydrostatic biaxial stress conditions in the nodal zones. The stresses in the nodal zones at the key corners are modeled by use of the concept of homogeneous stress fields. The concept was treated e.g. in Refs. [10–12].

2. Experimental program

The experimental program comprised 12 push-off specimens with identical loop configuration and with a variation of the key depth, d_k, from 10 mm to 20 mm. Compared to the first test campaign [1], this program used U-bars with a diameter of 6 mm instead of 8 mm and the shear keys in all specimens had a height equal to the thickness of the precast element, i.e. $h_k = t$, which enabled identification of the local failure of the individual shear keys by use of digital image correlation (DIC). The general geometry of the test specimens can be seen in Fig. 2 and the material properties are given in Tables 1 and 2. The specimen identification refers to the depth of the shear keys (e.g. D10 designates a key depth of $d_k = 10$ mm). Each design was replicated twice, denoted A and B. The connections were grouted with a mortar with a maximum aggregate size of 4 mm and a vertical locking bar was included to minimize the extent of diagonal cracking between the shear keys. The

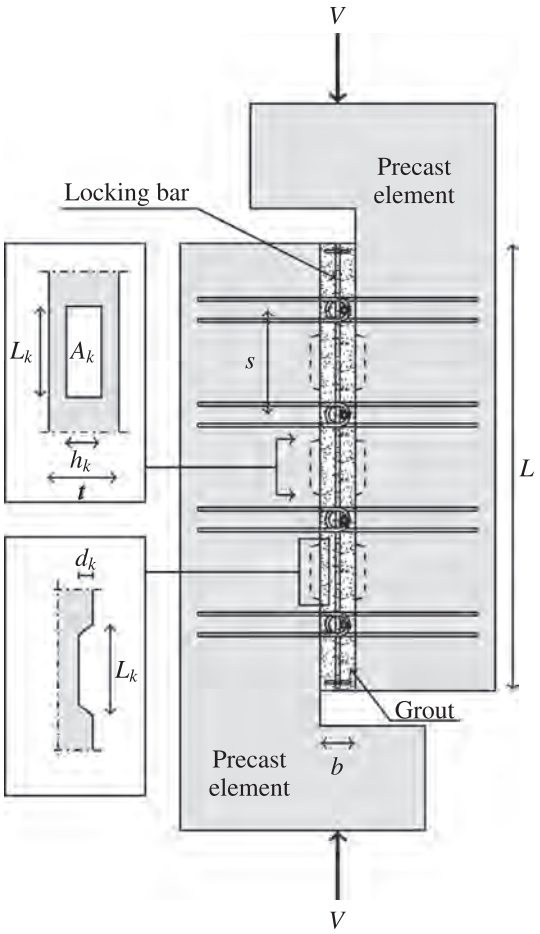

Fig. 2. General layout of push-off test specimens (illustration from [1]).

Table 1
Specifications of the test specimens, including material properties.

	No.	f_c [MPa]	L_k [mm]	A_k [mm^2]	d_k [mm]	A_s [mm^2]	V_{FP} [kN]
D10	A	44.6	120	24000	**10**	113	448.56
	B	44.6	120	24000	**10**	113	448.62
D12	A	44.6	120	24000	**12**	113	471.74
	B	44.6	120	24000	**12**	113	496.36
D14	A	44.6	120	24000	**14**	113	510.91
	B	44.6	120	24000	**14**	113	519.16
D16	A	44.6	120	24000	**16**	113	543.30
	B	44.6	120	24000	**16**	113	541.57
D18	A	42.0	120	24000	**18**	113	540.73
	B	42.0	120	24000	**18**	113	537.50
D20	A	42.0	120	24000	**20**	113	526.62
	B	42.0	120	24000	**20**	113	517.03

f_c refers to the compressive strength of the grout measured on $\phi 100 \times 200$ mm cylinders.

A_s describes the reinforcement area per loop connection, i.e. $4\frac{\pi}{4}\phi^2$.

Table 2
Material properties and geometric values.

Description	Symbol	
U-bar diameter	ϕ	6 mm
Yield strength of U-bar	f_y	517 MPa
Lacer bar diameter	ϕ_{Lacer}	12 mm
Yield strength of lacer bar	$f_{y,Lacer}$	552 MPa
Internal bend diameter of loops	D	45 mm
Width of Joint	b	80 mm
Distance between loops	s	300 mm
Inclination of key corner	θ_k	$\arctan\frac{1}{2}$
Total length of joint	L	1280 mm
Max aggregate size in mortar	d_{max}	4 mm
Diameter of locking bar	ϕ_L	12 mm
Yield strength of locking bar	f_{yL}	599 MPa
Panel thickness	t	200 mm
Strength of precast panels	$f_{c,element}$	58.2 MPa

U-bar loops were designed according to Refs. [4,6] to transfer the full yield force of the U-bars.

2.1. Test results

Fig. 3 shows examples of typical tested load-displacement relationships. The depicted displacements correspond to relative longitudinal displacements between the two precast elements, measured at both ends of the connection and averaged. The figure shows two different behaviors depending on the failure mode of the shear keys. The plots in Fig. 3(a) are the results of specimens with smaller key depths (d_k = 10–16 mm) where failure took place as a local shearing of the key corners (as illustrated in the graph). For larger key depths (d_k = 16–20 mm), complete shearing of the shear keys governed the first peak load, which leads to the load-displacement characteristics shown in Fig. 3(b).

The transition from key corner shearing to complete key shearing was dependent on a number of factors, including the geometry of the shear keys, the material properties of the mortar, and the strength of the reinforcement. From post-test examinations it was found that specimens with d_k = 16 mm could fail both by local key corner shearing (D16B) and by complete failure of the shear key (D16A). This indicates that the theoretical transition between the two failure modes for this particular test series takes place at approximately this key depth. The load–displacement relationships of D16A and D16B are both shown in Fig. 3. It was found that both had comparable first peak loads, V_{FP} (see Table 1). However, the residual load level after first peak was higher for specimen D16B which experienced key corner shearing. This was a general observation that specimens suffering local key corner shearing had a more ductile load-displacement relationship (i.e. residual load level closer to first peak load). In contrast to this, a relatively larger drop of the load immediately after first peak was observed for all the specimens, which failed by complete key shearing. Both types of failure were accompanied by development of diagonal cracks in the grout. Fig. 4 shows examples of local failure of the keys in combination with diagonal cracks which formed the global failure mechanism. Post-test examinations also showed large plastic deformations in the U-bars. This observation confirms that the design of the loop connection (i.e. the overlapping length, the diameter of lacer bar and the internal bend diameter of the U-bars) did enable transfer of the yield capacity of the U-bars through the overlap.

It was generally observed that the first peak load, V_{FP}, increased with increasing key depth until complete shearing of the keys becomes the critical failure mode. Then V_{FP} remained practically constant and independent of a further increase of the key depth, cf. Table 1. The residual load level after first peak appeared somewhat constant within the two types of failure and must thereby be related to the layout and the properties of the loop reinforcement, which were kept constant in this study.

Based on the experimental results, it seems that connections in practice should be designed to be governed by local shearing of the key corners, as this minimizes the difference between first peak load and the residual load level.

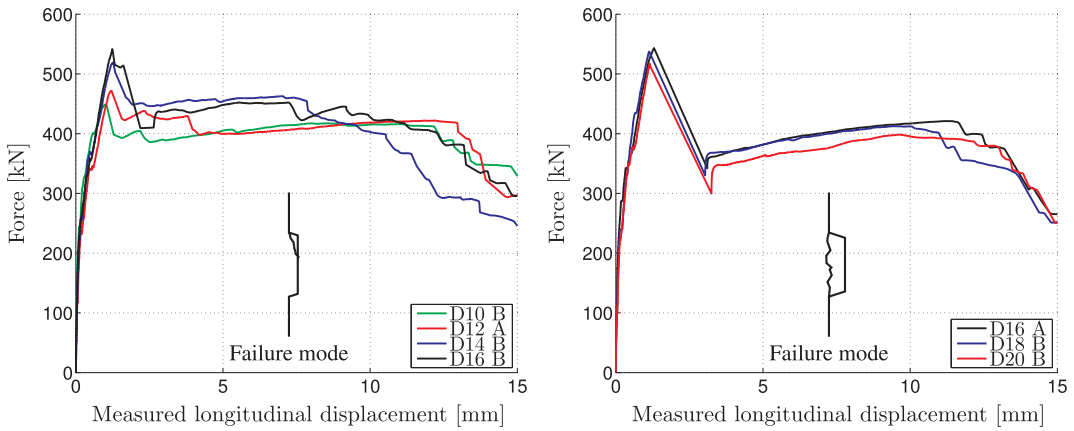

(a) *Smaller key depths, failure by key corner shearing* (b) *Larger key depths, failure by complete key shearing*

Fig. 3. Experimentally recorded load-displacement curves.

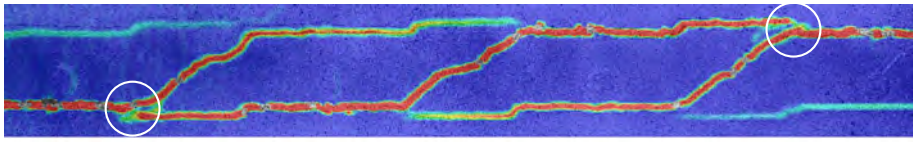

(a) Specimen D10 A - key corner shearing

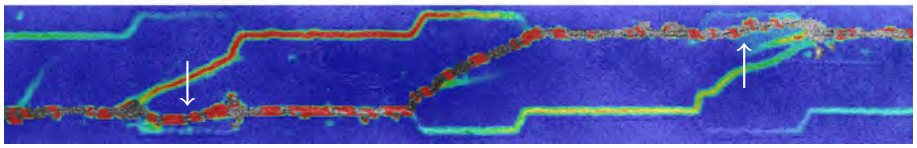

(b) Specimen D20 A - complete key shearing

Fig. 4. Identification of failure modes just after first peak load by use of digital image correlation.

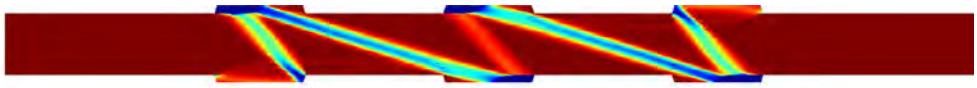

(a) $d_k = 10\ mm,\ V_{FP} = 340.5kN$

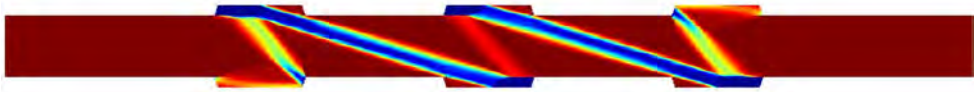

(b) $d_k = 14\ mm,\ V_{FP} = 404.1kN$

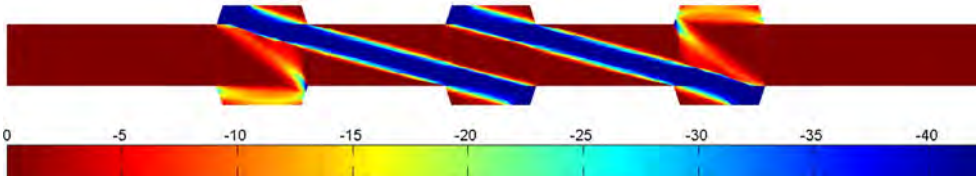

(c) $d_k = 20\ mm,\ V_{FP} = 486.1kN$

Fig. 5. Distribution of the smallest principal stress (MPa, tension positive) in connections with $d_k = 10$, 14 and 20 mm, obtained by FELA, $f_c = 42$ MPa.

3. Rigid-plastic analysis

The first peak load, V_{FP}, can be estimated by use of upper or lower bound models assuming rigid-plastic material behavior. Rigid-plastic modeling can also be used to obtain an estimate of the inelastic load–displacement curve. This, however, requires a second order plastic analysis where change of geometry and large displacements are taken into account [13–16].

The objective of this paper is limited to the calculation of V_{FP}. As mentioned, an upper bound model has already been established [1]. The model predicts the shear capacity of keyed connections in a satisfactory manner provided that an effectiveness factor, ν, is introduced. The problem, however, with a pure upper bound approach is that it remains an open question whether the adopted effectiveness factor, obtained by calibration with tests, to a significant extent also accounts for the fact, that the developed upper bound model is not necessarily the exact/correct one. To answer the question and eventually to evaluate the developed upper bound model, lower bound solutions will be established in the following. This includes both numerical solutions as well as analytical ones.

4. Numerical lower bound solutions based on finite element limit analysis (FELA)

The main purpose of the performed numerical lower bound calculations is to provide inspiration for the type of stress field to be adopted in an analytical lower bound model. FELA can be considered as a special case of the finite element method, where a rigid-plastic material model is assumed. For lower bound solutions, a set of constraints ensure that the equilibrium conditions and the yield criteria are satisfied, i.e. a statically admissible and safe stress field, while the load is sought to be maximized. A detailed description of the numerical framework for modeling of keyed connections can be found in Herfelt et al. [9] and a summary of the concept is given in Appendix A. Here only the main assumptions are needed for comparison with the analytical model.

The relevant parameters for the numerical analysis are the geometry of the shear keys, the mechanical degree of transverse reinforcement, interface properties, and the grout properties. Based on the experimental results the transverse reinforcement degree is determined by the yield force of the U-bars. In the model, the overlapping loops are simplified as continuous reinforcement crossing the connection. Moreover, plane stress condition is assumed and the mortar is modeled as a modified Coulomb material without tensile strength. For the interface between the grout and the precast concrete, a Coulomb friction criterion is assumed with a friction coefficient, $\mu = 0.75$ (corresponding to smooth casting joints [8,17]) and a neglectable cohesion. However, friction is only considered active in the indented areas. The main argument for this is that the normal stress required to activate friction stems from tension in the transverse reinforcement, which represents a form of passive confinement in contrast to active confinement from an external normal force. Hence, since the load is anticipated to be carried mainly by strut action between the shear keys (when no active normal force is applied), then only the indented areas (which experiences compression from the strut action) can transfer friction. The

longitudinal locking bar has not been included in the numerical model, as it is judged to entail stress fields that, at the current stage, are too complicated for the initial establishment of analytical lower bound models.

Fig. 5 shows the calculated distribution of the smallest principal stress (maximum compressive stress) in the joint mortar for some specimens from the experimental program. The stress field is only visualized for the joint mortar, since the precast elements in the experimental program as well as in the numerical model had over-strength. In the calculations, the strength of the mortar was taken as f_c, according to Table 1. This entails that the effectiveness factor, ν, was chosen as unity (note that the absolute value of ν is not important when the results are used only to compare with the analytical solutions).

From the optimized stress distributions, it can be seen that the load transfer mechanism consists of a combination of compression struts spanning over one or two shear keys, i.e. struts with different inclinations. This type of stress field is obviously more complicated than the single strut solutions [7]. The numerical results will in the following form the basis for how to choose the stress field in an analytical lower bound solution and finally the results of the two methods will be compared.

5. Analytical lower bound solutions

Inspired by the results of FELA, an analytical model for the load carrying capacity of keyed shear connections will be established. Some simplifications have to be introduced in order to carry out the analytical calculations. Two basic stress fields are considered, in the following denoted as Solution 1 and Solution 2, and the contribution from the locking bar is disregarded. Solution 1 consists of parallel struts spanning over a single shear key (Fig. 6). Solution 2 combines struts spanning over one shear key and two shear keys, respectively (Fig. 8). The struts carry uniaxial compression, while the nodal zones are stressed in biaxial compression. A lower bound for the load carrying capacity will in this context be taken as the larger of the two solutions. It turns out that Solution 1 is optimal for smaller key depths, whereas Solution 2 is optimal for larger key depths. For a further increase of the key depth, the load may be carried almost completely by struts spanning over two shear keys without combination with struts over a single key, see e.g. Fig. 5(c). This is in accordance with the model of Christoffersen [7] (see also Nielsen and Hoang [8]).

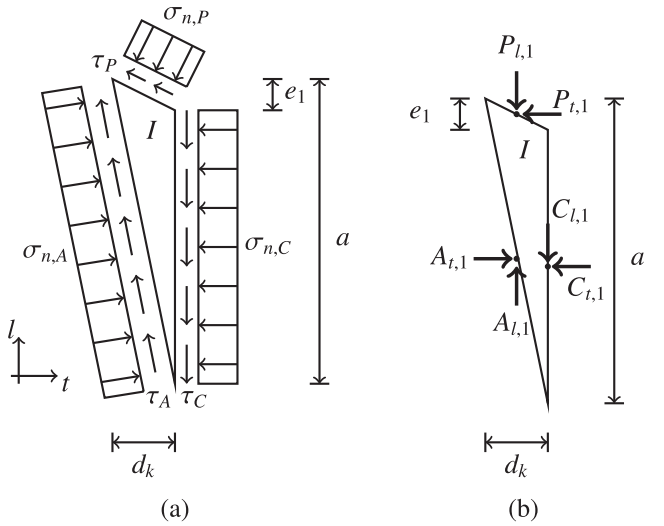

Fig. 7. (a) Stresses along boundaries of Triangle *I* (Solution 1) and (b) resultants of stresses on boundaries.

5.1. Solution 1: Single struts spanning over one shear key

For the purpose of analysis, a l–t coordinate system, referring to the longitudinal and transverse directions of the connection, is defined, see Fig. 6. The following relations for the geometrical parameters shown in Fig. 6 are introduced:

$$\tan\theta_k = \frac{e_1}{d_k} \tag{1}$$

$$\tan\theta_{A,1} = \frac{L_k - e}{b} \tag{2}$$

$$a = e - d_k \tan\theta_{A,1} \tag{3}$$

In Fig. 6(b) the parameter e is an optimization parameter related to the strut width. The capacity obtained by this solution is governed by either the compressive strength of the strut or the stress state in the key corner (in the following denoted Triangle *I*), which can be assessed as a homogeneous stress field. The stress components for this solution will be calculated in the following.

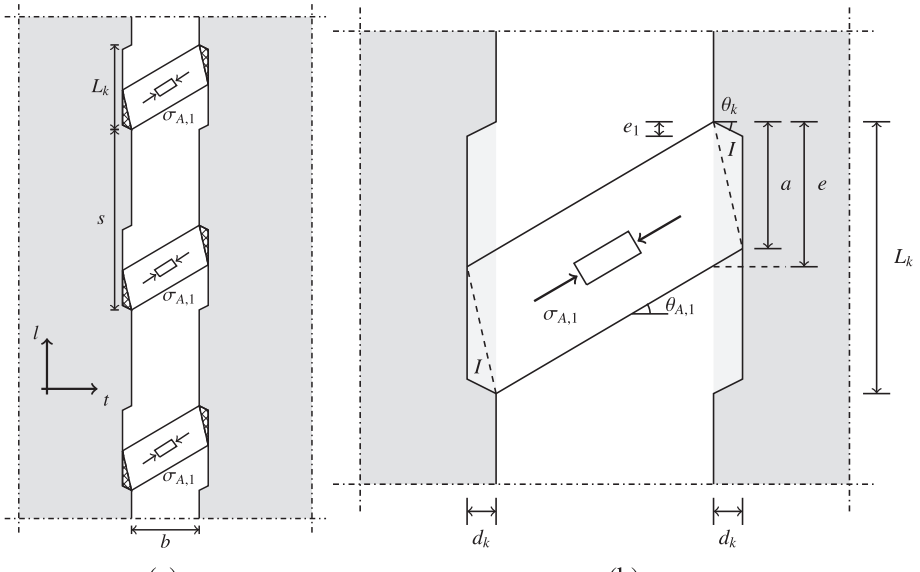

Fig. 6. (a) Distribution of struts spanning over a single key (Solution 1) and (b) definition of geometrical parameters at a key including the nodal zone, Triangle *I*.

5.1.1. Local equilibrium conditions for Solution 1

Fig. 7(a) depicts the nodal zone (Triangle *I*) of Solution 1 where each of the three boundaries is assumed to be uniformly stressed by normal and shear stresses. The stress field within the triangle is thus homogeneous. Compressive normal stresses are taken as positive. The stress resultants on the boundaries act at the centroid of each boundary and are illustrated in Fig. 7(b) as forces related to the l–t coordinate system.

The homogeneous stress field (σ_t,σ_l,τ_{lt}) within Triangle *I* may be expressed in terms of the stress resultants shown in Fig. 7(b):

$$\sigma_{t,I} = \frac{C_{t,1}}{(a-e_1)h_k} \tag{4}$$

$$\sigma_{l,I} = \frac{A_{l,1}\frac{a-e_1}{a} - C_{l,1}}{d_k\frac{a-e_1}{a}h_k} \tag{5}$$

$$\tau_{tl,I} = \frac{C_{l,1}}{(a-e_1)h_k} \tag{6}$$

The relations between $\sigma_{A,1}$ and the stress resultants, $A_{l,1}$ and $A_{t,1}$, are:

$$A_{l,1} = \sigma_{A,1}\cos\theta_{A,1}\sin\theta_{A,1}h_k e \tag{7}$$

$$A_{t,1} = \sigma_{A,1}\cos^2\theta_{A,1}h_k e \tag{8}$$

From the three equilibrium conditions for the triangular area, the following relations between the stress resultants can be established:

$$A_{l,1} - C_{l,1} - P_{l,1} = 0 \tag{9}$$

$$A_{t,1} - C_{t,1} - P_{t,1} = 0 \tag{10}$$

$$A_{t,1}\frac{a-e_1}{2} - C_{l,1}\frac{d_k}{2} - C_{t,1}\frac{a}{2} = 0 \tag{11}$$

5.2. Solution 2: Combination of struts spanning over one and two shear keys

In this solution, the struts are assumed to span in such a way so that the entire key length, L_k, is utilized to transfer stresses (compare Fig. 8(b) to Fig. 6(b)). Similar distributions can be seen in Fig. 5. The inclination of Strut *A* may also in this case be described by Eq. (2). The inclination of Strut *B* spanning over two keys is:

$$\tan\theta_B = \frac{s-e}{b} \tag{12}$$

where s is the distance between the shear keys and e describes the same geometrical parameter as in Solution 1, see Fig. 8(b). As indicated in Fig. 8(b) the nodal zone in the indented area has been subdivided into two triangular areas (*II* and *III*), which as shown later are stressed in biaxial compression. To describe the geometry of this zone, the distance e_2 is introduced as follows:

$$e_2 = L_k - (e + d_k\tan\theta_B) \tag{13}$$

This relation ensures that the above mentioned assumption of stress transfer over the entire indented length, L_k, is fulfilled. In this context, it is assumed that e_2 cannot attain negative values, and to fulfill this, a maximum effective key depth that can be utilized in the model is introduced:

$$d_{k,\mathrm{ef}} = (L_k - e)\cot\theta_B \tag{14}$$

Hence, for larger key depths, the maximum effective key depth, $d_{k,\mathrm{ef}}$, is adopted in the calculations. This eventually means that by using Solution 2, a capacity higher than that corresponding to a key depth of $d_{k,\mathrm{ef}}$ cannot be obtained. As for Solution 1, the capacity here will also be governed by either the stress state in the struts or in the triangles.

5.2.1. Local equilibrium conditions for Solution 2

The equilibrium equations for Triangle *I* in Solution 1 also apply for Solution 2 in which the outermost shear keys also contain a nodal zone of the same type, see Fig. 8(b). In addition, equilibrium equations for the nodal zone bounding Strut *A* as well as Strut *B*, i.e. Triangles *II* and *III*, need to be developed. The stresses and stress resultants acting on the boundaries of Triangle *II* and *III* are illustrated in Fig. 9. Triangle *III* borders on Struts *A* and *B* as well as Triangle *II*.

The homogeneous stress fields within Triangle *II* and Triangle *III* can be expressed in terms of the stress resultants (by use of equilibrium considerations). These stresses are:

$$\sigma_{t,II} = \frac{C_{t,2}}{(e + e_2 - e_1)h_k} \tag{15}$$

$$\sigma_{l,II} = \frac{F_l\frac{e+e_2-e_1}{e+e_2} - C_{l,2}}{d_k\frac{e+e_2-e_1}{e+e_2}h_k} \tag{16}$$

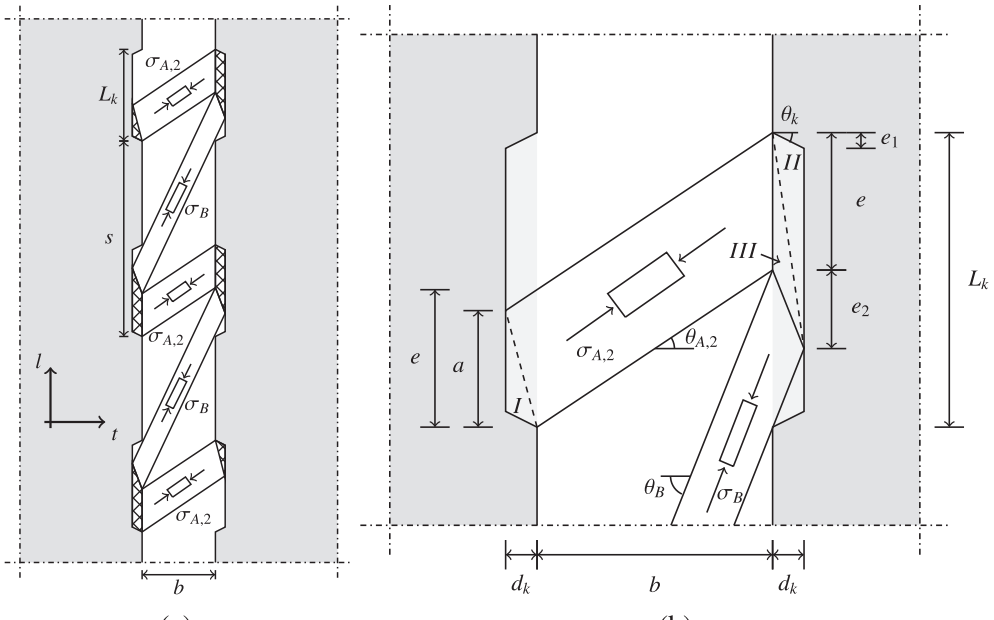

Fig. 8. (a) Distribution of struts in joint mortar (Solution 2) and (b) geometry at a key for verification of stress transfer.

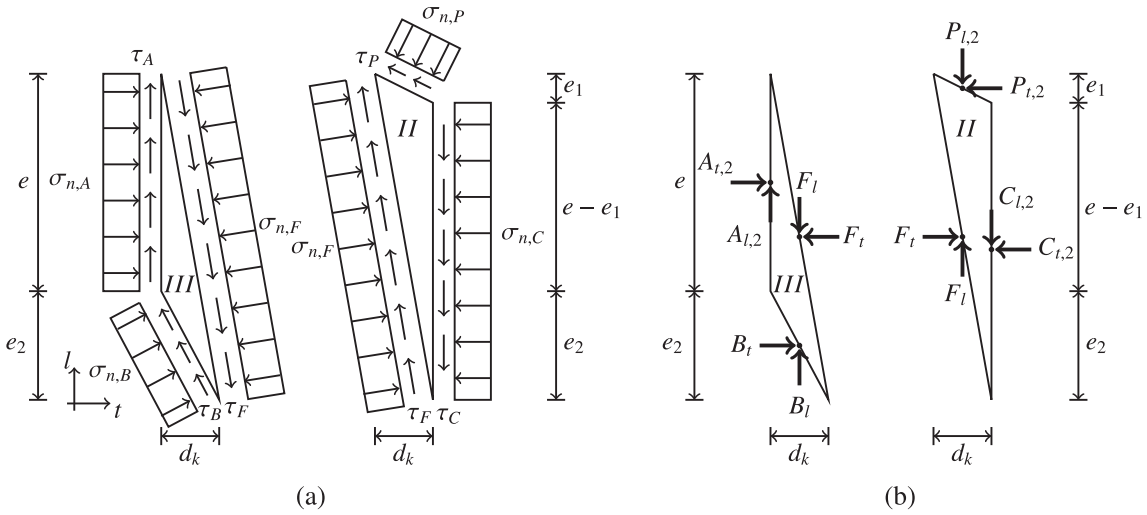

Fig. 9. (a) Stresses along boundaries of Triangles *II* and *III* (Solution 2) and (b) resultants of stresses on boundaries.

$$\tau_{tl,II} = \frac{C_{l,2}}{(e + e_2 - e_1)h_k} \tag{17}$$

$$\sigma_{t,III} = \frac{A_{t,2}}{eh_k} \tag{18}$$

$$\sigma_{l,III} = \frac{B_l - F_l \frac{e_2}{e+e_2}}{d_k \frac{e}{e+e_2} h_k} \tag{19}$$

$$\tau_{tl,III} = \frac{A_{l,2}}{eh_k} \tag{20}$$

The relations between $\sigma_{A,2}$,σ_B, and their stress resultants are given by:

$$A_{l,2} = \sigma_{A,2}\cos\theta_{A,2}\sin\theta_{A,2}h_k e \tag{21}$$

$$A_{t,2} = \sigma_{A,2}\cos^2\theta_{A,2}h_k e \tag{22}$$

$$B_l = \sigma_B\cos\theta_B\sin\theta_B h_k (L_k - e) \tag{23}$$

$$B_t = \sigma_B\cos^2\theta_B h_k (L_k - e) \tag{24}$$

From the three equilibrium conditions for Triangle *III*, the following relations are established:

$$A_{l,2} + B_l - F_l = 0 \tag{25}$$

$$A_{t,2} + B_t - F_t = 0 \tag{26}$$

$$\sigma_{A,2} = \sigma_B \frac{\cos^2\theta_B (L_k - e)}{\cos\theta_{A,2}\sin\theta_{A,2} d_k + \cos^2\theta_{A,2} e_2} \tag{27}$$

In Eq. (27), the relationships in (21)–(24) have been used to establish a relation between $\sigma_{A,2}$ and σ_B. Finally, equilibrium requirements for Triangle *II* lead to:

$$F_l - C_{l,2} - P_{l,2} = 0 \tag{28}$$

$$F_t - C_{t,2} - P_{t,2} = 0 \tag{29}$$

$$F_t \frac{e + e_2 - e_1}{2} - C_{l,2}\frac{d_k}{2} - C_{t,2}\frac{e + e_2}{2} = 0 \tag{30}$$

5.3. Global equilibrium for Solutions 1 and 2

With reference to the test specimen depicted in Fig. 2, the global equilibrium conditions can now be used to establish relations between the external load, V, and the internal stress resultants defined above. In the longitudinal direction, l, the applied load is balanced by the stress resultants $A_{l,i}$ and B_l stemming from Struts *A* and *B*, respectively, where $i = 1$ for Solution 1 and $i = 2$ for Solution 2. The resultant B_l only exists for Solution 2. The relation reads:

$$nA_{l,i} + (n-1)B_l = V \tag{31}$$

where n is the number of shear keys in the connection.

In the transverse direction, where there is no external load, the stress resultants of the struts must be outbalanced by tension in the transverse U-bar loops crossing the connection. This condition can be written as follows:

$$nA_{t,i} + (n-1)B_t - (n+1)A_s\sigma_s = 0 \tag{32}$$

where A_s is the total cross sectional area of transverse reinforcement in one loop connection and σ_s is the stress in the reinforcement. Similar to Eq. (31), B_t vanishes when applied to Solution 1. It should be noted that the equation for global moment equilibrium may serve as a check of the calculated stress distribution in the joint.

5.4. Yield condition for reinforcement

The stresses carried by the U-bars must fulfill:

$$\sigma_s \leqslant f_y \tag{33}$$

By utilizing Eqs. (32) and (8), the yield condition (Eq. (33)), may be reformulated in terms of the stress carried by Strut *A* in Solution 1:

$$\sigma_{A,1} \leqslant \frac{n+1}{n}\frac{A_s f_y}{\cos^2\theta_{A,1} h_k e} \tag{34}$$

For Solution 2, Eq. (33) may in a similar way be reformulated as a requirement to σ_B:

$$\sigma_B \leqslant \frac{(n+1)A_s f_y(\tan\theta_{A,2} d_k + e_2)}{\cos^2\theta_B h_k (L_k - e)((n-1)(\tan\theta_{A,2} d_k + e_2) + ne)} \tag{35}$$

This requirement in fact also contains the condition for the stress in Strut *A*, cf. Eq. (27).

5.5. Failure criteria for joint mortar

In the following, the failure criteria adopted in the analytical lower bound model to describe the joint mortar will be discussed. Distinction is made between zones with uniaxial compression and zones with biaxial compression. The tensile strength of the mortar is neglected and the uniaxial compression strength is f_c. For Struts A_i and *B* carrying uniaxial compression, the stress level is limited to:

$$\sigma_{A,i} \leqslant \nu f_c, \quad i = 1,2, \quad \nu \leqslant 1 \tag{36}$$

$$\sigma_B \leqslant \nu f_c, \quad \nu \leqslant 1 \tag{37}$$

where ν is the effectiveness factor. This factor normally takes into account the material brittleness as well as the strength reduction due to cracking and tensile strains perpendicular to the struts. It is argued that in the present lower bound problem, with steep direct strut actions within a narrow and long strip of mortar, the effect of tensile strains perpendicular to the struts may be neglected. Hence, ν mainly accounts for the material brittleness. In the following, ν will be taken as unity when the analytical lower bound model is evaluated against the numerical calculations (because $\nu = 1$ was used in the numerical calculations). However, when using the analytical lower bound model to compare with its upper bound counterpart [1] and with test results, a value of $\nu = 0.89$ is adopted as a qualified estimate of the effect of material brittleness. This value is obtained from the formula, $\nu = (f_{c,0}/f_c)^{1/3}$ proposed in the *fib* Model Code [18], with $f_{c,0} = 30$ MPa.

Normally, concrete/mortar is identified as a modified Coulomb material, which means that f_c will also be the strength in a biaxial compression field. However, as shown e.g. by Kupfer et al. [19], the strength of concrete under biaxial compression may be larger than the uniaxial strength. Furthermore, as the areas with biaxial compression represent nodal zones in the model, the effectiveness factor can here be taken as $\nu = 1$, also in practice. This means that the failure criterion for zones with biaxial compression may be expressed as:

$$\sigma_2 \leqslant cf_c, \qquad c \geqslant 1 \tag{38}$$

where c can be interpreted as a strength enhancement factor and σ_2 is the largest principal compressive stress. Test results of Kupfer et al. [19] showed that c depends of the σ_2/σ_1–ratio ($c = 1.27$ for $\sigma_2/\sigma_1 = 2$ and $c = 1.16$ for $\sigma_2/\sigma_1 = 1$). In the following, c is taken as unity when the analytical lower bound model is evaluated against the numerical calculations (in order to be consistent with the assumptions made for the numerical model). However, for comparison with the upper bound model and with test results, a qualified estimate of $c = 1.15$ is adopted. This value is slightly higher than the recommendation of the *fib* Model Code [18] for biaxially compressed nodes.

Due to the assumption of zero tensile strength, the following limitation also applies to the biaxially stressed areas:

$$\sigma_1 \geqslant 0 \tag{39}$$

5.6. Failure criterion for interface

As an averaged description, the interface between mortar and precast elements with keys may be categorized as very rough, with a pseudo cohesive resistance and a high pseudo frictional coefficient (see e.g. Eurocode 2 [20]). However, in a detailed calculation where the geometry of the keys is taken into account, the mechanical properties of the real interface should be used. This means that the properties of the formwork have an influence on the failure criterion of the interface. Hence, like for the numerical model, the following Coulomb friction criterion is adopted for the interface:

$$|\tau_{nt}| \leqslant \mu\sigma_n \tag{40}$$

where τ_{nt} is the shear stress on the boundary of the shear keys and σ_n is a compressive normal stress acting on the same boundary, e.g. $(\sigma_n,\tau_{nt}) = (\sigma_{t,II},\tau_{tl,II})$. It should be noted that Eq. (40) does not contain a cohesion term. The main argument for neglecting the cohesion is that smooth formwork was used to cast the reinforced concrete elements for the experimental program (smooth formwork is commonly used also in practice). Thus any small cohesive resistance in the interface may have (partly or completely) vanished at the ultimate limit state. The coefficient of friction will in the following be taken as $\mu = 0.75$, similar to the assumption of the numerical model. The friction criterion implies that the stress resultants, $C_{l,i}$ and $C_{t,i}$, see Figs. 7(b) and 9(b), must fulfill the following condition:

$$|C_{l,i}| \leqslant \mu C_{t,i}, \quad i = 1,2 \tag{41}$$

For the inclined part of the shear key, the friction criterion, expressed in terms of the resulting forces, can be established as:

$$\left| \frac{P_{l,i}\sin\theta_k - P_{t,i}\cos\theta_k}{P_{t,i}\sin\theta_k + P_{l,i}\cos\theta_k} \right| \leqslant \mu, \quad i = 1,2 \tag{42}$$

5.7. Optimization of lower bound solutions

By examining the geometrical and equilibrium conditions of Solution 1 as well as 2, it may be shown that the problems are indeterminate with two free optimization parameters, namely the parameter e and one of the statical parameters. The resultant $C_{l,i}$ will in the following be chosen as the statical optimization parameter.

If the interface is not utilized to transfer shear stresses, $C_{l,i}$ will vanish and the solution will eventually be identical to the single strut solution suggested by Christoffersen [7]. Therefore, to obtain better solutions, the interface friction must be utilized as much as possible. Hence, $C_{l,i}$ should be taken as large as possible. According to Eq. (41), this implies:

$$C_{l,i} = \mu C_{t,i}, \quad i = 1,2 \tag{43}$$

By choosing the relation given in Eq. (43), the only remaining parameter left for optimization of the load carrying capacity is e. The optimization is naturally subjected to the strength constraints established in Sections 5.4 and 5.5. Results are presented in the following.

6. Verification of analytical lower bound solutions

The results obtained by FELA (which are optimal under the assumptions made) will in the following be used to verify the analytical lower bound solutions. The purpose is to investigate if the analytical solutions actually capture the main tendencies of the numerical results. Calculations have been carried out based on the properties and parameters of the test specimens. The results, in terms of normalized shear stresses versus the key depth, can be seen in Fig. 10(a), where the result of the single strut solution [7] is also shown. The nominal shear stress has been determined as follows:

$$\tau = \frac{V}{nh_kL_k} \tag{44}$$

where V is calculated from Eq. (31). The full red curve in Fig. 10(a) corresponds to the upper envelope of Solutions 1 and 2 and represents the optimal results provided by the analytical lower bound model. It can be seen that Solution 2 applies to larger key depths ($d_k > 8$ mm) whereas Solution 1 provides better results for smaller key depths. For key depths larger than 13 mm, Triangle I vanishes in Solution 1, as the length a becomes smaller than e_1. In this case $\sigma_{A,1}$ will act only on the inclined part of the key corner, however, as the capacity is less than Solution 2, it is not calculated. Contrary to the single strut solution, the present model actually provides a significant capacity in the limiting case of $d_k = 0$ mm (i.e. when the design is no longer a keyed connection). In this case, there is no nodal zone and the compression from the diagonal struts is transferred through the interface by pure shear-friction. Fig. 10(b) depicts the optimal value of e versus the key depth. At the transition point, the optimal value of e for Solution 1 is different from that of Solution 2. This underlines that Solution 2 is not to be considered as an extension of Solution 1, which is also seen in the fact that the transition between the two solutions is not smooth.

Nevertheless, it is found that the analytical model provides results that are almost identical to the numerical results obtained by FELA (Fig. 10(a)). A small deviation is observed around the transition between Solution 1 and Solution 2. However, the deviation is insignificant compared to the overall agreement. This strong correlation shows that the analytical model is close to the optimal solution. In this context it

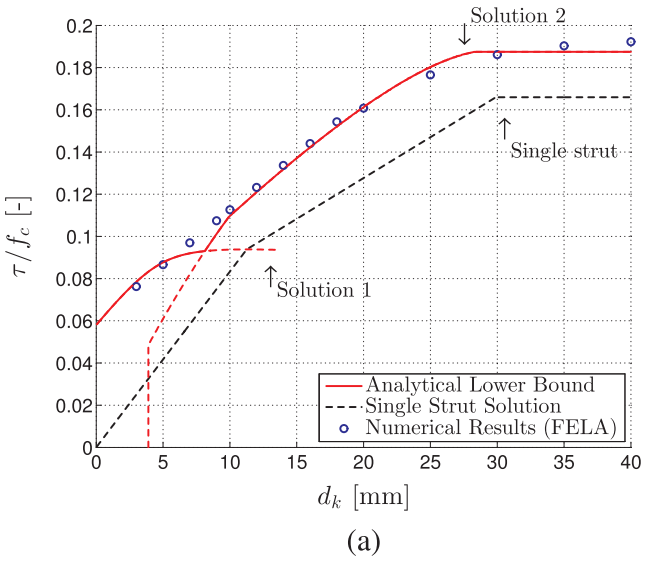

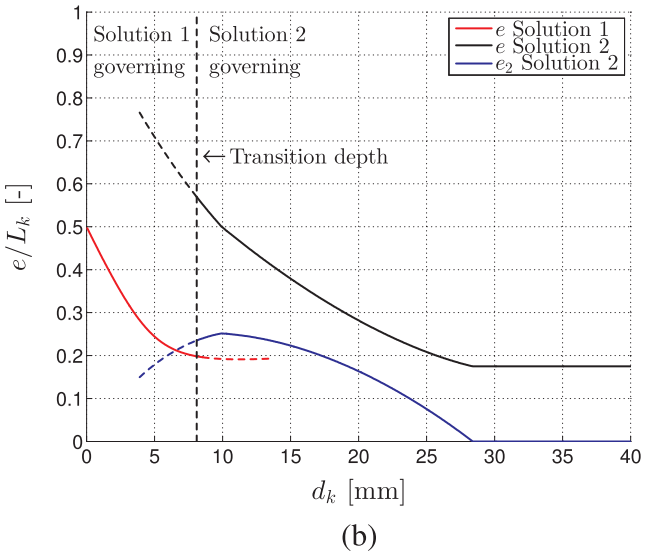

Fig. 10. (a) Comparison of analytical and numerical lower bound models and (b) the optimal distance e calculated for Solutions 1 and 2.

should be noted that optimality here only refers to the best results that can be obtained by the assumptions made and not necessary the 'true' results. Note further that other geometries and reinforcement degrees may favor other stress fields not captured by the two developed analytical solutions.

It can be seen in Fig. 10(a) that the analytical model as well as FELA estimate a higher capacity than the single strut solution developed in [7]. This is partly related to the inclusion of friction in the grout-to-panel interface at the keyed areas.

Fig. 11 depicts the stresses of Solution 1 versus the key depth. It can be seen that the maximum compressive principal stress, $\sigma_{2,I}$, acting in Triangle I is governing in the entire interval of d_k, where Solution 1 is optimal. Moreover it appears that the minor principal stress, $\sigma_{1,I}$, is also compressive and that the stress in Strut A,$\sigma_{A,1}$, is well below νf_c for all key depths. The magnitudes of the stresses depicted in Fig. 11 indicate a local failure of the key corners (only Triangle I is critical). This is in agreement with test results for specimens with small key depths.

The stresses of Solution 2 are plotted in Fig. 12. It can be seen that $\sigma_{1,II} = 0$ when the key depth is approximately 4 mm. This stress component in fact becomes negative (i.e. tension) for lower values of d_k, which means that Solution 2 does not provide valid results for smaller

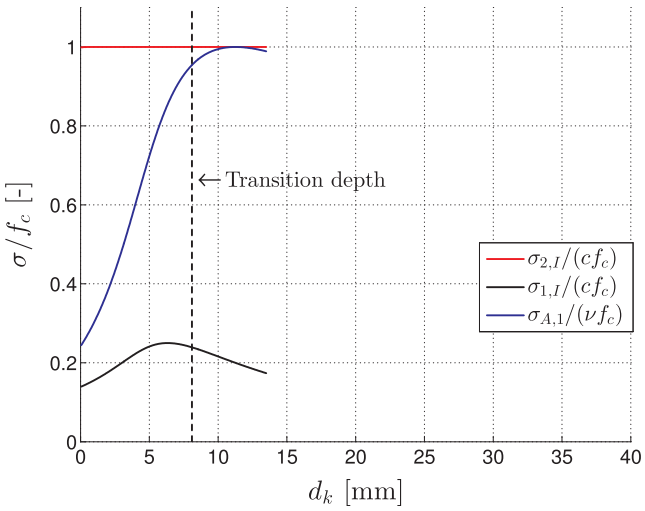

Fig. 11. Normalized stresses versus key depth in Solution 1, note that $c = 1$ and $\nu = 1$.

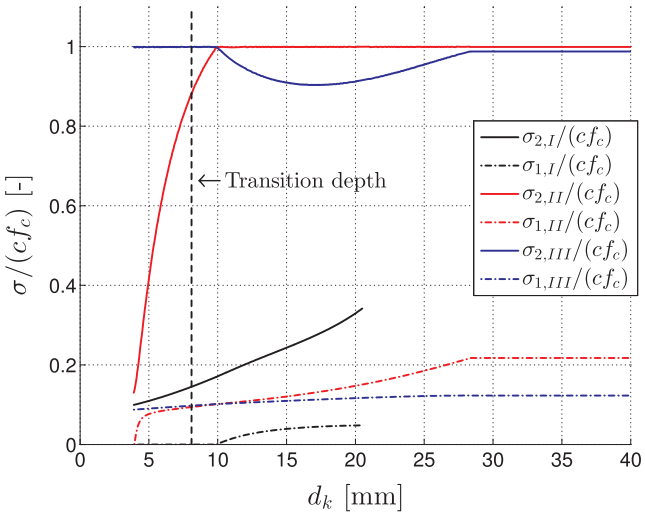

Fig. 12. Normalized stresses versus key depth in Solution 2, $c = 1$.

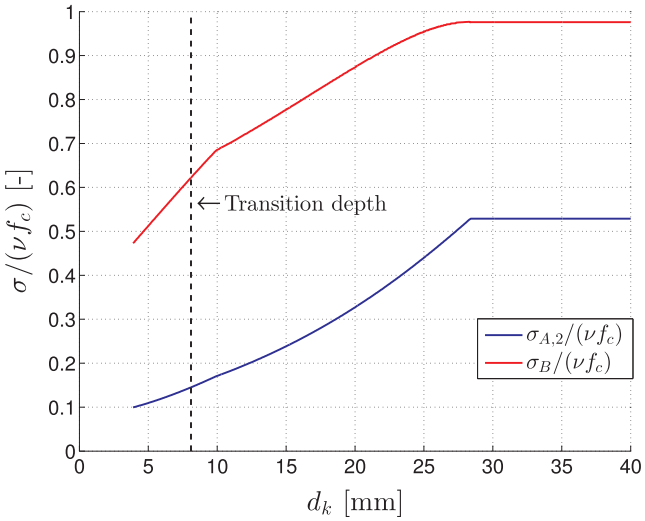

Fig. 13. Variation of $\sigma_{A,2}$ and σ_B as function of key depth in Solution 2, $\nu = 1$.

key depths (at least not for the assumed material parameters and geometry considered). Furthermore, it can be seen that $\sigma_{2,III}$ is the governing stress component for key depths between 4 mm and 10 mm,

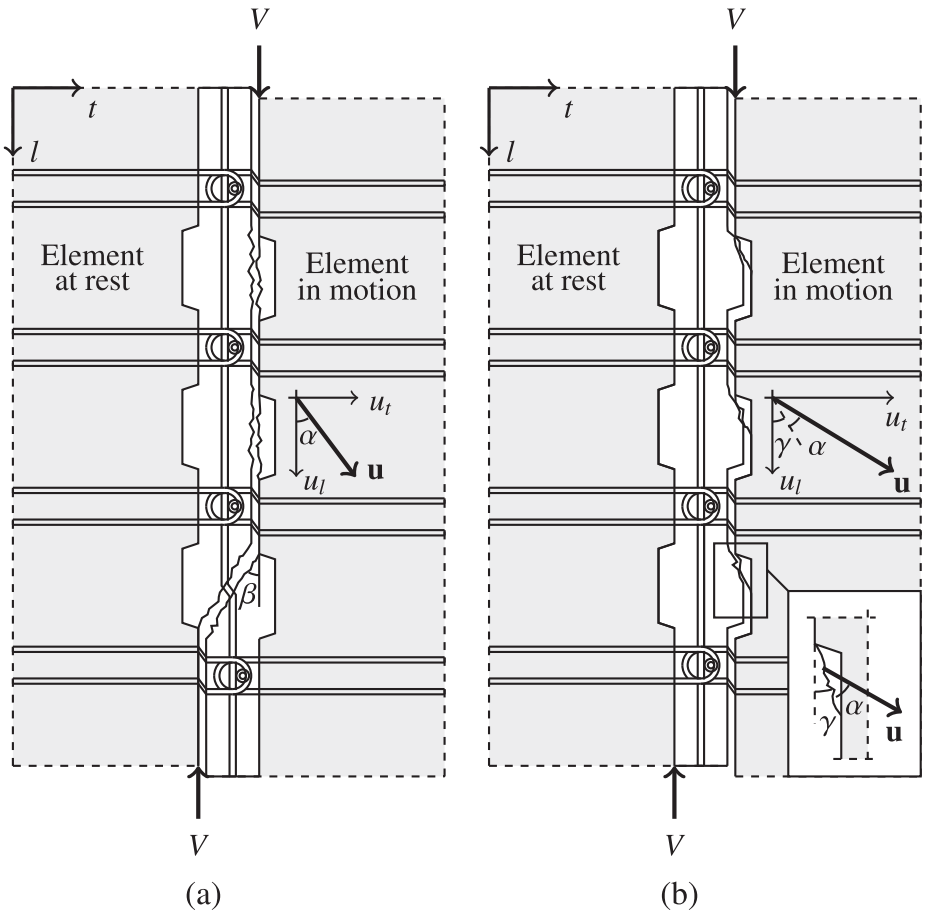

Fig. 14. Collapse mechanisms considered in upper bound model, (a) complete key shearing combined with diagonal yield line and (b) local key corner failure, illustrations from [1].

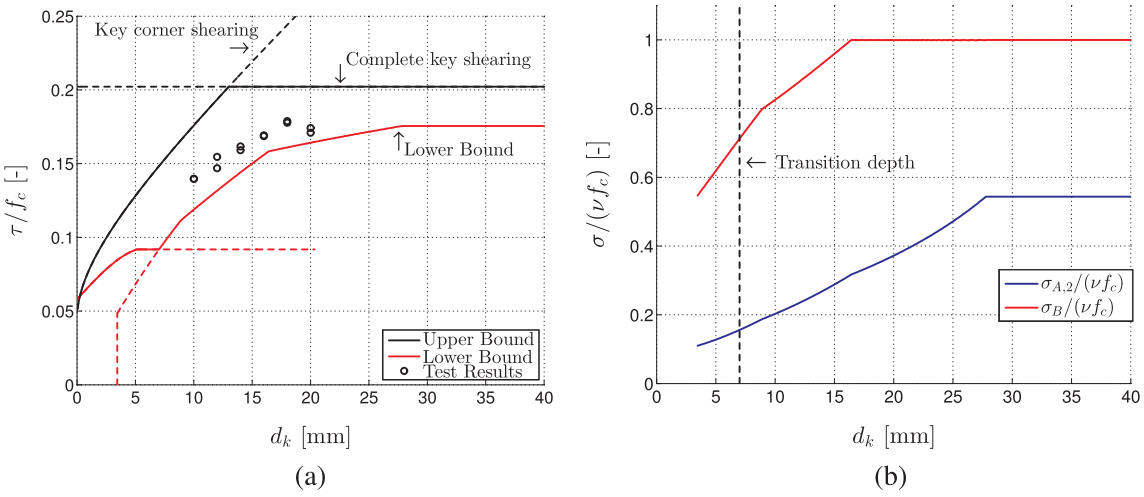

Fig. 15. (a) Comparison of upper and lower bound models with test results, (b) stresses in Struts *A* and *B* in Solution 2.

while $\sigma_{2,II}$ is governing for larger key depths. Triangle *I* vanishes at a key depth of approximately 21 mm. As $\sigma_{A,2} < \nu f_c$, the stress can be safely transferred without considering a nodal zone. At a key depth of about 28 mm, the maximum effective depth according to Eq. (14) is introduced and the capacity cannot be increased further beyond this key depth.

Fig. 13 shows how the stresses in Struts *A* and *B* vary in Solution 2. It can be seen that σ_B is larger than $\sigma_{A,2}$ in the entire interval of key depths. At the transition to the effective key depth ($d_k \approx 28$ mm), the stress in Strut *B* has almost reached the capacity of νf_c, however, it remains slightly below. These results of course reflect the modeled geometry and adopted material parameters $\nu = c = 1$.

7. Comparison of analytical lower and upper bound models

In the following, the analytical lower bound model will be compared with the previously developed upper bound model [1]. It is not expected that the two models lead to identical results (i.e. a theoretically exact solution) since they are not fully based on the same set of assumptions. For instance, plane stress condition is assumed in the lower bound model while plane strain condition is imposed in the upper bound model. However, the comparison can be used to evaluate the

tendencies of the two models and in particular the gap between them. Eventually, by comparison of both models with test results, a qualified discussion of the effectiveness factor adopted in the pure upper bound approach [1] can be carried out.

The upper bound model presented in Ref. [1] is based on two basic collapse mechanisms reflecting local key corner failure and complete key shearing, respectively, see Fig. 14. The interface properties between mortar and the precast elements are neglected and the mortar is treated as a modified Coulomb material with zero tensile strength and with an internal angle of friction taken as $\varphi = 30°$. The assumption of plane strain condition implies that the angle of displacement, α, due to the normality condition cannot be smaller than φ, i.e. $\alpha \geqslant 30°$. For a detailed derivation of the upper bound solution, the reader is referred to [1]. It should be noted that the upper bound solution, in contrast to the lower bound counterpart, can be formulated as closed-form equations and is therefore easier to use in practice.

The results of the upper bound and lower bound models can be seen in Fig. 15(a). As stated in the previous, $\nu = 0.89$ is adopted for the uniaxial compression struts while $\nu = 1$ and $c = 1.15$ are used for the biaxial compression zones in the lower bound model. Such a distinction between types of stress field can of course not be made in the upper bound model. Therefore, $\nu = 0.89$ has been used when determining the dissipation in all the yield lines in the upper bound model. The gap between the upper and the lower bound solutions (Fig. 15) is however not due to the difference in the material parameters. The gap would in fact have been larger, had the lower bound calculations also been based on $\nu = 0.89$ and $c = 1$ everywhere. It is mainly the assumption of plane strain condition versus plane stress condition that has an influence on the observed gap. In addition, other more sophisticated collapse mechanisms (not yet analyzed) may lower the upper bound results.

Another discrepancy between the two models should also be pointed out. A closer look at the two solutions (in Fig. 15) in the vicinity of $d_k = 0$ mm reveals that the upper bound solution is lying below the lower bound solution. This difference has no practical significant but is apparently inconsistent with the extremum theorems of plasticity. The reason is to be found in the fact, that the interface is assigned a friction failure criterion, Eq. (40), in the lower bound model while this criterion is ignored in the upper bound calculations. To obtain results consistent with the extremum theorems, the upper bound calculations should be modified to include the friction criterion for the interface and at the same time fulfill the normality condition at the interface. It may in that case be shown, that the upper bound solution will lie above the lower bound counterpart and that the two solutions will yield exactly the same result at the limiting case of $d_k = 0$ mm.

In the present calculations, the upper bound model reaches the upper limit (corresponding to complete key shearing) at $d_k \approx 13$ mm. This is actually close to $d_k = 16$ mm, which in the test series corresponds to the transition between the two failure modes. The lower bound Solution 2 on the other hand, reaches an upper limit at $d_k \approx 28$ mm corresponding to the maximum effective key depth (Eq. (14)). Furthermore, in Solution 2, the Triangle *II* is critical when d_k is between approximately 9 to 17 mm while Strut *B* is stressed to νf_c and therefore critical for d_k larger than 17 mm (see Fig. 15(b)). For $d_k > 17$ mm, the thickness of Strut *B* increases with increasing d_k which explains the increase of the capacity for d_k between 17 and 28 mm. As seen in Fig. 15(b), Strut *A* of Solution 2 is at no point critical. The fact that only Strut *B* is critical when Solution 2 reaches the upper limit makes it rather difficult to relate the result to a failure mechanism involving complete key shearing. This simply underlines that Solution 2 (although it may be optimal subjected to the assumptions made) is still a lower bound and thus a safe model for the real ultimate behavior of the connection.

It is important for practical application that the two models (developed independently of each other) in fact display the same overall tendencies, namely a shear capacity that increases with increasing key depth until an upper limit has been reached. This improves the reliability of the results. However, the most correct solution would probably be somewhere between the two models since in reality, the connection is not in a state of plane strain, nor plane stress, but somewhere in between. This is clearly seen in the fact that the test results as plotted in Fig. 15(a) are all lying in between the results of the upper and lower bound models. Hence, an important conclusion that can be drawn from the comparison in Fig. 15 is that the effectiveness factor adopted in the pure upper bound approach (see Ref. [1] for details) not only reflects the material brittleness but also partly contains an empirical reduction to compensate for the ideal assumption of plane strain. In this context, it is interesting to note that the width, i.e. b shown in Fig. 2, must have an influence on the stress and strain conditions in the connection, but this parameter is absent in the failure mechanisms based on the plane strain assumption that were considered in Ref. [1]. Hence, it is reasonable to believe that the effectiveness factor of the pure upper bound approach also compensates for the influence of b, which is not considered theoretically. The lower bound model, on the other hand, includes the width, b, as an important parameter. Still, if the plane stress lower bound solution should be calibrated to fit the test results (Fig. 15), then artificially higher values of ν and c would be required, most probably to compensate for the triaxial stress state that in reality would develop locally in the joint mortar.

It might be too optimistic to expect that a more correct/realistic solution can be developed which at the same time is as user-friendly as the closed-form upper bound solution. The upper bound model will therefore still have preference from a practical point of view, even though it has to be used in conjunction with an effectiveness factor that not only accounts for the real material behavior but also functions as an adjustment parameter to compensate for the unsafe nature of upper bound solutions. Awareness of this is important when applying the upper bound model to practical cases, which deviate significantly from the experimentally tested configurations. In such situations, the lower bound model presented in this paper will be useful.

8. Conclusions

This paper presented push-off tests of a recently developed keyed shear connection design for precast concrete wall elements. The investigation focused on the influence of the key depth on the failure mode and the load–displacement response of the connections. The experimental observations include:

- Connections with smaller key depths failed by local key corner shearing while failure by complete key shearing was observed for connections with larger key depths
- The maximum capacity (first peak load) was related to failure of the keys and increased with increasing key depth until complete key shearing became the critical failure mode
- The residual load level (beyond the first peak load) is relatively higher for connections suffering local key corner shearing

The experimental observations suggest that for practical applications the connection should be designed to be governed by local key corner crushing as this improves the ductility. In addition to the experimental results, an analytical lower bound model was developed for prediction of the first peak capacity. The model was validated with numerical calculations based on finite element limit analysis. The model differs from existing analytical lower bound solutions for keyed connections in the following way:

- The load can be carried by a combination of struts spanning over one or two indentations
- Local strength increase at nodal zones and effects of interface friction are accounted for
- The nodal zones can be subjected to non-hydrostatic biaxial stress

conditions

The lower bound model shows similar tendencies as a previously developed upper bound model and the test results fall within the gap between the two solutions. From the comparison, it can be concluded that the lower bound solution is a safe one due to the assumption of plane stress condition while the plane strain assumption adopted in the upper bound solution is theoretically unsafe and must be compensated for by adjustment with test results. This is reflected in the relatively low effectiveness factor that has to be applied. The upper bound solution should therefore only be used for configurations within the range covered by tests. In other cases, the lower bound model is applicable although it is more complicated to use. In conclusion, it can be stated that the paper has contributed to a more complete theoretical basis for practical design of keyed connections.

Acknowledgment

The experimental program was financially supported by the Danish Association for Precast Concrete Elements and the COWI Foundation. The test elements were produced at CRH Concrete and the experimental work was conducted with support from M.Sc. R.M. Hou and M.Sc. J.S. Olsen. The authors gratefully acknowledge these valuable contributions.

Appendix A. Lower bound finite element limit analysis (FELA)

As discussed in Section 4, FELA can be considered as a special case of the general finite element method, where a rigid-plastic material model is assumed. Unlike the finite element method, however, FELA is a so-called direct method where the collapse load is determined in a single step and no incremental procedure is needed. The method is therefore rather efficient and numerically stable for calculation of the collapse load of structures.

The fundamental idea of the method is to formulate a given limit analysis problem as a convex optimization problem, where the ultimate load is maximized. In order to obtain a lower bound solution, the determined stress field must be statically admissible and safe. This is ensured by a set of linear equality constraints, representing the equilibrium conditions, as well as a set of convex inequality constraints, representing the convex yield conditions. The general form of the optimization problem is given below:

$$\begin{aligned} &\text{maximize} && \lambda \\ &\text{subject to} && B^T\sigma = p\lambda + p_0 \\ & && f(\sigma_i) \leq 0, \qquad i = 1,2,...,m \end{aligned}$$

The external load comprises a constant part, p_0, and a scalable part, $p\lambda$, where λ is the load factor, which is sought to be maximized. The external load is balanced by the stress field described by the vector σ via the linear equilibrium equations, $B^T\sigma = p\lambda + p_0$, where B^T is the equilibrium matrix. The yield function $f(\sigma_i)$ is checked in the m points to ensure a safe stress field. For concrete, the Mohr-Coulomb yield criterion is commonly used which can be expressed as conic constraints [21,22].

The equilibrium matrix, B^T, depends on the chosen lower bound finite elements and discretization. In this paper, lower bound plane stress elements have been used together with bar and interface elements, representing the reinforcement and grout-to-panel interfaces of the keyed joint.

References

[1] Sørensen JH, Hoang LC, Olesen JF, Fischer G. Test and analysis of a new ductile shear connection design for RC shear walls. Struct Concr 2017;18(1):189–204.
[2] fib. Bulletin 43: structural connections for precast concrete buildings. Federation international du béton, Lausanne, Switzerland; 2008.
[3] Hansen K, Kavyrchine M, Melhorn G, Olesen SØ, Pume D, Schwing H. Keyed shear joints – SBI rapport 97. Tech rep. Danish Building Research Institute; 1976.
[4] Sørensen JH, Hoang LC, Olesen JF, Fischer G. Tensile capacity of loop connections grouted with concrete or mortar. Mag Concr Res 2017;69(17):892–904.
[5] Jensen BC. Nogle Plasticitetsteoretiske Beregninger af Beton og Jernbeton (English: Some applications of plastic analysis to plain and reinforced concrete). Report 111. Ph.D. thesis. Lyngby: Technical University of Denmark, Institute of Building Design; 1976.
[6] Jørgensen HB, Hoang LC. Tests and limit analysis of loop connections between precast concrete elements loaded in tension. Eng Struct 2013;52:558–69.
[7] Christoffersen J. Ultimate capacity of joints in precast large panel concrete buildings, series R No 25. Ph.D. thesis. Lyngby: Technical University of Denmark, Department of Structural Engineering and Materials; 1997.
[8] Nielsen MP, Hoang LC. Limit analysis and concrete plasticity. 3rd ed. Boca Raton: CRC Press, Taylor & Francis Group; 2011.
[9] Herfelt MA, Poulsen PN, Hoang LC, Jensen JF. Numerical limit analysis of keyed shear joints in concrete structures. Struct Concr 2016;17(3):481–90.
[10] Nielsen MP. Om jernbetonskivers styrke (English: On the strength of reinforced concrete discs). Polyteknisk Forlag; 1969.
[11] Muttoni A, Schwartz Joseph, Thürlimann Bruno. Design of concrete structures with stress fields. Basel (Switzerland): Birkhäuser Verlag; 1997.
[12] Pistoljevic N, Nielsen MP. HSTO-metoden. Plasticitetsteori for armerede betonskiver. Anvendelse af homogene spændingstilstande i trekantformede områder. Proc Danish Soc Struct Sci Eng 2009;80(2):19–54.
[13] Calladine CR. Simple ideas in the large-deflection plastic theory of plates and slabs. In: Heyman J, Leckie FA, editors. International conference on the applications of plastic theory in engineering design, Cambridge, UK; 1968. p. 93–127.
[14] Bræstrup MW. Dome effect in RC slabs: rigid-plastic analysis. J Struct Div – ASCE 1980;106(6):1237–53.
[15] Belenkiy LM. Upper-bound solutions for rigid-plastic beams and plates of large deflections by variation principles. J Eng Mech 2007;133(1):98–105.
[16] Sørensen JH, Hoang LC, Olesen JF, Fischer G. Testing and modeling dowel and catenary action in rebars crossing shear joints in RC. Eng Struct 2017;145:234–45.
[17] Dahl KKB. Construction joints in normal and high strength concrete. Tech rep. Lyngby: Technical University of Denmark, Department of Structural Engineering; 1994.
[18] fib. Model code for concrete structures 2010. Lausanne (Switzerland): Wilhelm Ernst & Sohn; 2013.
[19] Kupfer H, Hilsdorf HK, Rüsch H. Behavior of concrete under biaxial stresses. ACI Struct J 1969;66(8):656–66.
[20] CEN. EN1992-1-1 Eurocode 2: design of concrete structures Part 1-1: General rules and rules for buildings. 3rd ed. European Committee for Standardization, Brussels; 2004.
[21] Krabbenhøft K, Lyamin AV, Sloan SW. Formulation and solution of some plasticity problems as conic programs. Int J Solids Struct 2007;44(5):1533–49.
[22] Bisbos CD, Pardalos PM. Second-order cone and semidefinite representations of material failure criteria. J Optimiz Theory Appl 2007;134(2):275–301.

Paper IV

"Testing and modeling dowel and catenary action in rebars crossing shear joints in RC"

Jesper H. Sørensen, Linh C. Hoang, John F. Olsen, Gregor Fischer

Published in: *Engineering Structures (2017), 145:234-245*

Engineering Structures 145 (2017) 234–245

Contents lists available at ScienceDirect

Engineering Structures

journal homepage: www.elsevier.com/locate/engstruct

Testing and modeling dowel and catenary action in rebars crossing shear joints in RC

Jesper H. Sørensen *, Linh C. Hoang, John F. Olesen, Gregor Fischer

Technical University of Denmark, Department of Civil Engineering, Brovej, Bygning 118, 2800 Kgs. Lyngby, Denmark

ARTICLE INFO

Article history:
Received 9 February 2017
Revised 21 April 2017
Accepted 10 May 2017

Keywords:
Dowel action
Catenary action
Concrete plasticity
Second order modeling

ABSTRACT

This paper presents a detailed study of the shear behavior of two-sided dowel joints, which includes initiation of dowel action at small shear displacements and development of full catenary action in the reinforcement at large displacements. In addition to experimental results, the paper also presents a simple, second order plasticity model to describe the non-linear regime of the load-displacement relationship. In the model, kinematic relations and the normality condition of plastic theory are utilized to establish a unique link between the imposed shear displacement and combinations of moment and tension that develop in the rebar(s) crossing the joint. Interface friction is included in a consistent manner based on clamping stresses induced by the tension of the rebar(s). Comparison of experimental results with the model predictions shows satisfactory agreement. The model has, due to its simplicity, potential for practical applications related to assessment of structural robustness, where estimation of the available energy (area below load-displacement curve) is important.

1. Introduction

Dowel action in reinforcing bars is a well-known phenomenon which can be utilized as load carrying mechanism in structural concrete. Inclusion of dowel action in design is primarily relevant for problems that involve transfer of shear through casting joints and connections, see e.g. *fib* Bulletin 43 [1].

Pure dowel action is experimentally most clearly observed when a rebar has part of its length embedded in a large block of concrete while being loaded by a transverse force at the concrete surface. In most practical cases, the load carrying capacity will be governed be development of a plastic hinge in the rebar and by local crushing of the concrete. The first attempt to study this basic problem (which in the following will be termed 'one-sided dowel action') was carried out by Friberg [2] who modeled the dowel as a linear elastic beam transversely supported on elastic springs. Many researchers have since adopted this approach to model the load-displacement response of the dowel [3–10]. However, the obvious shortcoming of this approach is the fact that it is a linear elastic model. Some attempts have therefore been made to adjust the transverse spring stiffness [11,12] and others again have empirically suggested a gradual change of stiffness to fit the non-linear test results [4–6].

Due to the non-linear material behavior, a model based on the theory of plasticity seems more appropriate to describe dowel action at the ultimate limit state. Such a model was first developed for one-sided dowel action by Rasmussen [13], who assumed crushing of concrete simultaneously with yielding of the reinforcement. In contrast to the basic problem studied by Rasmussen, Fig. 1 schematically illustrates a so-called two-sided dowel joint, where the rebar is fully embedded in concrete on both sides of the casting joint. In this case, pure dowel action (represented by rotation, θ, in the plastic hinges) is only the first phase of the load transfer mechanism of the joint. When the shear displacement in the joint, u, increases, the dowel action will gradually be accompanied by axial tension (represented by elongation, Δ, in the plastic hinges). The load transfer mechanism is in this phase a combination of the two actions. At the final stage, dowel action may be completely replaced by axial tension, i.e. the load may be carried by pure catenary action in the rebar. Development of full catenary action requires relatively large shear displacements. For this reason, this effect is seldom utilized in the ultimate design of structural joints even though the load related to pure catenary action is usually higher than that corresponding to pure dowel action. However, for assessment of structural robustness as well as verification of structural performance under accidental load cases, catenary action may play an important role, not only for the behavior of shear joints but also when considering the behavior of slabs after initial bending and/or punching failure (Refs. [14–20]).

* Corresponding author.
E-mail address: jhaso@byg.dtu.dk (J.H. Sørensen).

http://dx.doi.org/10.1016/j.engstruct.2017.05.020
0141-0296/

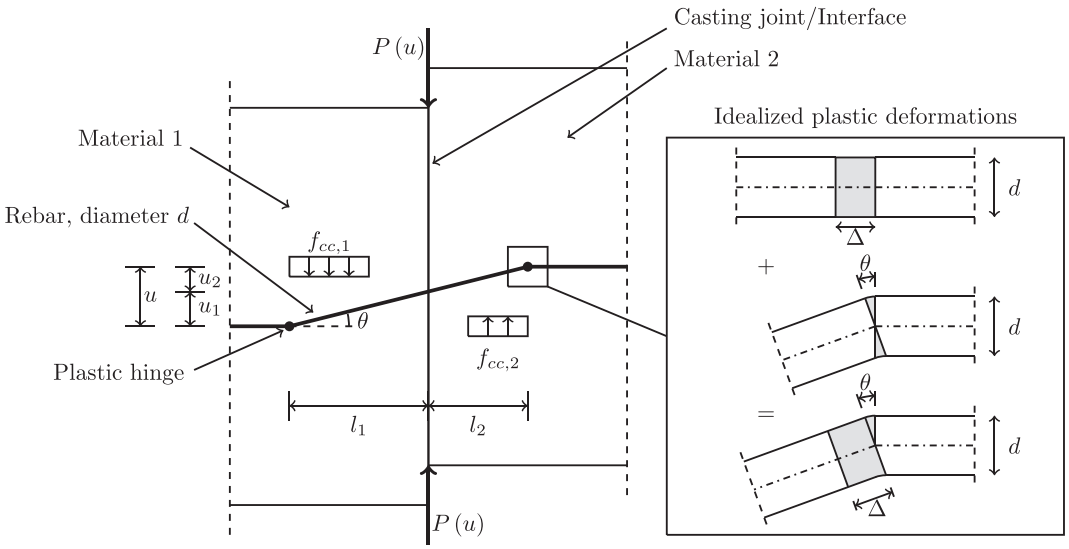

Fig. 1. Casting joint between two different concretes subjected to shear displacements and crossed by a rebar.

Several authors have recognized that for two-sided joints, the development of axial tension reduces the bending capacity of the dowel. In order to account for this reduction, a criterion for the combination of axial tension and bending is needed [21–25]. Basically, this criterion is the same as the MN-interaction diagram for the rebar cross section. The real challenge here is to establish a unique link between the shear displacement, u, and the points on the MN-interaction diagram. In the literature, this link is often established on a more or less empirical basis, e.g. based on experimental measurements of the axial tension in the rebar.

This paper presents an investigation into the behavior of two-sided dowel joints (i.e. rebars crossing an interface between concretes cast at different times), exposed to large shear displacements. The investigation covers both an experimental program as well as a theoretical study. Some few initial tests as well as basic ideas have been presented in a previous work-in-progress paper (Ref. [26]). One of the focus points of the experimental program has been to study the efficiency of rebar groups in comparison with single dowel behavior. This is relevant for practical applications because rebars crossing casting joints between precast concrete elements are often lumped in groups, e.g. in the form of overlapping U-bars. Furthermore, in addition to tests of the classical concrete-to-concrete interface, the program also includes concrete-to-mortar interfaces. Tests of such combinations have, to the best knowledge of the authors, not been published before. The combinations are nevertheless important in practice, for instance when dealing with shear connections between precast concrete wall elements, which are often grouted with mortar.

The experimental results have been used to calibrate and verify a theoretical model of the load-displacement response of two-sided dowel joints. The primary motivation for developing such a model is to provide a more accurate calculation of the displacement dependent resistance of shear joints under e.g. accidental load cases, as this information may facilitate an estimate of the overall robustness for the structural system. The model is based on a second order rigid-plastic approach, where change of structural geometry has to be considered in order to correctly model the response at large shear displacements. The adopted approach differs from most of the previous works on this topic and has the advantage of being able to provide a simple and unique link between the relative displacement in the joint and the MN-interaction diagram for the rebar cross section. The link is established by combining the normality condition of plastic theory with the kinematical conditions of the dowel. As will be shown, the link eventually also allows for inclusion of interface friction in a consistent manner.

2. Experimental program

2.1. Material properties and test setup

The experimental program was designed to examine the development of dowel and catenary action in rebars crossing an interface loaded in pure shear. For this purpose, push-off tests were carried out on specimens with one single rebar, two rebars and four rebars (i.e. $n = 1$, 2 or 4) crossing the casting joint. In most cases, three replicates of the same layout were successfully tested. The general specimen layout is shown in Fig. 2. The rebars were placed symmetrically about the principal axis of the specimen cross section. In the case of $n = 2$ and $n = 4$, the rebars were placed with a mutual distance of 42 mm. The shear load was applied in the direction of the z-axis shown in Fig. 2. Specifications and material properties have been summarized in Table 1. As indicated in Fig. 2, confinement reinforcement in the form of rectangular stirrups was used to prevent premature splitting failure of the concrete block. The rebars crossing the casting joint had threads at both ends for installation of anchorage plates (to ensure development of full tensile capacity when catenary action developed). The specimens were cast in two sequences. At first, half of each specimen was cast in plywood formwork with smooth surfaces. The second half was cast the day after. Before the second cast, grease was applied to the casting joint in order to reduce friction.

A regular concrete (denoted C in Table 1) with a maximum aggregate size of 16 mm and a commercial mortar (denoted M in Table 1) containing aggregate sizes of 0–2 mm were used to obtain three combinations of casting joints. The combinations were (see also Table 1): concrete-to-concrete (C/C), mortar-to-mortar (M/M), and mortar-to-concrete (M/C). The main differences between the two materials are the aggregate composition and the compressive strength, see Table 2 for the proportions of the concrete mixture. All specimens were provided with rebars with diameter $d = 8$ mm.

The specimens were tested in a classical push-off setup, where the thrust line of the applied load coincides with the plane of the casting joint in order to simulate pure shear loading, see Fig. 3.

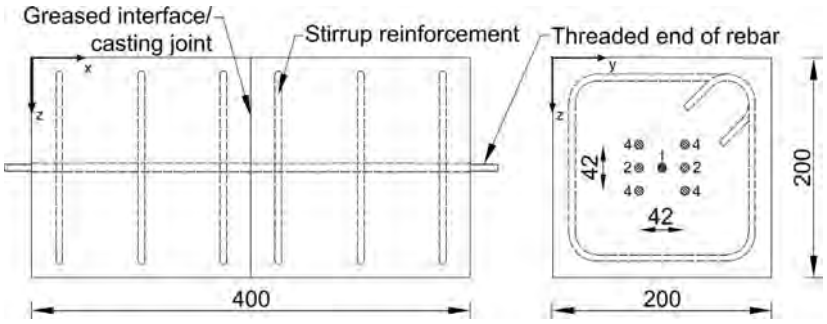

Fig. 2. General geometry of test specimens for push-off shear tests and indication of position of rebars in specimens with $n = 1$, 2 and 4 rebars.

Table 1
Specifications and material properties for test series (C = concrete, M = mortar, n = number of rebars).

n	Interface combination	d [mm]	f_y [Mpa]	f_u [MPa]	f_{c1} [MPa]	f_{c2} [MPa]	No. of rep.
1	C/C	8	614	729	48.0	48.0	3
1	M/M	8	614	729	33.1	33.1	3
1	M/C	8	614	729	33.3	47.7	3
2	C/C	8	614	729	46.5	46.5	3
2	M/M	8	614	729	34.1	34.1	2
2	M/C	8	614	729	30.3	35.3	3
4	C/C	8	551	708	43.0	43.0	3
4	M/M	8	614	729	34.5	34.5	2
4	M/C	8	551	708	37.2	45.4	3

Table 2
Proportions of the concrete mixture.

	[kg/m^3]
Cement	321.4
Water	156.1
Superplasticizer	2.0
Aggr. 0–4 mm	848.6
Aggr. 4–8 mm	330.0
Aggr. 8–16 mm	753.3
w/c	0.49

The tests were performed in quasi-static deformation control with a constant rate of piston movement of 2.5 mm/min. Relative shear displacements in the joint were measured on both sides of the specimens using linear variable differential transducers.

2.2. Test results

Fig. 4 shows the measured load-displacement relationships for all tests. Within each test series (i.e. interface combinations C/C, M/M, and M/C) the load level for any given value of displacement, u, is roughly speaking proportional to the number of rebars crossing the joint. This indicates that the mutual distance (42 mm) between the rebars was sufficient to avoid group action. It was generally observed, that the specimens behaved almost linear elastic in the beginning. Then, gradually, the response curves became non-linear with loss of stiffness. By imposing further shear displacement, the load-displacement curves developed in a concave manner which led to increasing tangent stiffness. At a certain point, the tangent stiffness decreased again due to a convex development of the response curves. The convex development initiated partly as a result of the stress–strain relation of the reinforcement

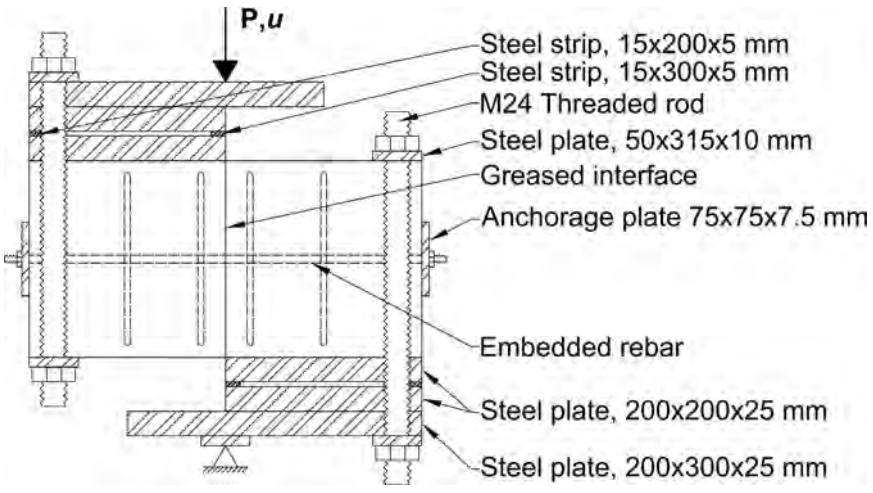

Fig. 3. Test setup for push-off testing of casting joints crossed by rebar(s).

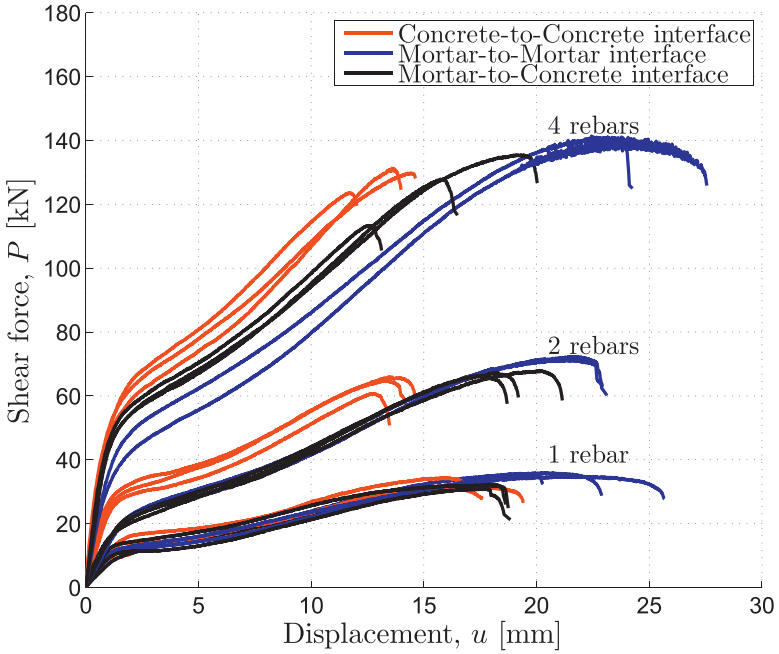

Fig. 4. Test results from all specimens.

which at this point must have experienced hardening after initial yielding and hence the tangent stiffness decreases with increased shear displacement. This continues until the ultimate load, which was found at a maximum shear displacement in the range of 15–25 mm. All tests were terminated by rupture of the rebars, and for the specimens with the same number of rebars, larger maximum shear displacement also resulted in higher ultimate loads. From post-test examinations of the specimens, severe local crushing of the concrete/mortar was observed near the interface as shown in Fig. 5(a). Fig. 5(b) shows a photo of the deflected shape of a ruptured rebar removed from a test specimen after testing. The plastic deformations of the rebar were concentrated within a length that corresponds to a few rebar diameters on both sides of the interface. Outside this region, the rebars remained straight, see Fig. 5(b).

When comparing the response of specimens containing the same number of rebars, it is observed that specimens with C/C interface carried the highest load at the point where the non-linear part of the response clearly emerges. This point is lowest for the curves belonging to specimens with M/M interface. As can be seen, this tendency is most pronounced for specimens with four rebars ($n = 4$) which seems reasonable since the largest difference between the compressive strengths of concrete and mortar was found for these tests, cf. Table 1. It should be noted, however, that although the response curves of the concrete specimens lie above those of the mortar specimens, then, at the final stage, specimens with mortar-to-mortar interface were actually able to carry the highest ultimate load. The results are interesting and indicate that while the compressive strength has a positive influence on the transition to non-linear behavior, then in the end, a higher compressive strength leads to lower ultimate load. The reason for this will be discussed in Section 4.

On an overall level, the tested specimens behaved similar to tests reported by Engström [24] and Randl and Wicke [25]. However, Engström tested bolts with larger diameters which induced greater action in the concrete block and for this reason premature splitting failure of the concrete specimens was observed before rupture of the reinforcement/bolts occurred. Randl and Wicke reported similar load-displacement curves from tests on T-headed bars embedded in concrete. They observed shear displacements up to 20 mm and failure by rupture of the reinforcement. In their study, the interface properties were varied which influenced the shape of the load-displacement curves, especially at the transition to non-linear behavior.

(a) Local crushing of mortar/concrete (b) Rupture of rebar

Fig. 5. Local crushing at rebars at the casting joint (a) and deflected shape of ruptured rebar (b).

3. Second order plastic modeling

The non-linear part of the load-displacement response of two-sided dowel joints will in this paper be modeled by use of a simple second order plasticity approach where concrete as well as reinforcing steel are treated as rigid-plastic materials with finite deformation capacity. In the model, displacements are therefore the sole results of accumulated plastic deformations. The model will be established for the general case, where the casting joint is the interface between two different concretes (having different compressive strengths). Initially, the model is established for perfectly smooth joints. The effect of friction in the joint interface is then included by an extension of the model.

3.1. Mechanism and kinematic relationships

The starting point of the model is to assume a failure mechanism for the rebar, see Fig. 1, where two plastic hinges must develop to allow for relative displacement, u, in the joint. The position of the plastic hinges (defined by the distances l_1 and l_2 from the joint) depends on the strength of the concretes and the moment capacity of the rebar cross section. In order to comply with compatibility requirements, the plastic hinges must in addition to rotations also undergo elongations when u increases. The rates of plastic deformations can be determined by establishing the kinematic relationship for the assumed mechanism. Then, by imposing the normality condition of plastic theory and by applying the work equation for increments of displacement, the necessary equations to determine the load P as a function of displacement, u, can be derived.

The problem is treated as a static displacement controlled problem, where the relative shear displacement in the joint, u, is considered as a monotonic function of time. For convenience, a displacement velocity equal to unity is assumed:

$$u(t) = t \tag{1}$$

From simple geometrical considerations, the following relationship can be established between u and the angle of rotation, θ, in the plastic hinges:

$$\tan\theta = \frac{u}{l_1 + l_2} = \frac{u_1}{l_1} = \frac{u_2}{l_2} \tag{2}$$

where $u_1 + u_2 = u$, see Fig. 1. To accommodate the change of geometry when u increases, it is necessary to impose elongation in the rebar in addition to rotation of the plastic hinges. Since rigid-plastic material behavior has been assumed, it is convenient to consider the elongation as a plastic extension, Δ, concentrated in the hinges (as indicated in Fig. 1). In this way, θ and Δ may be regarded as the general strains in the plastic hinges, which are subjected to general stresses in the form of bending moments, M, and normal forces, N. The following relationship between u and Δ can be established:

$$\Delta = -\frac{l_1 + l_2}{2} + \frac{l_1 + l_2}{2}\sqrt{1 + \left(\frac{u}{l_1 + l_2}\right)^2} \tag{3}$$

Based on Eqs. (1)–(3), the rates of plastic deformations in the hinges can be determined as follows:

$$\dot{\theta} = \frac{d\theta}{dt} = \frac{d\theta}{du}\frac{du}{dt} = \frac{l_1 + l_2}{(l_1 + l_2)^2 + u^2} \tag{4}$$

$$\dot{\Delta} = \frac{d\Delta}{dt} = \frac{d\Delta}{du}\frac{du}{dt} = \frac{u}{2\sqrt{(l_1 + l_2)^2 + u^2}} \tag{5}$$

Finally, by use of Eqs. (4) and (5), the following condensed expression for the kinematical condition of the rebar can be established:

$$\frac{\dot{\Delta}}{\dot{\theta}} = \frac{u}{2}\sqrt{1 + \left(\frac{u}{l_1 + l_2}\right)^2} \tag{6}$$

3.2. Constitutive relationship and sectional forces in the plastic hinges

The assumption of rigid-plastic material behavior implies that in the case of pure tension, plastic deformation in the rebar is only possible when the cross section is subjected to the plastic tensile capacity N_p. Further, in the case of pure bending, plastic deformation is only possible when the cross section is subjected to the plastic moment capacity M_p. These sectional capacities are:

$$N_p = \frac{\pi}{4}d^2 f_y \tag{7}$$

$$M_p = \frac{1}{6}d^3 f_y \tag{8}$$

where d is the cross sectional diameter of the rebar and f_y is the yield stress of the rebar. For combinations of bending and axial tension, plastic deformations may initiate when the yield condition of the cross section is fulfilled, i.e. when $f(M,N) = 0$. The yield condition (or the MN-interaction diagram) can be derived by requiring static equivalence between the sectional forces (M,N) and the distribution of normal stresses shown in Fig. 6. The result appears as follows:

$$f(N,M) = \frac{N}{N_p} + \frac{2}{\pi}\left(\arcsin\left(\left(\frac{M}{M_p}\right)^{\frac{1}{3}}\right) - \left(\frac{M}{M_p}\right)^{\frac{1}{3}}\sqrt{1 - \left(\frac{M}{M_p}\right)^{\frac{2}{3}}}\right) - 1 = 0 \tag{9}$$

As an approximation, the mathematically simpler yield condition for a rectangular cross section is sometimes adopted when studying dowel and catenary action in rebars, see e.g. [21–23,25].

Now, according to the normality condition of plastic theory, the rates of plastic deformations must fulfill the following constitutive relationship:

$$\dot{\theta} = \lambda\frac{\partial f}{\partial M} = \lambda\frac{8}{\pi d^3 f_y}\frac{1}{\sqrt{1 - \left(\frac{M}{M_p}\right)^{2/3}}} \tag{10}$$

$$\dot{\Delta} = \lambda\frac{\partial f}{\partial N} = \lambda\frac{4}{\pi d^2 f_y} \tag{11}$$

where λ is a positive constant proportional to the displacement velocity. The constant vanishes when Eqs. (10) and (11) are used to establish the following ratio of plastic strain rates:

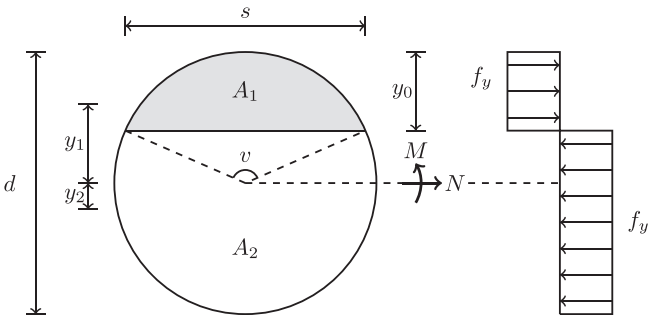

Fig. 6. Plastic stress distribution in a circular cross section subjected to M and N.

$$\frac{\dot{\Delta}}{\dot{\theta}} = \frac{d}{2}\sqrt{1-\left(\frac{M}{M_p}\right)^{2/3}} \tag{12}$$

It can be seen that Eq. (12) together with Eq. (6) provides a link between the kinematical conditions and the state of stresses in the plastic hinges. This means that the bending moment, $M(u)$, carried by the plastic hinges for any given value of displacement, u, can be determined by equating the right hand side of Eq. (6) to the right hand side of Eq. (12). The tension force, $N(u)$, may thereafter be determined by imposing $f(M,N)=0$ according to Eq. (9). The results are:

$$\frac{M(u)}{M_p} = \left(1-\left(\frac{u}{d}\right)^2\left(1+\left(\frac{u}{l_1+l_2}\right)^2\right)\right)^{3/2} \not< 0 \tag{13}$$

$$\frac{N(u)}{N_p} = 1-\frac{2}{\pi}\left(\arcsin\left(\left(\frac{M(u)}{M_p}\right)^{\frac{1}{3}}\right)-\left(\frac{M(u)}{M_p}\right)^{\frac{1}{3}}\sqrt{1-\left(\frac{M(u)}{M_p}\right)^{\frac{2}{3}}}\right) \not> 1 \tag{14}$$

The ratio $M(u)/M_p$ in Eq. (14) may be replaced by the right hand side of Eq. (13) in order to obtain an explicit expression for the normal force in the rebar as a function of u.

3.3. Effective stress distribution in the concrete

The assumed displacement field for the rebar implies that it has to cut its way through the concrete and thereby cause local crushing failure. It is in this context not possible on the basis of the present simplified approach to determine in details the entire stress distribution in the concrete. For triaxial stress conditions of the type developed in the concrete at the dowel, an enhanced compressive strength, f_{cc}, is therefore usually assumed:

$$f_{cc} = cf_c \tag{15}$$

where $c \geqslant 1$ is the so-called enhancement factor which has to be determined by calibration with test results. Rasmussen [13] found c-values in the range of 3.7–5.4 from tests on one-sided dowels. Similar c-values have also been suggested in Refs. [1,23,27]. There is a close link between the average triaxial compressive strength, f_{cc}, and the position of the plastic hinges. Rasmussen [13] used a simple plasticity approach to establish this link, which eventually led to an estimate of the load carrying capacity related to pure dowel action (i.e. the so-called first order plastic solution). The same approach is adopted in the following for two-sided dowels in order to determine the distances l_1 and l_2. As shown in Fig. 7(a), it is assumed that contact pressures of magnitude $f_{cc,1}$ and $f_{cc,2}$ are acting uniformly on the rebar over the lengths l_1 and l_2, respectively, when the rebar starts to carry load by pure dowel action (see also Nielsen and Hoang [28]). The corresponding shear and moment diagrams for the rebar are shown in Fig. 7(a) as well. By setting up the vertical force equilibrium and moment equilibrium for the part of the rebar between the two plastic hinges, it is possible to establish the following equations to calculate l_1 and l_2:

$$l_1 = \sqrt{\frac{2}{3}}\frac{d}{\sqrt{1+\frac{f_{cc,1}}{f_{cc,2}}}}\sqrt{\frac{f_y}{f_{cc,1}}} \tag{16}$$

$$l_2 = \sqrt{\frac{2}{3}}\frac{d}{\sqrt{1+\frac{f_{cc,2}}{f_{cc,1}}}}\sqrt{\frac{f_y}{f_{cc,2}}} \tag{17}$$

When setting up the equilibrium equations leading to Eqs. (16) and (17), it has been utilized that the moment capacity, M_p, of the rebar cross section is given by Eq. (8). In the case of identical material properties on both sides of the joint, i.e. $f_{cc,1}=f_{cc,2}$, Eqs. (16) and (17) will, as expected, be identical to the results presented in Nielsen and Hoang [28]. It should be noted that the assumed uniform distribution of contact pressures only leads to zero moment in the rebar at the interface when $f_{cc,1}=f_{cc,2}$ (see moment diagram in Fig. 7(a)). Hence, to maintain equilibrium when $f_{cc,1}\neq f_{cc,2}$ and when the external action corresponds to pure shear (i.e. thrust line coinciding with interface plane), tension must develop in the rebar which eventually leads to a distribution of so-called clamping stresses in the interface. The tension force together with the clamping stresses will then be able to outbalance the (small) bending moment in the rebar at the interface cross section. According to Eq. (14), tension develops in the rebar as soon as $u>0$. Therefore, strictly speaking, the assumption of uniformly distributed contact pressure is not able to fulfill all equilibrium requirements at $u=0$ (i.e. initiation of pure dowel action) when $f_{cc,1}\neq f_{cc,2}$. This is, however, acceptable since the assumption primarily was motivated by the aim of obtaining a simple estimate of the position of the plastic hinges. In reality, the rebar will probably experience combinations of tension and bending moments already in the elastic range.

The simple stress distribution shown in Fig. 7(a) cannot be adopted for analysis of the entire load-displacement response. When dowel action is accompanied by tension in the rebar (and in the end completely replaced by catenary action) the average contact pressure must decrease due to the assumed material properties and the equilibrium conditions. Since concrete is not a perfectly rigid-plastic material, there will be a softening effect which in turn reduces the concrete pressure when the concrete experiences too large compressive strains. The displacement, u, and thereby the local deformations may become so large that the concrete near the joint interface spalls off/crushes thus leaving this zone to be stress free, see e.g. Fig. 5(a). Therefore, due to material properties, redistribution of the contact pressure will take place as u increases. In addition to this, the redistribution of stresses must take place in such a way, that equilibrium can be maintained when catenary action starts to develop in the rebar.

It is not possible in a rigid-plastic model to theoretically account for the above mentioned softening of the concrete. Therefore, in the following, as u increases, the effect of softening (and spalling of concrete) will indirectly be taken into account by introducing effective lengths, $l_{1,ef}$ and $l_{2,ef}$, over which contact pressures $f_{cc,1}$ and $f_{cc,2}$ are assumed to act uniformly, see Fig. 7(b). This may be interpreted as an assumption of rigid-plastic behavior with finite deformation capacity, although there is actually no real information about the deformation capacity of the concrete when it is subjected to contact pressure by the dowel. The only simple way to establish the condition for $l_{1,ef}$ and $l_{2,ef}$, as u increases, is therefore through equilibrium considerations. Hence, by establishing vertical force equilibrium and moment equilibrium for the part of the rebar between the plastic hinges, see Fig. 7(b), and by utilizing that the plastic hinges now are subjected to $M(u)$ and $N(u)$ as given by Eqs. (13) and (14), the following relationship between u and the effective lengths $l_{1,ef}$ and $l_{2,ef}$ can be established:

$$l_{i,ef} = l_i\left(1-\sqrt{1-\frac{M(u)}{M_p+\left(\frac{u}{2}\right)^2 d\frac{f_{cc,1}f_{cc,2}}{f_{cc,1}+f_{cc,2}}}}\right) \not< 0 \tag{18}$$

where $i=1$ and 2. It appears that the effective length is equal to the initial lengths, cf. Eqs. (16) and (17), when $u=0$ and reduces to zero when u has reached a value that makes $M(u)=0$. The latter situation corresponds to a transition to full catenary action where the plastic hinges turn into moment-free hinges. Therefore, the rebar will no longer experience contact pressure between the two hinges, but instead acts as a tie.

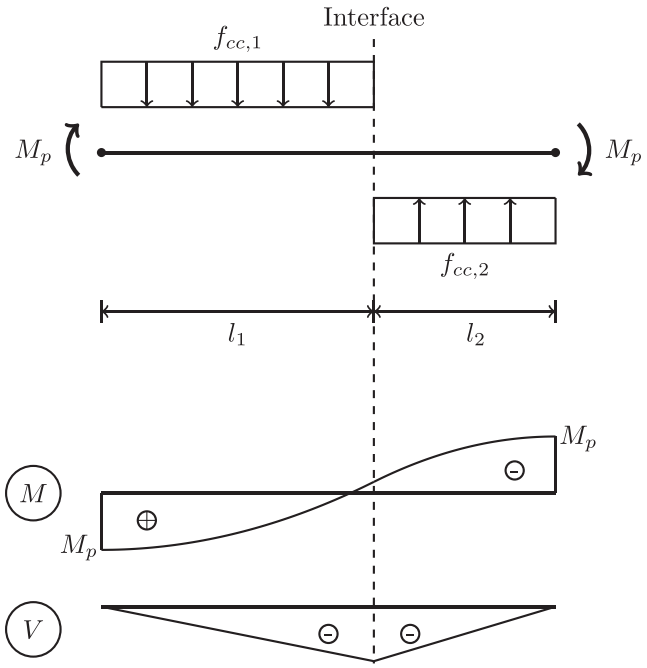

(a) *Undeformed state and distribution of moment and shear in rebar*

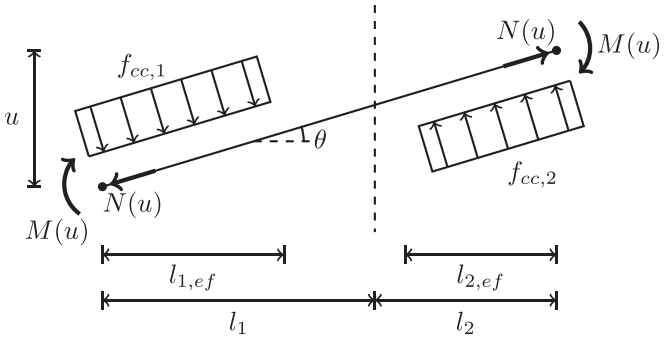

(b) *Deformed state with distribution of contact pressure*

Fig. 7. Position of plastic hinges and extent of distribution of contact pressure at initiation of pure dowel action (a) and at combined dowel action and catenary action (b).

3.4. Deformation capacity of rebars

As described in the previous, all push-off tests were terminated when rupture of the rebars took place, i.e. when the deformation capacity of the rebar was reached. To capture this effect in the model, it is necessary to express the deformation capacity of the rebar in terms of the plastic elongation in the hinges. This means that an upper limit, Δ_{max}, must be introduced such that Eq. (3) may be used to determine the displacement capacity, u_{max}, of the system.

An estimate of Δ_{max} can be obtained from a detailed study of the tension tests of the reinforcement. Fig. 8(a) shows four tested stress-elongation relationships for the type of rebar used in this study. The measured elongations represent the strain accumulations over the so-called necking zone. The results were obtained by using digital image correlation (DIC) analysis based on images taken at approximately 0.25 hertz with a 36 megapixel camera. An example of results of a DIC analysis, showing strain localization in the rebar just before rupture, can be seen in Fig. 8(b). The curves in Fig. 8(a) were determined by post-processing of the digital strain measurements, where it was possible to isolate the elongation over a distance of two times the rebar diameter, $2d$, within which strain localization took place. Based on the results in Fig. 8(a), an elongation capacity of Δ_{max}= 3 mm is adopted. It should in this context be noted that the standard methods for determination of nominal strain capacity of reinforcing steel cannot be used to estimate Δ_{max}. This is so because the nominal strain capacity is based on a reference length, which is much longer than the necking zone as well as the characteristic length of the present problem, i.e. the distance between the two plastic hinges.

3.5. Load-displacement response of frictionless joints

Based on the obtained results and the assumptions made, it is now possible to determine the load-displacement response by use of the work equation. For this purpose, a stationary situation with displacement u and load $P(u)$ is used as the starting point from which an increment of displacement, δu, is considered. The external work, W_E, is then given by:

$$W_E = P(u)\delta u \tag{19}$$

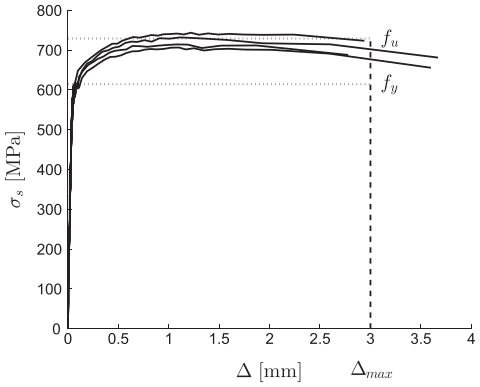

(a) *Stress-elongation relation*

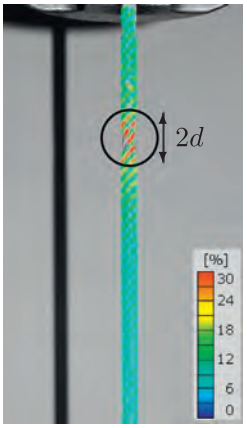

(b) *Aramis results at necking (major principal strain)*

Fig. 8. Local stress-elongation relationship for rebars and indication of the measurement length spanning the zone where necking occurs.

The internal work, W_I, has contributions from the energy dissipated in the plastic hinges as well as the energy absorbed when the concrete crushes at the rebar. The following formula can be derived:

$$W_I = f_{cc,1} l_{1,\mathrm{ef}} d\left(\frac{1}{2}\frac{l_{1,\mathrm{ef}}}{l_1}\delta u_1\right) + f_{cc,2} l_{2,\mathrm{ef}} d\left(\frac{1}{2}\frac{l_{2,\mathrm{ef}}}{l_2}\delta u_2\right) + 2N(u)\delta\Delta + 2M(u)\delta\theta \tag{20}$$

where the incremental displacement and deformation quantities, $\delta u_1, \delta u_2, \delta\Delta$, and $\delta\theta$, can be expressed in terms of δu through the following relationships (with $\delta t = \delta u$ according to Eq. (1)):

$$\delta\theta = \dot{\theta}\delta u \tag{21}$$

$$\delta\Delta = \dot{\Delta}\delta u \tag{22}$$

$$\delta u_1 = \frac{l_1}{l_1 + l_2}\delta u \tag{23}$$

$$\delta u_2 = \frac{l_2}{l_1 + l_2}\delta u \tag{24}$$

Now, by inserting the right hand side of Eqs. (21)–(24) into Eq. (20) and by setting up the work equation, i.e. $W_E = W_I$, the following solution is obtained for the load-displacement response of a perfectly smooth two-sided dowel joint:

$$P_s(u) = \begin{cases} \frac{1}{2} f_{cc,1} d \frac{l_{1,\mathrm{ef}}^2}{l_1 + l_2} + \frac{1}{2} f_{cc,2} d \frac{l_{2,\mathrm{ef}}^2}{l_1 + l_2} + 2N(u)\dot{\Delta} + 2M(u)\dot{\theta}, & \text{for} \quad N(u) < N_p \quad (25a) \\ 2N_p\dot{\Delta}, & \text{for} \quad N(u) = N_p \quad (25b) \end{cases}$$

Here $M(u), N(u), \dot{\Delta}, \dot{\theta}, l_{1,\mathrm{ef}}$, and $l_{2,\mathrm{ef}}$ can be expressed as explicit functions of the displacement u as shown earlier. The solution is valid as long as u is less than the displacement capacity, $u_{\max}$, which can be calculated from Eq. (3) by inserting the deformation capacity of the rebar, $\Delta_{\max}$. The index s in $P_s(u)$ indicates that this solution applies to a smooth interface without friction. How to include effects of friction will be shown in the next section.

Solution (25a) applies to the regime, where a combination of dowel action and catenary action exists in the rebar while pure catenary action (i.e. $M = 0$ in the plastic hinge) is described by Eq. (25b).

Fig. 9 shows an example of a response curve, $P_s(u)$, as predicted by Eq. (25). The calculations were performed by use of the parameters given in Table 3. In the figure the different contributions to the response are indicated with dashed colored lines and the total is represented by a solid line. The transition from combined dowel and catenary action to pure catenary action is indicated with a cross. It appears that the load-displacement response follows a descending branch (local drop) when the regime with in-elastic deformations initiates. The local drop is a result of the material assumptions adopted in the model which at the onset of in-elastic deformation estimates the capacity assuming a uniform distribution of contact stresses at the dowel, see Fig. 7(a). When the in-elastic shear displacement is increased, the equilibrium considerations applied in the deformed state, see Fig. 7(b), cause the load to drop locally. As the contribution from the normal force, $N(u)$,

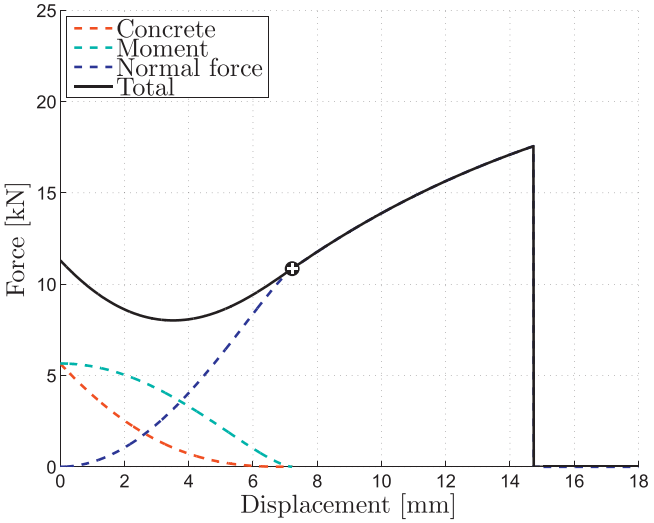

Fig. 9. Load-displacement response of a single rebar crossing a frictionless joint.

Table 3
Parameters used for presentation of load-displacement response for a single rebar crossing a frictionless interface.

Parameter	Value
d	8 mm
f_y	500 MPa
c_1	5.0
$f_{c,1}$	30 MPa
c_2	5.0
$f_{c,2}$	50 MPa
Δ_{max}	3 mm

increases with increasing displacement, the load starts to increase monotonically until a point where the deformation capacity of the rebar is exhausted and the load drops to zero.

3.6. Inclusion of friction

The model presented in the previous applies to perfectly smooth joints. However, casting joints can seldom be characterized as totally frictionless and it is therefore important for practical applications to take into account the contribution from interface friction. It turns out that the model actually provides most of the information needed to include the effect of friction on the load-displacement response. Fig. 10 illustrates a free body diagram of half of the specimen. It is assumed that the interface has a roughness that corresponds to a friction coefficient of μ. At any given displacement, u, the tension force in the rebar, $N(u)$, can be determined by Eq. (14). The tension force causes compressive normal stresses to develop in the interface. The resultant of these so-called clamping stresses is equal to the horizontal projection of $N(u)$. Then, from simple shear-friction considerations, the following would be the contribution from friction to the load carrying capacity:

$$P_f(u) = \mu N(u) \cos\theta \tag{26}$$

Here index f indicates that the contribution relates to friction and the angle θ is given by Eq. (2). The total load-displacement response when including the effect of dowel and catenary action as well as the effect of friction then amounts to:

$$P_{\text{total}}(u) = P_s(u) + P_f(u) \tag{27}$$

Recently Santos and Júlio [29] gave an overview of the suggested values for the coefficient of friction related to shear-friction theory. The values vary widely and some of the earlier contributors to this area, e.g. Birkeland and Birkeland [30], suggested values for artificially roughened surfaces (in the order of $\mu = 1.4$) and $\mu = 0.8 - 1.0$ for construction joints. However, it should be noted that these rather high values were suggested/calibrated for a model, where all resistance in the joint was assumed to be due to friction without consideration of dowel action. Bennett and Banerjee [31] suggested a combination of friction (with $\mu = 0.6$) and dowel action including a moment in the interface, however, without combination of bending and tension in the rebar. Engström [24] introduced a model which combines friction and dowel action, taking combinations of bending and tension in the rebar into account, and he suggested that $\mu = 0.3 - 0.6$ should be used for concrete-to-concrete interface friction. Randl and Wicke [25] also considered combinations of dowel action and tension with friction and suggested $\mu = 0.5$ for smooth interfaces. These previous works did, however, not contain a solution for how to relate the shear displacement, u, in the joint with the sectional forces carried by the rebar. The suggested coefficients of friction (based on model calibration) are therefore partly influenced by the estimate of the clamping forces.

In the experimental program of this study, the smooth interfaces were, as mentioned, treated with grease before casting of the second batch to minimize friction. The friction coefficient should therefore be less than that suggested by Randl and Wicke and most probably in the lower end of the range suggested by Engström. In the following a coefficient of friction in the order of $\mu = 0.3$ is adopted. This value of μ has been used to determine the load-displacement relationships shown in Fig. 11, calculated by Eq. (27). The capacity without friction, i.e. $P_s(u)$, as well as the development of the frictional contribution, $P_f(u)$, are also shown as dashed lines. It can be seen that after the point of transition to pure catenary action (i.e. $N(u) = N_p$), the contribution from friction decreases. The reason for this is of course that the clamping force decreases as the angle of rotation, θ, increases. It appears from Fig. 11 that friction does not have an influence on the first order plastic solution for pure dowel action. The response curve, however, is shifted upwards once the rebar starts to carry tensile forces and friction is activated.

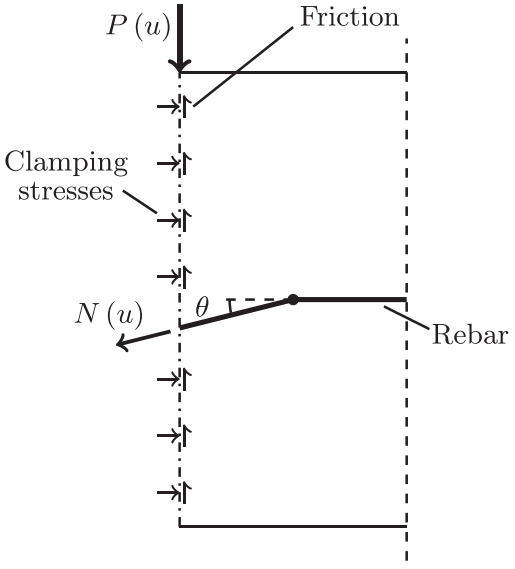

Fig. 10. Contribution of friction in the interface.

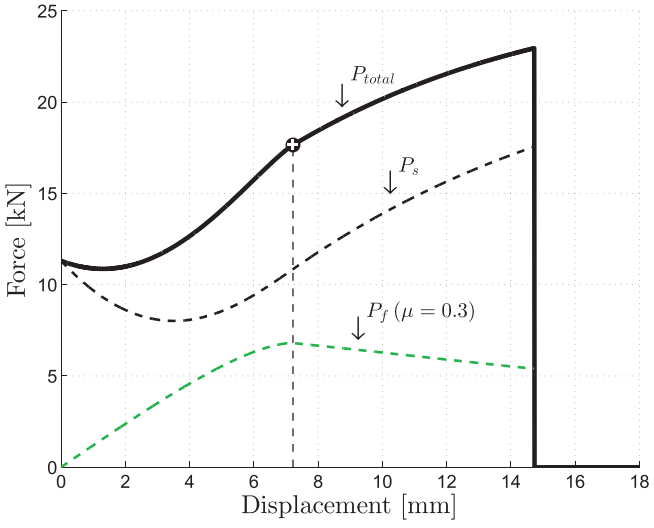

Fig. 11. Inclusion of interface friction to the model response.

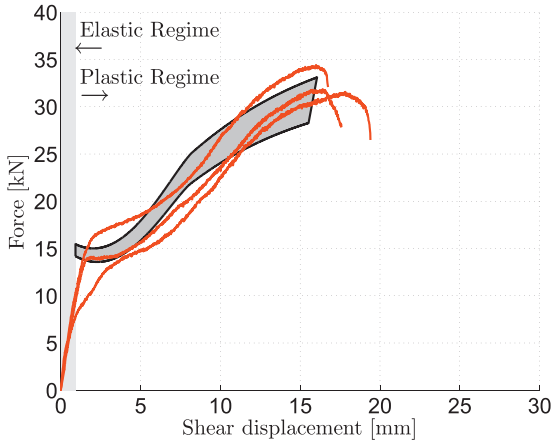

(a) C/C 1 rebar

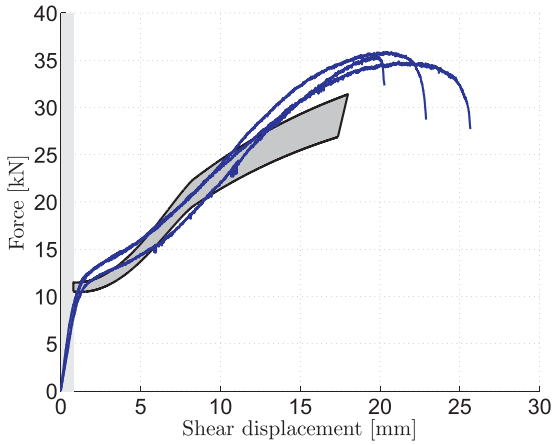

(b) M/M 1 rebar

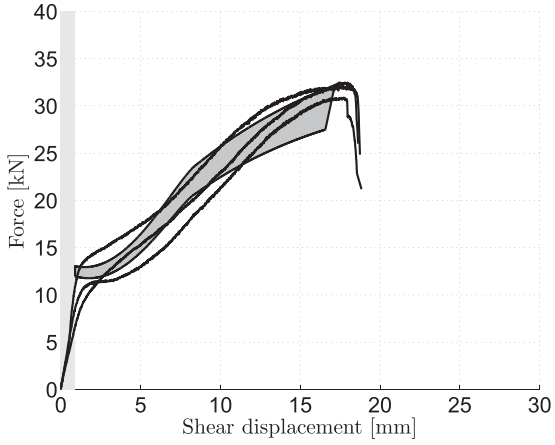

(c) M/C 1 rebar

Fig. 12. Comparison of model with test results - 1 rebar.

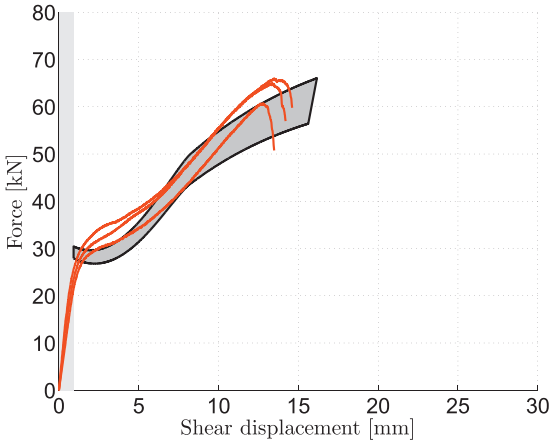

(a) C/C 2 rebars

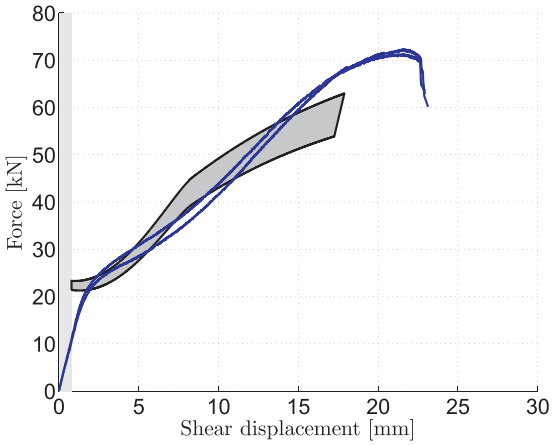

(b) M/M 2 rebars

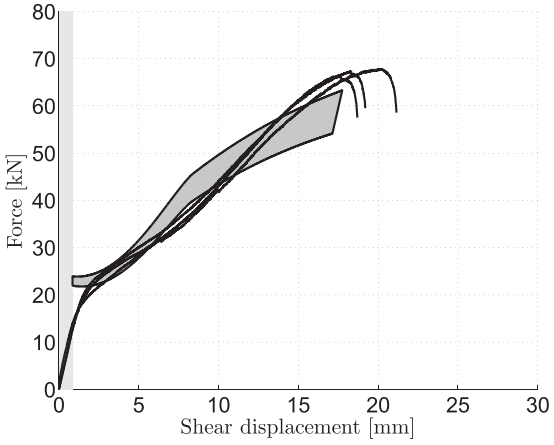

(c) M/C 2 rebars

Fig. 13. Comparison of model with test results - 2 rebars.

4. Comparison of model with test results

The load-displacement response predicted by the model, Eq. (27), has been compared with the experimental results and depicted in Figs. 12–14. The basic input parameters have been obtained from Table 1. By adopting a friction coefficient of $\mu = 0.3$ as argued for in the previous, there is only the enhancement factor, c, left to calibrate the model with test results.

For concrete, a value of $c = 5$ is adopted, similar to the findings of Vintzēleou and Tassios [3]. To obtain reasonable agreement with tests, a smaller value has been adopted for mortar, namely $c = 4$. The fact that the enhancement factor should be smaller in the case of mortar may possible be explained by the relatively more brittle behavior of mortar (as compared to concrete) due to the relatively less aggregate content as well as the relatively smaller average aggregate size.

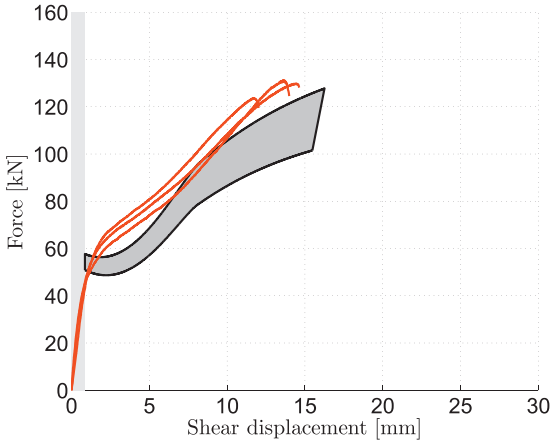

(a) C/C 4 rebars

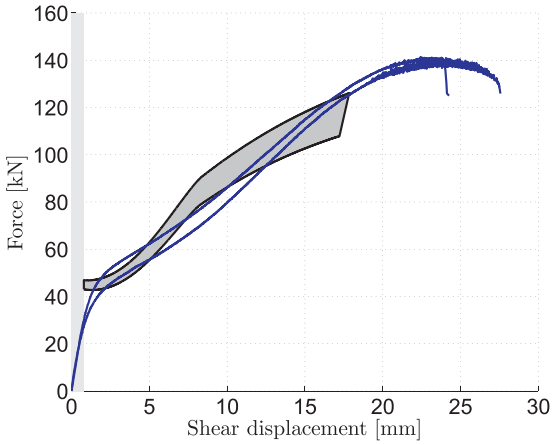

(b) M/M 4 rebars

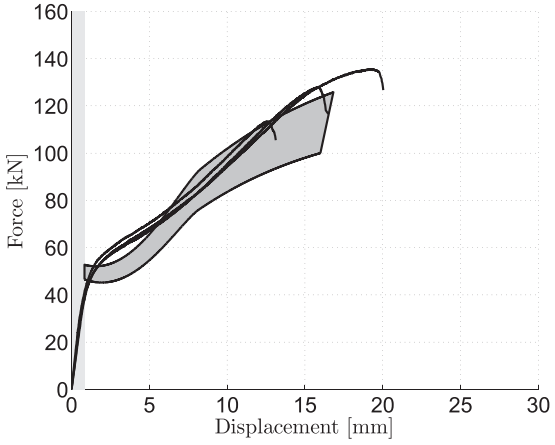

(c) M/C 4 rebars

Fig. 14. Comparison of model with test results - 4 rebars.

As can be seen in Figs. 12–14, the model predictions consist of an upper and a lower curve with the area in between shaded in grey. The lower curves represent calculations based on the yield stress, f_y, while the upper curves are based on calculations where f_y in the model has been replaced by the tensile strength f_u. Calculations with f_u have been included because hardening of reinforcement is not included in the model. The shaded area between the two limiting curves thus indicates the expected range of test results.

The model only predicts the non-linear behavior. The calculated response curves have therefore been shifted horizontally to a displacement, u_0, where the plastic behavior begins. This is shown in the figures with a shaded light grey area and is in Fig. 12(a) indicated by arrows showing 'elastic regime' and 'plastic regime'. To determine the horizontal shift, an estimate of the maximum displacement in the elastic regime has to be derived. In the present work, this estimate has been obtained by modeling the rebar as a beam on an elastic foundation with a constant stiffness, e.g. as shown in Refs. [2–10]. The calculations can be seen in Appendix A. Despite the simplicity of the elastic model, Eq. (A.1) actually provides a reasonable estimate of the displacement, u_0, where the in-elastic displacement regime begins.

It can be seen that with the adopted enhancement factors, c, and the coefficient of friction, μ, the general development of the tested response curves is captured rather well. The predicted response also displays a concave development followed by a convex development, although not entirely coinciding with the tested response. As mentioned earlier, the test responses show a dependency of the compressive strength of the concrete. The model explains some of these observations. As already shown by Rasmussen [13], the load that causes transition to the non-linear behavior is proportional to the geometric mean of f_c and f_y, which is observed e.g. in Fig. 4. On the other hand, the ultimate load at a high shear displacement is a result of catenary action, where change of geometry plays an important role. Here, a lower compressive strength of the concrete (or mortar) is beneficial for catenary action because this requires plastic deformation over a longer length of the rebar and at the same time makes it easier for the rebar to cut its way through the concrete (or mortar). This eventually leads to larger maximum displacement and thereby also a higher ultimate load. This is, to some extend, captured by the model. In addition, the calculations based on f_u provide the best estimate of the ultimate peak load. This result is as expected since the peak load corresponds to reinforcement rupture (as observed in tests).

As a final remark, it should be noted that although the model does not agree with test results in all aspects, then for robustness assessment, the model seems to have potential for practical use. The reason for this is that in a robustness analysis, the dissipated plastic energy (i.e. the area below the response curve) is a main concern. In this respect, and based on Figs. 12–14, the model seems to be able to provide a reasonable estimate of the available plastic energy.

5. Conclusions

Push-off tests of two-sided dowel joints have been performed and a simple, second order plasticity model has been developed to predict the in-elastic regime of the load-displacement response. The main experimental observations were:

- The load-displacement relationships were non-linear and consisted of convex followed by concavely shaped curves. The load increased with increasing shear displacement until the ultimate capacity corresponding to rupture of the rebar(s) was reached
- A mutual distance of $5.25d$ between the rebars in the interface plane did not lead to any observable group effect, as the magnitude of the results from specimens with $n > 1$ were proportional to the results of specimens with a single rebar ($n = 1$)
- Higher compressive strength of the concrete/mortar led to a higher load at the transition point between linear and non-linear behavior
- Specimens with a relatively lower compressive strength had a greater displacement capacity and a higher ultimate load than specimens with a relatively higher compressive strength

Despite the simplicity and the relatively small number of required input parameters, the developed second order plasticity model captured the main characteristics of the tested load-displacement responses well. Calculations based on the yield stress of the reinforcement provided an appropriate estimate of the load level, where non-linear behavior initiated. A reasonable estimate of the ultimate capacity at large shear displacements could be calculated by use of the ultimate strength of the reinforcement. The model has potential for practical assessment of structural robustness, where estimation of available plastic energy (area below load-displacement response) is important.

Acknowledgment

The experimental research presented in this paper was financially supported by the COWI Foundation. The experimental work was supported by M.Sc. Nikolai Bach and M.Sc. Martin Hansen during their master thesis. The authors gratefully acknowledge these valuable contributions.

Appendix A. Modeling of elastic displacement for dowel joints

The elastic displacement can be estimated by the analogy of a beam on an elastic foundation [2–10]. By solving the fourth order differential equation, the maximum elastic displacement can be formulated as given in Ref. [4]:

$$u_0 = \frac{P_0}{2\lambda^3 E_s I_s} \tag{A.1}$$

where P_0 is the maximum shear force (e.g. estimated by the load required to form plastic hinges, i.e. Eq. (25a) with $u = 0$), E_s is the elastic modulus and I_s is the second moment of area for the circular rebar. The parameter λ expresses a stiffness per length and is given by [2]:

$$\lambda = \sqrt[4]{\frac{k_c d}{4E_s I_s}} \tag{A.2}$$

where k_c is the stiffness of the elastic foundation. For the concrete material a stiffness, k_c, is suggested by Soroushian [12]:

$$k_c = \frac{127\sqrt{f_c}}{d^{2/3}} \tag{A.3}$$

References

[1] fib, Bulletin 43: Structural Connections for Precast Concrete Buildings, Fédération international du béton, Lausanne, Switzerland; 2008.
[2] Friberg BF. Design of dowels in transverse joints of concrete pavements. Am Soc Civ Eng 1938;64(9):1809–28.
[3] Vintzeleou EN, Tassios TP. Mathematical models for dowel action under monotonic and cyclic conditions. Magaz Concr Res 1986;38(134):13–22.
[4] Dei Poli S, Di Prisco M, Gambarova PG. Shear response, deformations, and subgrade stiffness of a dowel bar embedded in concrete. ACI Struct J 1992;89(6):665–75.
[5] Dei Poli S, di Prisco M, Gambarova PG. Cover and stirrup effects on the shear response of dowel bar embedded in concrete. ACI Struct J 1993;90(4):441–50.
[6] Mannava SS, Bush Jr TD, Kukreti AR. Load-deflection behavior of smooth dowels. ACI Struct J 1999;96(6):891–8.
[7] Randl N. Load bearing behaviour of cast-in shear dowels. Beton- und Stahlbetonbau 2007;102(S1):31–7.
[8] Tanaka Y, Murakoshi J. Reexamination of dowel behavior of steel bars embedded in concrete. ACI Struct J 2011;108(6):659–68.
[9] He XG, Kwan AKH. Modeling dowel action of reinforcement bars for finite element analysis of concrete structures. Comput Struct 2001;79(6):595–604.
[10] El-Ariss B. Behavior of beams with dowel action. Eng Struct 2007;29(6):899–903.
[11] Marcus H. Load carrying capacity of dowels at transverse pavement joints. J Am Concr Inst 1951;23(2):169–94.
[12] Soroushian P, Obaseki K, Rojas MC. Bearing strength and stiffness of concrete under reinforcing bars. ACI Mater J 1987;84(3):179–84.
[13] Højlund Rasmussen B. Betonindstøbte tværbelastede boltes og dornes bæreevne, English: Resistance of embedded bolts and dowels loaded in shear. Bygningsstatiske Meddelelser 1963;34(2):39–55.
[14] Calladine CR, Simple ideas in the large-deflection plastic theory of plates and slabs. In: Heyman J, Leckie FA, (Eds.). International conference on the applications of plastic theory in engineering design, Cambridge, UK, 1968, p. 93–127.
[15] Bræstrup MW. Dome effect in RC slabs: rigid-plastic analysis. J Struct Div – ASCE 1980;106(6):1237–53.
[16] Belenkiy LM. Upper-bound solutions for rigid-plastic beams and plates of large deflections by variation principles. J Eng Mech 2007;133(1):98–105.
[17] Bailey CG, Toh WS, Chan BM. Simplified and advanced analysis of membrane action of concrete slabs. ACI Struct J 2008;105(1):30–40.
[18] Mirzaei Y. Post-punching behavior of reinforced concrete slabs [Ph.D. thesis]. École Polytechnique Fédérale de Lausanne; 2010.
[19] Fernández Ruiz M, Mirzaei Y, Muttoni A. Post-punching behavior of flat slabs. ACI Struct J 2013;110(5):801–12.
[20] Gouverneur D, Caspeele R, Taerwe L. Experimental investigation of the load-displacement behaviour under catenary action in a restrained reinforced concrete slab strip. Eng Struct 2013;49:1007–16.
[21] Dulácska H. Dowel action of reinforcement crossing cracks in concrete. ACI J 1972;69(12):754–7.
[22] Millard SG, Johnson RP. Shear transfer across cracks in reinforced concrete due to aggregate interlock and to dowel action. Mag Concr Res 1984;36(126):9–21.
[23] Vintzeleou EN, Tassios TP. Behavior of dowels under cyclic deformations. ACI Struct J 1987;84(1):18–30.
[24] Engström B. Combined effects of dowel action and friction in bolted connections. Nordic Concr Res 1990;9:14–33.
[25] Randl N, Wicke M. Schubübertragung zwischen Alt- und Neubeton. Beton- und Stahlbetonbau 2000;95:461–73. Heft 8.
[26] Sørensen JH, Hoang LC, Olesen JF, Fischer G. Catenary action in rebars crossing a casting joint loaded in shear. Proceedings of the 11th fib international PhD symposium in civil engineering 2016:735–42.
[27] fib, fib Model Code for Concrete Structures 2010, Wilhelm Ernst & Sohn, Lausanne, Switzerland; 2013.
[28] Nielsen MP, Hoang LC. Limit analysis and concrete plasticity. 3rd ed. Boca Raton: CRC Press, Taylor & Francis Group; 2011.
[29] Santos PMD, Júlio ENBS. A state-of-the-art review on shear-friction. Eng Struct 2012;45:435–48.
[30] Birkeland PW, Birkeland HW. Connections in precast concrete construction. ACI J 1966;63(3):345–68.
[31] Bennett EW, Banerjee S. Strength of beam-column connections with dowel reinforcement. Struct Eng 1976;54(4):133–9.

In precast reinforced concrete structures, the joints and connections between the precast components are essential for the structural performance. This thesis presents a new design for keyed connections typically used between shear wall panels. An extensive experimental program is presented in combination with sound design methods developed on the basis of the theory of plasticity. The theoretical models include first order upper and lower bound modeling of keyed connections as well as second order modeling of the load-displacement relationship for casting joints exposed to a simple displacement field.

DTU Civil Engineering
Technical University of Denmark

Brovej, Bygning 118
2800 Kongens Lyngby

www.byg.dtu.dk

ISBN 9788778774798
ISSN 1601-2917